Drop-on-demand metal additive manufacturing from droplet formation to 3D structures

Negar Gilani, BSc, MSc

Thesis submitted to the University of Nottingham for the degree of Doctor of Philosophy

Department of Mechanical, Materials and Manufacturing Engineering,

Faculty of Engineering

October 2022

Dedicated to the three elements of my life, my mother, father, and brother.

‘Life is like riding a bicycle. To keep your balance, you must keep moving.’

Albert Einstein

Abstract

Additive Manufacturing (AM) sits at the forefront of technologies that offer unprecedented capabilities to lead a new industrial revolution. The higher degrees of complexity and flexibility in manufacturing intricate structures whilst maintaining accuracy and precision is one of the key selling points of AM technologies. Drop-on-demand metal jetting (DoD-MJ) is a promising additive manufacturing technique, gaining interest for its direct high-resolution printing of complex single and multi-material components. It also has key advantages over other metal AM techniques, such as avoiding powder handling and extensive post-processing. DoD-MJ processes are categorised based on the droplet generation actuation method. MagnetoHydroDynamic (MHD) actuators are the most advanced devices to date that have overcome the challenges of producing high-temperature droplets at high rates. MetalJet, the MHD-based system used in this thesis, has the capacity to produce molten micro-droplets (60–90 µm) at temperatures up to 2000 °C to form single and multi-material objects at 500 Hz. Applications for this technology include flexible circuits, advanced electronic components, intricate 3D mesoscale objects, and biotechnologies. In this method, 3D parts are built via spatially controlled deposition of individual molten droplets onto a substrate. Therefore, the success of the process entirely depends on the behaviour of these single droplets from deposition to solidification.

Owing to its novelty, further utilization of this technology is impeded to date by a lack of understanding of various aspects of the process, including droplet generation and interface formation, residual stress development and microstructure evolution, which have been scarcely investigated to date. This thesis uses an integrated numerical, experimental, and analytical approach to provide insights into these research questions. The in-house MetalJet platform was used to investigate formation, spreading, and solidification of metallic micro-droplets at low Weber numbers. This was undertaken by ejection and deposition of single and multiple droplets of low (Sn) and high-temperature (Ag and Cu) metal onto various substrates using a range of

jetting and substrate temperatures. High-speed photography provided insight into the mechanism of droplet generation. Analytical modelling based on the scaling method was performed to investigate the dynamics of droplets on deposition. Thermal Finite Element (FE) models were used alongside to explain the experimentally-observed morphology of droplets and investigate the droplet-to-substrate and droplet-droplet adhesion. Moreover, thermo-mechanical FE modelling was used to study the residual stress evolution during the solidification and cooling processes, and investigate its role in the observed droplet warping and delamination. Furthermore, various characterisation techniques, including FIB-SEM, EDX, EBSD, and TEM, were used to evaluate the microstructure of printed droplets.

For the first time, the generation mechanism of uniform microdroplets at high temperatures and the role of jetting voltages are explained in this thesis. Moreover, this study reports that increasing the substrate temperature intensified the diffusion between the droplet and substrate, which resulted in improved adhesion. It is also shown that ripples forming on a droplet's periphery during solidification disappeared at elevated substrate temperatures, resulting in enhanced inter-droplet bonding. Furthermore, the significant role of the substrate wettability and thermal properties, which control the droplet's dynamics and solidification behaviour, respectively, is elucidated. This highlights the importance of the substrate material selection for this technology. It is demonstrated that the steep temperature gradients during deposition result in residual stresses, and if they exceed the elastic limits of the material, stress-induced delaminating can occur. Finally, results presented in this thesis underpin the optimal process conditions under which the 3D structures produced with this technology can exhibit reliable integrity and consistency. Overall, the works represent a step forward towards the direct metal printing of high-resolution functional multi-material components.

Acknowledgements

An immense thank you to my supervisors: Dr Nesma Aboulkhair, Dr Marco Simonelli, Professor Ian Ashcroft, and Professor Richard Hague. I am deeply indebted to Nesma for her support throughout this journey, the time she spent with me in the lab, and her guidance on academic writing. Nesma, you have been a source of encouragement and inspiration in a technical field ***currently*** dominated by men. I could not have undertaken this journey without Dr Marco Simonelli, who generously provided knowledge and expertise. I am extremely grateful to Prof Ian Ashcroft for continuously challenging me to reflect deeper. Ian, without your involvement, this PhD would have never been accomplished at the same level. Your immense knowledge and plentiful experience have always encouraged me. I would like to express my deepest appreciation to Richard for his support and understanding over these past four years. Richard, thanks for the time you spent educating me, your patience, and your ***trust***. Your wisdom, knowledge, and leadership have always inspired me, but above all, I have always admired your kindness.

I wish to thank our esteemed lab technician Mr Mark East for his continuous support with our uneasy MetalJet system. I would like to thank my friends (close or miles apart), colleagues, and research team for the cherished time spent together online, in the office, lab, and social settings. My gratitude extends to the Faculty of Engineering for the funding opportunity to undertake my studies and to EPSRC for funding the MetalJet printing activity.

Last but definitely not least, I am eternally grateful to my mother, Mahnaz Farashahi, father, Asghar Gilani, and brother, Nima Gilani, for their unparalleled love, help, and support. Mum and dad, thanks for believing in me, supporting me, and respecting my rebellious choices. Maman, you are my hero and the reason for any of my successes in life. Baba, with your hard work, you proved to me that “where there is a will, there is a way”. Nima, my life-time best friend, I would never have been the person I am today without you. I am super lucky to have the three of you. ***Thank you***!

Publications and conferences

- Published Journal Papers:

Negar Gilani, Nesma T. Aboulkhair, Marco Simonelli, Mark East, Ian A. Ashcroft, Richard J.M. Hague, 'From impact to solidification in drop-on-demand metal additive manufacturing using MetalJet', Additive Manufacturing, Volume 55, 2022, DOI: 10.1016/j.addma.2022.102827.

N. Gilani, N.T. Aboulkhair, M. Simonelli, M. East, I. Ashcroft, R.J.M. Hague, 'Insights into drop-on-demand metal additive manufacturing through an integrated experimental and computational study', Additive Manufacturing, Volume 48, Part B, 2021, DOI: 10.1016/j.addma.2021.102402.

- Journal papers under preparation:

Negar Gilani, Nesma T. Aboulkhair, Marco Simonelli, Mark East, Ian A. Ashcroft, Richard J.M. Hague, 'Formation of high-temperature microdroplets in drop-on-demand Metal Jetting'.

Negar Gilani, Mykyta V. Chubynsky, Nesma T. Aboulkhair, Marco Simonelli, Mark East, Ian A. Ashcroft, James E. Sprittles, Richard J.M. Hague, 'In-flight cooling and solidification of microdroplets'.

Negar Gilani, Nesma T. Aboulkhair, Marco Simonelli, Mark East, Ian A. Ashcroft, Richard J.M. Hague, 'Drop-on-demand printing of silver structures with high aspect ratio and resolution using MetalJet'

Nesma T. Aboulkhair**, Negar Gilani**, Marco Simonelli, Mark East, Richard J.M. Hague, 'Drop-on-demand Metal Jetting of Pure Copper: On the interaction and forms of adhesion between molten metal droplets and various substrate materials'

- Accepted book chapters:

N. Gilani, A. Foerster, N. T. Aboulkhair, "Material jetting" chapter in the "Springer Handbook for Additive Manufacturing, 2022.

N. Aboulkhair, F. Bosio, **N. Gilani**, C. Phutela, R. Hague, and C. Tuck, "Additive Manufacturing Processes for Metals" chapter in the "Quality Analysis of Additively Manufactured Metals", Elsevier 2022.

- Conferences, workshops, talks, and awards:

N. Gilani, N. Aboulkhair, M. Simonelli, I. Ashcroft, R. Hague, "High-temperature Drop-on-demand Metal Jetting using MetalJet", N. Gilani, International Additive manufacturing workshop, Nottingham, UK, August 2019.

N. Gilani, N. Aboulkhair, M. Simonelli, I. Ashcroft, R. Hague, "Control of High-temperature Drop-on-demand Metal Jetting through Numerical Modelling and Experimentation", Materials Science & Technology MS&T, Pittsburgh, Pennsylvania, USA, October 4-8, 2020 (virtual).

N. Gilani, N. Aboulkhair, M. Simonelli, I. Ashcroft, R. Hague, "Investigation on drop-on-demand metal deposition using MetalJet through an integrated experimental and computational approach", TMS 2021, San Diego, California, USA, March 15-18, 2021 (virtual).

N. Gilani, N. Aboulkhair, M. Simonelli, I. Ashcroft, R. Hague, "Insights into the droplets' behaviour to control the quality of 3D parts: MetalJet"**,** Annual International Solid Freeform Fabrication Symposium (SFF Symp 2022), Austin, TX, USA, July 25-27, 2022.

N. Gilani, "How Computational Mechanics Empowers Surfing the 'Wind of Change', Ada Lovelace Day: A celebration of research and careers of women in computational sciences and engineering", University of Nottingham, 10th October 2022.

Conference, Travel and Training Funding award from the University of Nottingham, March 2022.

Contents

Abstract IV

Acknowledgements VI

Publications and conferences VII

List of abbreviation XV

Nomenclature XVII

List of figures XIX

List of tables XXXII

1. Introduction 1

2. Literature Review 6

2.1. Metal additive manufacturing 6

2.2. Metal Jetting 9

2.2.1. Piezoelectric actuators 14

2.2.2. Pneumatic actuators 15

2.2.3. Magneto-Hydro-Dynamic actuators 17

2.2.4. Other droplet-based techniques 19

2.2.4.1. Laser-induced forward transfer 19

2.2.4.2. Electrohydrodynamic redox printing 20

2.2.4.3. Microcasting 21

2.2.4.4. Digital particle ejection melting 22

2.2.4.5. Thermal spray techniques 23

2.3. Droplet formation 24

2.4. Droplet deposition behaviour 30

2.4.1. Droplet impact 31

2.4.2. Isothermal spreading of droplets 33

- Effects of impact speed on droplet's spreading 35

- Effects of surface wettability on droplet spreading 36
- Effects of surface tension on droplet spreading.....37

2.4.3. Droplet's spreading and solidification 38

2.4.4. Spreading and solidification of multiple droplets 46

- Droplet next to droplet deposition 46
- Droplet on droplet deposition 48

2.4.5. Bonding at the interfaces.....49

- Droplet-to-substrate bonding 50
- Droplet-to-droplet bonding.....52
- Droplet-on-droplet bonding 54
- Quantitative characteristics of bonding 55

2.4.6. Microstructure 56

- Single droplet.....57
- Multiple droplets.....59

2.4.7. Residual stress.....60

2.5. Modelling of droplet deposition 61

2.5.1. Modelling of droplet spreading (isothermal) 62

- Solving Navier-Stokes solution 62
- Scaling solution.....66
- Solving energy Balance equations.....67

2.5.2. Modelling of droplet solidification 68

- Solving Energy Conservation with the Navier-Stokes solution 69
- Solving the Heat Transfer equations without considering the fluid flow 72
- Solving the Stefan problem without considering the fluid flow.....73

- Solving the Energy Balance equations and considering the solidification 75

2.5.3. Modelling of residual stress development 76

2.6. Characteristics of 3D printed structures 78

2.6.1. Surface finish 78

2.6.2. Electrical conductivity 79

2.6.3. Density 80

2.6.4. Mechanical properties 81

2.7. Summary of Literature Review 83

2.8. Research problem and motivation 84

2.9. Aim and objectives of the study 85

3. Methodology 87

3.1. Experimental 90

3.1.1. MetalJet platform 90

3.1.2. Materials 93

3.1.3. Temperature control, jetting pulses and frequencies, other parameters 95

- Droplet temperature control 95
- Jetting pulses 96
- Jetting frequency and speed 97
- Other parameters 97

3.1.4. Printing experiments 98

3.1.5. Characterisation techniques 99

3.1.5.1. Techniques to study the droplets characteristic in flight 99

3.1.5.2. Technique to investigate the surface roughness 101

3.1.5.3. Techniques to study droplets' morphology 102

3.1.5.4. Techniques used to study the bonding levels....102
3.1.5.5. Techniques to study the microstructure....105
3.2. Computational....107
3.2.1. In-flight cooling of droplets....108
3.2.2. Thermal model definition....109
3.2.3. Mechanical model definition....112
3.2.4. Parameters and material properties....114
3.2.5. Mesh and boundary conditions....117
3.2.6. Time step and solution control....118
3.3. Summary....119
4. Droplet Formation in The MetalJet Process: Silver....121
4.1. Mechanism and sequences of droplet ejection....123
4.2. Effects of jetting voltage on breakup length and droplet formation....124
4.3. Effects of jetting voltage on droplets characteristics....130
4.4. Summary....135
5. Droplet Dynamics and Solidification in The MetalJet Process: Copper, Tin, and Silver....137
5.1. Model verification....138
5.2. Morphology of individual copper droplets....141
5.2.1. Droplet's spreading and solidification....143
5.2.2. Effects of surface roughness on droplet's morphology....146
5.3. Morphology of individual tin droplets....148
5.3.1. Effect of superheat temperature....151
5.3.2. Effect of initial substrate temperature....156
5.3.3. Effect of substrate material....159
5.4. Morphology of individual silver droplets....163

5.4.1. Droplet's dynamic and solidification 166
5.5. Summary 174
6. Formation of Droplet- Substrate Interface and Microstructure: Copper, Tin, and Silver 177
6.1. Adhesion of Cu droplets to a Cu substrate 179
6.1.1. The mechanism of droplet-substrate bonding 180
6.1.2. Effects of substrate temperature on the droplet-substrate bonding 182
6.1.3. The effects of surface roughness on the droplet-substrate bonding 184
6.1.4. Effects of droplet size on the droplet-substrate bonding 186
6.2. Adhesion of Sn droplets to various substrates 187
6.2.1. Effects of droplet temperature 189
6.2.2. Effects of substrate temperature 191
6.2.3. Effects of substrate material 192
6.3. Adhesion of Ag droplets to an Ag substrate 194
6.3.1. High substrate temperatures 194
6.3.2. Medium substrate temperatures 196
6.3.3. Low substrate temperature 199
6.4. Summary 201
7. Formation of Droplet- Droplet Interface and Microstructure: Copper, Tin, and Silver 203
7.1. Copper inter-droplet bonding 204
7.1.1. Effects of substrate temperature on inter-droplet bonding 207
7.2. Tin inter-droplet bonding 211
7.3. Silver inter-droplet bonding 213
7.4. Summary 217
8. Residual Stress Evolution in the MetalJet Process: Copper 219
8.1. Residual stress generation during a single droplet deposition 220

8.2. Effects of various process parameters on residual stresses 225
8.2.1. Effect of initial substrate temperature 225
8.2.2. Effect of initial droplet temperature (superheat) 227
8.2.3. Effect of surface roughness 228
8.3. Summary 230
9. Implications of the Developed Knowledge 232
9.1. Implications of droplet formation investigation in 3D printing through DoD-MJ 234
9.2. Implications of droplet morphology investigation in 3D printing through DoD-MJ 236
9.3. Implications of interface formation investigation in 3D printing through DoD-MJ 239
9.4. Implications of microstructure investigation in 3D printing through DoD-MJ 241
9.5. Implications of residual stresses investigation in 3D printing through DoD-MJ 242
9.6. The implication of the current study in developing new materials and the system's limitations 243
10. Conclusions and Recommendations for Future Research 245
10.1. Recommendation of Future Work 247
10.1.1. Process and modelling 248
10.1.2. Characterisation 249
Reference 250

List of abbreviation

AM	Additive Manufacturing
ASTM	American Society for Testing and Materials
CAD	Computer Aided Design
CTE	Coefficient of Thermal Expansion
DED	Direct Energy Deposition
DPEM	Digital Particle Ejection Melting
DoD	Drop on Demand
DoD-MJ	Drop on Demand Metal Jetting
EBM	Electron Beam Melting
EBSD	Electron Backscatter diffraction
EB-PVD	Electron beam- Physical vapour deposition
EDX	Energy Dispersive X-ray
EHD-RP	Electrohydrodynamic redox printing
FE	Finite Element
FIB	Focused Ion Beams
HF	High Frequency HF
IPF	Inverse Pole Figure
MHD	Magnetohydrodynamic
L-PBF	Laser-Powder Bed Fusion
LENS	Laser Engineered Net Shaping
LIFT	Laser-induced forward transfer

LMD	Laser Metal Deposition
MIG	Metal Inert Gas
NPJ	Nano-Particle Jetting
OFHC	Oxygen-Free High Thermal Conductivity
PDM	Plasma Deposition Manufacturing
RF	Radio Frequency
SDM	Shape Deposition Manufacturing
SEM	Scanning Electron Microscope
TEM	Transmission electron microscopy
TIG	Tungsten Inert Gas

Nomenclature

ρ	Density (Kg/m^3)
σ_s	Surface tension ($N/\ m$)
ϑ	Kinetic viscosity (m^2/s)
μ	Dynamic viscosity ($Pa.s$)
ϵ_{em}	Emissivity
σ_{SB}	Stefan-Boltzmann constant ($W/\ m^2\ °C^4$)
θ	Solidification contact angle (°)
θ_e	Equilibrium contact angle (°)
μ	Dynamic viscosity ($Pa.s$)
ϑ	Kinetic viscosity (m^2/s)
$\sigma_{angular}$	Angular trajectory deviation (°)
α_t	A user-defined parameter to correlate thermal resistance to surface tension and contact pressure
B	Magnetic flux density (T)
Bi	Biot number
C_{mf}	conductivity multiplier factor
C_P	Specific heat capacity (J/ $Kg\ °C$)
Ca	Capillary number
D	Droplet's diameter (m)
D_{max}	Droplet's spreading
F	Surface tension
Fr	Froud umber
h	A user-defined combined radiative and convective heat transfer coefficient ($W/\ m^2\ °C$)
h_{conv}	Free heat convection coefficient ($W/\ m^2\ °C$)

h_{if}	Convective heat transfer for droplets in-flight ($W/m^2\,°C$)
K_{eff}	effective thermal conductivity (W/m^2C)
K	Thermal conductivity (W/m °C)
K_c	Thermal conductance coefficient (W/m^2C)
L	Latent heat of solidification (KJ/Kg)
Nu	Nusselt number
Oh	Ohnesorge number
Pr	Prandtl number
r	Droplet's radius (m)
R_c	Thermal contact resistance (m^2C/W)
Re	Reynolds number
R_a	Surface roughness
Ste	Stephan number
T_s	Substrate temperature ($°C$)
T_∞	Ambient temperature ($°C$)
T_l	Liquidus temperature ($°C$)
T_d	Droplet temperature ($°C$)
We_j	Jetting Weber number
We	Weber number
V	Droplet's in-flight speed (m/s)
x	Droplet's height (m)
y	Interface length (m)

List of figures

Figure 2.1- Schematic presentation of the continuous jetting operational concept. .13
Figure 2.2- Schematic presentation of the operational concept of discontinuous jetting. 14
Figure 2.3- a) a schematic presentation of a material jetting system using piezo-electric actuation [63], b) pillar array in AlSi12 [64], c) inclined pillar in Sn63Pb37 [64]. 15
Figure 2.4- a) a schematic representation of a jetting mechanism deploying pneumatic actuation, thin-walled 3D objects in Sn fabricated by pneumatic metal jetting systems b) [67], c) [65]. 16
Figure 2.5- SEM pictures of StarJet nozzle a) top view, b) cross-sectioned view, c) working principle of the StarJet dispenser [68], d) three solder columns printed with the StarJet system [72]. 17
Figure 2.6- a) The cross-sectioned view of Canon-Océ actuator [28], b) an electronic circuit in Sn printed through the MetalJet platform [27], c) the cross-sectioned view of Magnetojet actuator, d) a cylinder in Al printed through Xerox metal jet printer(Magnetojet) [25].....18
Figure 2.7- a) A schematic presentation of the Laser-induced forward transfer working principle, b) SEM image of LIFT-printed copper logo of the on an epoxy glass laminate, c) a zoom at the middle of the letter “m” [81].....19
Figure 2.8- a) the schematic presentation of the EHD-RP working principle, b) bi-metal pillars printed with alternating segments of Ag and Cu–Ag c) concentric, out-of-plane sine waves printed with a layer-by-layer strategy [82]. 20
Figure 2.9- Schematic representation of microcasting process, a) MIG microcaster, b) TIG microcaster, c) Plasma-arc microcaster.....22
Figure 2.10- a) schematic representation of the digital particle ejection and melting (DPEM) process, b) line of overlapping 150 μm solder droplets on a tin substrate, c) polished and etched cross-section of the printed line shown in a [42].....23

Figure 2.11- the principle of thermal spraying [87]. 24
Figure 2.12-Sequences of aqueous glycol solutions droplet formation using a piezoelectric actuator: a) when the satellite droplet merges with the main droplet, b) formation of satellite droplets [90]. 25
Figure 2.13- Velocity profiles of the drop tail and head during and after the droplet breakup [91]. 26
Figure 2.14- Printability map proposed by Lui and Derby based on the jetting We and Z numbers in inkjet printing [93]. 27
Figure 2.15- a) non-dimensional droplet diameter as a function of the dwell time at various voltages, optical images of solder droplets obtained for b) $td = 0.5\ ms$ and $V = 20\ V$, c) $td = 0.05\ ms$ and $V = 20\ V$, d) $td = 0.5\ ms$ and $V = 30\ V$, e) $td = 0.05\ ms$ and $V = 30\ V$ [100]. 29
Figure 2.16- Possible scenarios during the impact of a droplet onto a surface, a) spreading, b) splashing, and c) rebounding. 32
Figure 2.17- Illustration of a droplet on a solid substrate with surface free energies and equilibrium contact angle. 33
Figure 2.18- The classification of droplet spreading based on their driving and resisting force. 35
Figure 2.19- Impact of a water microdroplet of a) 60 µm with an initial velocity of 0.74 m/s (we=0.45), and b) 66 µm with a velocity of 11.4 m/s (We=119) onto a solid surface [123]. 36
Figure 2.20- Evolution of 49 µm water droplets' shape during the impact and spreading onto a) hydrophilic and b) hydrophobic surfaces (the number at the top left of each frame indicates the time in µs) [125]. 36
Figure 2.21- Impact of 1.4 mm water droplets with an impact velocity of 0.7 m/s onto a) wettable, b) partially wettable, and c) not-wettable substrate [124]. 37
Figure 2.22-Droplet morphology evolution during the impact of droplets of a) pure water, b) water with 100 ppm of surfactant solution, and c) 1000 ppm surfactant solution [126]. 38
Figure 2.23- Schematic representation of various hypotheses with regards to the mechanism of contact line arrest based on: a) the critical solidification contact angle [119], b) solidification of a critical volume at the contact line [32], c) the liquid at the

contact line reaches a critical temperature [30], d) a critical thickness of the droplet is solidified [31]. 40
Figure 2.24- Evolution of morphology of solder microdroplets of 210 C onto a gold-coated semiconductor substrate a) at 48 C with an impact velocity of 1.54 m/s and b) at 135 C with an impact velocity of 1.49 m/s (droplets' diameters are 80 µm and 84 µm in a and b, respectively) [40]. 42
Figure 2.25- Spreading and solidification evolution of a 1.2 mm Sn droplet onto a stainless steel substrate at various temperatures [130].....43
Figure 2.26- Top and side view images during the impact of a 1.7 to 2 mm Sn droplet at a velocity of 0.5-5.5 m/s onto a Sapphire substrate at a) 249 °C (Isothermal deposition), b) 150 °C, and c) 39 °C [31]. 44
Figure 2.27- Mechanism of contact line arrest in a hexadecane droplet of 0.85 mm gently deposited onto a Saphir substrate [127]. 45
Figure 2.28- a) Horizontal and L-shaped solidification ripples on the surface of the 1st droplet and 2nd droplet, respectively. b) numerical simulations predicting the formation of solidification ripples inter-droplet pores [13]. 47
Figure 2.29- Final morphology of solder successive solder droplets as a function of Al substrate temperature [138]. 47
Figure 2.30- Effects of substrate temperature a)25 C, b) 75 C, c) 125C and jetting velocity d) 1.12 m/s, e)1.38m/s, f)1.63 m/s on the morphology of solder pillar made by microdroplets of 80um in diameter (modified) [83]. 48
Figure 2.31- a) Evolution of solid fraction in time, b) the diagram of remelting zone during the deposition of a pillar of Al alloy droplets [141]. 49
Figure 2.32- Cross-section of a xx mm Stainless Steel (SS) droplet at 2500 °C on a SS substrate at 30 °C, a) 50 x magnification, b) close zoon at the interface [139]. ...51
Figure 2.33- Single Ag droplet on a Cu substrate a) FIB-SEM image indicating a poor bonding to the substrate, b) the element distribution at the interface, c) EDX of the zone in (b) with Ag depicted in green and Cu in orange [11]. 51
Figure 2.34- The inter-droplet bonding at various droplet and substrate temperatures. a) $Tdrop = 660\ °C\ \&\ Tsub = 350\ °C$, b) $Tdrop = 700\ °C\ \&\ Tsub = 450\ °C$, c) $Tdrop = 740\ °C\ \&\ Tsub = 500\ °C$ [143]. 52

Figure 2.35- a) temperature evolution of the 1st droplet during the deposition of the second droplet at four locations based on the numerical simulations, b) Lack of inter-droplet bonding at zones with pores [63]. 53
Figure 2.36- a) the melting and no-remelting conditions predictions based on an analytical model in various droplet and substrate temperature ranges for Sn droplets. Cross-section of vertical columns of 0.75 mm Sn droplets at b) $Td = 275\ C$ and $Ts = 100\ C$, c) $Td = 275\ C$ and $Ts = 190\ C$, d) $Td = 250\ C$ and $Ts = 100\ C$, e) $Td = 325\ C$ and $Ts = 100\ C$ [67].....54
Figure 2.37- In situ SEM instrumented indentation showing the a) droplet before and b) after applying the force [149].....55
Figure 2.38- SEM images of a single 7075 Al alloy droplet showing a) the droplet's morphology, b) internal microstructure in the transition zone between ripples and rosette regions, c) the microstructure of the rosette area (images modified from [58]). 58
Figure 2.39- SEM images of the top surface of a 3 mm lead droplet deposited at 495 °C onto room temperature a) Cu, b) Al, and c) Pyrex substrates. d-c) SEM images of the droplet-substrate interfaces of the corresponding cases [132]. 59
Figure 2.40- The microstructure of a pillar made of 7075Al alloy droplets of 0.8 mm [58]. 59
Figure 2.41- Experimental images during the solidification of Hexadecane drops, showing the delamination behaviour for undercooling of a) ΔT= 4.5 K, and b) 11 K [160]. 61
Figure 2.42- a) Spreading factor and b) dynamic contact angle evolution of a glycerol droplet impacting on a hydrophilic substrate using various dynamic contact angle models [172]. 65
Figure 2.43- Spreading of a microdroplet (D=50 um) at Re = 130 (V=5 m/s) on a hydrophilic substrate (grey) and a hydrophobic substrate (green) at dimensionless time scales (t=1 → t=5 us) [116].....66
Figure 2.44- Thermal resistance at the interface at a: macroscopic and b: microscopic levels [189]. 71

Figure 2.45- The optimal droplet and substrate temperature ranges to obtain a good metallurgical inter-droplet bonding for 7075 Al alloy according to equation 38 [200]. 74
Figure 2.46- Geometry and boundary condition of the 2D thermomechanical model in the microcasting process [191]. 77
Figure 2.47- a: temperature and stress in a fixed point on the substrate for slow rate deposition, b: final radial stress distribution for one and multilayers during slow and rapid deposition [191]. 78
Figure 2.48- a) 3D topography of a cube from 270 µm solder droplets, b) top view image, and c) roughness profile in the red arrow indicated in (b) [215].....79
Figure 2.49- a) printed Sn lines using DoD-MJ and its cross-sectional view, b) the electrical resistivity of printed lines vs. the bulk material [9].....80
Figure 2.50- Reconstructed porosity (in red) obtained through X-Ray CT scan in a) as-built and b) sintered DoD-MJ Ag samples [11]. 81
Figure 2.51- SEM images of tensile fractography for DoD-MJ as-deposited AA7075 aluminium for various droplet/substrate temperature combinations [220]. 83
Figure 3.1- Flowchart summarising the methodology used in the thesis.....89
Figure 3.2- Schematic representation of MetalJet platform.....91
Figure 3.3- Side-view image of cartridge demonstrating the actuation chamber. 92
Figure 3.4- a)3D and top view images of the MetalJet substrate holder design, b) and its integration to the MetalJet stage.....93
Figure 3.5-The manual heating setup.....95
Figure 3.6- Jetting waveforms.....97
Figure 3.7- Schematic representation of deposition error caused by lateral speed and high standoff distances.....98
Figure 3.8- The printing experiment layout used in this thesis to investigate the morphology of droplets, droplet-substrate, droplet-droplet bonding, and microstructure evolution. The SEM image is taken from an experiment of Ag deposition at 1040 °C onto an Ag substrate at 775 °C.....99
Figure 3.9- Schematic representation of droplet formation observation through the JetXpert system. a) the set-up including the camera, printhead, LED strobe, and strobe controller, b) Data obtained from the JetXpert camera demonstrating a) a

successful purge, b) double-droplet-based analysis, and c) calculated and measured information. 101
Figure 3.10- The schematic representation of a) in-situ milling using FIB, b-d) steps used to cross-section the interface of droplets with substrates. 103
Figure 3.11- Steps of sample preparation using FIB milling, a-b) selecting the zone, c) tilting stage to have ion beams parallel to the surface, and setting the cross-sectioning dimension, including the milling depth and beam current, d) verifying the cross-section area to identify the beam parameters for the refining step, e) cleaning the surface using low current on a small cross-section area, f) etching the sample using medium ion beam current. 104
Figure 3.12- Sample preparation steps using FIB milling, a-b) selecting the zone, c) tilting stage to have ion beams parallel to the surface, and setting the cross-sectioning dimension, including the milling depth and beam. 105
Figure 3.13- Steps of EBSD and EDX sample preparation using a xenon-plasma FIB, a) deposition of a Pt layer to protect the lift-out lamella, b) milling both sides of the droplets, c) milling the bottom and side section of the lamella, d) welding the needle to the lamella using Pt deposition, and milling the last portion of the lamella, e) lifting the lamella out, f) welding the lamella to the Cu crown using Pt deposition. 106
Figure 3.14- Geometry of droplet and substrate for a) single droplet deposition and b) multiple droplet deposition. 110
Figure 3.15- Initial mesh of droplet and substrate for a) single droplet deposition and b) multiple droplet deposition model. 117
Figure 3.16- Flowchart summarising the methodology used in the thesis. 120
Figure 4.1- The first challenge to be addressed in this thesis referring to Figure 52. 122
Figure 4.2- Various stages of droplet formation demonstrating the formation of satellite free Ag microdroplets at 1020 °C with a frequency of 250 Hz and jetting voltage of 5 V. 124
Figure 4.3- Various stages of droplet formation for Ag at 1020 °C with a jetting frequency of 500 Hz a) jetting voltage of 4.5 V showing the retraction of satellite droplet to the nozzle, b) jetting voltage of 5 V showing the formation of uniform and

satellite-free droplets, and c) jetting voltage of 5.5 V showing the formation of single satellite droplets. 126
Figure 4.4- Ligament length of Ag at 1020 °C from the nozzle in time for various jetting voltages. 128
Figure 4.5- Droplet formation map based on dimensionless numbers a) Jetting We and Oh numbers, b) Jetting We and Re number. 130
Figure 4.6- In-flight droplet characteristics measurement using the JetXpert camera. 131
Figure 4.7- Distribution of droplets' diameter of droplets for events of 150 ejections with various jetting voltages **a)** 4.5 V, **b)** 5V, **c)** 5.5 V, **d)** in-flight solidified Ag droplets with the jetting voltage of 5.0 V, collected at 10 cm below the nozzle, **e)** SEM image of the droplets presented in d. 132
Figure 4.8- Characteristics of individual droplets in-flight for various jetting voltages a) droplets speed and b) trajectory of droplets.....133
Figure 4.9- Droplet's radius and speed variation as a function of jetting voltage for Ag at 1020 °C. The error bars represent the maximum and minimum values.....134
Figure 5.1- The second challenge in DoD-MJ and the methodology implied in this thesis to address it, referring to Figure 52.....138
Figure 5.2- FIB-SEM cross-section of individual Sn droplets deposited on an Sn substrate **a)** $Tdrop = 655\ °C$ and $Tsubstrate = 50\ °C$ indicating partial remelting of the substrate interface, and **b** $Tdrop = 755\ °C$ and $Tsubstrate = 50\ °C$ indicating partial remelting of the substrate interface, **c)** $Tdrop = 955\ °C$ and $Tsubstrate = 50\ °C$ indicating complete remelting of the substrate interface, and **d)** $Tdrop = 655\ °C$ and $Tsubstrate = 100\ °C$ indicating partial remelting of the substrate interface.....139
Figure 5.3- Sn substrate temperature evolution at the interface of an Sn droplet when: **a)** $Tdrop = 655\ °C$ and $Tsubstrate = 50\ °C$ for nodes below the droplet centre, 25 µm from the droplet edge, and the droplet edge, **b)** $Tdrop = 755\ °C$ and $Tsubstrate = 50\ °C$ for nodes below the droplet centre, 12 µm from the droplet edge, and the droplet edge, **c)** $Tdrop = 955\ °C$ and $Tsubstrate = 50\ °C$ for nodes below the droplet centre, 3 µm from the droplet edge, and the droplet edge, and **d)**

$Tdrop = 655\ °C$ and $Tsubstrate = 100\ °C$ for nodes below the droplet centre, 18 µm from the droplet edge, and the droplet edge. 141
Figure 5.4- Morphology of single Cu droplet deposited on a Cu substrate, forming ripples on their periphery during the solidification: **a)** side view, **b)** top view.....143
***Figure 5.5**- 3D profile temperature whilst single droplet cooling, taken at a real-time of a) t=7 µs, b) t=27 µs, c) t=47 µs, d) temperature evolution of nodes in the top, middle, and interface of the droplet.* 145
Figure 5.6- Effect of surface roughness on Cu droplet morphology.....147
Figure 5.7- Effect of surface roughness on the repeatability of droplet morphology. 148
Figure 5.8- Schematic representations of droplet impact and spreading timeline, and dynamic contact angle evolution.....150
Figure 5.9- Morphology of individual Sn droplets deposited onto a copper substrate at 130 °C, for droplets ejected at temperatures **a)** 670 °C, **b)** 850 °C, **c)** 1000 °C. .152
Figure 5.10- Cooling curves at the central nodes in the interface and top of the droplets when deposited with various superheat temperatures. 153
Figure 5.11- Evolution of oscillation and damping periods for the droplets when deposited with various superheat temperatures.....154
Figure 5.12- The spreading factor and solidification contact angle as a function of initial droplet temperature for substrate at 130 °C. The error bars represent the standard deviation. 155
Figure 5.13- Morphology of individual molten Sn droplets at 670 °C onto a Cu substrate with an initial temperature of **a)** 30 °C, **b)** 130 °C, and **c)** 220 °C. 156
Figure 5.14- Cooling curves at the central nodes in the interface and droplet top deposited on the substrate at various temperatures. 157
Figure 5.15- Evolution of oscillation and damping periods for the droplets when deposited with various undercooling temperatures. 158
Figure 5.16- The spreading factor and solidification contact angle as a function of initial substrate temperature for droplets jetting at 670 °C. The error bars represent the standard deviation. 159
Figure 5.17- Morphology of individual molten Sn droplets at 670 °C deposited onto **a)** Cu, **b)** Sn, and **c)** Zn substrates at 30°C.....160

Figure 5.18- Cooling curves at the central nodes in the interface and droplet top deposited on various substrates. 161
Figure 5.19- Evolution of oscillation and damping periods for droplets deposited on various substrates. 162
Figure 5.20- The spreading factor and solidification contact angle as a function of the substrate material for droplets jetted at 670°C onto substrates at 30°C. The error bars represent the standard deviation. 163
Figure 5.21- Schematic representations of impact and spreading evolution of Ag microdroplets.....167
Figure 5.22- Morphology of individual Ag droplets for various droplet temperatures a) 1200 °C, b) 1120 °C, c) 1025 °C deposited onto an Ag substrate at 775 °C. 167
Figure 5.23- Droplets' solidification timeline based on simulation and analytically predicted ripple distances based on the droplets dynamics for various droplet temperatures deposited onto an Ag substrate at 775 °C.....169
Figure 5.24- Morphology of individual Ag droplets for various droplet temperatures a) 1200 °C, b) 1120 °C, c) 1025 °C deposited onto an Ag substrate at 400 °C. 170
Figure 5.25- Droplets' solidification timeline based on simulation and analytically predicted ripple distances based on the droplets dynamics for various droplet temperatures deposited onto an Ag substrate at 400 °C.....171
Figure 5.26- Morphology of individual Ag droplets for various droplet temperatures a) 1200 °C, b) 1120 °C, c) 1025 °C deposited onto an Ag substrate at 25 °C. 172
Figure 5.27- Droplets' solidification timeline based on simulation and analytically predicted ripple distances based on the droplets dynamics for various droplet temperatures deposited onto an Ag substrate at 25 °C.....173
Figure 6.1- The third and fourth challenges in DoD-MJ and the methodology implied in this thesis to address it, referring to Figure 52.....178
Figure 6.2- FIB-SEM cross-section of individual Cu droplet deposited on a Cu substrate showing **a)** droplet's polycrystalline microstructure with large grains, **b)** absence of substrate remelting or diffusion at the interface, and droplet delamination in the edges.....181

Figure 6.3- Cross-sectional profile views of temperature during single droplet deposition, taken in real-time of **a)** t=7 µs, **b)** t=27 µs, **c)** t=547 µs after deposition. 182
Figure 6.4- Cross-section of individual Cu droplets deposited at 1090 °C onto Cu substrates at 500 °C and 750 °C to investigate effects of the substrate temperature on droplet-substrate. The inset presents the close-up of the interface indicated in the black box. 183
Figure 6.5- Effect of surface roughness ($Ra = 0.01$ µm and $Ra = 0.1$ µm) on the droplet-substrate bonding for deposition of Cu droplet on Cu substrate at 750 °C. The inset presents the close-up of the interface indicated in the black box. 186
Figure 6.6- Effect of droplet size of 60 µm and 80 µm in diameter on the droplet-substrate bonding for deposition of Cu droplet on Cu substrate at 750 °C. The inset presents the close-up of the interface indicated in the black box. 187
Figure 6.7- Thermo-Calc generated Sn-Cu phase diagram and schematic representation of Cu atom diffusion into liquid Sn to form intermetallic layers. 190
Figure 6.8- FIB-SEM cross-sections of the interfaces for droplets deposited at **a)** =670 °C, **b)** 850 °C, and **c)** 1000 °C onto a Cu substrate at 130°C showing the formation of IM layers with various consistency, **d)** the substrates temperature evolution at the interface during the solidification and cooling of droplets. 190
Figure 6.9- FIB-SEM cross-sections of the interfaces for droplets deposited at 670°C onto a Cu substrate at **a)** 30°C, **b)** 130°C, and **c)** 220°C, showing the formation of IM layers with various thicknesses, d) the substrates temperature evolution at the interface during the solidification and cooling of droplets. 192
Figure 6.10- FIB-SEM cross-sections of the interfaces for droplets deposited at 670 °C onto **a)** Cu, **b)** Sn, and **c)** Zn substrates at 30 °C, **d)** the substrates temperature evolution at the interface during the solidification and cooling of droplets. 193
Figure 6.11-The interface of Ag droplets deposited at a) 1200°C, b) 1120°C, and a) 1040°C onto the Ag substrate at 7750°C and the substrate temperature evolution at the centre of droplets obtained from the numerical simulations. 195
Figure 6.12- The interface of Ag droplets deposited a) 1200°C, b) 1120°C, and a) 1040°C onto the Ag substrate at 400°C and the substrate temperature evolution at the centre of droplets obtained from the numerical simulations. 197

Figure 6.13- The recrystallization of the substrate interface during the deposition of Ag droplet at 1200 °C on a substrate at 400 °C. 198
Figure 6.14- The interface of Ag droplets deposited at a) 1200°C, b) 1120°C, and a) 1040°C onto the Ag substrate at 25°C and the substrate temperature evolution at the centre of droplets obtained from numerical simulations. 200
Figure 7.1: FIB-SEM cross-section of two successively deposited droplets demonstrating the lack of remelting at the interface between droplets, and various grain structures for the first and the second droplet. 204
Figure 7.2- EBSD IPF-X map of two successively deposited droplets in the region highlighted in figure 103 indicating the absence of epitaxy at the interface between droplets. 205
Figure 7.3- Cross-section profile views of temperature whilst second droplet solidification, taken at a real-time of **a)** t=0.4 µs, **b)** t=19 µs, **c)** t=48 µs, **d)** temperature evolution of various nodes at $droplet1$'s interface with $droplet2$ in the bottom, middle, and top sections.....206
Figure 7.4- Temperature evolution of nodes at the centre of droplets during the deposition of $droplet1$ and $droplet2$.....207
Figure 7.5- FIB-SEM cross-section of two successively deposited Cu droplets onto a Cu substrate at 750 °C, EBSD IPF-X map over the cross-sectioned area. 208
Figure 7.6- EBSD IPF-X map of two successively deposited droplets shown in Figure **7.5** indicating an epitaxial growth from the interface of the previously deposited droplet. 209
Figure 7.7- EBSD-IPF-X map two successively deposited droplets with highlighted grain boundaries and special boundaries indicating twin boundaries at the inter-droplet interface. 210
Figure 7.8- a) FIB-SEM image of two successively deposited Sn droplets ejected at 670 °C on a Cu substrate at 30 °C, b) FIB-SEM image of the cross-section demonstrating a strong inter-droplet bonding through remelting, b) temperature evolution of a central node at $droplet1$'s interface with $droplet2$.....212
Figure 7.9- a) FIB-SEM cross-section of two successively deposited Sn droplets ejected at 670 °C on a Cu substrate at 130 °C, demonstrating a strong inter-droplet

bonding through remelting, b) temperature evolution of a central node at $droplet1$'s interface with $droplet2$. 213
Figure 7.10- FIB-SEM vertical cross-section of two successively deposited Ag droplets at 1200 °C on an Ag substrate at 775 °C, demonstrating a strong inter-droplet bonding through remelting.....214
Figure 7.11- a) FIB-SEM image of a 3D structure in Ag at 1200 °C on an Ag substrate at 775 °C, b) cross-section of the zone highlighted with a black square, demonstrating a strong inter-droplet bonding through remelting. 216
Figure 8.1- The fifth challenge in DoD-MJ and the methodology implied in this thesis to address it, referring to Figure 52. 220
Figure 8.2- SEM cross-section of individual Cu droplet after FIB milling of : **a)** 16 µm, **b)** 20 µm, **c)** 45 µm from the edge showing the partial delamination of the droplet from the substrate.....221
Figure 8.3- σyy and $\sigma Max\ pricncipal\ stress$ fields (MPa) in the Y-Z plane whilst first droplet cooling at real-time of **a)** t=7 µs, **b)** t=27 µs, and **c)** t=2000 µs after deposition. 222
Figure 8.4- Droplet's deformation in µm in Y direction exaggerated 20 times at **a)** 7 µs, **b)** 27 µs, **c)** 2000 µs after deposition. 223
Figure 8.5- Schematic representation of the residual stresses in the droplet and substrate during the early stage of solidification, yielding to edge curling. 224
Figure 8.6- The maximum principal stress to temperature-dependent yield strength ratio in **a)** the radial path at the interface of droplet and substrate (Y line shown in Figure 11), **b)** droplet and substrate thickness at the edge (Z line shown in Figure 11). 225
Figure 8.7- Temperature evolution for various substrate temperatures at **a)** the central node in the droplet, **b)** substrate interface. Maximum principal stress to temperature-dependent yield strength ratio for various substrate temperatures at time frames corresponding to similar interfacial temperatures in **c)** the radial path at the interface of droplet and substrate (Y line shown in Figure 115), **d)** droplet and substrate thickness at the edge (Z line shown in Figure 115). 226

Figure 8.8- Temperature evolution during droplet deposition considering different superheat temperatures for a node **a)** at the centre of the droplet and **b)** at the interface of the substrate with the droplet. 228
Figure 8.9- Temperature evolution during droplet deposition considering different substrate roughness for a node **a)** at the centre of the droplet, **b)** at the interface of the substrate with the droplet. Maximum principal stress to temperature-dependent yield strength ratio for various substrate roughness in **c)** the radial path at the interface of droplet and substrate (Y line shown in Figure 115), **d)** droplet and substrate thickness at the edge (Z line shown in Figure 115. 230
Figure 9.1-Demonstration of MetalJet capacity in printing 2D and 3D defect-free structures: a) an electronic circuit in Sn on a Cu substrate, b)a pyramid in Cu on a Cu substrate, c) a 2D honeycomb pattern in Cu on a Cu substrate, d) Ag propeller on an alumina substrate, e) Cu walls of various thicknesses on a Cu substrate, f) Ag overhang pillars on a Cu substrate, g) an Sn cone on a Cu substrate, h) Boris spider in Sn on a Cu substrate, i) a lattice structure in Ag on a Cu substrate. 233
Figure 9.2- The graphical abstract demonstrating the five principal elements involved in the metal jetting processes. 234
Figure 9.3- (I) Issues related to the formation of satellite droplets a) geometrical failure due to deposition of satellite droplets in undesired locations, b) structural failure due to the non-uniform size of droplets. (II) The necessity of in-situ monitoring to avoid c-d) staircasing and inter-droplet gaps due to the small and large overlap between droplets, respectively, both related to the lack of information about the droplet size, e) the inaccuracy in the droplet deposition due to the misalignment of droplet trajectory. 236
Figure 9.4- a) *Inter-droplet gap and* ***b)*** *droplet staircasing due to overlapping misadjustment,* ***c)*** *high surface roughness and inter-droplet void due to high solidification contact angle,* ***d)*** *loss of accuracy due to over-spreading of droplets,* ***e)*** *pores due to lack of fusion formed at mating surfaces when ripples are present,* ***f)*** *droplet delamination due to the poor droplet-to-substrate bonding.*.....238
Figure 9.5- a) delamination of a single droplet from the substrate due to a poor adhesion, b) crack propagation at the droplets' interface due to the lack of bonding. 241

List of tables

Table 2.1- The advantages and disadvantages of various Metal Additive Manufacturing technologies. 11
Table 3.1- Temperature-dependent properties of pure Cu. 115
Table 3.2- Temperature-dependent flow stress of Cu. 116
Table 3.3- Temperature-dependent properties of pure Sn. 116
Table 3.4- Temperature-dependent properties of pure Ag. 117
Table 5.1- Specific set of parameters used to investigate the Sn droplets' final morphology. 151
Table 5.2- Specific set of parameters used to investigate the Ag droplets' final morphology deposited onto Ag substrates. 166
Table 5.3- The solidification period of Ag droplets deposited to Ag substrates at various droplet and substrate temperatures and the spreading sequence during which the contact line was halted. 174
Table 6.1- specific set of parameters used for evaluating the adhesion of Cu droplets to the Cu substrates. 180
Table 6.2- Specific set of parameters used for evaluating the adhesion of Sn droplets to various substrates. 188
Table 6.3- Specific set of parameters used for evaluating the adhesion of Sn droplets to various substrates. 194
Table 8.1- Specific set of parameters to investigate the residual stresses evolution during the solidification of Cu droplets on Cu substrates. 220

1. Introduction

Manufacturing, the process of transforming raw materials into goods or products that are ready for use by the respective consumers, is constantly evolving to cope with the growing product demand. There are several forms of manufacturing processes, where additive manufacturing (AM) is one of the most recent categories and has revolutionized the production industry in the past decades. AM, also known as 3D printing, is a method of directly fabricating 3D structures by additively depositing material in a pixel-by-pixel or layer-by-layer fashion [1]. ASTM (American Society for Testing and Materials), defines Additive Manufacturing (AM) as “a process of joining materials to make objects from 3D model data, usually layer upon layer, as opposed to subtractive manufacturing methodologies” [2]. The higher degrees of complexity and flexibility in manufacturing intricate structures whilst maintaining accuracy and precision is one of the key selling points of AM technologies. AM is often a more sustainable manufacturing process since it can create products with increased efficiency and reduced wastage of material [3]. AM parts are already used in various industrial and academic fields, yet it is expected that it will increasingly affect and be relevant to global businesses as the credibility of AM increases.

Metal jetting, also known as liquid metal jet printing, is a nascent additive manufacturing (AM) technology that has the potential to fabricate metallic components, both single and multi-material, at a resolution not achievable with the more common metal additive manufacturing techniques. The metal jetting approach primarily consists of dispensing and depositing individually-controlled droplets of molten metal onto a substrate at precise locations. From an operational perspective, there are similarities between metal jetting and micro-casting, spray shape deposition manufacturing (SDM) [4], and thermal spraying [5]. However, the control over the size of droplets, jetting speed and the precision of manufacturing set metal jetting apart from these other processes.

Metal jetting has advantages over other AM technologies, such as Laser Powder Bed Fusion (L-PBF), Directed Energy Deposition (DED), and binder jetting, due to the higher resolutions, improved surface quality [6], and simplified fabrication approach. This simplicity is granted by the wide availability of potential feedstock materials [7], no residual impurities, elimination of the need for pre-processing, such as powder handling, and post-print processing, such as polishing or grinding, to achieve an acceptable surface finish. Importantly, compared with conventional L-PBF and DED processes, metal jetting has the potential for almost entirely waste-less multi-material 3D printing of metal parts. In addition, the extended degree of freedom in metal jetting promises new avenues in fabricating functional multi-material metallic devices.

Metal jetting shows promise for many sectors, such as printing of 3D electronic circuits, advanced microelectronic components [8]–[10], complex 3D mesoscale objects [11], biotechnologies such as orthopaedic implants [12], metal 3D printing in space [13]–[16], and producing directional terahertz radiation [17]. The vision for multi-metal jetting is to produce parts using various materials according to the local requirements within a single printed object. The multi-metal printing paves the way to additively manufacture batteries, thermocouples, and objects with locally customized electrical resistance, chemical reactivity or microstructures.

In metal jetting, molten material is ejected in either a continuous or drop-on-demand (DoD) fashion. In the DoD method, well-defined droplets are expelled from a nozzle in a periodic or aperiodic controlled manner, resulting in a highly precise printed

component, making it advantageous compared to continuous jetting [18]. The various mechanisms of actuation in DoD printing include pneumatic [19]–[21], piezoelectric [6], [22], and Magneto-Hydro-Dynamic (MHD) actuators. The first two are either limited in the droplet size (>200 µm), frequency of droplet generation (<200 Hz), or to low melting point materials (<700 °C). The size of the droplets sets the resolution, the jetting frequency controls the manufacturing time, and most functional metals have high melting temperatures. Hence, the research to find a solution that fulfils these manufacturing objectives has been carried out up to recent years. The MHD technique [23]–[25] has been shown to overcome the limitation of droplet generation frequency seen in other DoD methods. MetalJet [11], [26], [27], a novel DoD metal jetting additive manufacturing technology based on the MHD principle, was the first to overcome the melting point and droplet size limitations, listed above, concurrently. The MetalJet printheads, originally patented by Océ (now Canon Production Printing) [28], produce micro metallic droplets (< 80 µm in diameter) of high temperature (up to 2000 °C), at frequencies up to 2 kHz. Due to the capability of MetalJet system to produce microdroplets of high melting metals, new avenues in the

In metal jetting, regardless of the actuation system, objects are built in a repetitive droplet-by-droplet fashion, hence the precision and properties of components are dictated by the behaviour of the individual droplets (droplet-substrate and droplet-droplet interactions). Due to the independent nature of the droplets upon impact until solidification, investigations on this process can be reduced to studying the characteristics of single droplets. These characteristics, including the droplet morphology, crystal structure and bonding to the substrate, or previously deposited droplets, are based on several factors, such as the thermo-physical properties of the feedstock material and substrate, the droplet and substrate temperatures, the size of droplets, the jetting velocity among others [29]. In order to obtain parts with high integrity, these parameters should be optimised. For this purpose, it is essential to acquire fundamental knowledge about the mechanism of the process through a detailed investigation of single droplet ejection and deposition in the first instance.

Secondly, the deposition of multiple droplets, which dictates the parts integrity, should be investigated. Seemingly simple, these tasks are significantly challenging since several complex phenomena occur simultaneously during the ejection, deposition, and

solidification of liquid metal droplets onto a substrate [30]. Phenomena that need to be understood include the droplet's dynamics, reactive wetting, multiphase and multimode heat transfer, and residual stress evolution. Even though these parameters define the consistency and quality of the printed parts, they are still not well understood since the process is still in its infancy. This limits the optimisation of the process for particular applications and poses a challenge to the ultimate exploitation of the technology. The impact, spreading, solidification, and residual stress evolution of droplets during the transient stages of deformation and oscillation have been separately investigated in the state of art [13], [31]–[39]. However, to the best of the author's knowledge, only a limited number of studies have targeted the characteristic of molten microdroplets at low We numbers to-date [40]–[42].

This research aims to comprehensively understand the MHD metal jetting (MetalJet) process and explore the physical factors that govern the quality and properties of the net-shapes produced by the system. These factors include the temperature at the interfaces, which defines the level of bonding, the cooling rate, which is one of the key factors to control for a desired microstructural development, and the residual stresses, which may lead to distortion and/or de-bonding. This is achieved through an integrated experimental and computational approach. For this purpose, single and multiple droplets were deposited onto substrates using our experimental, non-commercial MetalJet process and were characterised. In parallel, a computational model was established to predict the thermal evolution of the droplets and substrate, as well as the residual stress evolution during the deposition of single and multiple droplets.

This thesis is structured as follows:

- Chapter two summarises the literature in the area of interest, where the current study stands out, and how it fits in. Furthermore, the gaps in the current state of knowledge are highlighted. This leads to the definition of this research's specific aim and objectives.
- Chapter three describes the materials and methods used in conducting the research. The details of the experimental and numerical work carried out over the course of this investigation are explained.

- Chapters four to seven present the results obtained throughout the current research work. Chapter four covers the characteristics of the droplets before impact, including the jetting stability, droplet's diameter, speed, and trajectory; moreover, the droplets' cooling in-flight is investigated.
- Chapter five describes the behaviour of droplets from impact to solidification for Cu, Sn, and Ag through an integrated numerical, analytical, and experimental approach. Moreover, the effects of various process parameters on final droplets' morphology, including surface roughness, droplet temperature, substrate temperature, and substrate material, are mentioned.
- In Chapter six, the mechanism of interface formation between the droplet and substrate during the deposition of Cu, Ag, and Sn droplets is explained. Moreover, the effects of various process parameters on the level of adhesion are elucidated.
- In Chapter seven, the interface formation at the droplet and substrate is discussed, and the effects of selected process parameters on the bonding are explained.
- In the eighth Chapter, computational modelling is used to provide insight into the residual stress evolution during the solidification and cooling processes. Furthermore, several solutions to mitigate the level of residual stresses are investigated.
- A general discussion is presented in chapter nine, where the research findings of the current study are elaborated on, and the significance and implication of this study are discussed.
- Finally, the conclusions of this work are presented in chapter ten, where an outlook on the future developments work is proposed.

2. Literature Review

The scope of this chapter is to provide a summary of the literature regarding various aspects of DoD-MJ. In the first section, various metal AM techniques are briefly described, and their advantages and limitations mentioned. This guides to the motivation of the research in the metal jetting area and is followed by a comprehensive literature review on the advances in the field to date. Various aspects of DoD depositions, including pre-deposition characteristics, droplet deposition behaviour, droplet deposition modelling, and printed structures' characteristics through this technology, are reviewed. Toward the end of the chapter, the gaps in the literature in the area of DoD-MJ that this thesis aims at approaching are elucidated.

2.1. Metal additive manufacturing

The physical and thermomechanical properties of metals make them more advantageous compared to other materials for many applications and, consequently, they are considered the most important engineering materials. AM technologies provide the possibility of fully exploiting this important class of materials at a reduced cost and waste to create intricate structures while eliminating the limitations of traditional fabrication techniques. Consequently, metal additive manufacturing is

developing at a rapid pace to cope with the current industrial needs to utilise the unmatched capabilities that these technologies offer [43].

Metal AM can be classified into five groups: Powder-Bed Fusion (PBF), Direct Energy Deposition (DED), Binder jetting, Nano-Particle Jetting (NPJ), and droplet-based techniques. Although very different in solution, principle, and embodiment, significant functional similarity exists among the technologies.

The most common PBF systems are Electron Beam Melting (EBM) and Laser Powder bed Fusion (L-PBF). They use metal powder as raw material feed, and a high-energy source is used to melt the pre-laid material selectively. In EBM, a high-power electron beam is the heat source for melting the powder particles, which requires the procedure to be carried out under vacuum conditions to prevent electron beam scattering [44]. Whereas in L-PBF, a focused laser beam fully melts the powder particles and the process chamber is only flushed with an inert gas [45]. Once the first layer is scanned, the build platform is lowered, and the next layer of powder is spread. The process repeats until the 3D part is built. 3D parts built by these methods are prone to several issues due to the complicated thermal history. A large degree of shrinkage tends to occur during liquid-solid transformation, which results in accumulating considerable stresses in the components. Moreover, high-temperature gradients during cooling cause residual thermal stresses that accumulate as the layers are built up, leading to distortion, cracking, layer delamination and wrapping of products [46], [47]. Due to the difficulties of powder layering, multi-material printing is still challenging with this process.

Blown powder deposition and Wire based disposition are two main categories of DED. In powder-feed DED, metal powder is fed through a nozzle, which is melted using a laser or plasma beam, forming a layer. The laser-based method is called Laser Metal Deposition (LMD), or Laser Engineered Net Shaping (LENS). The plasma-based method, called Plasma Deposition Manufacturing (PDM), starts by supplying a continuous powder feed to a plasma-melted zone in an inert gas environment to help reduce oxidation. In this method, some oxidized particles can still form when the powder is melted and solidified as the plasma beam scans across the deposited layer [46], [48]. In wire-feed DED technology, a wire of a small diameter is fed and melted,

binding to the previous layers through welding. Compared to laser deposition or electron beam welding, a wider range of metals can be used in this method, and there is less opportunity for oxidized particles to form. Moreover, they provide the possibility of depositing multiple materials in one part. Despite a reasonable ultimate strength, the microstructure of parts is less homogenous in this technique. In addition, difficulties arise due to the weld pool control and its impact on dimensional and geometrical accuracies [48].

Binder jetting generally uses one or more nozzles to jet liquid binder on the top of a powder bed, effectively glueing the powder together. The printing can be potentially faster than other metal AM methods, since it operates at lower temperatures and multiple nozzles can print simultaneously. However, the green parts need time-consuming post-process for densification. It includes heat treatments to remove the binder and sinter the powder particles and other techniques such as infiltration (using a metal with a lower melting point) or hot isostatic pressing [49]. Consequently, the overall fabrication speed of binder jetting is slower. The main issues associated with this technology are that part shrinkage cannot be avoided during the post-sintering process [47], [48], [50], and high porosity level. Moreover, the selection of binding material and the surface finish of products are other challenging aspects of the process. Reactive Metal Jet Fusion (RMJF) [51] which emerged in 2018, is analogous to binder jetting and seems to be a promising method to overcome the drawbacks mentioned above. This technology uses so-called functional binders instead of conventional binders. The functional binders comprise a reactive material and nano- to micro-particulate materials. The reactive binder infiltrates the voids between the powder-bed particles and fuses them in situ through chemical transformations or physical processes such as adsorption, diffusion, or melting.

Fabrication of 2D and 3D conductive structures for printed electronics uses inkjet printing technology to deposit a liquid dispersion of metal nanoparticles onto a substrate. Considerable research has been devoted to the technology in the past decades since it has opened new avenues for realising 3D-printed electronics. The use of metal nanoparticles allows sintering processing at lower temperatures due to their lower melting temperatures compared to their bulk counterparts [52], making them compatible with various types of substrates, including flexible polymer substrates.

However, pores and microcracks formed during the sintering process, organic residues of stabilising ligands, nonuniform morphology due to the coffee-ring effect, and nozzle clogging are still common challenges associated with this process [53]. Moreover, the synthesis of nanoparticles is challenging for some metals [54]. An alternative approach has emerged to overcome the challenges related to sintering through the development of reactive organometallic inks, which enables the deposition of ink formulations at a low temperature [55]. These inks overcome aggregation problems and yield conductive metal films, but they are more expensive and reducing agents are required to trigger the chemical reaction [56].

The reviewed metal AM techniques require either pre-processing, such as powder production or extensive post-processing, such as heat treatments or machining. Moreover, the high-power lasers, ink formulation, and defects are inevitable aspects of most of these processes. More importantly, they are mostly limited to using a single material to build a part, hence the production of multi-metal, multi-functional devices is not attainable. An alternative AM technology that shows promise for overcoming these challenges is metal jetting or Liquid metal printing, used in this study. Potentially a wider range of metals and alloys can be printed through metal jetting since the only requirement is to melt the material before jetting, and there is usually no post-printing restriction. This method is fully explained in the following section.

2.2. Metal Jetting

Metal jetting, also known as liquid metal jet printing, is a promising additive manufacturing (AM) technology that has the potential to fabricate metallic components, both single and multi-material, at a resolution not achievable with the more common Metal AM techniques. Metal jetting is based on a technology which is analogous to traditional ink-jet printing. The operational concept of metal jetting is that the feedstock material is loaded into a crucible that can be heated to transform the feedstock material into a liquid form, by melting. The molten material is ejected through a nozzle and deposited at precise locations onto a substrate. The nozzles can be designed with various actuator systems or mechanisms, depending on the feedstock material class and the mode of operation. Interestingly, the freedom offered by the variability in nozzle sizes potentially enables fabricating parts using a wide range of

scales. The size of the ejected material can vary between the order of a few microns up to the mm range. The deposited material then spreads and solidifies upon landing on the substrate or adjacent to the previously deposited material until the 3D object of interest is created.

Metal jetting is a novel AM technology, and most devices are not yet industrialised and are at the academic research level. It is foreseen that this technology will be beneficial for various industrial sectors. The application of the technology depends on the droplet size, which in turn defines the resolution and the object size. The potential applications for this technology are the printing of 3D electronic circuits and advanced electronic components [8]–[10], complex 3D mesoscale objects [11], biotechnologies such as orthopaedic implants [12], metal 3D printing in space [13]–[16]. Moreover, the possibility of multi-metal printing paves the way to additively manufacture parts of various materials in the same print without the need for welding or other joining processes.

From an operational perspective, there are similarities between metal jetting and micro-casting, spray shape deposition manufacturing (SDM) [4], and thermal spraying [5]. However, the control over the size of droplets, jetting speed, and the precision of manufacturing set metal jetting apart from these other processes. Moreover, metal jetting has prospective advantages over other AM technologies, such as L-PBF, DED, and binder jetting, due to its simplified fabrication approach. Metal jetting integrate melting and jetting processes simultaneously, avoiding extra time and costs for pre-processing, such as powder preparation in powder-based additive manufacturing processes. In addition, this simplicity is granted by the elimination of post-print processing, such as sintering, to remove the binding agents. As a result, material jetting processes can be faster and cheaper compared to other additive manufacturing techniques. Furthermore, the high solidification rates of individual droplets generate a fine microstructure with reduced segregation in metallic alloys. In addition, metal jetting has the potential to create parts with graded microstructure and mechanical properties, thanks to the control over the solidification path of individual droplets. Last but not least, the extended degree of freedom in metal jetting promises new avenues in fabricating functional multi-material metallic devices. **Table 2.1** compares the

advantages and disadvantages of various metal additive manufacturing techniques reviewed in this thesis.

***Table 2.1**- The advantages and disadvantages of various Metal Additive Manufacturing technologies.*

	Advantages	**Disadvantages**
Powder-Bed Fusion	Wide range of materials, possibility of multi-metal AM manufacturing, printing complex 3D geometries, possibility of powder reusability.	Powder manufacturing is required, the process is relatively expensive and complex, a considerable level of distortion, surface finish varies depending on the powder quality, size limitation, the multi-metal printing is restricted due to the powder layering challenges.
Direct Energy Deposition	High deposition rate, possibility of fabricating large structures, multi-metal printing is possible, high density.	Poor surface finish, printing complex geometries are challenging, microstructure is heterogeneous, low dimensional accuracy, high levels of distortion.
Binder jetting	Distortions are limited compared to beam-based techniques, scalable process, high printing speed, complex 3D shapes can be printed.	Powder manufacturing is required, extensive post-processing is required, relatively low material properties (mainly high level of porosity), anisotropic mechanical properties, considerable shrinkage due to post-treatments, poor surface finish, high overall cost.
Nano-Particle Jetting	High accuracy and resolution, isotropic material properties, sintering processing at lower temperatures compared to the bulk material, adaptability with various substrate materials, multi-material printing is possible.	Synthesis of nanoparticles is required, relatively low printing speed, post processes are required, which can cause further defects, high costs associated with the technology, nozzle clogging, nonuniform morphology (such as coffee rings).
Metal Jetting	Simplified fabrication approach: usually no pre- or post-processing	Liquid metal containers must withstand high temperatures, lack of

	is required, high resolutions, high surface finish, possibility of multi-metal manufacturing with high accuracy, high material properties, printing complex 3D geometries.	consolidation between droplets of high-temperature materials, surface finish depends on the droplet size (nozzle size), protective build chamber is required.

As the molten metal is ejected from specifically-designed nozzles, it is expelled in the form of either (a) a continuous jet or (b) discontinuous jet, also known as Droplet-On-Demand (DoD) jetting. In the case of continuous jetting, the liquid material is pushed out of the crucible through the nozzle in the form of a continuous stream of fluid (**Figure 2.1**). This liquid stream is broken up into a steady stream of droplets at a defined distance from the nozzle because of the Plateau-Rayleigh instability. The Plateau-Rayleigh instability is explained by the tendency of liquids to minimize their surface area by virtue of their surface tension. This jet of liquid can be stimulated by assisted vibration to have better control over the droplets' uniformity and consistency and reduce the satellite droplet formation. Satellite droplets' formation is a common defect in jetting processes exacerbated by jetting instabilities, leading to the formation of significantly smaller droplets that deviate from the uniform stream. Having uncontrolled trajectories and sizes, these satellites pose challenges in terms of compromising the micro-and macroscopic fidelity of the 3D printed structures.

There are two continuous jetting methods: (1) binary and (2) multiple. In the former, at the point of jet break-up, an electrostatic charge is induced into the selected droplets as they travel through charging electrodes. Subsequently, these charged and uncharged droplets pass through a deflection plate, producing a uniform electric field to sort droplets to be collected (charged droplets) or deposited (uncharged droplets) onto a substrate. In this method, the charging process is relatively simple since there is a single level of charging, however, it is limited to printing single lines. To produce 2D areas, multiple jets or relative motion of the jet to the substrate will be required. In the binary mode, the deflected droplets are either discarded as waste or collected for re-use. In the multi-deflection process, the charging level of droplets is variable. Hence, droplets are deflected to various positions on the substrate, enabling a single jet to

print 2D structures at once. The operational concept in **Figure 2.1** demonstrates the continuous jetting function of a binary deflection method.

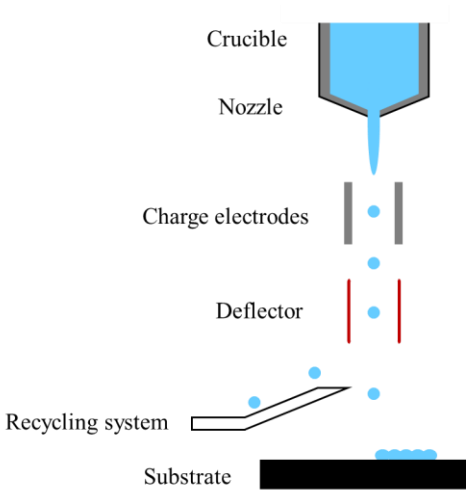


***Figure 2.1**- Schematic presentation of the continuous jetting operational concept.*

In contrast to the continuous jetting modality, in the case of discontinuous or DoD jetting, well-defined droplets are directly created and expelled from a nozzle in a discontinuous, periodic or controlled aperiodic manner. These individual droplets are generated by applying a momentum to the liquid material, which results in the ejection of a precise volume of individual drops of metal. The operational concept of DoD jetting is illustrated in **Figure 2.2**. There are various actuation mechanisms to introduce this pressure into the liquid material, including piezoelectric [6], [57], [58], pneumatic [19]–[21], and Magneto-Hydro-Dynamic actuators [24], [59], [60]. One advantage of the DoD over continuous jetting is that it produces no unused droplets, i.e., more resource-efficient. Moreover, DoD offers more control over the droplets' sizes, timing, and speed, making it advantageous to continuous jetting despite being slower. DoD methods have become more popular in recent years, hence a wider range of printable materials.

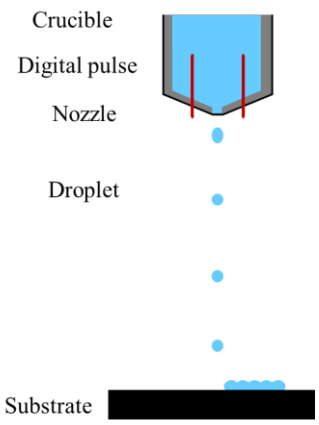


***Figure 2.2**- Schematic presentation of the operational concept of discontinuous jetting.*

2.2.1. Piezoelectric actuators

The primary method of DoD actuation has historically been piezoelectric-based since its usage was well established in DoD inkjet printing. The push-mode piezoelectric actuators are more frequently employed for molten metal jetting, in which there is no direct contact between the piezo-based actuator and molten material to overcome challenges associated with the Curie temperature (the temperature at which the material permanently loses its immanent polarization, which can be ~150°C to 300°C for a typical piezoelectric material such as PZT). As shown in **Figure 2.3**, an electrical pulse causes the piezoelectric ceramic to contract or expand. This mechanical vibration pulse is transferred into the liquid metal through a piston, creating pressure and forcing the liquid droplet out of the nozzle [6]. The piezoelectric actuators are the most common method owing to their simplicity, flexibility, and possibility of reaching higher frequencies (>500 Hz). However, their application remains limited to relatively low-temperature metals. In recent years, the temperature limitation caused by these systems has been lifted by applying a cooling system and thermally insulating the piezoelectric elements. The capability of these mechanisms has now extended to higher temperatures of up to 950°C [61]. In this method, the droplet size changes as a function of nozzle diameter and can be controlled by varying the drive period in the waveform applied to the piezoelectric [62].

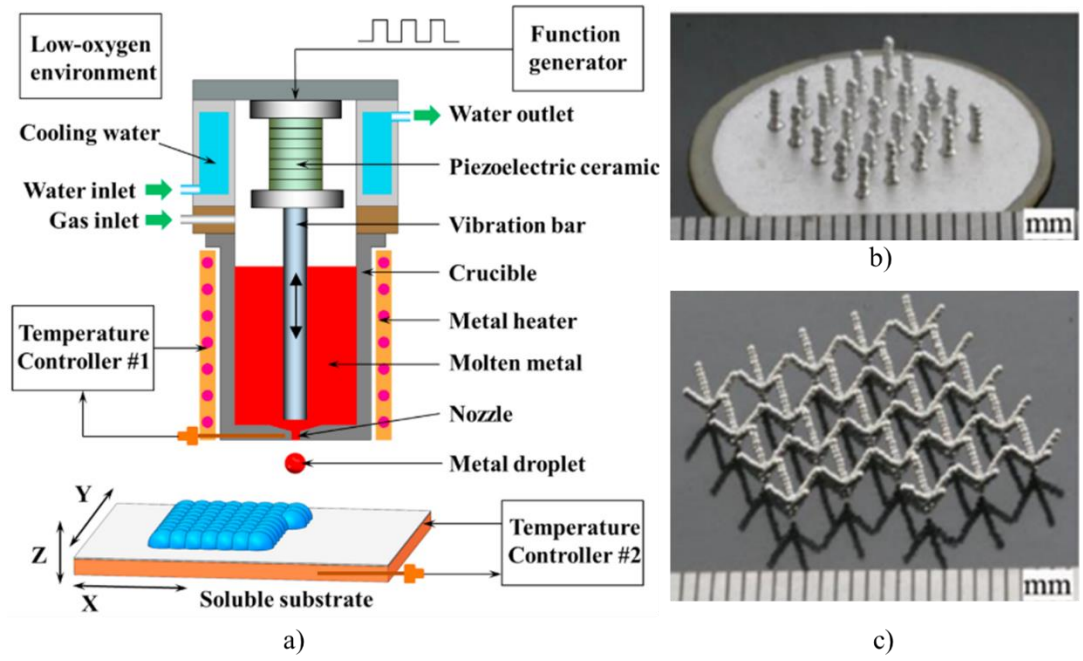


Figure 2.3*- a) a schematic presentation of a material jetting system using piezo-electric actuation* [63]*, b) pillar array in AlSi12* [64]*, c) inclined pillar in Sn63Pb37* [64].

2.2.2. Pneumatic actuators

As per **Figure 2.4,** in pneumatic actuators, droplets are ejected from a nozzle by applying pulses of pressurised gas to the liquid reservoir. The pressure pulses are created by a rapid closure and opening of a solenoid valve [19]. Pneumatic actuators are widely used among researchers due to their simplicity and resistance to high working temperature conditions. In recent devices, the working temperatures have been increased to 1600°C [21]. The nozzle diameter mainly defines the size of droplets in this technique [65], moreover, process parameters such as pressure pulse time and amplitude are also influential [66]. Even though these actuators are still widely used among researchers for droplet deposition studies, the slow droplet rates (<100 Hz) and lack of stability make them the least favourite option for metal additive manufacturing. The low frequency originates from the slow response rate due to the high compressibility of the gas and results in a slow production rate.

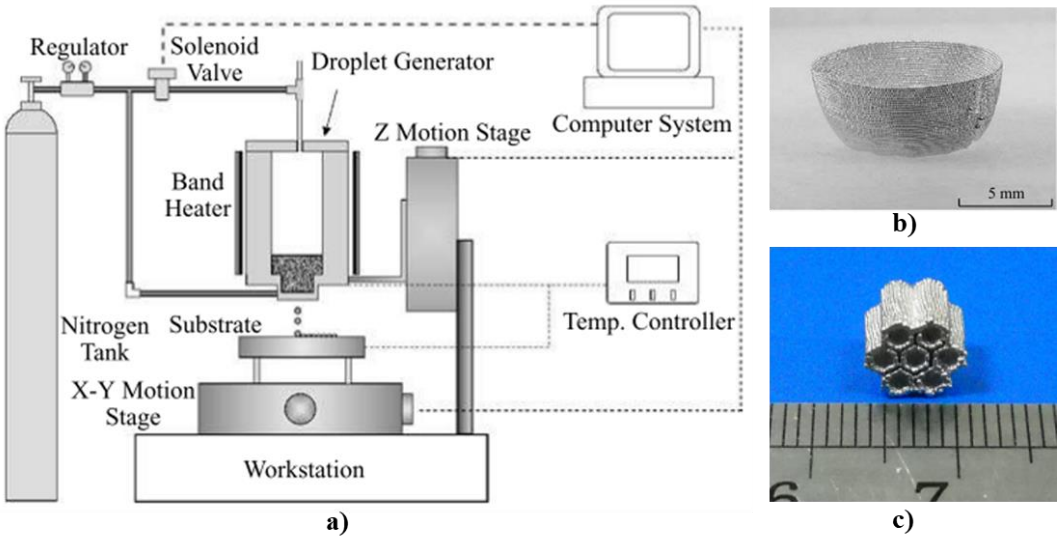


Figure 2.4- *a) a schematic representation of a jetting mechanism deploying pneumatic actuation, thin-walled 3D objects in Sn fabricated by pneumatic metal jetting systems b)* [67], *c)* [65].

StarJet (2009) [68] is a pneumatic droplet generator device with improved droplets' uniformity and accuracy compared to the traditional pneumatic systems. The main characteristic of this device is a star-shaped nozzle, which facilitates the flow of liquid in the centre of the nozzle by capillary forces and reduction of the contact line friction. The design of this atypical nozzle was initially proposed by Metz et al. in 2008 [69]. In the DoD mode, individual droplets are generated due to the interplay between the gas pressure on the liquid metal in the reservoir and the gas flow in the star-shaped grooves indicated in **Figure 2.5**. Short pressure pulses are applied by opening the pneumatic valve for short periods of time. By applying this gas flow through the inlet, a driving pressure on the liquid metal is provided, however, the liquid is held inside the reservoir due to the capillary pressure of the nozzle centre. Thanks to the star-shaped design, the gas flow causes a pressure drop in the gas supply channel, which can overcome this capillary pressure and hence a liquid droplet can be produced on-demand. Microdroplets of nano- to pico-litres can be produced using the StarJet system. In the more recent versions of the device, frequencies of up to 25 Hz [70] were reached in DoD mode, with working temperatures as high as 950 °C [71].

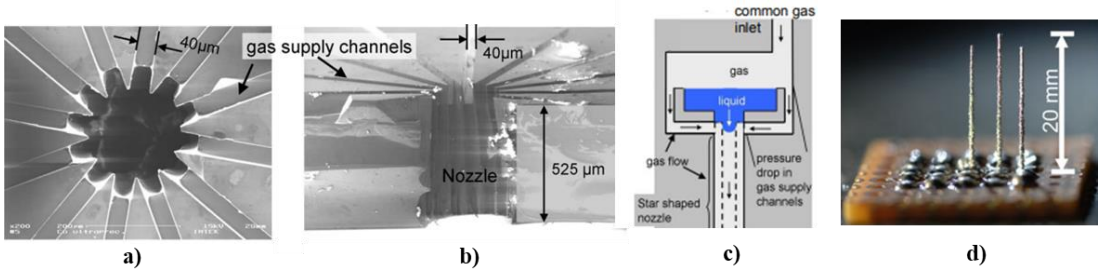


***Figure 2.5**- SEM pictures of StarJet nozzle a) top view, b) cross-sectioned view, c) working principle of the StarJet dispenser* [68], *d) three solder columns printed with the StarJet system* [72].

2.2.3. Magneto-Hydro-Dynamic actuators

In MHD, by virtue of applying an electric current pulse to a conducting molten material, which is surrounded by a magnetic field, a Lorentz Force is induced ($\vec{F} = \vec{I} \times \vec{B}$) (**Figure 2.6**). This electromagnetic force, directed toward the flow direction, acts as a pressure pulse to expel the material from the nozzle [25]. The MHD technique, which is the focus of this research and which has been the subject of just a few studies, has been shown to overcome some limitations in other DoD methods. MetalJet [11], [27], [73], a novel DoD metal jetting additive manufacturing technology based on the MHD principle, has shown the capability of producing micro metallic droplets (< 80 µm in diameter) of high temperatures (up to 2000 °C), at frequencies up to 2000 Hz. MetalJet uses printheads originally patented by Océ (now Canon Production Printing) [28], as shown in **Figure 2.6**. In this system, a magnetic field is produced by two permanent magnets. A variable electrical current is provided through two tungsten electrodes, which are in contact with the liquid metal via the cartridge and placed perpendicular to the magnetic field direction.

Xerox's Liquid Metal 3D Printer (Magnetojet™) [74], [75], the first commercialised DoD printer, uses an MHD actuator mechanism to produce microdroplets with a frequency of 40 to 1000 Hz. This system uses a transient magnetic field instead of a permanent one. Electrical pulses sent to a Cu coil produce the transient magnetic field, which couples with the circulating electrical current. The main advantage of this device is the elimination of direct contact of electrodes with molten metal. Moreover, continuous wire feedstocks are used. However, the system is limited to producing

molten droplets of up to 950 °C, and the contactless actuation methods can result in pumping inefficiency.

The use of MHD actuators can potentially revolutionize the metal jetting industry, thanks to their capability to produce small microdroplets of high-temperature material at high frequencies. Moreover, jetting properties such the pulse length, pulse voltage, and jetting frequency can be independently controlled to optimize the dynamics of droplet ejection [8]. However, the technique is still restricted to the limited choice of suitable materials for electrodes. The materials must possess sufficient electrical conductivity while withstanding the chemically aggressive melt condition (in the case of direct contact). Also, the material choice for fabrication of the container and nozzle is governed by the compromise between the wettability properties without inducing chemical reactions. These limitations can impose challenges to the pace of the progression of the technology.

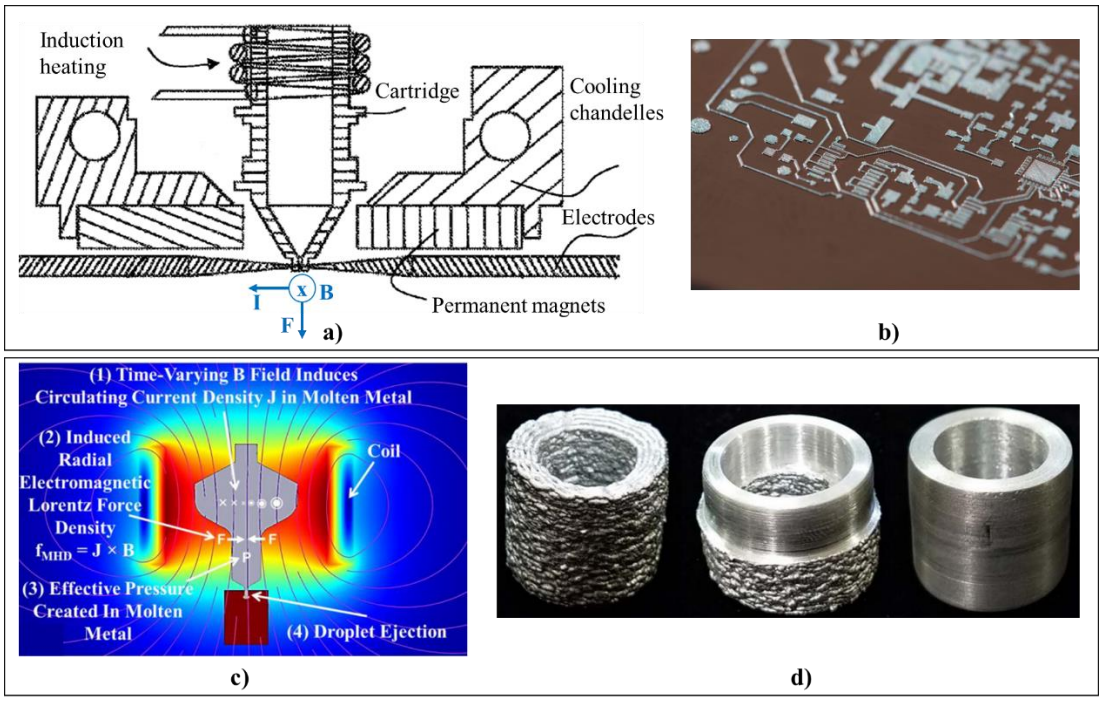


Figure 2.6*- a) The cross-sectioned view of Canon-Océ actuator [28], b) an electronic circuit in Sn printed through the MetalJet platform* [27], *c) the cross-sectioned view of Magnetojet actuator, d) a cylinder in Al printed through Xerox metal jet printer(Magnetojet)* [25].

2.2.4. Other droplet-based techniques

There are other droplet-based additive manufacturing techniques in which 3D objects are built in a droplet-by-droplet fashion; however, in these techniques, droplets are not necessarily jetted from a nozzle. Yet they share similar fabrication principles with metal jetting and merit to be briefly overviewed.

2.2.4.1. Laser-induced forward transfer

Laser-induced forward transfer (LIFT) [76]–[78] is a droplet-based AM method allowing the printing of a wide range of pure metals and alloys from low to high temperatures at high resolutions. This method applies a focused pulsed laser on a thin film layer, pre-deposited on an optically transparent support. The laser melts a portion of metal and subsequently produces a liquid metal micro-droplet. Objects can be additively built by placing a substrate in the drop's trajectory, as shown in **Figure 2.7**. LIFT is a non-contact digital printing technology (i.e., the molten metal is not ejected from a nozzle), enabling the fabrication of complex shapes and multi-material structures. Despite the capacity of the technology to produce nano to micro-scale droplets, the fabrication of high-resolution objects through this technique is hindered by the irregular morphology of droplets due to laser inputs and satellite formation. Moreover, the pre-deposition of a thin metallic layer onto a transparent support adds an extra level of complexity (for example, wetting-related issues). In addition, the electrical and mechanical properties of printed parts are inferior to bulk material due to poor bonding at interfaces, oxidation, inter-droplet voids, and delamination [79], [80].

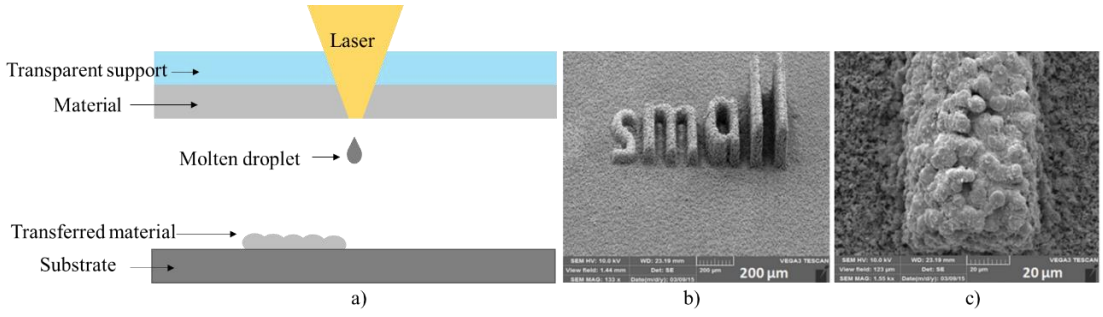


Figure 2.7*- a) A schematic presentation of the Laser-induced forward transfer working principle, b) SEM image of LIFT-printed copper logo of the on an epoxy glass laminate, c) a zoom at the middle of the letter "m"* [81].

2.2.4.2. Electrohydrodynamic redox printing

Electrohydrodynamic redox printing (EHD-RP) [82] uses the basic electrochemistry to in-situ dissolve a metal anode M^0 in a liquid solvent (acetonitrile), as demonstrated in **Figure 2.8**. These immersed metal ions M^{z+} are ejected from the printing nozzle using EHD actuators. The in-flight modulation of the printed chemistry is achievable by switching the oxidative voltage between different electrodes in a multichannel nozzle. Finally, ions are reduced to zero valence metal as they are deposited through electron transfer from the substrate. This technique enables direct printing and mixing of multiple metals from a single nozzle at high spatial resolutions. However, the method is limited to the fabrication of objects with only several hundred micrometres in width, and the manufacturing rate is relatively low (10 voxels per second).

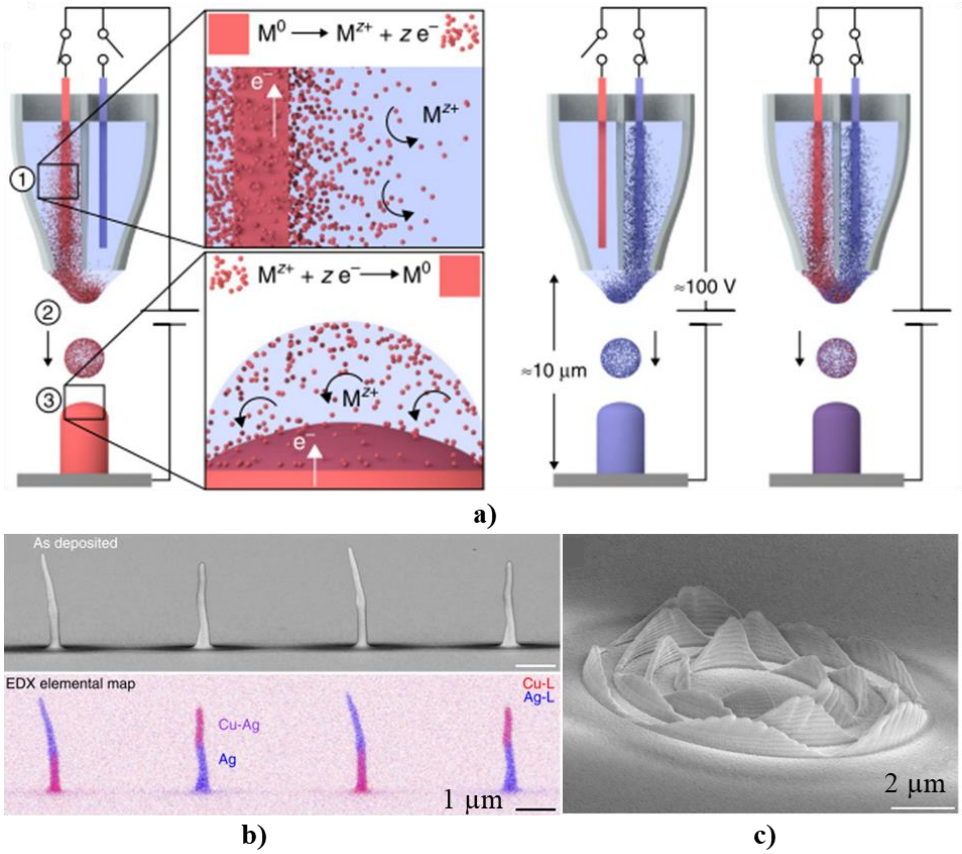


Figure 2.8*- a) the schematic presentation of the EHD-RP working principle, b) bi-metal pillars printed with alternating segments of Ag and Cu–Ag c) concentric, out-of-plane sine waves printed with a layer-by-layer strategy* [82].

2.2.4.3. Microcasting

Microcasting [83], [84], developed at Carnegie Mellon University in 1994, is a drop-based deposition process to create 3D objects of desired shapes. In this process, high melting point metallic objects (for example, steel) are produced by depositing individual drops of 1 to 4 mm in diameter at rates of 1 to 3 drops per second in a discrete fashion. The various microcasters using: MIG (Metal Inert Gas) torch, TIG (Tungsten Inert Gas) torch, and plasma-arc welding approaches are schematically presented in **Figure 2.9**. In the MIG microcaster, an electrode wire is fed through the MIG torch and is melted using an arc to form drops at the end of the wire. In the TIG microcaster, an arc is established between a tungsten electrode and a water-cooled copper electrode, while the feedstock wire is fed externally into the arc. In both techniques, a shielding gas is supplied through the troches. Alternatively, plasma-arc welding can produce drops of higher melting metals at higher jetting velocities. Here, an electric arc, generated from a standard plasma welding power source, is transferred between the torch and the feedstock wire. The tip of the metal wire, positioned perpendicular to the torch, is melted to produce drops. The recent so-called Laser-assisted drop deposition [85] uses the same principle as microcasting to build 3D parts. Even though large drops provide the condition for a metallurgical inter-droplet bonding, this manufacturing technique lacks precision. Usually, post-printing milling processes are required to shape the objects to the final dimensions, and the surface finish quality is inferior to other methods.

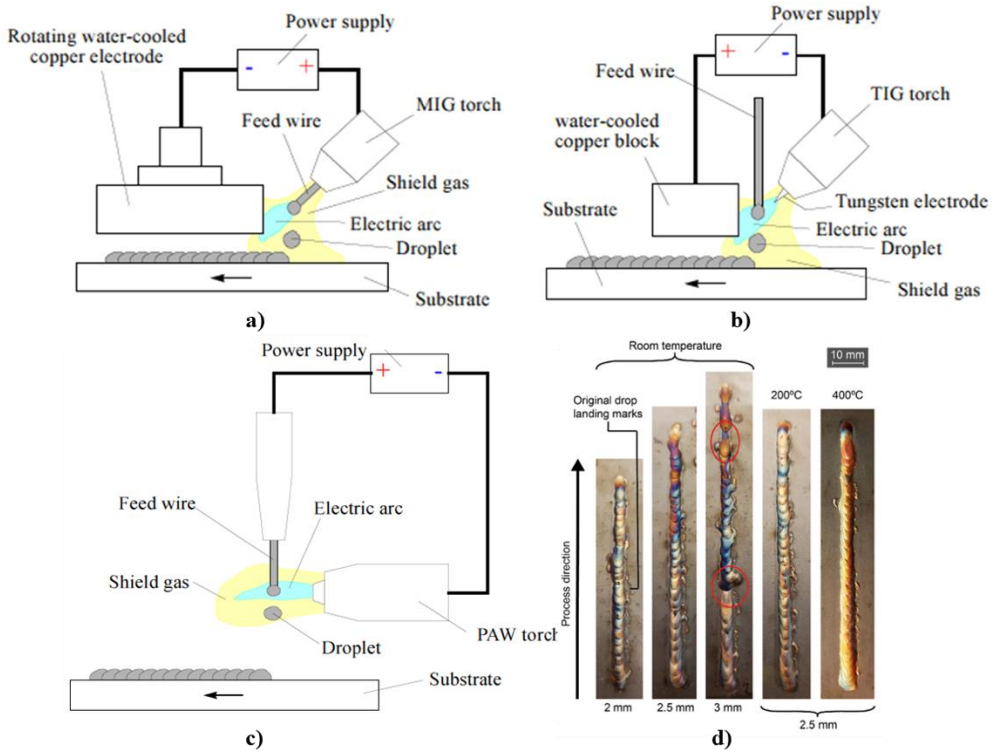


***Figure 2.9**- Schematic representation of microcasting process, a) MIG microcaster, b) TIG microcaster, c) Plasma-arc microcaster.*

2.2.4.4. Digital particle ejection melting

The Digital Particle Ejection Melting (DPEM) [42] for generating and printing molten metal droplets from a nozzle on-demand was introduced in 2021 by researchers from MIT (**Figure 2.10**). This technique combines the principles of Deterministic Particle Ejection (DPE) [86] and LIFT. DPE is similar to inkjet technology, where droplets are generated by applying force to the liquid inside a container. However, in DPE, a specific voltage potential between the carrier liquid needle and the substrate is used locally to eject an individual particle. After ejection, a laser beam is applied to the in-flight particle to melt it before the deposition. A wide range of materials can be used in this technique since most materials can be found in the form of nano-micro particles. Moreover, there is no need to melt the metal, so the compatibility between the molten feedstock metal and reservoir does not raise an issue. Up to date, the printability of a lead-free solder alloy (Sn96.5-Ag3-Cu0.5) and a platinum-ruthenium alloy (Pt95.5-Ru4.5) has been demonstrated. High-accuracy objects can be printed through this

technique due to the small droplet size, as small as 30 µm in diameter. However, the poor bonding between droplets of high melting point materials remains a major issue. Moreover, the powder handling and laser use add to this method's complexity.

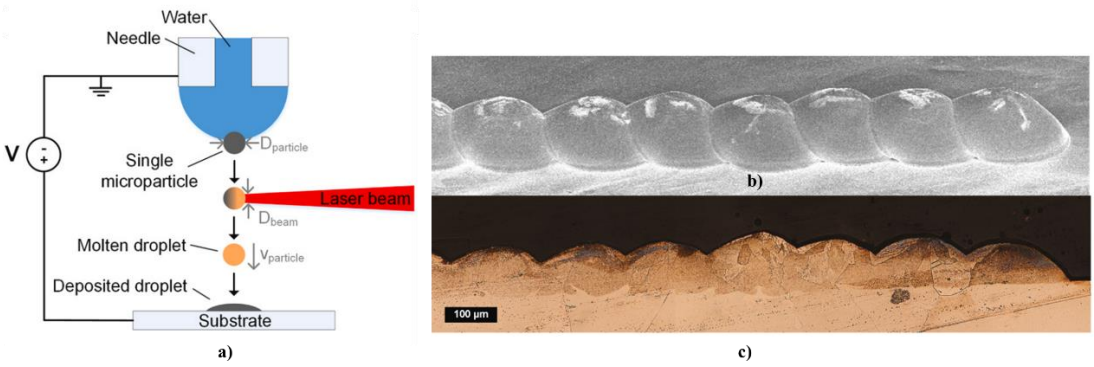


***Figure 2.10**- a) schematic representation of the digital particle ejection and melting (DPEM) process, b) line of overlapping 150 µm solder droplets on a tin substrate, c) polished and etched cross-section of the printed line shown in a [42].*

2.2.4.5. Thermal spray techniques

Thermal spraying [87] refers to various techniques used to restore a solid material's surface. In these processes, fine softened molten or semi-molten particles are projected onto a surface to which they are adhered, forming a continuous layer. Typically, multiple passes of the coating device are required to form the total coating. The feedstock materials can be in the form of powder, wire or rod, which is fed into a jet that may heat the material near or above its melting point and accelerates the resulting molten droplets in a gas stream to the substrate to form a coating. The electrical or combustion sources can be used to heat the material and create the jet stream. Plasma spraying, combustion flame spraying, cold spraying, and some vacuum processes such as EB-PVD (Electron beam- Physical vapour deposition) and PS-PVD (Plasma spray-OVD) belong to the family of thermal spraying. Even though the main application of these technologies is to coat surfaces, the potential to use them in the context of additive manufacturing has been highlighted in recent years [88], [89]. The challenges associated with using this method as an AM process are controlling the bonding level, structural integrity, manufacturing resolution, material brittleness due to work hardening, and post-processing requirements.

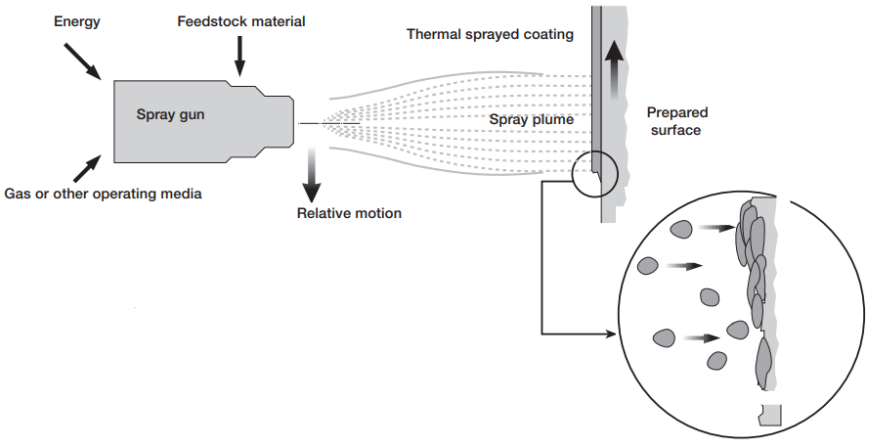


Figure 2.11- *the principle of thermal spraying* [87].

2.3. Droplet formation

This section presents the research work in the literature on investigating the characteristics of the droplets before they impact on the substrate. This is important since the precision of 3D parts printed by metal jetting processes depends partially on the formation of uniform droplets with consistent diameter, velocity, and trajectory.

The primary element to investigate in all drop-on-demand jetting techniques is the formation of droplets to reassure controlled and uniform droplets with a precise volume, speed, and trajectory. The principle of drop formation is to provide the required momentum inside the fluid through the actuating mechanism to push the material out of the nozzle. In DoD techniques, a push-pull actuation is typically applied at the orifice to extrude the meniscus out of the orifice using a positive pressure pulse and then retracting it using a negative pressure. The flow reversal concept reduces the pinch-off time and satellite formation during ejection [75]. Droplets are formed from an initial extended fluid stream that thins and eventually pinches off into a droplet with an elongated tail (ligament). The final separation of the ligament is of high importance, and if not well controlled, it can cause satellite droplet formation. **Figure 2.12** illustrates the sequence of droplet formation for two scenarios. In **Figure 2.12 a,** a satellite droplet is formed during the breakup, but it rapidly catches up with the main droplet, while in **Figure 2.12 b,** the satellite droplet cannot merge with the

main droplet [90]. The satellites are deposited randomly on the substrate and can eventually cause deterioration of precision, resolution, and accuracy in the printed part.

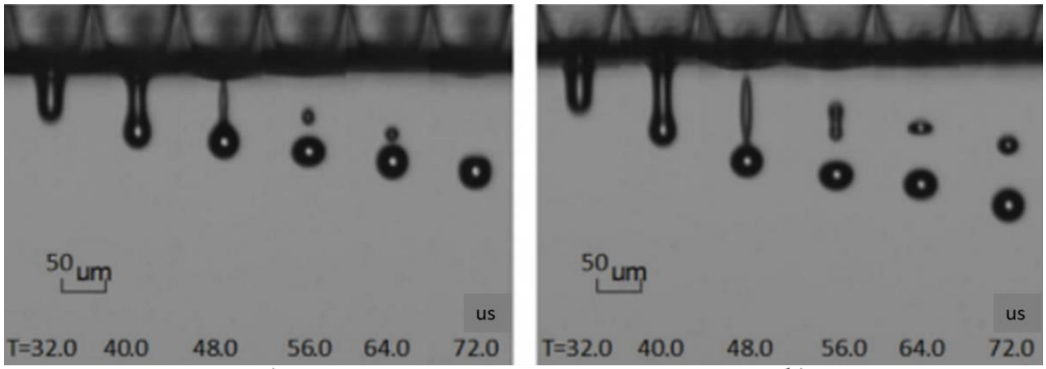


Figure 2.12*-Sequences of aqueous glycol solutions droplet formation using a piezoelectric actuator: a) when the satellite droplet merges with the main droplet, b) formation of satellite droplets* [90].

He et al. [91] used a lattice Boltzmann-based modelling approach to simulate the droplet formation mechanism in the inkjet printing process. As shown in **Figure 2.13**, these simulations provide information about the droplet's velocity at the tail and head during and after the breakup. They demonstrated that at optimal voltages (sufficiently low), the ligament pinches off at the nozzle, and the droplet's velocity at the tail is sufficient to catch up with the main droplet (head), which has a slower velocity. The tail forms naturally as a consequence of contraction in the ligament caused by the capillary forces. If the velocity of the main droplet at the head is too high (generally caused by high voltages), the tail droplet is unable to catch up with the head droplet, and satellite droplets are formed. The ligament can sometimes break into several satellite droplets due to the Rayleigh-Plateau instability.

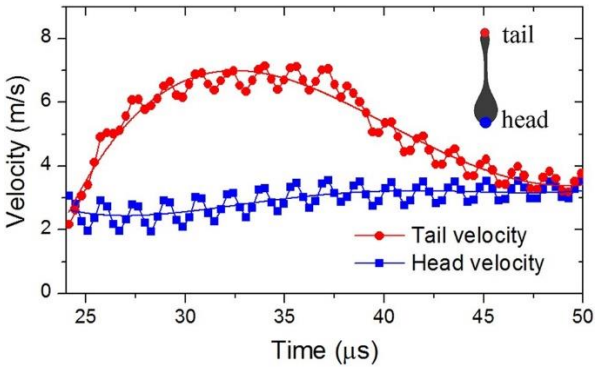


***Figure 2.13**- Velocity profiles of the drop tail and head during and after the droplet breakup* [91].

The droplet formation has been extensively studied for ink jetting, and Derby's [92] review article investigated the topic thoroughly. In most studies, jetting Weber (We_j), Ohnesorge (Oh), and Z parameter ($1/Oh$) are used to characterise the behaviour of liquid droplets and to provide a simple printability guideline for jetting processes.

$$We_j = \rho V_j^2 D/\sigma_s \qquad \text{(Equation 1)}$$

$$Oh = \frac{\mu}{\sqrt{\rho \sigma_s D}} = \frac{1}{Z} \qquad \text{(Equation 2)}$$

Reis and Derby [93] used Computational Fluid Dynamic methods to define a printability map. They suggested that for jetting inks with the piezoelectric actuators, stable droplet formation is obtained at the range of $1 < Z < 10$. For smaller Z, the viscous dissipation prevents droplets' ejection, and satellite formation causes an issue at higher Z. This printability criterion was widely used until recently when Lui and Derby [94] proposed new empirical printability boundaries based on their experimental observations (**Figure 2.14**), which covers the aqueous inks in the range of $2 < Z < 30$ and $2 < We_j < 25$.

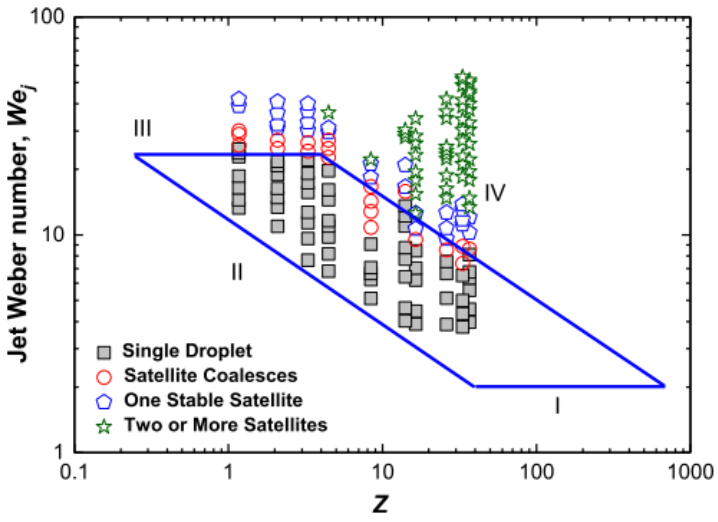


***Figure 2.14**- Printability map proposed by Lui and Derby based on the jetting We and Z numbers in inkjet printing* [93].

In recent years, with the emergence of DoD-MJ, the formation of metallic droplets has gained increasing attention, with only a few studies addressing the problem [21], [75], [95], [96]. The significant difference between ink jetting and metal jetting is the properties of liquid metal, including density, viscosity and surface tension, all of which makes metal jetting more challenging. Compared to typical inks, liquid metals have lower viscosities (0.8 - 4 mPa.s vs. 10 - 40 mPa.s [97]), higher densities (17,000- 2,700 $Kg/m3$ vs. ~ 1,100 $Kg/m3$ [98]) and much higher surface tensions (1350-540 mN/m vs. 20-60 mN/m [97]). As a result, the Oh and We numbers for metallic materials fall in an unexplored range of the printability maps that are conventionally used for inkjet printing.

It has been recognized that the formation of droplets at low Oh numbers is possible if the ejection pulse's strength is adapted accordingly. This eventually leads to lower ejection velocities and hence lower We numbers. Piezoelectric and magnetohydrodynamic actuators share similarities in terms of the formation of metallic droplets, whereas pneumatic actuators use a completely different mechanism. In pneumatic actuators, the pressure and valve opening time mainly control the droplets' dynamics, size, and velocity [20], [21]. Beck et al. [95] investigated the formation of metallic droplets of 300 µm in a wide range of We and Oh numbers using

a push-only pneumatic actuator through an experimental and numerical approach. While the modelling results matched the experimental result at a high Oh number, they observed some discrepancies at a lower Oh number (Oh < 0.5). The authors speculated several possibilities for the mismatch at the low Oh regime, with the change of surface tension due to oxidation being the most valid argument. However, they concluded that further investigations are necessary to elucidate the factors influencing the formation of metallic droplets. Watkins et al. [96] studied the formation of metallic material using a pneumatic actuator (push only) and suggested to use $\frac{Z}{\sqrt{D}}$ as a printability criterion. Dividing Z to the diameter's square root eliminates the criterion's dependency on the nozzle diameter and makes it adaptable for a wide range of droplet diameters. They discovered a new printability zone in the map established by Lui and Derby, where Sn, Al, and Ge droplets of $2 < We_j < 4$ and $339 < Z < 2526$ were shown to be printable. Zou et al. [99] investigated the effects of the wetting conditions between the liquid metal and the nozzle and found that the nonuniform wetting condition causes a deflection in the droplet's trajectory. They observed that the jet flow deflected toward the region where the wettability was lower, i.e., regions where the liquid could spread easier.

Feng et al. [100] used an integrated computational and experimental approach to optimize the waveform in the piezoelectric actuators. They found that longer rising times induced smaller droplets, whereas increasing the dwell time and the jetting voltage resulted in larger droplets (**Figure 2.15**). They also observed that the formation of satellite droplets could be mitigated by applying shorter dwell times.

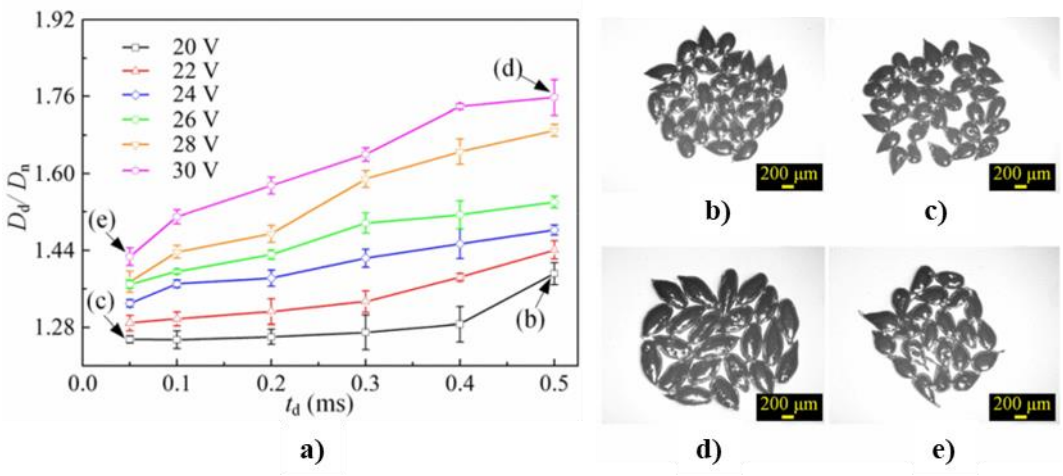


***Figure 2.15**- a) non-dimensional droplet diameter as a function of the dwell time at various voltages, optical images of solder droplets obtained for b) $t_d = 0.5\ ms$ and $V = 20\ V$, c) $t_d = 0.05\ ms$ and $V = 20\ V$, d) $t_d = 0.5\ ms$ and $V = 30\ V$, e) $t_d = 0.05\ ms$ and $V = 30\ V$* [100].

Ma et al. [101] developed a model to analyse droplets' dynamics during the jetting of microdroplets through piezoelectric actuators and validated their model by jetting Sn63Pb37 alloy. Similar to Feng et al.'s [100], larger droplets were obtained at higher dwell times and voltages. Additionally, they discovered that droplets' size increases linearly as a function of the melt temperature. Furthermore, their results indicated that these three parameters should be finely optimised since no ejection and satellite droplet can be formed if these values are too low or too high, respectively.

The formation of metal droplets through MHD actuators is limited to the research performed by Sukhotskiy et al. [75]. They used a computational model to establish a printability map for pure metal droplets of hundreds of microns in a contactless push-pull MHD actuator. They established a new criterion ($S = \frac{\sigma_s B^2 D_2^2 \vartheta_j}{\gamma}$, where B is the magnetic flux density) in which the Lorentz force induced in the molten metal is comparable with the surface tension at the nozzle. They demonstrated that satellite-free droplets could be produced in the range of 1000 < S < 2000 and for 10 < We_j < 20. To the best of the author's knowledge, the formation mechanism of microdroplets using MHD actuators is missing in state-of-the-art and merits an investigation.

2.4. Droplet deposition behaviour

In metal jetting, objects are built in a repetitive droplet-by-droplet fashion, hence the precision and properties of components are dictated by the behaviour of the individual droplets on two levels: (I) droplet-substrate and (II) droplet-droplet interactions. Due to the independent nature of the droplets upon impact until solidification, investigations on this process can be reduced to studying the characteristics of single droplets (deposited onto the substrate, deposited onto the substrate and adjacent to the previously deposited droplet, or deposited on the top of the previously deposited droplet). The characteristics that should be thoroughly investigated are:

1. Droplet morphology.
2. Droplet adhesion to the substrate.
3. Boning between droplets.
4. Crystal structure.
5. Residual stresses.

These five characterises are based on several factors. These include: the thermal-physical-mechanical properties of the feedstock material and substrate, the droplet and substrate temperatures, the size of droplets, the jetting velocity, and nozzle-substrate distance, among others [27].

The final objective, which is building 3D parts with high integrity and precision, is obtained if these parameters are well understood and optimised. For this purpose, it is essential to acquire fundamental knowledge about the mechanism of the process through a detailed investigation of single droplet deposition in the first instance. Secondly, the deposition of multiple droplets, which sets the integrity, should be investigated. Breaking down the project into these building blocks allows a fundamental understanding of the process instead of costly and lengthy trial and error approaches. Seemingly simple, these tasks are significantly challenging since several complex phenomena occur simultaneously during the deposition and solidification of liquid metal microdroplets onto a substrate. This is due to the complex heat transfer behaviour of striking droplets caused by the intricate internal fluid flow field, the time-varying geometry of droplets, and the progressive phase transformation [102].

Phenomena that need to be understood include the droplet's dynamics, reactive wetting, and multiphase and multimode heat transfer leading to a rapid solidification and possible remelting of the substrate, contact line motion and arrest, the dynamic behaviour of contact angle, interfacial deformation, nucleation, and growth of grains within the solidified droplet.

Research about the numerous physical phenomena involved in the droplet's impact and spreading onto substrates has been conducted for over a century due to its relevance in many industrial applications [103]–[108]. These include spray cooling, painting, insecticides and pesticides, inkjet printing, thermal spraying, fuel injection, windshield films, aircraft icing, electronic-component welding, coating, raining, nebulizers for medical use, and additive manufacturing. Despite decades of investigations, droplet deposition is not yet fully understood and keeps attracting researchers due to the diversity of its underlying physical phenomena. This section reviews the studies on various aspects of individual and multiple droplet deposition, with specific attention to micro-scale droplets, which are the main target of the current study. Initially, the impact and isothermal deposition of single droplets is investigated, and in the following sections, simultaneous spreading and solidification are reviewed. Afterwards, deposition of multiple droplets and bonding at the created interfaces are studied. Finally, microstructure and residual stress evolution during the process are explored.

2.4.1. Droplet impact

Generally, when a droplet impacts on a substrate, three various scenarios are possible, as shown in **Figure 2.16**. The droplet may spread onto the surface, rebound, or splash [109]–[111]. The occurrence of each scenario is controlled by various parameters, including the droplet speed (V), initial droplet diameter (D), density (ρ), viscosity (μ), temperature (T_d), surface tension (σ_s) of the droplet, the surface roughness (R_a), substrate temperature (T_s), and wettability of the substrate, which manifests as the contact angle (θ), thermal conductivity (K), specific heat (C_P), latent heat of solidification (L). These parameters can be organised into dimensionless numbers such as Weber (We), Ohnesorge (Oh) Reynolds (Re), Prandtl (Pr), Capillary (Ca), Bond (Bo), and Froud (Fr) numbers to characterize the dynamics of spreading.

$$Re = \frac{\rho VD}{\mu} = \frac{\sqrt{We}}{Oh} \quad \text{(Equation 3)}$$

$$Pr = \frac{\mu c_p}{k} \quad \text{(Equation 4)}$$

$$Ca = \mu V/\sigma \quad \text{(Equation 5)}$$

$$Bo = \rho g D^2/\sigma_s \quad \text{(Equation 6)}$$

$$Fr = V^2/gD \quad \text{(Equation 7)}$$

$$Ste = \frac{C_p(T_l - T_s)}{L} \quad \text{(Equation 8)}$$

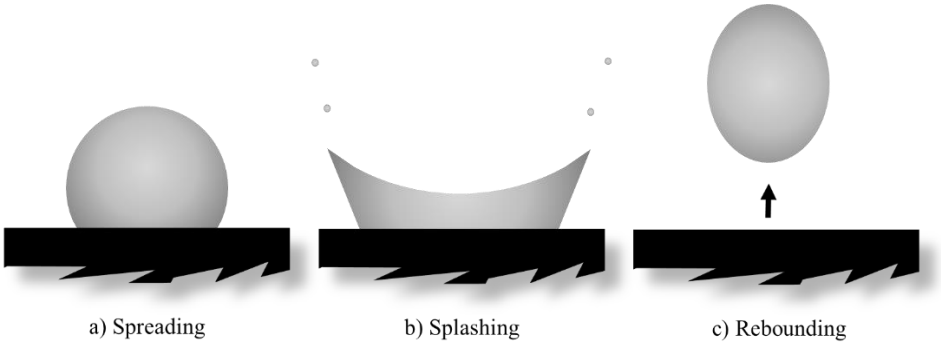


***Figure 2.16**- Possible scenarios during the impact of a droplet onto a surface, a) spreading, b) splashing, and c) rebounding.*

One or a combination of these parameters could be considered to characterise the droplet spreading. In the case of small droplets, and if $Bo \ll 1$ and $Fr \gg 1$, the gravitational effects are negligible (Bond and Froude number) [109], [112]–[114]. Thus, the dominant forces will be inertial and capillary. The We number (**Equation 1**) is the ratio between the inertial and the surface tension forces. The Ohnesorge number (**Equation 2**) is the ratio of the internal viscosity dissipation to the surface tension. These two parameters determine the driving force for droplets spreading onto the substrate and the resistance force, respectively. At high We numbers, the impact-induced dynamic drives the droplet outward at the contact line, while at lower We numbers, it is pulled out by the capillarity forces.

2.4.2. Isothermal spreading of droplets

To reduce the complexity of the problem, the effects of heat transfer are separated from the droplet spreading in this section. Consequently, three parameters suffice to characterise the spreading, which are Oh, We, and equilibrium contact angle (θ_e) (**Equation 9**). The wettability of the substrate by droplet is defined by the equilibrium contact angle, obtained from the horizontal force balance at the contact line (**Figure 2.17**). The correlation of θ_e with the surface tension, the interfacial tension between a liquid and a solid surface, and the surface free energy of the solid is given by Young's equation:

$$cos\theta_e = (\sigma_{SG} - \sigma_{SL})/\sigma_{LG} \quad \text{(Equation 9)}$$

Where σ_{SG} and σ_{LG} are the surface energies of the solid and liquid, respectively, and σ_{SL} is the energy at the solid-liquid interface.

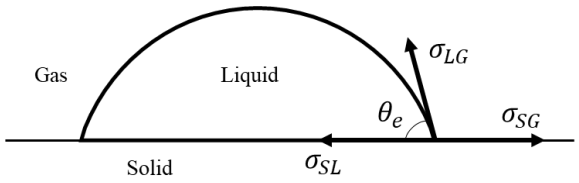


Figure 2.17- *Illustration of a droplet on a solid substrate with surface free energies and equilibrium contact angle.*

When a droplet is deposited onto a surface, it does not spread infinitely and pulls back to form a spherical cap shape. The droplet spreads more if it has lower surface tension and the surface has higher surface energy. The three-phase contact line advances and recedes depending on the solid/liquid interfacial energies until it reaches the equilibrium condition. If $\theta_e < 90°$, the surface is considered to be wettable by the liquid, and the smaller the θ_e, the better the wetting conditions.

The four principal phases during the isothermal impact and spreading of droplets at low We numbers and with a high surface tension onto a substrate are the Kinematic, Spreading, Relaxation and Wetting phases [112], [113]. At the early stage of impact, i.e., the kinematic phase, the contact diameter increases with time ($D \propto t^{0.5}$), regardless of the wettability between the droplet and the substrate [30], [115], [116].

In the spreading stage, the contact line is pushed outward radially until it reaches its maximum extent, and the surface forces act against the further spreading of the droplet. Here, the dynamic contact angle (θ_d) is smaller than the equilibrium contact angle (θ_e). It has been shown numerically and experimentally that, as in the kinematic phase, wettability does not play a role in the spreading phase [112], [116]. In the first two stages, the liquid motion is dominated by inertia forces. The contact line of the droplet continues to retract and then advances ($\theta_d > \theta_e$) during the relaxation phase, and the dynamic contact angle decreases. During this phase, which usually lasts longer than the previous ones, wettability becomes an influential parameter, and it will be determined if the droplet will continue to recoil and oscillate or rebound. The receding is more significant for surfaces with a poorer wettability condition [117]. Lower Oh number and higher We numbers also induce more recoiling [118]. The liquid motion in the droplet decelerates at the wetting phase until the droplet dissipates its impact energy and obtain a steady contact diameter. The contact angle is equal to the equilibrium contact angle in the non-reactive wetting, and the steady contact angle in the reactive wetting. The post-spreading dynamics, mainly the oscillations are occurring for droplets with a low Oh number. While for the higher Oh number in materials such as glycerol, these oscillations are quickly damped by viscous force.

Schiaffino [119] established an operational regime window for an incompressible flow with constant viscosity, obtained from the fluid flow dynamics. He classified the characteristics of droplet spreading into four groups based on their driving and resisting forces, as shown in **Figure 2.18**. In Zone one and two, the viscous effects during spreading are insignificant. Here, the viscosity influences the dynamics of droplets only at the later stages of spreading to slow down the contact line advance or dampen the oscillations [120]. The primary difference between these zones is their driving force for spreading, which is the impact pressure for zone one ($We \gg 1$) and the capillarity forces for zone two ($We \ll 1$). Thus, for the impact-driven zone, the kinetic energy of the drop just before the deposition determines the subsequent outcome. While for the capillarity-driven zone, the interfacial forces play the determining role in the final morphology of the droplet. Most metals [42], [120], [121], water [120], [122], most DoD printing inks [92], [111] fall in these two categories, which is the main target of this thesis.

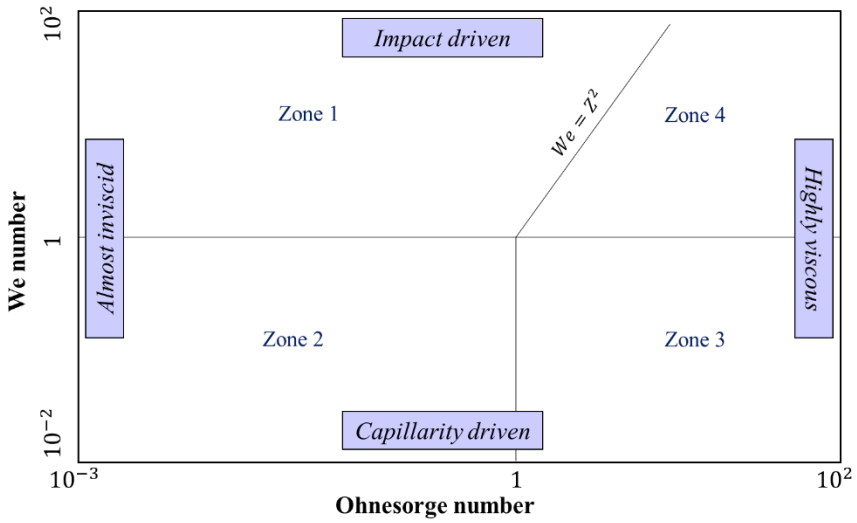


Figure 2.18*- The classification of droplet spreading based on their driving and resisting force.*

- ***Effects of impact speed on droplet's spreading***

Dirkjan et al. [123] studied the impact of water microdroplets under various impact velocities, i.e., various We numbers. The shape evolutions of a 60 µm droplet with an initial velocity of 0.74 m/s and a 66 µm droplet with an initial velocity of 11.4 m/s are shown in **Figure 2.19** a and b, respectively. At the low impact speed (We=0.45), the spreading was capillary-driven (zone 2 in Figure **2.18**), consequently, the shape of the droplet changed simultaneously with the spreading. While at the higher impact speed (We=119), the spreading was impact-driven, i.e., zone1 in Figure **2.18**. In this case, the upper section of the droplet remains relatively unchanged during the spreading since the spreading time scale is shorter than that of deformation caused by the surface tension. At higher impact velocities, the droplet might splash and form a prompt or Corona splash [113]. The Prompt splash refers to a scenario in which small droplets are generated from the contact line during the early spreading stage when the lamella has a high radial velocity. In Corona splash, small droplets are formed around a corona rim during the early stages of spreading. For high impact velocities and mostly for non-wetting situations ($\theta > 90°$ at equilibrium) [124], droplets may partially recede or even completely lift off the surface. In the context of DoD additive manufacturing, deposition and spreading are favourable scenarios that permit the construction of 3D parts in a drop-by-drop fashion.

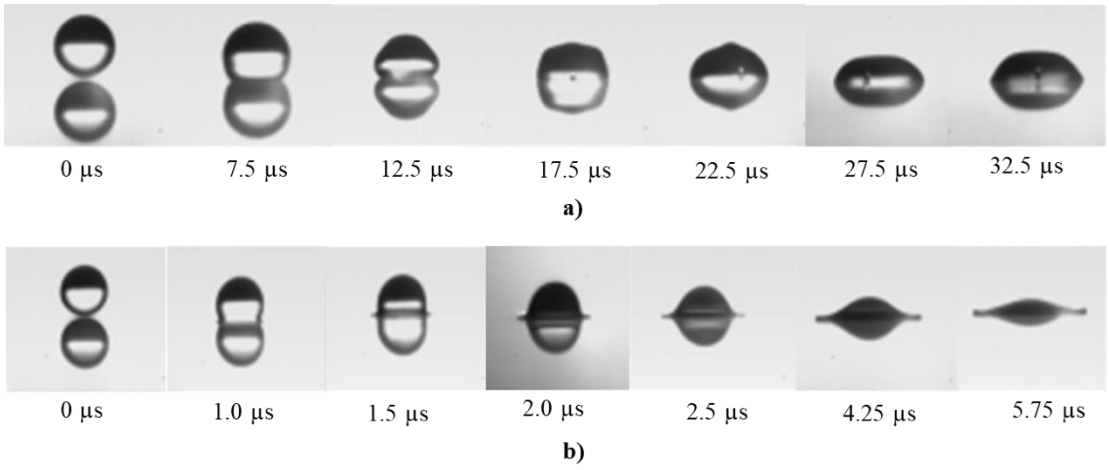


Figure 2.19- *Impact of a water microdroplet of a) 60 µm with an initial velocity of 0.74 m/s (we=0.45), and b) 66 µm with a velocity of 11.4 m/s (We=119) onto a solid surface* [123].

- ***Effects of surface wettability on droplet spreading***

The morphology evolution of 49 µm water droplets impacting onto hydrophilic and hydrophobic surfaces with a velocity of 4 m/s was investigated by Dong et al. [125], as shown in **Figure 2.20** a and b, respectively. The contact line increased rapidly during the spreading phase for a good wetting condition. This was followed by a slight retraction and an eventual and gradual increase, until the equilibrium condition was reached. A pancake shape with a very small contact angle (6°) was obtained at the end. Similarly, the spreading factor increased rapidly in the spreading phase for a hydrophobic surface, however, its extent was more limited than the hydrophilic surface. After that, the contact line retracted considerably and spread again. The droplet fluctuated several times until it stabilised. The final spreading factor was lower in the non-wetting condition, and the contact angle was higher (110°).

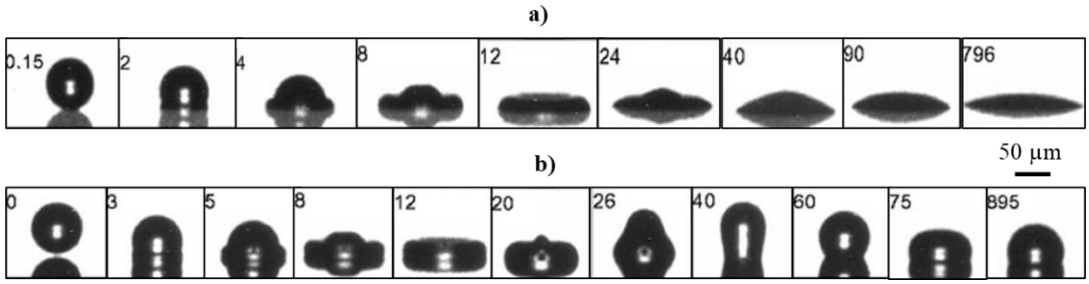


Figure 2.20- *Evolution of 49 µm water droplets' shape during the impact and spreading onto a) hydrophilic and b) hydrophobic surfaces (the number at the top left of each frame indicates the time in µs)* [125].

Bayer et al. [124] studied the deposition of 1.4 mm water droplets on a surface with various wettability, as shown in **Figure 2.21**. While the droplet spread to form a small equilibrium contact angle for the wettable surface, the contact angle for a partially wettable substrate was close to 90°. In the case of a non-wettable surface **Figure 2.21 c,** the water droplet bounced off from the substrate. Indeed, ripples were formed on the periphery of these droplets due to severe free-surface deformation in this case. These oscillations were more pronounced for surfaces with a lower wettability, resulting in an eventual rebounding from the surface.

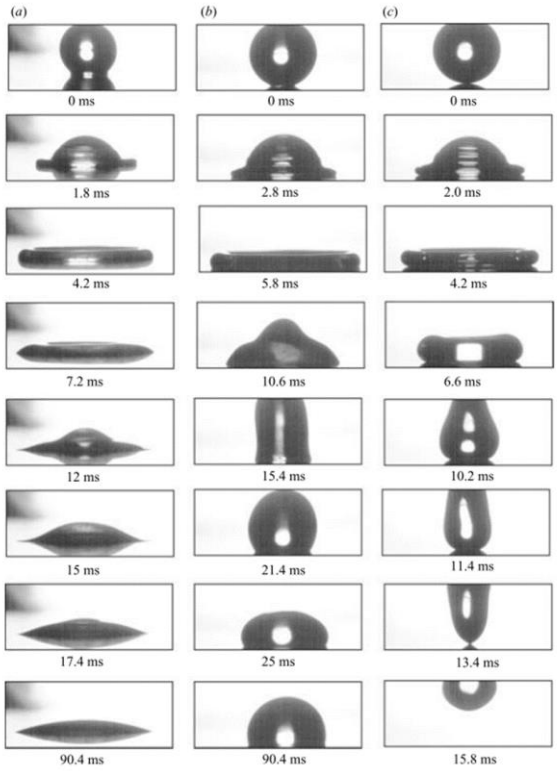


***Figure 2.21**- Impact of 1.4 mm water droplets with an impact velocity of 0.7 m/s onto a) wettable, b) partially wettable, and c) not-wettable substrate* [124].

- ***Effects of surface tension on droplet spreading***

Pasandideh-Fard et al. [126] investigated the spreading of 2 mm water droplets with various surfactant levels, i.e., various surface tensions, onto a stainless steel substrate at a velocity of 1 m/s. As shown in **Figure 2.22**, for all cases, the droplet kinetic energy

was not enough to overcome the surface tension (due to a low We number, $We = 27$), consequently, there was no splashing or breaking up. They observed that adding surfactant of various levels did not impact the droplet spreading significantly, and its influence was only evident during the recoiling stage. This observation was attributed to the inertia-dominated nature of the spreading phase and the capillary-dominated nature of the recoiling stage. Another important outcome of this experiment was observing entrapped bubbles in the central area, where the droplet initially impacted the substrate.

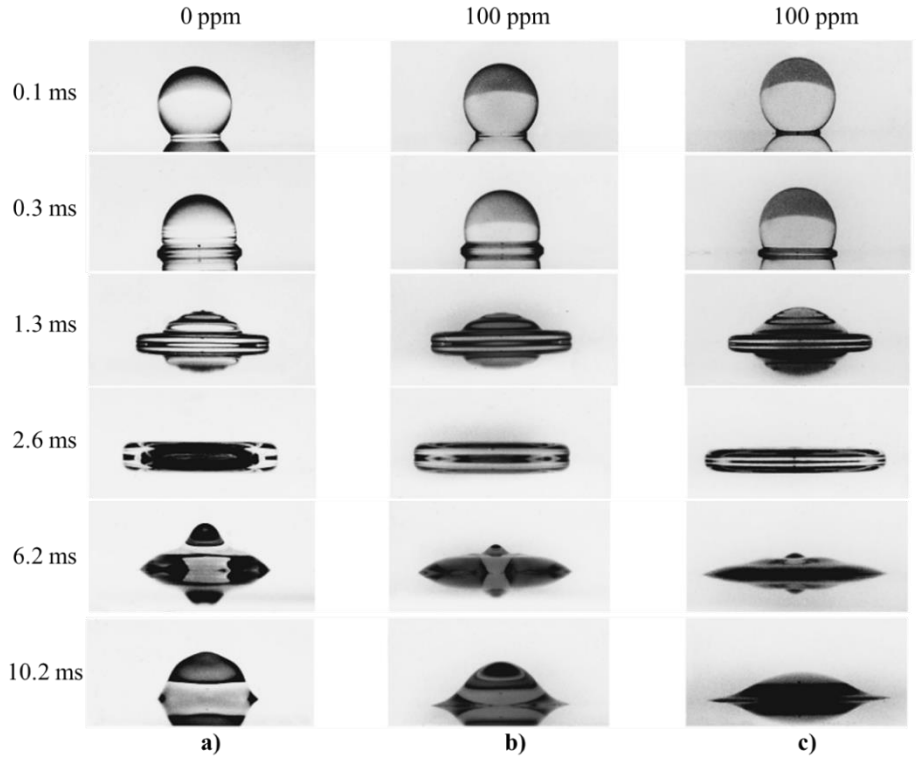


Figure 2.22*-Droplet morphology evolution during the impact of droplets of a) pure water, b) water with 100 ppm of surfactant solution, and c) 1000 ppm surfactant solution* [126].

2.4.3. Droplet's spreading and solidification

For isothermal depositions, the equilibrium contact angle determines the final shape of droplets. However, in a non-isothermal process, the final morphology is determined simultaneously by the spreading characteristics and solidification behaviour. Solidification and spreading for droplets of similar material and dimensions occur in altered time scales as a function of the substrate and droplet's superheat temperatures.

Generally, solidification influences droplet deposition by arresting the contact line motion and dissipating the kinetic energy of the droplet. The local solidification mainly controls the time and location of the contact line arrest during the spreading, which usually occurs at the interface with the previously deposited droplets or the substrate. The solidification front line can potentially be arrested in various spreading phases, i.e., Kinematic, Spreading, Relaxation or Wetting phases, as a function of the substrate temperature.

The key question is if dynamic wetting and solidification are independent phenomena or if they occur concurrently. The spreading time for larger droplets is usually shorter than the onset of local solidification [119]. However, for microdroplets (especially metallic material), the spreading and solidification periods are comparable. It has been established in the literature that the droplet follows the iso-thermal spreading schematic presented earlier until its base solidifies onto the substrate. Moreover, the initial temperature of the substrate (substrate undercooling) does not influence the spreading behaviour at any time before the onset of local solidification [40], [115], [120].

Despite the intense research in the field of droplet spreading and solidification, the mechanism of contact line arrest remains poorly understood. This ambiguity is intensified by the lack of experimental equipment that can fully capture this rapid phenomenon [127]. Currently, there exist five hypotheses (**Figure 2.23**) on how and where the contact line of a molten material comes to a halt during the spreading: I) The contact line arrests when the dynamic contact angle reaches a critical value, defined by the Stefan number ($\theta \propto St^{1/2}$) [120], [128], [129]. The main issue with this theory is the prediction of this contact angle due to the singularity of heat flux at the trijunction. II) The spreading is halted when a critical volume of liquid at the contact front is solidified. Tavakoli et al. [32] obtained the critical volume by solving a 1D solidification problem from the contact line. The issue of the hypothesis is the accuracy of the solution for solidification at the front line. To date, this theory has only been validated for low Stefan numbers and hexadecane droplets. III) The droplet spreading is arrested when the temperature at the contact line goes below a critical value. At the critical temperature, which is influenced by the kinetic undercooling, the

crystal growth rate at the contact line is equal to the front-line velocity. Ruiter et al. [30] solved the Navier-Stokes and heat transfer problems locally near the contact line to obtain the speed and temperature evolution. This theory has been validated for hexadecane droplets only [127]. The main drawback of this hypothesis is that the effects of contact resistance and solidification latent heat are neglected to account for the rapid wetting in the arrest condition. IV) The contact line arrests when the solidified layer, grown from the substrate, reaches the height of the spreading droplet. In this theory, it is assumed that the droplet has a final pancake shape. It is also considered that the spreading is limited by solidification and not by the surface tension or viscous effects, so their effects are neglected. The theoretical results on Sn droplets somehow matched the experimental results [31]. V) In this novel approach, the underlying physical laws of chemical potentials in the contacting phases set the advancement of liquid-solid interface. This approach aims to eliminate the need to prescribe the front's velocity or such feature of process. In other words, the speed of solidification at the contact line and its arrest are an outcome of a particular problem [115]. This theory promises to overcome the limitations counted earlier, however, there is no experimental evidence to prove this hypothesis yet.

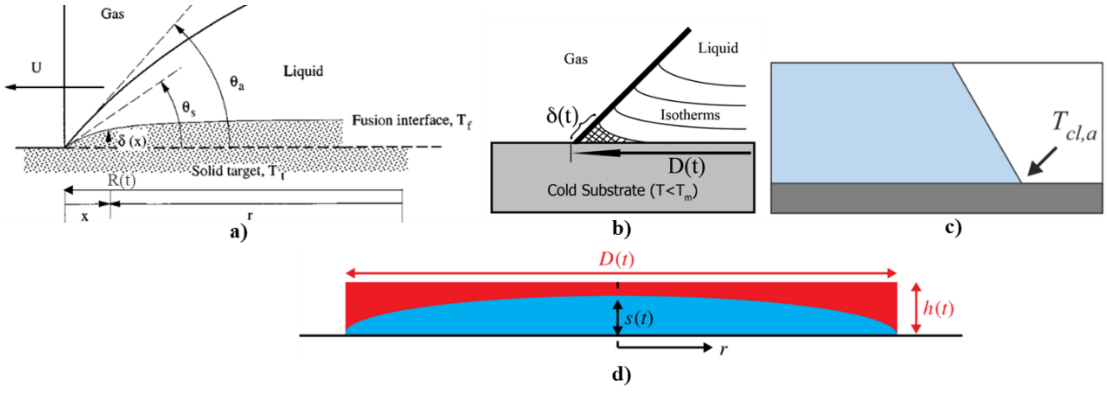


Figure 2.23*- Schematic representation of various hypotheses with regards to the mechanism of contact line arrest based on: a) the critical solidification contact angle* [119], *b) solidification of a critical volume at the contact line* [32], *c) the liquid at the contact line reaches a critical temperature* [30], *d) a critical thickness of the droplet is solidified* [31].

After the contact line is arrested, liquid parts of the droplet keep oscillating during the progressive solidification, whilst the footprints remain unchanged. The oscillations continue until they are dampened by the viscous effect, or the droplet is fully solidified. For microdroplets in zone one and two in **Figure 2.18**, the time required for viscous forces to dampen the oscillations is very long. Unless the substrate temperature is close to the melting point of the droplet, the solidification time is much shorter than the damping period. Hence, the oscillations freeze in place and create ripples on the periphery of droplets.

Most research on droplets' solidification dynamics has focused on millimetre-sized droplets. Whereas the research on microdroplets has been hindered by the time and size scale of the process. The experimental study on microdroplet solidification is limited to the investigation of Attinger et al. [40]. They studied the behaviour of eutectic tin-lead solder microdroplets of ~ 80 μm onto a semiconductor P-Si wafer coated with a 0.1 μm thickness gold on the top of it. They captured the transient morphologies of droplets for substrate temperatures from 48 ℃ to 135 ℃ by combining the images from various identical impacts taken at multiple sequences from a stroboscopic camera (**Figure 2.24**). The spread factor increased monotonically with the substrate temperature up to a certain temperature (98 ℃ in this case), and it was almost constant afterwards. This signifies that the droplet's solidification occurs after an initial spreading at a higher substrate temperature. Whereas the local solidification prevents the complete spreading of droplets at lower substrate temperatures. They also claimed that the solidification time does not vary monotonically as a function of substrate temperature. This is because the maximum droplet height and spread factor are not linear with the substrate temperature. Furthermore, they observed that ripples only formed on the periphery of droplets at lower substrate temperatures but disappeared at higher substrate temperatures.

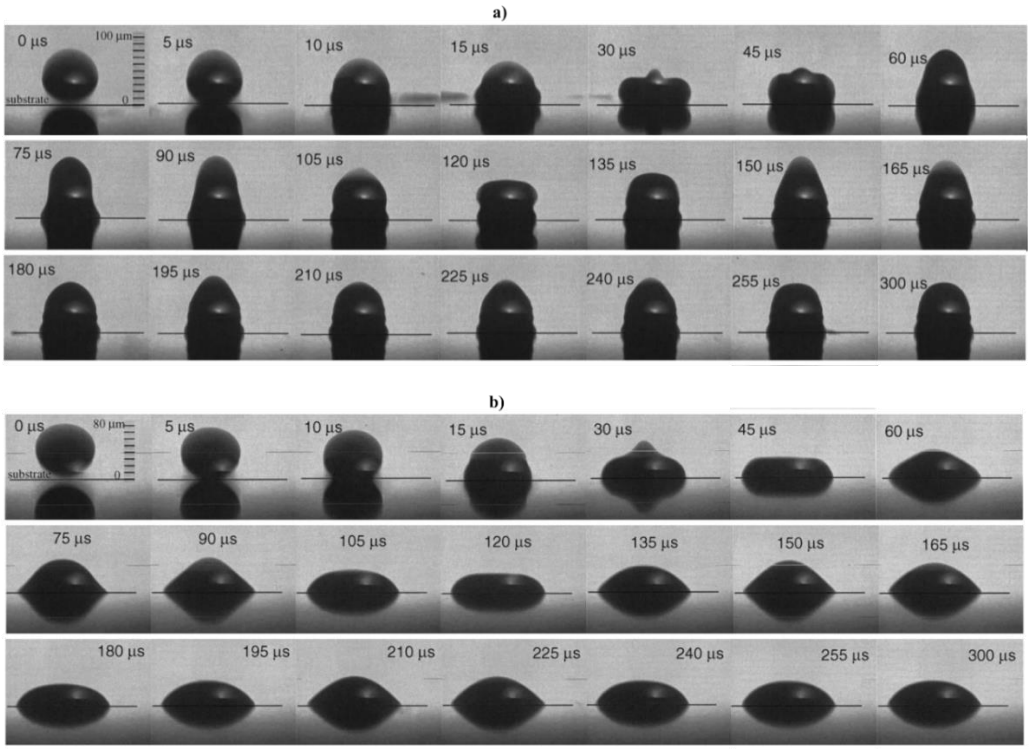


***Figure 2.24**- Evolution of morphology of solder microdroplets of 210 C onto a gold-coated semiconductor substrate a) at 48 C with an impact velocity of 1.54 m/s and b) at 135 C with an impact velocity of 1.49 m/s (droplets' diameters are 80 µm and 84 µm in a and b, respectively) [40].*

Even though the dynamics of solidification for millimetre-scale droplets is different from the microdroplets, it is essential to review them since they can bring insights into the physical phenomena behind this question. Pasandideh-Fard et al. [130] photographed the spreading and solidification evolution of 1.2 mm Sn droplets impacting on a stainless steel substrate at a velocity of 1.6 m/s for various substrate temperatures (**Figure 2.25**). It was seen that the droplets followed similar dynamics before the solidification arrested the contact line. The solidification period was fastest for the room temperature substrate and slightly longer for the medium temperature. While for the isothermal condition, i.e., the deposition temperature equal to substrate temperature, the droplet pulled back after reaching the maximum diameter, raised off from the surface and finally fell back to reach the equilibrium contact angle.

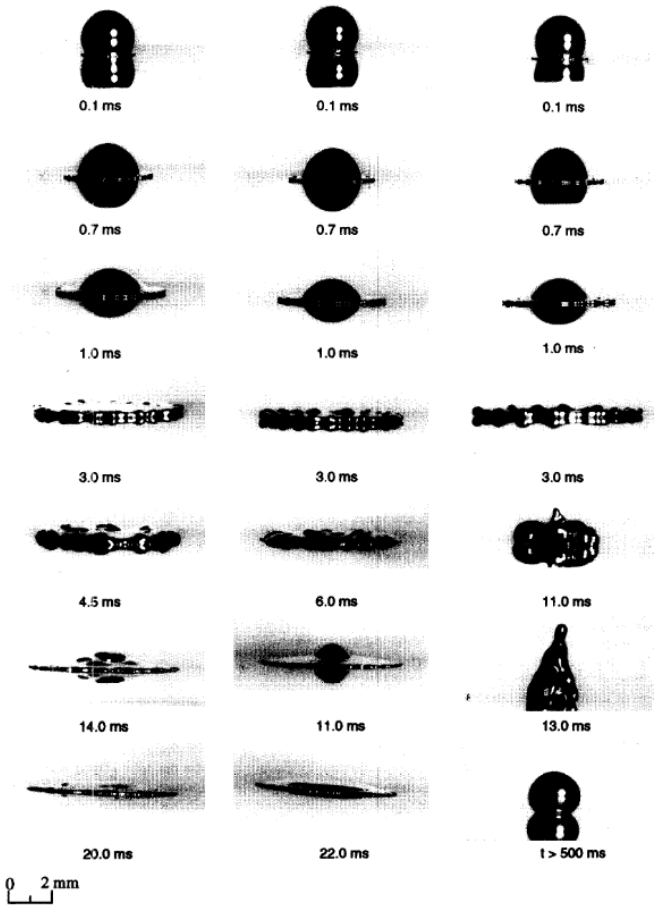


Figure 2.25- *Spreading and solidification evolution of a 1.2 mm Sn droplet onto a stainless steel substrate at various temperatures* [130].

Gielen et al. [31] used an interesting approach to investigate the dynamics of solidification for tin droplets of 1.7 to 2 mm at 250 °C impacting onto a Sapphire substrate with a velocity of 0.5 to 5.5 m/s at 39 °C, 150 °C, and 249 °C by capturing the bottom and side views. In the isothermal case, the droplet retraction (after the initial spreading phase) was followed by a partial bounce-off and detachment from the surface (**Figure 2.26** a). This was attributed to the poor wettability of the substrate. The droplet spreading seemed similar to the isothermal condition before the contact line arrests at the lower substrate temperatures and from the typical side view images. However, the bottom view images revealed that the spreading was indeed dissimilar from the early stages of impact. In non-isothermal cases, air bubbles were entrapped in the central zone of the contact. In contrast, the air entrapment was not visible in the

isothermal cases, possibly due to the pinch-off and detachment. It was seen that the solidification influences both the spreading velocity and the spreading factor.

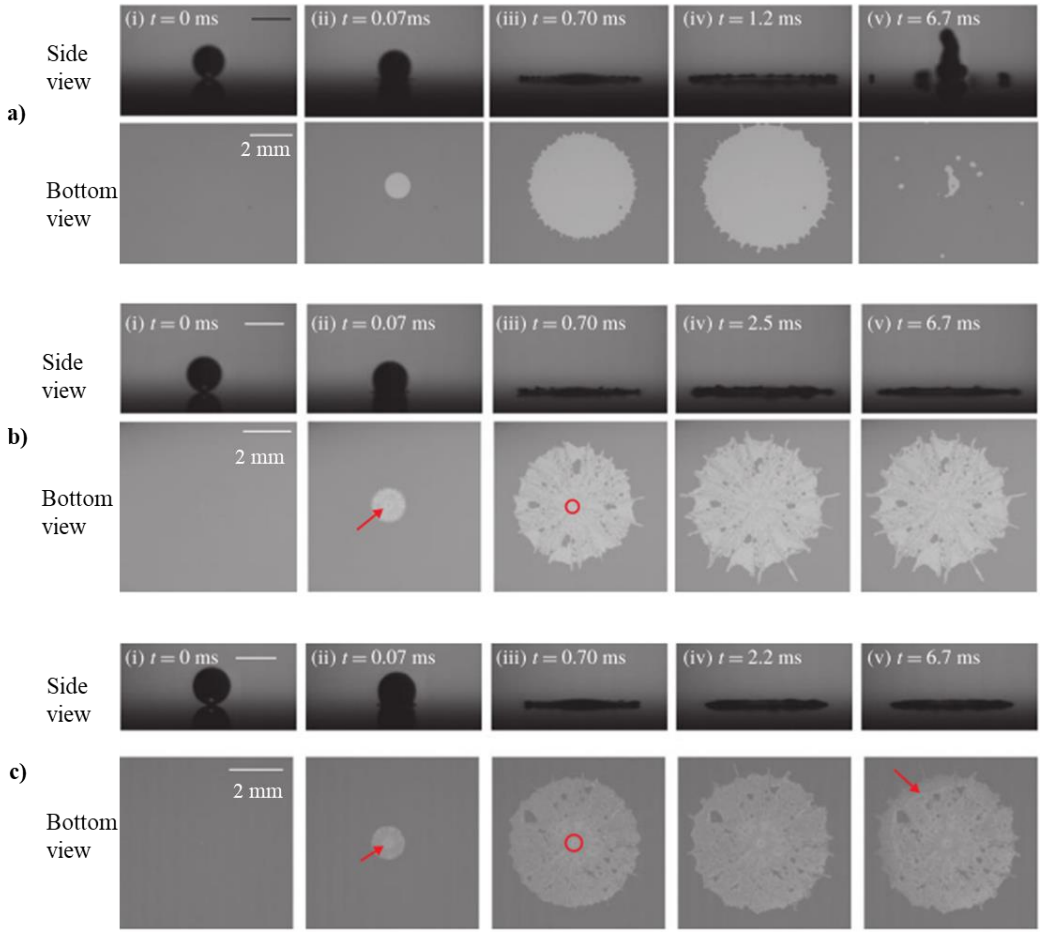


***Figure 2.26**- Top and side view images during the impact of a 1.7 to 2 mm Sn droplet at a velocity of 0.5-5.5 m/s onto a Sapphire substrate at a) 249 °C (Isothermal deposition), b) 150 °C, and c) 39 °C [31].*

Whether the equilibrium solidification models can correctly capture the rapid solidification of microdroplets is still a debate. Whereas Gielen et al. [31] claimed that metal droplet solidification follows equilibrium solidification, Fedorchenko and Wang [131] showed that the effects of nucleation delay cannot always be neglected. They showed that for Ag, Cu, and Ni microdroplets impacting on an Ag substrate at a velocity of 30 m/s, the equilibrium solidification model fails to describe the process, while for Al/ Ag, it can be used. Bennett et al. [132], however, demonstrated that solidification is mainly governed by heat transfer and not controlled by crystallization

kinetics. The high-speed photography of hexadecane and water droplets solidification in recent years has strengthened the hypothesis of nonequilibrium solidification. Koldeweij et al. [127] investigated the contact line arrest of a hexadecane droplet of 0.85 mm on a Saphire substrate at a very low impact velocity. Their observations validated the hypothesis of Ruiter et al. [30]. As presented in **Figure 2.27**, the interaction of a moving contact line with the crystal nucleation and/or growth results in the contact line arrest. As per **Figure 2.27**-a, if a crystal nucleates at the contact line, the contact line gets pinned to the substrate immediately. This random nucleation can be caused by heterogonies on the substrate. On the other hand, the contact line motion is not influenced by crystals formed away from the fluid front. However, the droplet spreading gets arrested if the crystal grows toward and reaches the contact front (Figure 26-b-2).

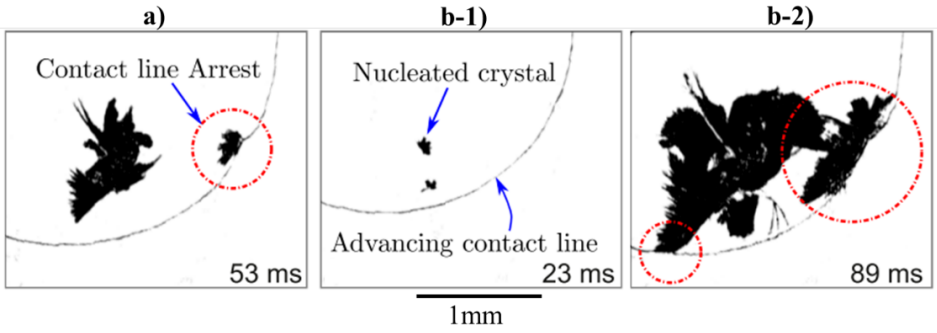


Figure 2.27- *Mechanism of contact line arrest in a hexadecane droplet of 0.85 mm gently deposited onto a Saphir substrate* [127].

To conclude, a thorough study on the solidification dynamics of micro metallic droplets is missing from the literature. Based on the available literature, the iso and non-iso thermal spreading cannot be experimentally differentiated until the contact line is arrested. Consequently, the substrate undercooling does not influence the droplet dynamics before the front is arrested. Hence dynamic wetting and solidification can be considered separate phenomena. Moreover, drops are arrested more quickly for lower substrate temperatures and a substrate with higher thermal conductivity. Last but not least, the monodical increase and decrease of the spread

factor and solidification contact angle, respectively, as a function of the substrate temperature, were reported in most studies.

2.4.4. Spreading and solidification of multiple droplets

The physical laws governing the behaviour of successive droplets upon deposition are similar to single droplet deposition. In the literature, this topic has been undertaken through (I) studying the deposition of successive droplets onto a substrate and in adjunct with previously deposited droplets[6], [64], [133], [134] (II) successive deposition of droplets in a vertical column [135]–[137]. In the majority of these studies, droplets are millimetre-sized, and to the best of the author's knowledge, multi-microdroplet deposition has been scarcely investigated. While the single droplet spreading and solidification are uniquely controlled by the interaction with the substrate, the multiple droplet deposition (case I) is influenced by the adjunct droplets and substrate. The spreading of $Droplet_{n+1}$ is restricted by the footprint of the $Droplet_n$, moreover, solidification of the new deposited droplet is massively influenced by the increase of the contact surface area with the previous droplet.

- ***Droplet next to droplet deposition***

Li et al. [13] studied the deposition of successive Al droplets onto a substrate through numerical modelling and experimental observation (**Figure 2.28**). They demonstrated that the horizontal solidification ripples on the surface of the 1st droplet transfer to L-shaped ripples on the 2nd droplet surface. This is due to a layer-by-layer solidification of the droplet from interfaces with the substrate and previously deposited droplet. They also demonstrated that the cooling speed of $dropelt_2$ is higher that $droplet_1$ because of the increased contact surface in the former. Moreover, they reported the formation of inter-droplet pores because the second droplet could not fill the space between the solidification ripples.

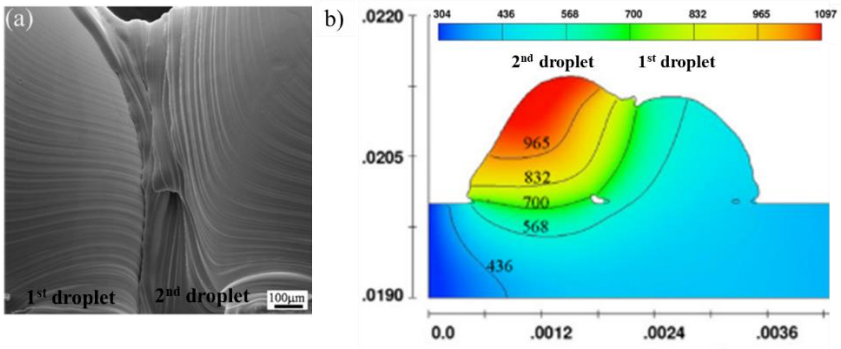


Figure 2.28*- a) Horizontal and L-shaped solidification ripples on the surface of the 1st droplet and 2nd droplet, respectively. b) numerical simulations predicting the formation of solidification ripples inter-droplet pores [13].*

Dou et al. [138] studied the interaction between two consecutively deposited solder droplets (300 µm) and its consequences on the final droplet morphology as a function of the substrate temperature. They showed that at low and high substrate temperatures (**Figure 2.29** a and b), where the interfacial temperatures are lower and higher than the melting point of the metal, respectively, landing errors occur. The landing error is the displacement of droplets from their original landing location due to the surface tension prior to the solidification. Based on numerical modelling, they suggested an interval for the substrate temperature, where the landing error is minimized. Qi et al. [139] used a simple geometrical model to predict the required overlap between droplets to attain high-density 3D parts.

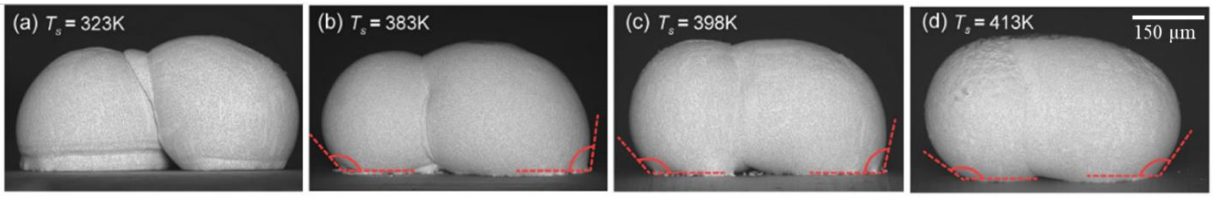


Figure 2.29*- Final morphology of solder successive solder droplets as a function of Al substrate temperature* [138].

Some studies investigated the effect of centre-to-centre distance and jetting frequency in the final morphology of lines printed by DoD-MJ [8]. If the centre to centre distance between droplets is too hight, scalloped or discontinuous lines are formed. However,

too much overlap can cause staircasing (lift-up lines) or bulging lines (when the delayed solidification permits surface tension effects to bring droplets together). They proposed a process map to avoid all these defects and obtain a straight line when printing Al 4043 on polyimide substrates.

- ***Droplet on droplet deposition***

Haferl et al. [83] studied fluid dynamics and solidification of solder microdroplets impacting on previously deposited microdroplets, i.e., on curved surfaces, using a numerical and experimental approach. As demonstrated in **Figure 2.30**, the droplet spreading is significantly influenced by the surface curvature of pre-deposited droplets compared to the spreading behaviour on a flat surface. Moreover, the effects of initial substrate temperature **Figure 2.30 a-c** on the morphology of the second droplet are more significant than the effects of the jetting velocity **Figure 2.30 d-f**.

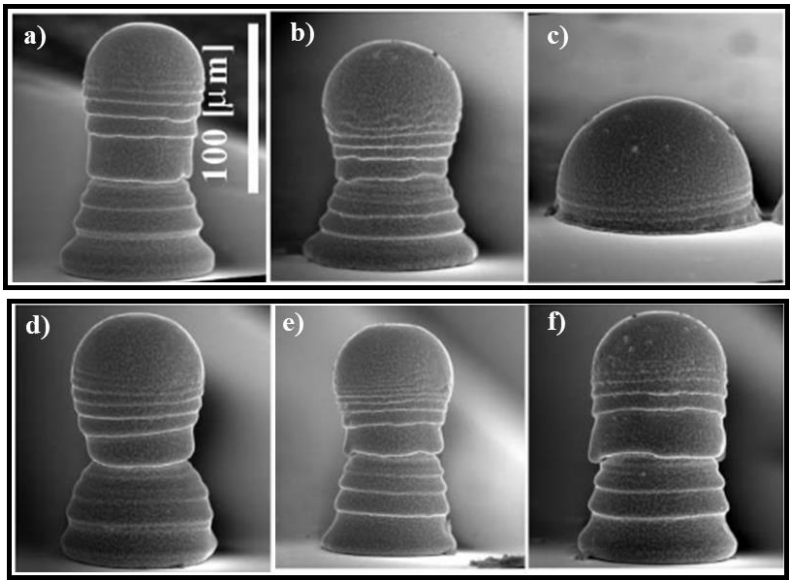


Figure 2.30*- Effects of substrate temperature a)25 C, b) 75 C, c) 125C and jetting velocity d) 1.12 m/s, e)1.38m/s, f)1.63 m/s on the morphology of solder pillar made by microdroplets of 80um in diameter (modified) [83].*

Liu et al. [141] investigated the heat accumulation issue during printing pillars of 1 mm droplets in Al 7075 alloy. They demonstrated that the heat accumulation deteriorates the pillar morphology and eventually causes a loss of accuracy. At a

constant deposition frequency, there is not enough time for previously deposited droplets to fully solidify before the impact of the following droplet. As a result, the liquid mass increases continuously (**Figure 2.31**), this liquid portion spreads more, and the final solidified diameter is larger.

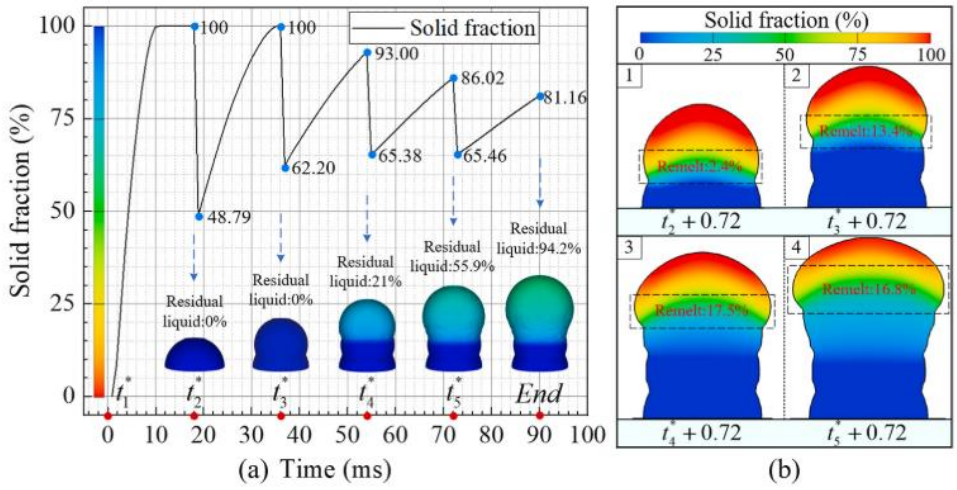


Figure 2.31*- a) Evolution of solid fraction in time, b) the diagram of remelting zone during the deposition of a pillar of Al alloy droplets* [141].

2.4.5. Bonding at the interfaces

There are three mechanisms of bonding during the droplet deposition. First, physical adsorption, where two surfaces are joined together through the weak van der Waals forces. Second, strong metallurgical bonding through melting the interface of substrate or previously deposited droplets. Third, diffusion of atoms between the substrate/ previously deposited droplet and the droplet, leading to epitaxial growth or formation of an intermetallic (IM) layer in dissimilar materials. The bonding level in the substrate melting is the strongest, hence, it is more favourable; however, a considerable energy level is required for this type. The substrate acts as a heat sink because of its significant mass difference from the droplets. Thus, droplets dissipate their thermal energy into the substrate at a high rate without significantly affecting the substrate temperature. In the literature, the bonding has been investigated in three levels (I) droplet to substrate bonding, (II) bonding between neighbour droplets, and (III) bonding between droplets deposited on the top of a previously deposited droplet. Despite slight differences,

arising from the differences at the contact surfaces, the underlying physics behind the bonding for all these levels is similar.

- ***Droplet-to-substrate bonding***

Adhesion of droplets to the substrate is a crucial aspect of the process in technologies such as thermal spraying, interconnects in integrated circuits, and DoD-MJ. The mechanism of bonding in thermal spraying processes is different from other processes. The high impact velocities in these processes cause high strain rate deformations at the interfaces, leading to thermal softening and adiabatic shear instability, consequently bonding at the interfaces [142]. While in the DoD-MJ, droplets are gently deposited onto the substrate, hence, the bonding is attributed to the droplets' thermal energies, and their kinetic energies are not influential. Among the three bonding mechanisms counted earlier, only the bonding through remelting has been investigated in the literature to date.

In a study by Zarzalejo et al. [139], a millimetre-scale Stainless Steel (SS) droplet at 2500 °C formed a strong bond to a room-temperature SS substrate through melting. As shown in **Figure 2.32**, the maximum melting depth (98 µm) was obtained at the droplet's centreline, with no melting at the edges. In another study [132], 3 mm in diameter lead droplets at 460 °C demonstrated poor bonding to room-temperature Al and Cu substrates, as evidenced by droplet curling up from the edges. In these cases, the adhesion to the substrate was not strong enough to overcome the thermal stresses generated during the cooling and solidification processes. However, for droplets of similar conditions, the bonding to the Pyrex substrate at room temperature was considerably improved such that a razor blade was needed to remove them from the substrate.

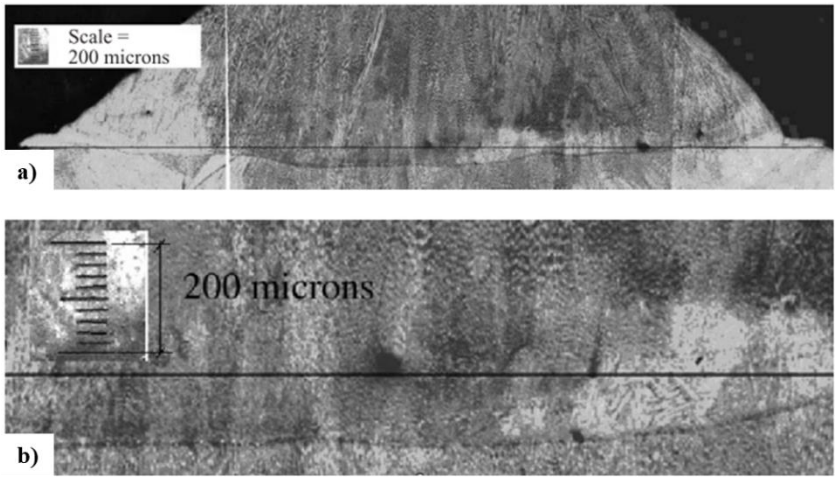


Figure 2.32*- Cross-section of a xx mm Stainless Steel (SS) droplet at 2500 °C on a SS substrate at 30 °C, a) 50 x magnification, b) close zoon at the interface [139].*

The warping of Cu microdroplets from the edges of a Cu substrate was observed in more recent DoD-MJ studies [26]. This observation was correlated to the lack of bonding at the interface, which in turn resulted in no constraint from the substrate to residual stress-induced deformation. According to the numerical results presented in the study, the poor bonding was initiated from the insufficient energy at the interface to melt the substrate and promote metallurgical bonding. Similarly, Simonelli et al. [11] found that Ag microdroplets were loosely attached to a Cu substrate in a DoD-MJ process due to the lack of metallurgical bonding at the interfaces (**Figure 2.33 a**). Moreover, they observed that a 200 nm Ag layer supersaturated in Cu formed at the interface (**Figure 2.33 b-c**).

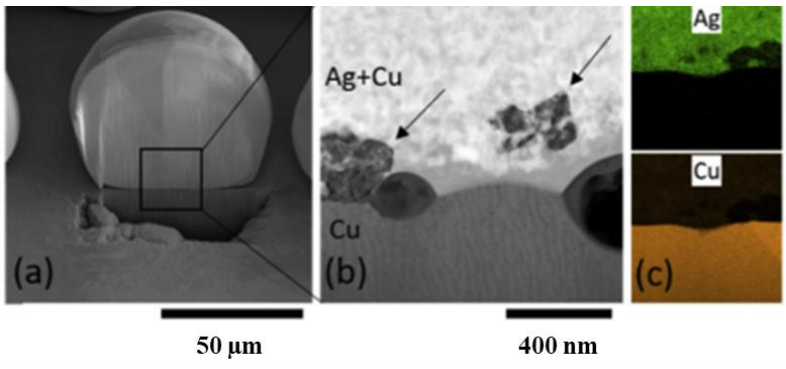


Figure 2.33*- Single Ag droplet on a Cu substrate a) FIB-SEM image indicating a poor bonding to the substrate, b) the element distribution at the interface, c) EDX of the zone in (b) with Ag depicted in green and Cu in orange [11].*

- ***Droplet-to-droplet bonding***

The bonding between droplets sets the integrity and consistency of printed parts in the droplet-based AM processes, and its mechanisms are similar to the drop-substrate bonding. A strong inter-droplet bonding is achievable through remelting the interface with the previously deposited droplets, for which the jetting frequency, droplet and substrate temperatures should be carefully selected. Chao et al. [143] demonstrated the effects of increasing the droplet and substrate temperatures on improving the inter-droplet bonding of 1.2 mm Al 7075 droplets in the DoD-MJ process, as shown in **Figure 2.34**. Their study showed that by selecting a correct set of parameters, the interfacial temperatures exceeded the material's melting point, and good metallurgical bonding was obtained. However, excessive initial temperatures caused over-melting at the interfaces, leading to the loss of geometrical fidelity. Yi et al. [63] examined the mechanism of hole-defect formation in 3D parts from 1 mm droplets of 7075 Al alloy. It was shown that these pores were formed due to an incomplete fusion and filling of molten metal between neighbouring droplets. They suggested that this issue can be eliminated by correctly selecting the droplets and substrate temperatures. In a study about the deposition of 2.2 mm Sn droplets, Ghafouri-Azar et al. [134] demonstrated that the overlap between the droplets is another influential parameter in defining inter-droplet bonding. The centre-to-centre distance determined whether the initial contact point of the second droplet is with the previously deposited droplet or the substrate.

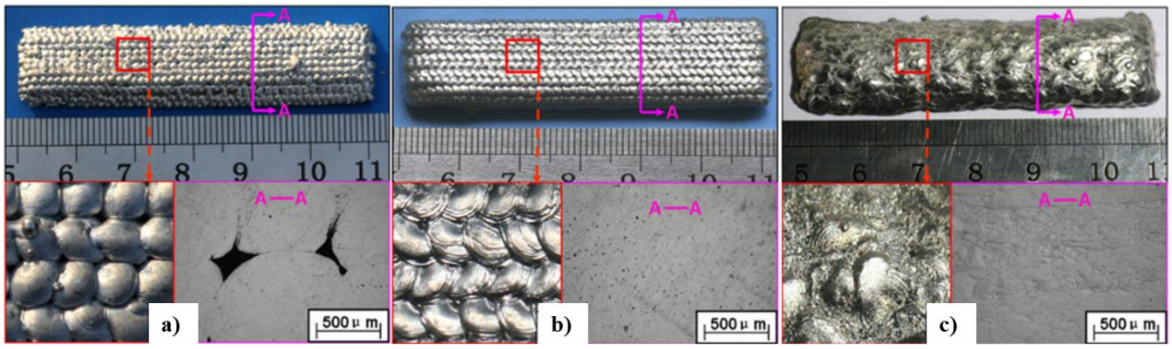


Figure 2.34- *The inter-droplet bonding at various droplet and substrate temperatures. a)* $T_{drop} = 660\ °C$ *&* $T_{sub} = 350\ °C$*, b)* $T_{drop} = 700\ °C$ *&* $T_{sub} = 450\ °C$*, c)* $T_{drop} = 740\ °C$ *&* $T_{sub} = 500\ °C$ [143].

Yi et al. [61], [63] investigated the effects of surface morphology and droplet/ substrate temperatures on the inter-droplet bonding during the DoD-MJ of Al 7075 (1 mm). They demonstrated that even if the conditions for a metallurgical bonding through remelting are theoretically provided, the presence of inter-droplet pores hinders a strong inter-droplet bonding. These pores are created since the molten material cannot fill the empty spaces created by the solidification ripple. The lack of consolidation stems from the consequent poor heat exchange through the porous areas. **Figure 2.35** demonstrates that the metallurgical inter-droplet bonding is obtained at the droplet's top which is the initial impact region between the droplet and is free of ripples. While closer to the substrate, where the ripples are more present, the remelting does not occur. Similarly, Simonelli et al. [11] demonstrated that the lack of inter-droplet bonding between Ag microdroplets is due to the lack of heat content in these droplets to melt the interfaces of previously deposited structure. Lack of inter-droplet bonding has also been reported in other DoD processes such as LIFT [79], and is believed to reduce the mechanical and electrical properties of the printed structures.

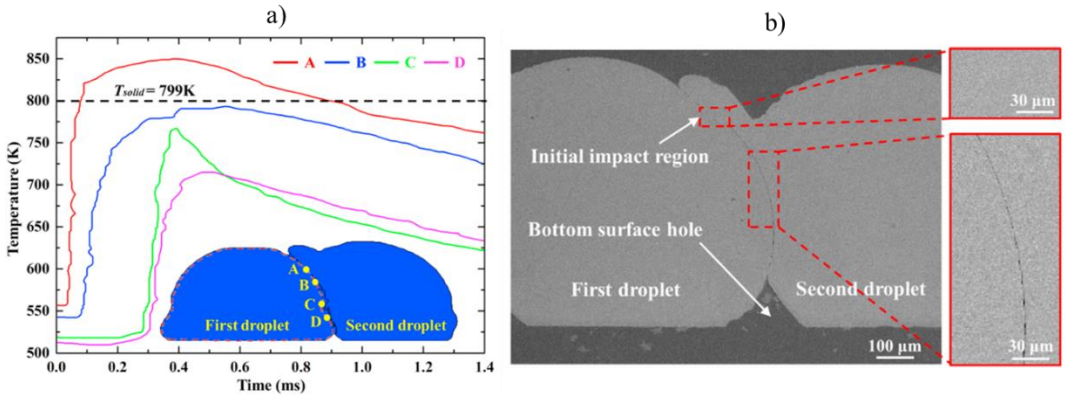


***Figure 2.35**- a) temperature evolution of the 1st droplet during the deposition of the second droplet at four locations based on the numerical simulations, b) Lack of inter-droplet bonding at zones with pores* [63].

The main reason for the lack of bonding is the low interfacial temperature. This has been reported in various techniques, such as thermal spraying. In most cases, by

increasing the substrate temperature, better bonding between the individual droplets/droplet and substrate was obtained [144].

- ***Droplet-on-droplet bonding***

Several studies have been conducted to investigate the optimal process windows to obtain a good inter-droplet bonding in a vertical column of successive droplets [81], [93]–[95]. These studies were usually accompanied by an analytical solution or numerical modelling to predict the minimum requirement to obtain a good bonding through interface remelting. Fang et al. [145] studied the effects of droplet temperature, substrate temperature, and deposition frequency on the bonding level of vertical columns of Sn droplets (600 µm) deposited onto Al substrates. They concluded that a good bonding is obtained if the temperature at the tip of the column is maintained close to the metal's melting point. To this end, the jetting frequency should be decreased as the column height increases. In another study [67], the remelting condition based on a simple analytical model (1D heat transfer) was predicted as a function of droplet and substrate temperatures (**Figure 2.36** a) for Sn droplets. The results were somehow in agreement with the experimental results, where 0.75 mm Sn droplets of various droplet and substrate temperatures were deposited in vertical columns (**Figure 2.36 b-e**).

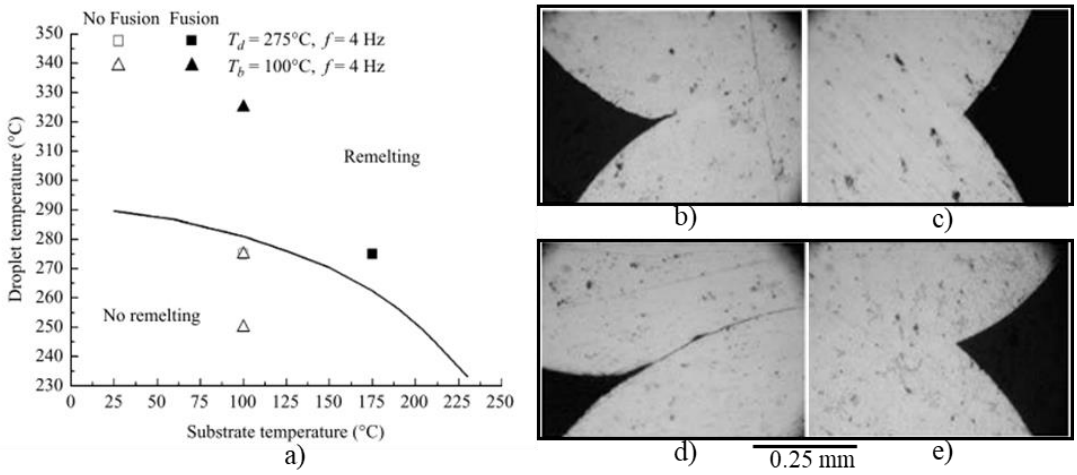


Figure 2.36*- a) the melting and no-remelting conditions predictions based on an analytical model in various droplet and substrate temperature ranges for Sn droplets. Cross-section of vertical columns of 0.75 mm Sn droplets at b)* $T_d = 275\ C$ *and* $T_s = 100\ C$*, c)* $T_d = 275\ C$ *and* $T_s = 190\ C$*, d)* $T_d = 250\ C$ *and* $T_s = 100\ C$*, e)* $T_d = 325\ C$ *and* $T_s = 100\ C$ [67].

- ***Quantitative characteristics of bonding***

To the best of the author's knowledge, the level of droplet-droplet and droplet-substrate bonding in the context of DoD-MJ has not been experimentally measured to date. The bonding strength in the thermal spraying process, which is a function of particle impact velocity, particle size, material properties, and initial temperatures [146], has been numerically estimated in some studies [147], [148]. However, only a few attempts have been made to measure the adhesion of single droplets in thermal spraying techniques, which is due to the technical difficulties originating from the micro-scale dimension of droplets [149]. Besides, the adapted methods are suitable for thin films and not applicable for DoD-MJ, where droplets keep a spherical cap shape on deposition.

Balic et al. [149] measured the adhesive strength of a single Alumina droplet on a steel substrate in the cold spraying process. They used the indentation technique, as demonstrated in **Figure 2.37**, followed by the interfacial droplet-substrate crack propagation. Through energy conservation, they assumed that the increase of indentation strain energy is fully expended to grow the interfacial crack. This approach may provide reasonable results for thin droplets, where the force application causes delamination. However, the technique is expected to fail in the case of strongly adhered droplets of ductile materials or spherical droplets.

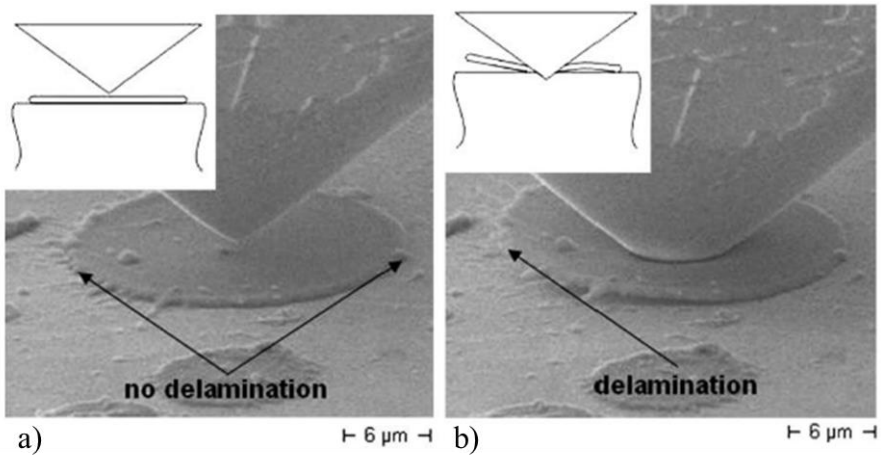


Figure 2.37*- In situ SEM instrumented indentation showing the a) droplet before and b) after applying the force* [149].

2.4.6. Microstructure

During solidification, the metal or alloy undergoes a transformation from a non-crystallographic to a crystallographic state. It is essential to obtain information about the mechanism of solidification, which defines the microstructure of the solid object and eventually sets the mechanical properties of parts. When a liquid material is undercooled below its equilibrium melting temperature, the driving force for solidification ($G_l - G_s$) may cause the appearance of dendrites. This transformation requires the presence of small solid particles or nuclei. In such cases, a spherical solid may nucleate inside the liquid and, later, grow in a preferred growth direction. However, in the absence of impurities or a contact surface, the liquid temperature can go below the freezing temperature without the onset of solidification (undercooling, also called supercooling) [150]. This condition for large undercooling is provided in processes such as thermal spraying or DoD-MJ when printing pure metals. For example, it has been reported that Si droplets can be undercooled under suitable conditions up to 234 K below the melting point [151]. The solid particles or nuclei grow in the undercooled liquid, and simultaneously the latent heat of solidification is conducted into the liquid. The interface of these initial spherical particles becomes unstable; thus by virtue of minimizing the surface energy, the surface will become smaller.

Consequently, the primary arms develop in crystallographic directions, meaning the tip of dendrites grows sharper. The primary arms keep growing until they become unstable and break up into secondary and tertiary arms. This shape is called a dendrite. The directional growth of dendrites in a specific crystallographic direction, for example, in the direction of heat flow, leads to the formation of columnar grains. The equiaxed structure results from a random growth of the dendrites without a preferential orientation towards the heat-flow direction. There are several explanations for such a grain structure: (I) the dendrites side-arms melting off, which will be then carried by convention in the fluid and act as seeds for new dendrites [152]. (II) the alloy's liquidus temperature may change due to the accumulation of solutes in the liquid, thus, the material can be undercooled. This is a sufficient condition for the creation of

multiple nucleations [153]. In general, the equiaxed polycrystalline microstructures are more favourable since it suppresses the anisotropy in mechanical properties [154].

Considering the challenges associated with the in-situ temperature monitoring in DoD-MJ processes, the final microstructure observation can be a powerful tool to provide some information about the process. The microstructure of the droplets and variation in the substrate microstructure contains critical information about the cooling rates during the solidification and cooling processes. Moreover, it can provide information about the occurrence of substrate melting and its depth. This section reviews the microstructural observations of single and multiple droplets in the literature.

- ***Single droplet***

In a study investigating the microstructure of single 7075 Al alloy droplets of 0.8 mm in diameter, Zuo et al. [58] reported that the microstructure of the droplet's bottom section, where most ripples are present, is mainly directional. The transition of microstructure demonstrated various cooling speeds inside the droplets. In the upper sections with non-directional microstructure, second and even third dendritic arms were visible (Figure 38). The refined vertical grains growing from the substrate show a faster solidification rate in these zones. The coarse non-directional dendrites in the top section result from a slow solidification rate. Amon et al. [155] investigated the microstructure of 1-4 mm Stainless Steel (SS) droplets with an initial temperature of 2000 °C to 2500 °C impacting on an SS preheated substrate at 300 °C. The droplets had martensite and Widmanstatten ferrite microstructure, which is consistent with the high solidification rate in the process. They also examined the substrate and found that far from the interface, the structure was ferrite-pearlite, with larger grains transforming to more refined grains closer to the interface. At the substrate interface, where the substrate melting occurred, the grains had martensite and ferrite structures, but the depth of remelting could not be precisely estimated. Indeed, the droplet's high thermal energy originated from the initial droplet's temperature and the latent heat of solidification provided conditions for austenite - ferrite transformation at the interface. Consequently, the substrate melting could not be distinguished from the solid-state phase transformation. Bishop et al. [153] investigated the primary and secondary dendrite arm spacing of pure Cu and SS droplets (in the order of millimetres) to obtain information regarding their cooling speed during solidification. The cooling rate of Cu

droplets was 10470 °C/s and 5380 °C/s when deposited onto a Cu and SS substrate, respectively. These results demonstrated the role of the substrate's thermal conductivity on the cooling rate and eventually on the microstructure of solid structures.

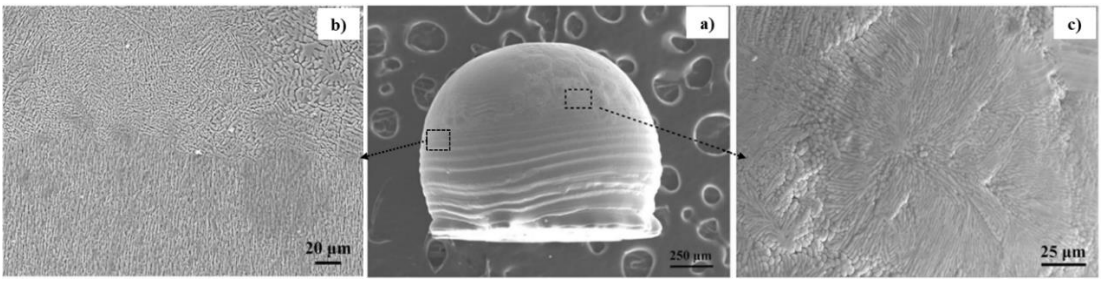


Figure 2.38*- SEM images of a single 7075 Al alloy droplet showing a) the droplet's morphology, b) internal microstructure in the transition zone between ripples and rosette regions, c) the microstructure of the rosette area (images modified from* [58]*).*

Bennett et al. [132] studied the microstructure of 3 mm lead ($T_m = 328\ °C$) droplets impacting on Cu, Al, and Pyrex surfaces under various substrate temperatures and jetting velocities (1.7 to 2.4 m/s). They observed that the solidification initiates below the melting point of lead. They correlated the amount of undercooling to the spreading dynamics of droplets by varying the impact velocity. They concluded that as the Re number increased, the amount of undercooling decreased, but they could not explain the physics behind it. They also observed that the substrate's thermal conductivity significantly influenced the grain size and structure. The top surface SEM images of droplets demonstrated a pre-dendritic, cellular microstructure for the Cu and Al substrates but not for the Pyrex substrate (**Figure 2.39** a-c). Moreover, the average grain size for Cu and Al substrate was 10 µm, while the smallest grain on the Pyrex substrate was 100 µm. The interface of droplets had a rough pattern similar to their corresponding Cu and Al substrates, while it had a relatively smooth surface for the Pyrex substrate (**Figure 2.39 d-e).** Surprisingly, the substrate temperature or impact velocity did not influence the grain size in their experiments. Nagashio et al. [151], [156] investigated the structure formation at the interface of the millimetre-sized Si droplets deposited onto Si substrate at low impact velocities. It was observed that the solidification occurred radially from the centre toward the edge. While non-faceted

denticities were observed in the centre, the grains' structure was equiaxed in the borders. Moreover, their results suggested that the microstructure formation was controlled by nucleation in various undercooling temperatures.

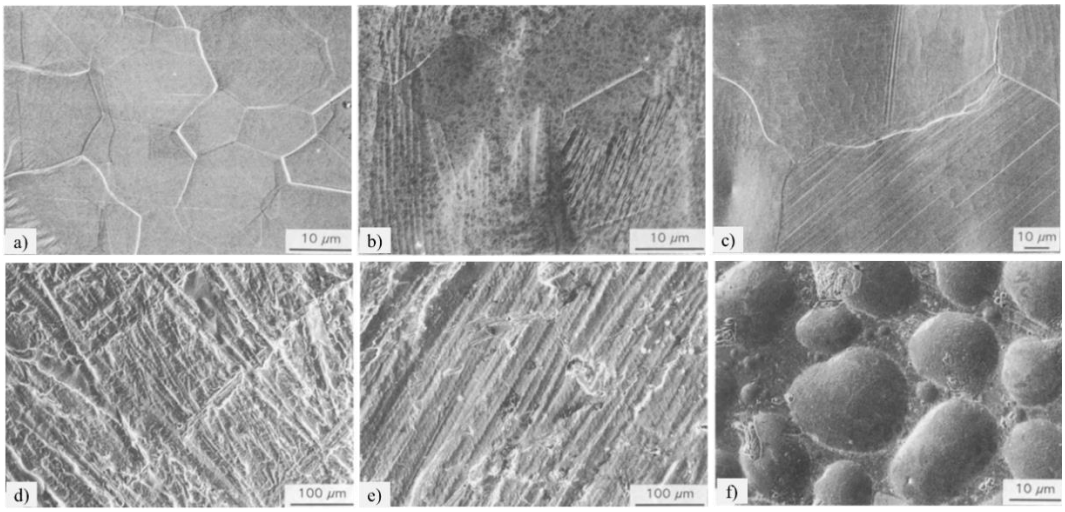


***Figure 2.39**- SEM images of the top surface of a 3 mm lead droplet deposited at 495 °C onto room temperature a) Cu, b) Al, and c) Pyrex substrates. d-c) SEM images of the droplet-substrate interfaces of the corresponding cases* [132].

- ***Multiple droplets***

In studies performed by Zhang et al. [58] and Zuo et al. [157], the predominant grain structure of Al alloy pillars printed by 1 mm droplets was columnar (**Figure 2.40**). The only region with equiaxial grains was the interface between droplets where remelting occurred.

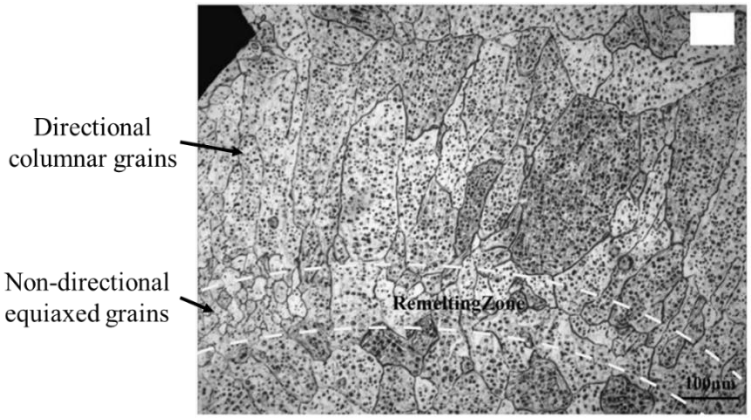


***Figure 2.40**- The microstructure of a pillar made of 7075Al alloy droplets of 0.8 mm* [58].

Idell et al. [158] studied the microstructure of as-built Sn parts made through DoD-MJ. They observed large, irregular, and elongated grains orientated along the build direction having only β-Sn phase. They observed that the microstructure in the pileup regions resembled a partially heat-treated pure metal. Indeed, the heat flow from the newly deposited droplets was enough to initiate recrystallization within the existing grains, transforming them from large irregular into several equiaxed grains.

Although the results obtained from these studies provide insights into the grain structure of millimetre-sized droplets, they are not comparable with the microstructure obtained from the microdroplet deposition. It is mainly due to the higher cooling rates during the solidification of microdroplets, which is expected to result in a more refined microstructure. To the author's knowledge, the microstructure of droplets at a micro-scale has not been investigated to date.

2.4.7. Residual stress

To the best of the author's knowledge, the quantitative measurement of residual stresses in the structures built by metal jetting techniques has not been addressed in the literature. Although X-ray microdiffraction is an established technique for residual stress measurement, it is limited to interaction volumes of 50 to 800 µm. Consequently, it is challenging, even impossible, to reproduce an accurate focus onto small droplets in DoD-MJ processes. Furthermore, the residual stress signal acquired in this method is an average value over the interaction volume. Thus, it is impossible to distinguish the contributions of various directions in the sample.

In a study, Ruiter et al. [159] concluded that the bending stress due to shrinkage of the Sn millimetric-size droplet as they cool down leads to self-peeling of droplets if they surpass the adhesion strength. They demonstrate that the droplets self-peel from a silicon substrate, whereas the droplets stick to a glass substrate under similar conditions. Similarly, for water drops, the generation of bending stresses due to solidification has been shown to result in dramatic cracking and fragmentation events [31]. Kant et al. [160] reported self-peeling phenomena in Hexadecane droplets of 1.58 mm impacting on the substrate at 2.8 m/s, which was not similar to the delamination of metallic droplets reported in earlier studies. Whereas molten Sn drops peeled from the edges, the delamination of Hexadecane drops occurred predominantly in the

central region of the frozen droplet. Interestingly and in contrast to metal drops, the increase in undercooling reduced the extent of delamination (**Figure 2.41**). The thermomechanical stresses developed during the cooling and solidification provided the required force for the delamination of the frozen droplet through a relative movement of the solidified material, which had a transient crystalline phase.

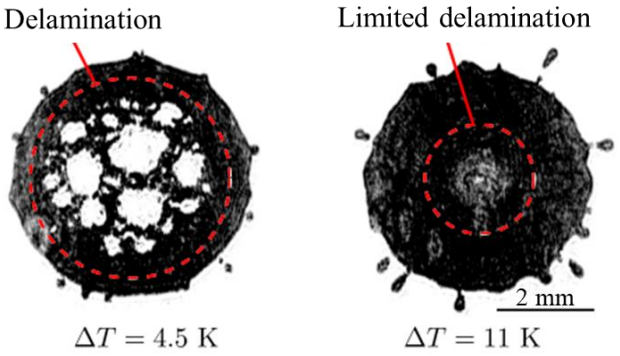


Figure 2.41*- Experimental images during the solidification of Hexadecane drops, showing the delamination behaviour for undercooling of a)* ΔT*= 4.5 K, and b) 11 K* [160].

2.5. Modelling of droplet deposition

As soon as a droplet is deposited onto a surface, a flow is set in motion until the equilibrium contact angle is obtained. The mathematical description of the spreading of a viscous liquid onto a surface is an interesting physical process that has attracted extensive research effort for over half a century [161]. Many engineering applications such as cooling hot surfaces (e.g., electronic circuits), internal combustion engines, spray coating, aviation industry (ice formation on the surface of aerofoils), and droplet-based additive manufacturing benefit from understanding and predicting fluid spreading. Despite numerous attempts and some promising progress in the past century, the accurate simulation and prediction of the droplet morphology during deposition have been hindered by the lack of understanding of its underlying physical phenomena. On another note, modelling the residual stress evolution during the droplet deposition, which is highly dependent on the thermal profile, is very important. In this section, a summary of various modelling approaches to address these modelling problems is presented.

2.5.1. Modelling of droplet spreading (isothermal)

Numerical modelling of droplets spreading onto a surface brings higher spatial and temporal resolutions than any experiment and sheds light on the hidden physical phenomena at a lower cost and time. Hence, the importance of such modelling, yet a highly challenging task from a numerical point of view due to the simultaneous occurrence of multi-scale events in both time and space. In this thesis, we categorize the theoretical approaches into three categories: (I) investigating the full fluid mechanical problem by solving the Navier-Stokes equations, (II) scaling solutions, in which an order of magnitude of various terms in the Navier-Stokes is estimated to bring a broad understanding of the effect of various dimensionless parameters, (III) the prediction of the spreading factor using the energy conservation equations.

- ***Solving Navier-Stokes solution***

The fluid flow over a solid surface is governed by the Navier-Stokes equations for an incompressible flow. The conservation of mass and momentum are obtained by

$$\frac{\partial \rho}{\partial t} + \nabla.(\rho u) = 0 \qquad \text{(Equation 10)}$$

$$\frac{\partial(\rho u)}{\partial t} + \nabla(\rho u u) - \nabla[\mu(\nabla u + \nabla u^T)] + \nabla p = F \qquad \text{(Equation 11)}$$

Where ρ, u, p, and F are the fluid density, speed, pressure, and external force related to the surface tension, respectively. In order to solve the Navier-Stokes equations, the wall boundary conditions, surface tension, and dynamic contact angle need to be addressed carefully. These topics are discussed in the following.

Wall boundary condition:

The primary challenge in solving this problem arises from the inherently multi-scale nature of the moving contact line. The hydrodynamic description of the liquid motion on a solid surface is incompatible with the no-slip boundary condition. Consequently, the classical boundary conditions in the Navier-Stokes equations are inadequate to describe the contact line motion, such that the no-slip condition at the solid surface leads to an unbounded velocity gradient which results in stress singularity at the contact line. A second problem is connected to the dynamic contact angle in the dynamic wetting process that depends on the contact line motion and the fluid flow in

the vicinity of the moving contact line [162]. Despite extensive research in this field in the past century, the accurate prediction of droplet morphology during deposition has been hindered by the inefficiency of classical Continuum Methods in describing the dynamic wetting phenomenon. This phenomenon, which is usually in the mesoscopic scales, is related to microscopic phenomena, thus impossible to be understood through classical continuum methods.

Besides the Continuum Mechanics approach, there are several other mechanisms to obtain the solution of the contact line motion, including the Molecular Dynamic methods, Lattice Boltzmann methods, and Diffuse-interface or recently Phase field Methods.

In the molecular-kinetic approaches [163], [164], the macroscopic behaviour of contact line motion is described through a thermally activated process and is obtained from overall molecular displacements (adsorption/desorption) within the three-phase. If the absorption of liquid molecules is more frequent in the forward direction than their desorption in the reverse direction, the contact line will advance.

In the Lattice Boltzmann methods, intermolecular interaction forces are integrated into the governing equations for the particle distribution functions. The intermolecular interaction forces are obtained by minimizing the systems' total free energy [165].

In the diffuse-interface models, thermodynamics coupled with hydrodynamics are applied to the fluid flow. An auxiliary order-parameter variable (i.e., phase-filed) is included in the Navier-Stokes equations, where its value varies from one inside the droplet to zero in the surrounding phases. The transition between these two extreme values takes over thin interfacial layers is referred to as the diffuse interface. This technique resolves the stress singularity at the moving contact line [166].

Based on the size scale of the problem and the required level of description, the numerical framework can be chosen. Even though Molecular Dynamics, Lattice Boltzmann, and Phase filed methods provide a detailed description of the problem and the singularity problem at the contact line can be avoided, these methods can only be used for sub-micron scales due to the substantial computational efforts they require in bigger scales. Consequently, the continuum theory is still widely used and is

implemented in most commercial software packages. The singularity problem is usually solved by allowing for slip or partial slip (Navier slip) at the contact line to relax the singularity issue. However, these methods are not fully applicable at the micro-scale level and can potentially lead to false results. The only continuum model that claims to solve the singularity issue was proposed by Shikhmurzaev [167] and is known as the interface formation model. A detailed review of various approaches is done by Sui et al. [168].

Surface tension:

The surface tension can be implemented into the equations using various models. The most common model is the Continuum Surface Force (CSF) established by Brackbill et al. [169], in which the surface tension force is approximated as a body force defined by

$$F = \sigma k \nabla \alpha \qquad \text{(Equation 12)}$$

Where k is the curvature of the free surface (gas-liquid interface) and is given by local gradients of the surface normal

$$k = \nabla .\ \hat{n} \qquad \text{(Equation 13)}$$

$\hat{n}$ is normal to the interface and is defined as the normalised volume fraction gradient

$$n = \frac{\nabla \mathrm{F}}{|\nabla \mathrm{F}|} \qquad \text{(Equation 14)}$$

Dynamic contact angle:

The definition of static angles is insufficient to describe the complex physics at the trijunction point during the droplet spreading. Hence, it is important to account for the dynamic contact angle, which varies as a function of inertial and viscous forces. Various models describe the dynamic contact angle, most of which correlate the angle to the contact line velocity. Examples are Kistler[170], Shikhmurzaev [167], Cox [171] and the Quasi-Dynamic Contact Angle Models [172]–[174], which are most widely used due to their simplicity. In the Quasi-Dynamic model, a constant advancing or receding contact angle is imposed when the contact line spreads or recoils, respectively. Despite its simplicity, the receding and advancing contact angle should

be obtained from experiments. Gohl et al. [172] compared the various mentioned dynamic contact angle models as a boundary condition in their equations with the spreading factor and dynamic contact angle shown in **Figure 2.42**. All models follow the experimental data of spreading factor except the quasi-dynamic model, which spreads too much because of the small contact angle estimation. Their results showed that Shikhmurzaev's model is the best in predicting the experimental observations.

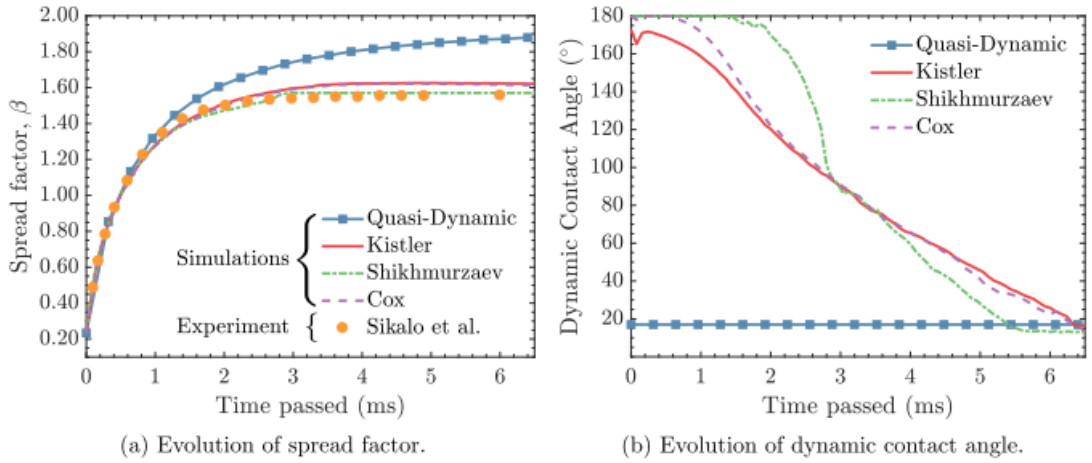


***Figure 2.42**- a) Spreading factor and b) dynamic contact angle evolution of a glycerol droplet impacting on a hydrophilic substrate using various dynamic contact angle models* [172].

A large number of computational studies on the droplet impact and spreading, solving the full fluid mechanical problem, have been conducted to date [114], [126], [175]. Most of these models reasonably agree with experimental results for large droplets (above millimetres) at high impact velocities. The reason is that at higher impact velocities, the kinetic energy of droplets is more important than the surface energy; hence the surface tension and contact angle effects become eventually negligible. However, investigation on the impact and spreading at low We number [174], where the capillary forces are influential, and for microdroplets [116], [176] is still limited only to a few studies. Sprittles and Shikhmurzaev [116] demonstrated the influence of substrate wettability on the spreading mechanism and final morphology of microdroplets (D= 50 um) at V= 5 m/s, as shown in **Figure 43.** Their computational framework, which solves the full fluid mechanical problem using the interface formation model, brought insights into aspects which were not measurable in

experiments. The droplets spreading on hydrophobic and hydrophilic substrates were identical at the early stage (t= 5 µs), where inertia is the dominant force. Later, when the wettability became influential, droplets on a non-wetting surface rebounded while fully spreading to the equilibrium contact angle in the substrate with good wetting conditions.

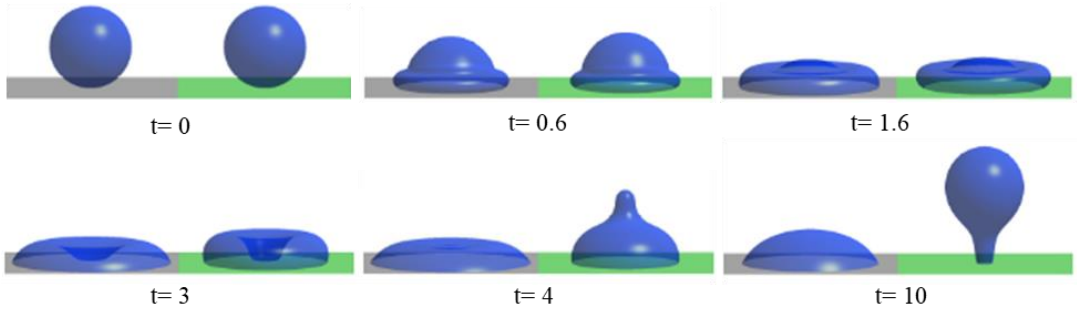


Figure 2.43- *Spreading of a microdroplet (D=50 um) at Re = 130 (V=5 m/s) on a hydrophilic substrate (grey) and a hydrophobic substrate (green) at dimensionless time scales (t=1 → t=5 us)* [116].

- ***Scaling solution***

In this approach, proposed by Schiaffino [119], the fluid mechanic's basics and dimensionless parameters, such as Oh and We numbers are used to describe the droplet's characteristics on spreading. In this method, the objective is not to find an exact solution to the Navier-Stokes equations; instead, solutions to the droplet dynamics are obtained by estimating an order of magnitude for various terms (for example, by their average values). Based on this analysis, the droplet dynamics are categorized into different zones, as explained in Section 2.4.1. The oscillation time of droplets at the low We and Oh numbers are obtained by

$$t_{osc} = 2.3\sqrt{\rho x^3/\sigma} \qquad \text{(Equation 15)}$$

Where x is the liquid droplet height. During this period, droplets wobble up and down until the viscous effects dampen their movement or they solidify (in non-isothermal deposition). The damping period for a droplet in Region II (Figure **2.18**) is calculated via

$$t_{damp} = 0.035\frac{x^2}{\vartheta} \qquad \text{(Equation 16)}$$

Owing to its simplicity, this method has been extensively used in droplet-based studies to estimate the governing forces of droplet spreading and to estimate the oscillation and damping time scales [111], [123], [177]. However, these analytical solutions do not provide an in-depth understanding of the droplet dynamics nor predict their final morphology. Such analysis can only be used to better interpret the experimental results.

- ***Solving energy Balance equations***

As opposed to solving a full or partial fluid mechanical problem, some studies have used the energy balance to predict the spreading factor of droplets upon impact [108], [118], [178].

$$E_k + E_{s1} = E_{s2} + E_v \qquad \text{(Equation 17)}$$

In which E_k is the initial kinetic energy of the droplet, E_{s1} is the surface energy of a spherical droplet before the impact, E_{s2} is the surface tension energies after impact, and E_v is the vicious energy the droplet dissipates upon impact (the work done in deforming the droplet against viscosity). The initial energy of the droplet is:

$$E_k = \frac{\pi}{12} D_0^3 \rho V_0^2 \qquad \text{(Equation 18)}$$

$$E_{s1} = \pi D_0^2 \gamma \qquad \text{(Equation 19)}$$

Where D_0 is the droplet's initial diameter, ρ is the density, and V_0 is the impact velocity. The surface and vicious energies are calculated in various manners. The common assumption of these models is that drops have a disc-like morphology when it reaches their maximum spreading factor. Moreover, they assume that the droplet's kinetic energy dissipates entirely at the impact.

Chandra and Avedisian [179] integrated both viscous energy dissipation and surface tension in the energy balance equation and considered the wettability effects through the advancing contact angle for droplets spreading onto preheated substrates and obtained:

$$\frac{9/2D^4}{Re} + \frac{3(D^2(1 - cos\theta) - 4)}{We} = 1 \qquad \text{(Equation 20)}$$

Their model overestimated the spreading factor values by up to 40% compared to the experimental results due to the inaccuracy of the viscous energy dissipation modelling. Pasandideh-Fard et al. [126] further developed the model of Chandra and Avedisian by modifying the viscosity term in the energy balance equation:

$$D = \sqrt{\frac{We + 12}{3(1 - cos\theta) + 4\left(We/\sqrt{Re}\right)}} \qquad \text{(Equation 21)}$$

Chandra and Avedisian assumed that kinetic energy was dissipated in the total droplet thickness. In contrast, Pasandideh-Fard et al. considered a viscous boundary layer at the solid-liquid interface. This adjustment improved the agreement between the experimental and predicted results to 15%. However, this equation is not accurate at low Weber numbers since the assumption of a thin boundary layer is no longer valid. Mao et al. [180] modified the model established by Chandra and then further developed by Pasandideh-Fard et al. through a novel expression of the surface tension of the flattened disk and obtained:

$$[0.2\,Oh^{0.33}We^{0.665} + \frac{1}{4}(1 - \cos\theta)]\beta_{max}^{2} + \frac{2}{3}\beta_{max}^{-1} = \frac{We}{12} + 1 \qquad \text{(Equation 22)}$$

They claimed that their model could predict the spread factor with 90% of accuracy when compared to the experimental data from various sources. This was confirmed in a study by Attané et al. [178].

These models may reasonably estimate the droplet spreading for a specific set of process parameters, particularly for large droplets. However, they do not perform well on the micro-scale.

2.5.2. Modelling of droplet solidification

In the non-isothermal conditions, where the droplet is deposited onto a surface at a temperature below the droplet's melting point, the contact line will be arrested to the substrate, and the entire droplet will solidify in the next stage. There have been several attempts to simulate the spreading and solidification during the droplets depositions by solving the full fluid dynamic and heat transfer problem with 2D [35], [181] and 3D models [13], [36], [37], [182]. In a less complex approach, some authors have

solved the heat transfer problem without considering the fluid mechanic aspects [155], [183]–[185].

- ***Solving Energy Conservation with the Navier-Stokes solution***

Solving for a full fluid flow and heat transfer solution in droplet deposition combines the challenges of isothermal deposition and contact line arrest. However, accurate prediction of the final morphology and temperature field requires a complete numerical solution of the continuity, momentum and energy equations. The solidification is accounted for by adding a source term (S) to the continuum equation [13], [63], [181], [186], which is equal to zero when the droplet is liquid and a very large value when the droplet is fully solidified. In the solid state, the source term is predominant in the momentum equation, resulting in no fluid motion. A finite intermediate value based on the solid fraction in the mushy zone is considered.

$$\frac{\partial(\rho u)}{\partial t} + \nabla(\rho u u) - \nabla[\mu(\nabla u + \nabla u^T)] + \nabla p = F + S \qquad \text{(Equation 23)}$$

The drag concept [181] can be used to define the source term via

$$S_i = DRG = -Ku_i \qquad \text{(Equation 24)}$$

In which K varies between zero and infinity, such that the drag, defined based on Equation 25 varies between 0 and 1.

$$DRG = \frac{1}{1+\delta t K} = \begin{cases} 1 & if\ T > T_{liq} \\ ((1 + \delta t K(T_{liq} - T))/(T_{liq} - T_{sol}))^{-1} & if\ T_{sol} < T < T_{liq} \\ 0 & if\ T < T_{sol} \end{cases} \qquad \text{(Equation 25)}$$

Some studies [13], [35], [63] integrate the source term through a similar concept but using a different formulation

$$S = -\frac{f_s^2}{(1 - f_s)^3}\, u \qquad \text{(Equation 26)}$$

where f_s is the solid fraction, and its value varies between zero and one and is defined by

$$f_s = \begin{cases} 0 & if\ T > T_{liq} \\ T_{liq} - T/(T_{liq} - T_{sol}) & if\ T_{sol} < T < T_{liq} \\ 1 & if\ T < T_{sol} \end{cases} \quad \text{(Equation 27)}$$

Along with the Navier-Stokes equations, the heat transfer inside the droplet needs to be addressed by solving the conservation of energy (Enthalpy equation)

$$\frac{\partial(\rho H)}{\partial t} + \nabla(\rho u H) = \nabla.(k \nabla T_d) \quad \text{(Equation 28)}$$

Where H represents the enthalpy equation. To consider the effects of the latent heat release, defined by an appropriate change in the enthalpy during the solidification [13], [35], [37], [181]

$$H = \int C_p(T_d) dT_d + L(1 - f_s) \quad \text{(Equation 29)}$$

The heat exchange between the droplet and the substrate is usually added to the heat transfer formulation as a boundary condition [36], [134], [187], where Fourier's equation is solved via

$$q = h(T_s - T_d) = \frac{(T_s - T_d)}{R_c} \quad \text{(Equation 30)}$$

Where q is the heat flux at the interface, and h is the heat transfer coefficient. The heat transfer coefficient varies as a function of the temperature and position. However, a constant value obtained from experimental observations is adapted in most studies. The heat transfer between the droplet and substrate is the primary cooling mechanism in droplet cooling, during which the thermal contact resistance plays an essential role and should be taken into consideration. Thermal interface resistance occurs whenever two solids of different or similar materials are brought together to form an interface [188]. As shown in **Figure 2.44**, the imperfections at the interface come into play in the macroscopic (flatness) and microscopic (roughness) levels [189], [190] to partially impede the heat transfer between surfaces.

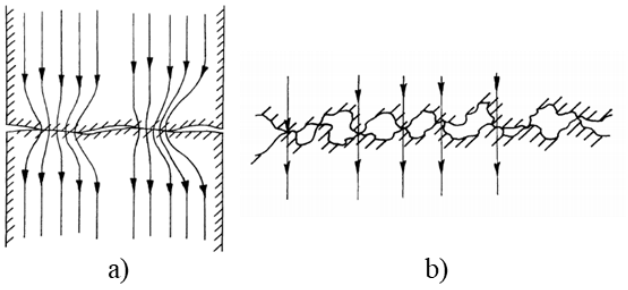


***Figure 2.44**- Thermal resistance at the interface at a: macroscopic and b: microscopic levels* [189].

Although it is well known that this parameter has a major influence on the heat transfer between two surfaces, no universal model can predict the resistance between the surfaces to date [190]. In previous works in the literature, it was either arbitrarily chosen [13], [181] or neglected altogether [4], [25], [184], [191] due to the lack of information on how to estimate it. In some prior research, this parameter was experimentally measured, however, the response time of temperature sensors is usually longer than the spreading time of the droplets, which can lead to inaccuracies in the results [136]. Aziz et al. [192] calculated the thermal contact resistance between molten Sn droplets and a stainless-steel substrate by matching the measured surface temperature variation with an analytical solution. Their measured values varied been $10^{-6}\ m^2K/W$ and $5 \times 10^{-6}\ m^2K/W$. Similarly, Kumar et al. [35] estimated the thermal contact resistance between Al–33 wt.% Cu droplets and stainless steel at $7 \times 10^{-4}\ m^2K/W$. Trapaga et al. [181] considered several values of thermal resistance ranging between $10^{-4}\ m^2K/W$ and $10^{-6}\ m^2K/W$ for Cu droplet impinging on a Cu substrate.

The heat transfer within the substrate occurs through conduction and is governed by

$$\frac{\rho_s C_s \partial T_s}{\partial t} = \nabla(\mathrm{k_s}\ \nabla \mathrm{T}_s) \qquad \text{(Equation 31)}$$

Commercial FE solvers such as ANSYS, Flow-3D, COMSOL or numerical frameworks have been used to solve these equations. To simplify the numerical solution, the effects of heat radiation, thermal resistance, and temperature-dependent thermo-physical properties have been ignored in most studies, yet solving these multiscale problems requires a large computational effort. One of the main problems with the heat transfer solution is the singularity at the trijunction, where, effectively,

an infinite heat flux occurs. In most cases, simplifications to avoid heat transfer and spreading singularities lead to further errors. The inaccuracy of numerical solutions for the micro-scale droplets can be higher than millimetre-size droplets. To the best of the author's knowledge, the full fluid mechanics and heat transfer solution of droplet deposition have not yet been achieved to date. The promising conceptual and mathematical framework by Shikhmurzaev [115] proposed in 2021 is the first singularity-free modelling of non-isothermal solidification so far developed. In traditional solidification theories, the solidification front advances as a function of temperature, activation energy, enthalpy, or such concepts. While in Shikhmurzaev's approach, the front speed and contact angle are obtained from the underlying physical laws describing them, instead of being prescribed as an initial input to the model. The possibility of solving such equations and the accuracy of results obtained from this model are yet to be proved.

- ***Solving the Heat Transfer equations without considering the fluid flow***

To manage the computational challenges in solving the full fluid and heat transfer problems and in a computationally efficient modelling approach, droplet spreading has been considered a precursor to droplet solidification in some studies. Thus, the droplet geometry was kept constant during the heat transfer solution. In this approach that has been used in the context of 3D free from fabrication [193], L-PBF [194], thermal spraying [195], and droplet-based AM [26], the Fourier heat transfer equation is solved via

$$\frac{\partial}{\partial x}\left(k\frac{\partial T}{\partial x}\right)+\frac{\partial}{\partial y}\left(k\frac{\partial T}{\partial y}\right)+\frac{\partial}{\partial z}\left(k\frac{\partial T}{\partial z}\right)+Q=\rho c\frac{\partial T}{\partial t} \qquad \text{(Equation 32)}$$

Where k is the thermal conductivity, ρ is density, and L is the latent heat of solidification. Since the fluid flow during spreading is ignored in such modelling, a conductivity multiplier (K_{factor}) is often used to account for the convection effects at temperatures above the melting point of materials [196]

$$K_{eff}=c_{mf}K \qquad \text{(Equation 33)}$$

where K_{eff} is the effective thermal conductivity and c_{mf} is the conductivity multiplier factor, which is greater than one and is a function of the Nusselt number (Nu), the

droplet height (x), and the interface length. c_{mf} has been experimentally measured in several studies [4], [184], [196] and is equal to 2.

Most authors [184], [193] have considered the latent heat of fusion by an increase in the material's specific heat during the phase transition via

$$C_{eff} = \begin{cases} C & T < T_s \\ C + \frac{L}{\Delta T} & T_s \leq T \leq T_L \\ C & T > T_L \end{cases} \quad \text{(Equation 34)}$$

Commercial FE packages such as ANSYS or ABAQUS have been used to solve the equations using this approach. In these studies, the authors have usually ignored the thermal contact resistance at the interface, thus, overestimating the temperature. Moreover, for large droplets, the temperature gradient inside the molten droplet results in surface tension variation that drives a Marangoni-type flow. For such cases, the effective thermal conductivity cannot fully capture the flow of the fluid.

- ***Solving the Stefan problem without considering the fluid flow***

Stefan problem, the simplest form of mathematical description of phase transition, are free boundary problems that are widely used to estimate the solidification front during the deposition processes [67], [184], [192], [196], [197]. One-dimensional solidification was used to obtain the solution to the problem. S(t) is the interface or the freezing front, where two semi-infinite media, i.e., liquid and solid, are considered at $0 < x < S(t)$ and $S(t) < x < \infty$, respectively. The solidification problem is defined via [198]

$$C_s\rho_s \frac{\partial T_s}{\partial t} = K_s \frac{\partial^2 T_s}{\partial x^2} \quad 0 < x < S(t) \quad \text{(Equation 35)}$$

$$C_l\rho_l \frac{\partial T_l}{\partial t} + C_l\rho_l u_x \frac{\partial T_l}{\partial t} = K_l \frac{\partial^2 T_l}{\partial x^2} \quad S(t) < x < \infty \quad \text{(Equation 36)}$$

The latent heat of solidification can be considered with adjustments similar to what was previously explained. By applying the Neumann solution, the analytical expression of the solidification front can be obtained by [67], [155]

$$S(t) = \left[\frac{k_s(T_m - T_s)e^{\lambda^2}}{\sqrt{\alpha_s}erfc(\lambda)} - \mathrm{k_l}\frac{(T_l - T_m)e^{-\lambda^2\left(\frac{\alpha_s}{\alpha_l}\right)}}{\sqrt{\alpha_s}erfc\left(\lambda\sqrt{\frac{\alpha_s}{\alpha_l}}\right)}\right].\frac{2\sqrt{t}}{\rho L\sqrt{\pi}} \qquad \text{(Equation 37)}$$

This equation ignored the thermal resistance effect at the interface, which can significantly alter the results. Using a similar approach and accounting for the thermal contact resistance, the temperature at the interface can be obtained using [192], [199]

$$T_{int} = T_{sub-int} + (T_d - T_{sub-int})\left[1 - \exp\left(\frac{\alpha_s t}{R_c^2 k_s^2}\right)\mathrm{erfc}\left(\frac{\sqrt{\alpha_s t}}{R_c k_s}\right)\right] \quad (Equation\ 38)$$

This equation has been used [63] to estimate the minimum droplet and substrate temperatures to achieve a strong metallurgical bonding through melting the substrate or remelting the previously deposited droplets. **Figure 2.45** shows this concept for Al 7075. The remelted zone highlighted in green indicates the optimal droplet and substrate temperature ranges, where the interface temperature is above the melting point.

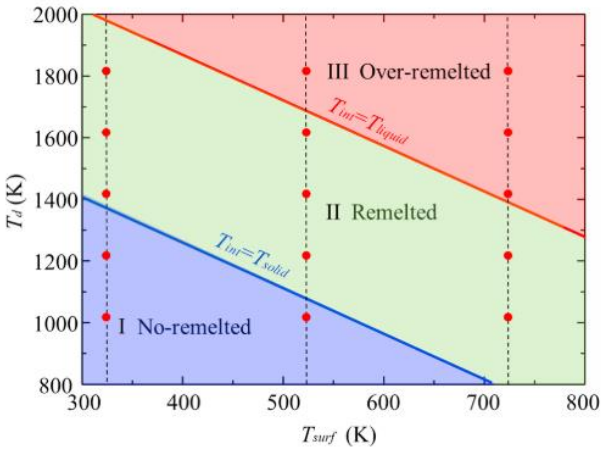


Figure 2.45- *The optimal droplet and substrate temperature ranges to obtain a good metallurgical inter-droplet bonding for 7075 Al alloy according to equation 38* [200].

It should be noted that these values are just an approximation since the morphology of droplets and the effect of fluid flow are not taken into account in this equation.

- ***Solving the Energy Balance equations and considering the solidification***

The maximum extent of spreading can be obtained by equating the droplet's initial (kinetic) energy to the sum of the surface energy at the maximum spreading and the energy dissipated during spreading and solidification. Madejski [201] established one of the first analytical models to predict the spreading factor considering viscous energy dissipation, surface tension effects and solidification simultaneously by solving the Stefan problem. Several approximations were introduced in the attempt to simplify the problem: (I) the droplet was modelled as a cylindrical disk with a laminar fluid flow, (II) the substrate wettability in the energy balance was neglected (Equation 17), (III) droplet temperature was at its melting point, (IV) the solidification at the impact was instantaneous, and (V) the solidification front advanced in the equilibrium limit at the rate in which the latent heat was dissipated to the substrate. The numerous simplifications incompatible with rapid solidification theories can be seen as the main reason for the difference between experimental and numerical data. Collings et al. [102] accounted for the surface and interfacial energies between the droplet, substrate and ambient gas (substrate wettability effect) in the energy balance equation. The use of *Young's equation* (Equation 9) significantly limited the application of their model to equilibrium conditions. Moreover, they neglected the viscous energy dissipation. Pasandideh-Fard et al. [130] included the effect of droplet solidification in their equation by assuming that the solidified layer contains no kinetic energy and obtained

$$D = \sqrt{\frac{We + 12}{3(1 - cos\theta) + 4\left(We/\sqrt{Re}\right) + \sqrt{3Ste/(4Pe)}}} \qquad \text{(Equation 39)}$$

However, the effects of thermal contact resistance were neglected, heat transfer was supposed to be one-dimensional heat conduction with the substrate, and the substrate was considered isothermal. Due to the inaccuracy of these estimations, the results were not accurate at high Stefan numbers, for example, in the case of a tin droplet deposited on a cold surface. Aziz et al. [192] updated Equation 39 by solving the heat transfer for the 1D conduction problem and obtained

$$D = \sqrt{\frac{We + 12}{WeSte\sqrt{3\gamma_s/2\pi Pe\gamma_d} + 3(1 - cos\theta) + 4\left(We/\sqrt{Re}\right)}} \qquad \text{(Equation 40)}$$

Yet, in this model, the thermal contact resistance was not taken into account, and the properties of droplet and substrate were not temperature dependent. These models can, to some extent, predict the spreading factor at higher impact speeds. However, they overestimate the maximum diameter at low impact speed where the droplet forms a bid shape rather than a flat thin layer which can be considered a boundary layer to estimate the viscous dissipation.

2.5.3. Modelling of residual stress development

As soon as droplets solidify, residual stresses develop due to the thermal gradient between the deposited droplet and substrate or previously deposited material. The magnitude of these residual stresses evolves as the cooling continues, and delamination at the interfaces may occur if they surpass a specific limit. The in-situ measurement of residual stresses during the deposition process is not possible to this date. Also, measurement of the final state of residual stress at the scale of a single droplet is challenging. Consequently, modelling is the only alternative to bring insights into the mechanism behind the residual stresses evolution, and it has the potential to find solutions to mitigate their detrimental effects. Despite the large research efforts in simulating droplets' dynamics and temperature evolution during deposition, only a few attempts were made to simulate the evolution of residual stresses on cooling and solidification.

Researchers in other fields, such as high-impact thermal spray processes, have extensively studied the modelling of residual stress evolution [202]–[204]. However, the residual stresses in these processes build-up due to the plastic deformations resulting from high impact velocities. The impact of particles is usually analysed through an explicit and dynamic temperature displacement under high strain rates.

Simulations of coating processes, in which thermal stresses are generated due to the different CTE (Coefficient of Thermal Expansion) and impact-generated stresses are not considered, share similar principles with the DoD-MJ process. In these studies, the majority of authors [205]–[207] have considered 2D axisymmetric models in which the droplets are modelled as thin solid disks. They have used FE analysis to calculate the thermally induced strains and the consequent thermal stresses.

Despite the different working principles, the mechanism of distortions and residual stress generation in the AM metal process is similar [208]. The thermal contractions and expansions during the deposition, cooling, and solidification, while the part is constrained by the substrate or rest of the body, originate the residual stresses. Most authors have used sequentially-coupled thermomechanical solutions to simulate the residual stress evolution in DED [209], [210] and L-PBF [194], [211], [212] processes. In Microcasting, thermomechanical models based on similar formulations were used, where droplets were modelled as 2D disks as per **Figure 2.46** [38]. Chin et al. [38] solved 1D thermal and 2D axisymmetric mechanical problems using custom and commercial FE codes to simulate the residual stress evolution in a single droplet. They further extended their model to simulate the residual stress development in successive droplet deposition [191]. Klingbeil et al. [213] used the same modelling approach to investigate the residual stress-induced warping and compared their results to their experimental observation. Simulation results showed high tensile stresses in the droplet and the top portion of the substrate at the steady state, which could be significantly improved by substrate preheating. They showed that the maximum stress near the interface decreased by 170 MPa and 270 MPa when the substrate was preheated to 473 K and 673 K, respectively. In addition, as shown in **Figure 2.47,** the authors observed that despite a transient change in temperature and, consequently, stress field during the deposition of various layers, the final residual stress state is not substantially different at the end of each layer, independent of the deposition rate [191].

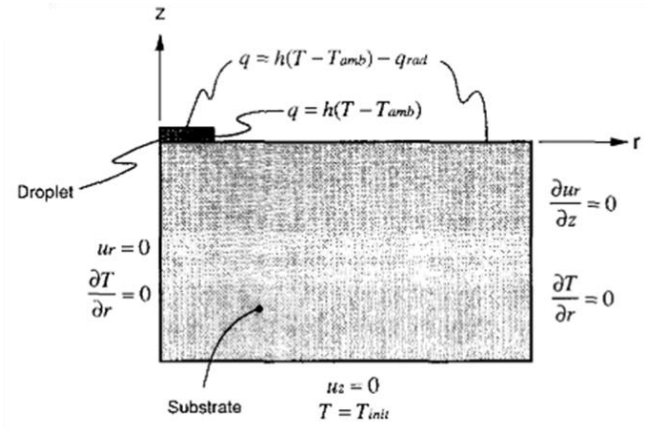


***Figure 2.46**- Geometry and boundary condition of the 2D thermomechanical model in the microcasting process* [191].

The mechanical solutions used in these two studies had accuracy limitations due to the inability of 1D thermal solutions to accurately represent the multi-dimensional conduction effects seen experimentally. Moreover, several phenomena were ignored: the effects of fluid flow and contact line arrest, the contact resistance, the mechanical induced temperature changes, and a perfect bonding between the droplet and substrate was assumed. These approximations can have a significant impact on the accuracy of the results.

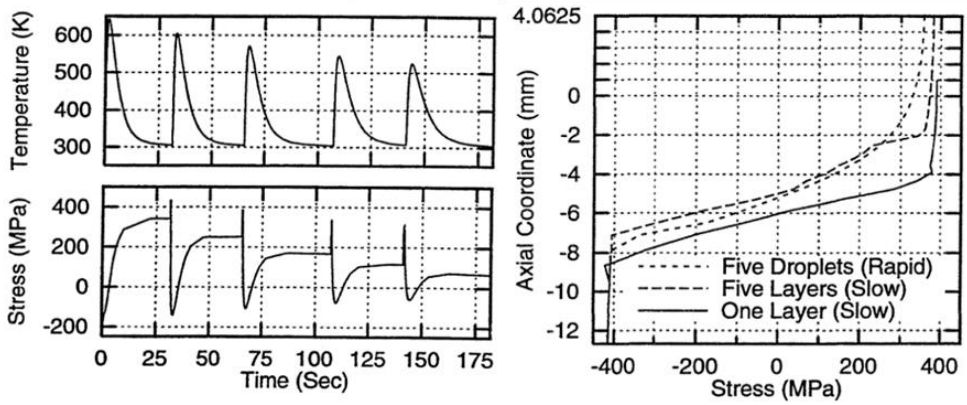


Figure 2.47*- a: temperature and stress in a fixed point on the substrate for slow rate deposition, b: final radial stress distribution for one and multilayers during slow and rapid deposition* [191].

2.6. Characteristics of 3D printed structures

Despite the diversity of research on various aspects of droplet deposition, very little attention has been paid to analysing the properties of the 3D objects produced by these deposition techniques. Among these studies, the density, the surface finish, the electrical conductivity, and the mechanical properties of parts have been investigated. A summary of these studies is reviewed in this section.

2.6.1. Surface finish

One of the main concerns related to DoD-MJ, according to the literature, is the poor surface finish of printed parts [139], [214], [215]. In these studies, the overlap between droplets and the printing strategy were counted as the main process parameters

influencing the surface quality. In other studies [216], droplet and substrate temperature effects were also accounted for as influencing factors. It was shown that the more extended solidification period reduces the height deviation of the droplets and consequently improves the final surface finish. Qi et al. [215] improved the topography of printed 3D cubes by optimising the overlap distance of 270 µm droplets in Sn60– Pb (**Figure 2.48**). Due to the large droplet size in most DoD-MJ techniques, controlling the surface finish remains challenging.

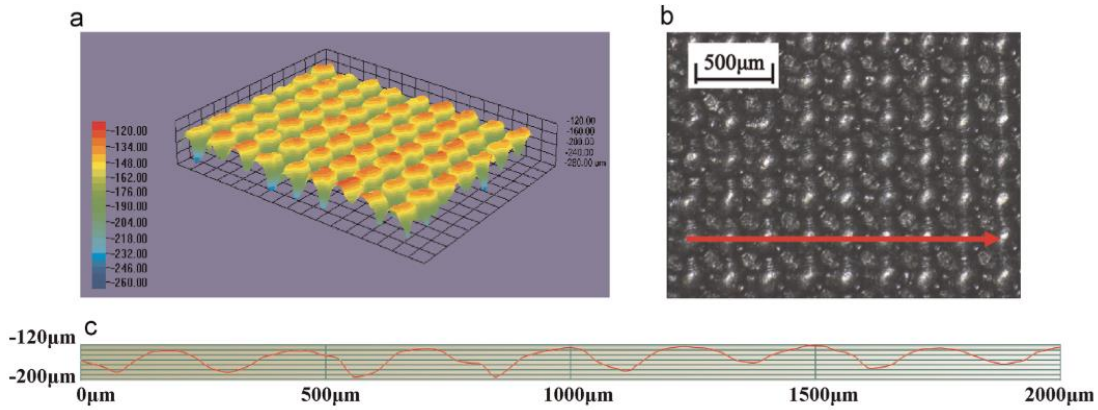


Figure 2.48*- a) 3D topography of a cube from 270 µm solder droplets, b) top view image, and c) roughness profile in the red arrow indicated in (b)* [215].

2.6.2. Electrical conductivity

One of the main advantages of metal jetting compared to ink jetting is the potential high electrical conductivity of printed parts through this technology, thanks to the direct deposition of metal without the need for carrier inks. However, the electrical conductivity of the components can be reduced due to poor inter-droplet bonding or oxidation of the droplets. Dou et al. [9] demonstrated that by optimising the droplets' overlap and substrate temperature, the electrical resistivity of printed lines of Sn solder printed by DoD-MJ on plastic substrates could be as low as the bulk metal as shown in **Figure 2.49.**

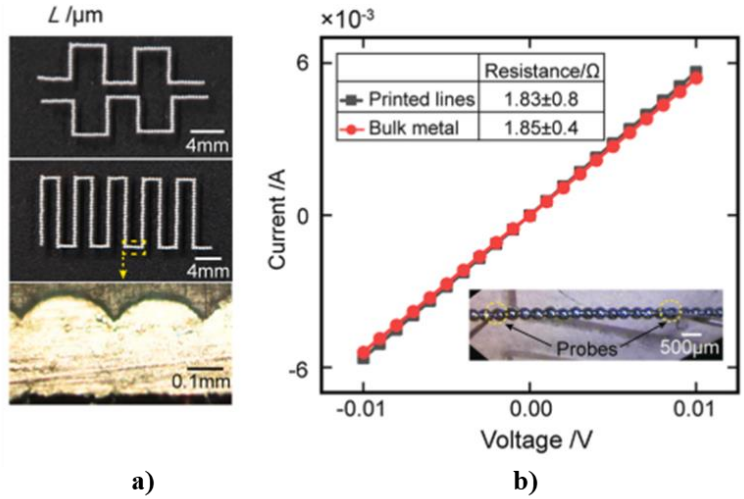


Figure 2.49*- a) printed Sn lines using DoD-MJ and its cross-sectional view, b) the electrical resistivity of printed lines vs. the bulk material [9].*

Jehle et al. [217] used a four-point measurement to evaluate the resistance of lines in a printed electronic circuit by the StarJet technology. The line resistance of solder droplets printed on Au-pads in PCBs increased from 13.8 ± 0.6 $m\Omega$ to 119.0 ±1.4 $m\Omega$ as the pad's distance increased from 1 mm to 3 mm. These measurements can be a good indication of the level of bonding. Simonelli et al. [11] reported that despite a metallurgical bonding between droplets, the electrical resistivity of printed structures in Sn was slightly higher than the bulk material (1.79 Ωm against 1.17 Ωm). They concluded that the loss of conductivity is related to small porosity by gas entrapment between contacting droplets or geometrical inaccuracies. The electrical conductivity of inkjet printed parts is usually one or more orders of magnitude lower than these reported values; hence, metal jetting still offers an advantage.

2.6.3. Density

High porosity is one of the main concerns in metal AM where even small porosities (less than 1%) will affect the mechanical properties of parts, such as fatigue. Higher porosities (more than 5%) can detrimentally affect the monotonic mechanical response [218]. The relative density of the printed parts is a good indicator of the porosity level. Despite its significant importance, not much research on the density measurement of DoD-MJ parts has been conducted to date. Among which, IDell et al. [158]

demonstrated that the density of printed parts in pure Sn was almost identical to the feedstock material (7.31 g/cm^3 against 7.32 g/cm^3). Himmel et al. [219] demonstrated that the density of Al 4047 billets made of 1.15 mm drops increased almost linearly with the interface temperature. The interface temperature depends on the droplet and substrate temperatures and can be obtained by solving the Stefan problem. The relative density of these 3D objects can be as high as 98% when the interface temperature is close to the material's melting point. High-density 3D structures (above 99.9%) were obtained from DoD-MJ of pure tin microdroplets [11]. The same study used high-resolution X-ray micro-computed tomography (µCT) to estimate the porosity of as-build and sintered parts. As shown in **Figure 2.50**, the volume fraction of porosity for a 3D Ag part was estimated at 8% for both cases, even when no inter-droplet bonding was observed. The results demonstrated that the heat treatment does not reduce the porosity level but significantly changes its morphology. The irregular elongated porosity of as-built parts (originated from the inter-droplet gaps) changes to a spherical shape due to droplets necking in the sintered parts.

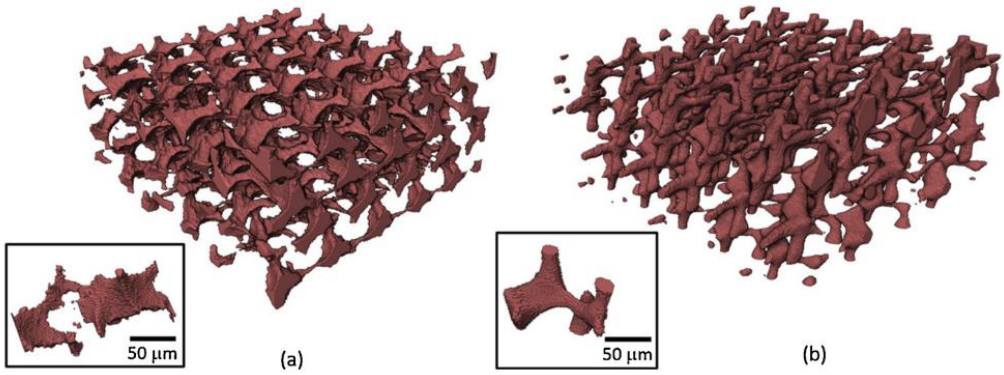


Figure 2.50- *Reconstructed porosity (in red) obtained through X-Ray CT scan in a) as-built and b) sintered DoD-MJ Ag samples [11].*

2.6.4. Mechanical properties

To the best of the author's knowledge, only three references have investigated the mechanical properties of DoD-MJ parts to date. Zou et al. [220] demonstrated that the tensile properties of AA7075 aluminium alloy specimens (droplet size ~ 1.5 mm) fabricated by a DoD metal jetting system were comparable to those of as-cast and

extruded bar samples. It was shown that by applying a suitable substrate/ droplet temperature adjustment, which leads to a good inter-droplet metallurgical bonding, high tensile strength of 373 MPa could be achieved. This is better than as-cast and very close to the extruded bar specimens. Besides, a comparable elongation (~9.5 %) to extruded bar samples was achieved in that case. These results were obtained due to a good inter-droplet metallurgical bonding and microstructure. As shown in **Figure 2.51**, the fracture behaviour of the material changes with incremental changes in the droplet and substrate initial temperatures. A more ductile transgranular fracture can be observed if the correct set is applied. Overheating or underheating negatively influences the microstructure or bonding level, respectively, and thus worsens the fracture properties.

Similarly, the tensile properties of 4047 Al alloy samples were investigated at various droplet/ substrate temperatures [219]. It was concluded that adequate interfacial temperatures could be obtained if an appropriate ratio between the droplet and substrate temperatures were used, resulting in very good mechanical properties. The tensile strength of the bars was 373 MPa with an elongation of 9.95%, which are very similar to the extruded samples. It was also seen that as the interface temperature increases, the elongation increases linearly (reaching a maximum value of 12%), and the yield strength decreases. Idell et al. [158] measured the hardness of structures in Sn printed through an MJ-DoD process with an orifice of 400 um. The VHN values were 7.5±0.6, 8.2±0.8, and 8.0±0.6 for the tin feedstock, cross-sectional orientation, and plan-view, respectively, which can be correlated to the tensile strength of 25±2 MPa, 27±3 MPa, and 26±2 MPa. These values are comparable to the feedstock material produced by conventional manufacturing technologies, despite the larger grain size and a strain-relieved microstructure obtained in this DoD-MJ process.

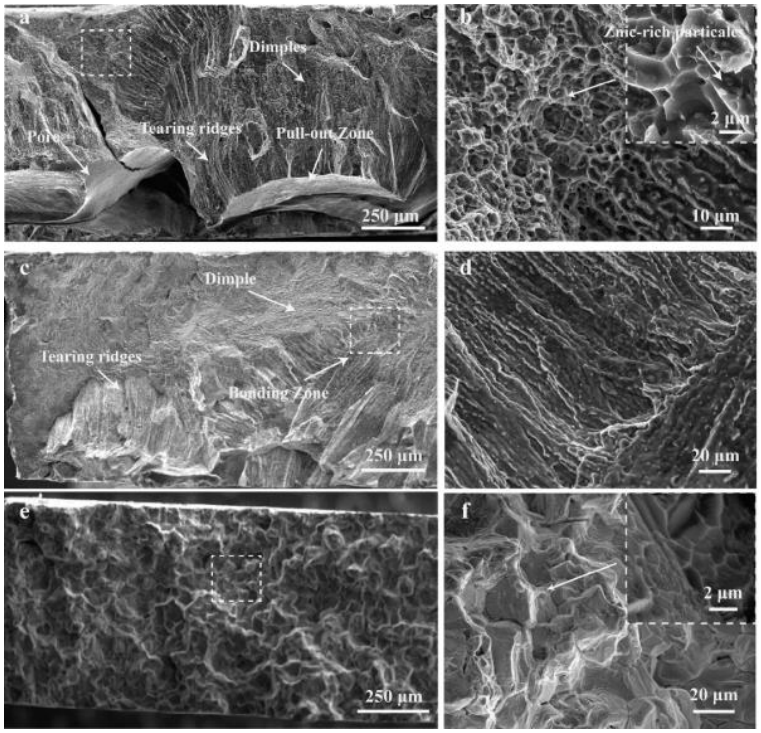


Figure 2.51*- SEM images of tensile fractography for DoD-MJ as-deposited AA7075 aluminium for various droplet/substrate temperature combinations* [220].

2.7. Summary of Literature Review

The literature review highlighted that the additive manufacturing of meso-scale and high-temperature metallic structures with high structural integrities and high resolutions through a rapid process is still not addressed. DoD-MJ opens new avenues to achieve these targets, however, the research in this field is still limited. It was also discussed that MHD actuators offer the opportunity to explore higher temperature materials at higher resolutions without scarifying the production rate (jetting frequency). To date, there are only two MHD DoD-MJ devices: (I) the Xerox liquid metal printer, which is limited to ejection of Al droplets of 500 um, (II) MetalJet, which has the potential to overcome the challenges associated with high temperature and droplet size. It was observed that due to the novelty of this technology, there is little published data about this topic.

Since DoD-MJ is a droplet-based technology, extensive previous studies about droplet behaviour from ejection to solidification can be used to understand the fundamental

aspects of the process. The literature demonstrated that despite fundamental differences in the physics of droplet formation using various actuation techniques and materials, there are some similarities in sequences of droplet formation, pinch-off, and satellite formation, in particular for the MHD and Piezoelectric actuators. However, the formation of high-temperature metallic droplets at a micro-scale is still absent in state of the art. It was also shown that despite decades of research on modelling the droplet deposition, the complex physics at the trijunction point during the microdroplet spreading at low We number is not yet solved.

The bonding at droplet-droplet and droplet-substrate levels in the context of DoD-MJ are limited to low- to medium-temperature materials. Moreover, due to the limited number of research in the field, the underlying physics of interface formation is not yet elucidated. It was seen that the microstructure of objects built through this technology had received scant attention in the research literature. Finally, up to now, far too little attention has been paid to the residual stress evolution in the droplet deposition process, which can be detrimental to the final quality of printed objects. This can cause undesired delamination at the interface if not well controlled.

2.8. Research problem and motivation

Owing to its novelty, the physical factors governing the quality and properties of the net shapes produced by the MetalJet system are yet to be comprehensively understood. This consists of temperature at the interfaces, which defines the level of bonding, the cooling rate, which is one of the key factors to control for a desired microstructural development, and the residual stresses, which may lead to distortion and/or de-bonding. The lack of knowledge in this regard limits the optimisation of the process for particular applications and poses a challenge to the ultimate exploitation of the technology. However, investigating these important aspects of the process experimentally is challenging due to the resolution limitations of the experimental techniques available and the time and size scales involved. A powerful alternative method of investigation is via computational simulation of the process, though this also faces challenges and limitations, as explained in the literature review.

2.9. Aim and objectives of the study

This thesis aims to comprehensively understand the MHD metal jetting (MetalJet) process and establish a scientific basis for selecting process parameters to produce consistent 3D structures that meet the desired quality in terms of mechanical or electrical performances. In other words, to provide insight into the droplet formation, spreading, solidification, interface formation mechanisms, residual stress, and microstructure evolution during printing metallic microdroplets using DoD-MJ.

To achieve this aim, the following technical objectives were set:

1. Experimental characterisation:
    - Investigating the **droplet formation** and its characteristics in flight.
    - Evaluating the **morphology of deposited droplets**.
    - Assessing the **adhesion of individual droplets** to the substrate and interface formation.
    - Evaluating the **inter-droplet bonding**.
    - Studying the **microstructure evolution** of deposited droplets.
2. Analytical modelling:
    - Determining the **dynamics of liquid droplets**.
3. Computational modelling:
    - Predicting the **solidification and cooling** of molten micro-droplets onto the substrate.
    - Predicting the **evolution of residual stresses** during the cooling process.
    - Establishing the **optimal processing windows**.

The finite element modelling enables the prediction of temperature evolution of the droplets and substrate during solidification and cooling. These simulations allow the investigation of features of the process beyond the resolution available to experimental analysis. Moreover, the time scales of droplets' oscillation and damping obtained from analytical methods provide information on the dynamics of droplet spreading. The combination of analytical and FE modelling yields the final morphology of droplets under various process conditions. Moreover, validated numerical models would provide a predictive tool for the deposition process to investigate the effect of operating conditions such as initial droplet and substrate temperatures on the

temperature distribution, the thickness of remelting, and cooling rates of the droplet and the substrate.

3. Methodology

This study uses an integrated experimental, analytical, and computational approach to investigate the deposition of single and multiple droplets onto substrates using the non-commercial MetalJet process (**Figure 3.1**). The morphology of the droplets of various materials under various process parameters was studied. Later, the interface between the droplets and substrate and between droplets were examined using multiple characterisation techniques to investigate the level of bonding between them. In parallel, a computational model was established to predict the thermal evolution of the droplets and substrate, as well as the residual stress evolution during the deposition of single and multiple droplets. The intensive computational effort to simulate the spreading dynamics of droplets was avoided by utilising the experimentally observed morphology of droplet and implementing this into a 3D Finite Element (FE) thermo-mechanical model. The convective effects in the liquid droplets were considered by applying a modified thermal conductivity for the liquid metal.

The thermal resistance between the droplet and substrate, and temperature-dependent material properties were also considered. It is believed that this combined experimental and modelling approach provides a sufficiently accurate and

computationally efficient method for investigating the MetalJet process to achieve the aim of the study.

Research challenges to be addressed:

1. Droplet Formation.
2. Droplets Dynamics and Solidification.
3. Interface Formation.
4. Microstructure Evolution.
5. Residual Stress Evolution.

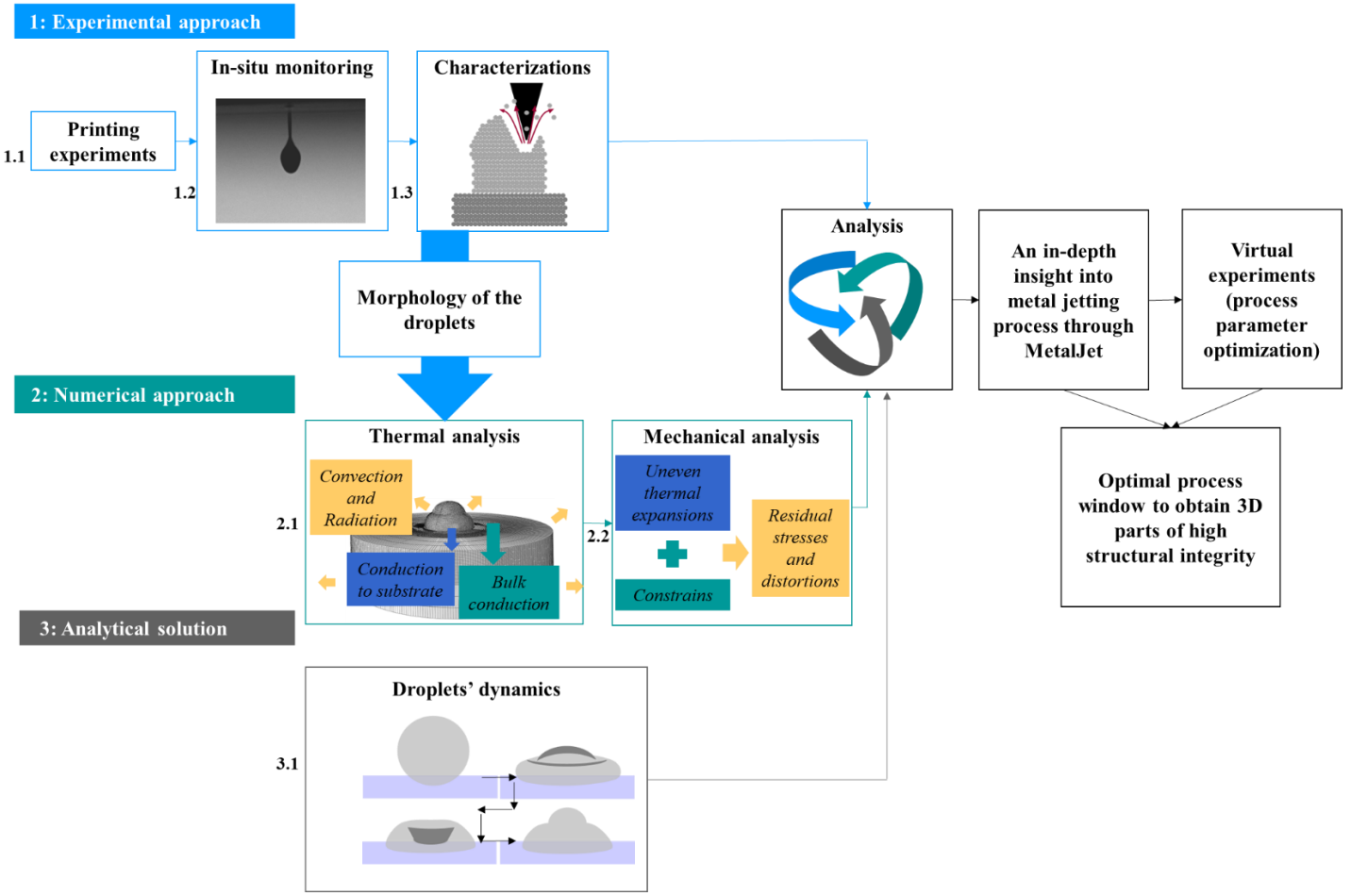


Figure 3.1- *Flowchart summarising the methodology used in the thesis.*

3.1. Experimental

MetalJet, a bespoke DoD AM technology which adopts MHD actuation for droplet generation, was used in this work. Description of the system, technical set-ups, and material used are explained. Additionally, the characterisation techniques used to examine the quality of the parts are presented.

3.1.1. MetalJet platform

In MetalJet, 3D parts are built in a droplet-by-droplet fashion using an MHD actuator, in which molten metal is expelled from the orifice in a controlled manner by an electromagnetic force (Lorentz force). The schematic representation of the platform is presented in **Figure 3.2**. Initially, the conductive metal in the form of rods or shots is melted inside a cartridge by induction heating and flows toward the orifice by gravity. The induction heating is controlled by a High Frequency (HF) generator (Himmel HU 2000 +), and the temperature is monitored by a one-colour pyrometer (METIS M309, Sensortherm GmbH). A 1.3M pixel long working distance USB microscope (Dino-lite, AM4113T) is used to adjust the pyrometer's position and capture images during experiments. The pyrometer used in the current system reads temperatures above 650 °C; consequently, the heating is performed manually and gradually through the HF generator by the user until reaching this temperature. At 700°C, a PID (Proportional, Integral, and Derivative) temperature program is used to control the temperature.

The phase transformation temperature is monitored during the cooling down process to ensure the temperature reading by the pyrometer is accurate. The jetting temperatures should be recalibrated based on this reading if the actual temperature (phase transformation temperature) differs from the read temperature. For temperatures higher than 1000 °C, a second Radio Frequency (RF) heating source can be used through the electrodes. This local heating is applied (I) to reduce the thermal gradient between the top section of the cartridge, where the induction heating is applied, and the actuation chamber (shown in **Figure 3.3**) and (II) to avoid overheating the metal and mitigate the evaporation possibility. For this purpose, a Sine waveform with a frequency of 50 kHz and a maximum amplitude of 3.5 V is used.

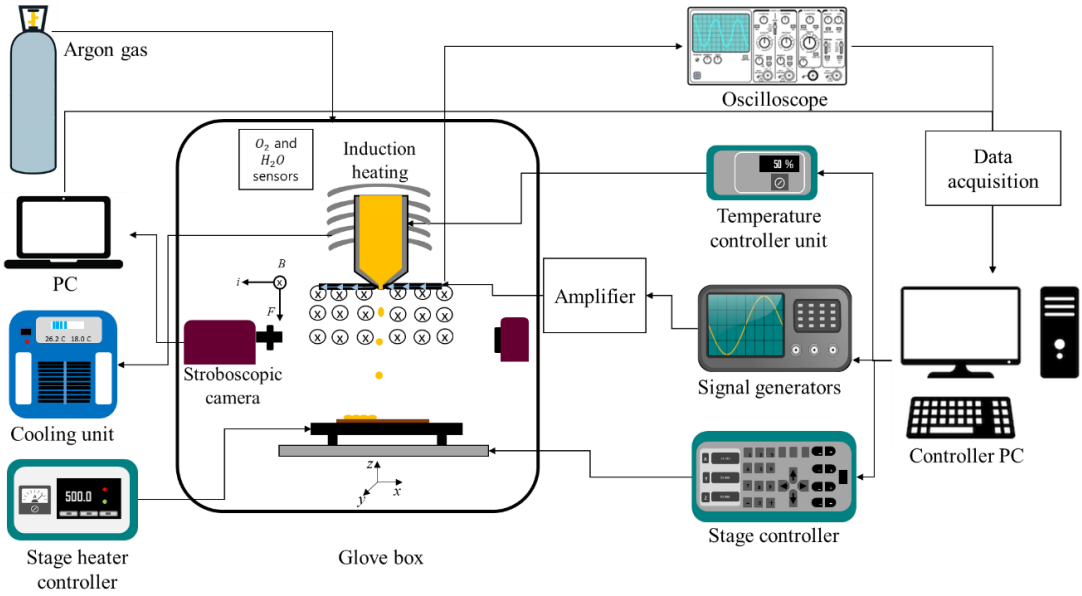


Figure 3.2- *Schematic representation of MetalJet platform.*

Close to the orifice, a magnetic field is produced by two permanent magnets with a magnetic flux density (B) of 2 T. A variable electrical current (I), in the range of 20 A to 120 A, is provided through two electrodes, which are in contact with the liquid metal via the cartridge and are placed perpendicular to the magnetic field direction. The current pulses are controlled by a waveform generator (Agilent Technologies, 33220A) and are amplified by the current amplifiers (ServoWatt DCP780/30A). As a result of these magnetic and electrical fields, a manageable Lorentz force ($\vec{F} = \vec{I} \times \vec{B}$) is created to eject droplets through the orifice. In specific cases, an overpressure of 350 mbar on the top of the cartridge is supplied by a high purity argon gas. Gas purging, which is applying a higher overpressure (1000 mbar) through the same channel, can be used to unclog a temporarily blocked nozzle.

The particular concept of using Lorentz force to produce metallic microdroplets alongside the specific design for the cartridges were invented by Rasa et al. [28]. **Figure 3.3** presents a close view over the tip of the cartridge where the electrodes are in direct contact with the molten metal inside the actuation chamber. To maintain a tight sealing where the electrodes are in contact with the fluid, a spring force is exerted on the electrodes, pushing them into the fluid chamber. The electrodes are made of

tungsten (W), suitable for carrying high currents, while being resistant against high temperatures. The magnetic field is initially provided by the magnetic material of NdFeB and is locally focused close to the orifice using pyramid-shape iron concentrator elements. The permanent magnets used in the system may lose their magnetization properties above ~ 80 °C, so they are thermally isolated and are permanently cooled with the cooling units. The fluid chamber is replaceable and is made of graphite, a conductive and high-temperature resistant material, which increases the heating efficiency provided by induction heating. The inner surface of the fluid chamber, in particular at the nozzle level, should be wettable by the fluid metals having high surface tensions. For this purpose, the interior wall of the fluid chamber is coated with a special material, which cannot be disclosed due to proprietary rights. In order to avoid the oxidation of liquid metal or reaction of the coating material with oxygen (at high temperatures), both of which could potentially block the nozzle, the system should be kept inside argon gas rich chamber to ensure a low oxygen (<1ppm) environment.

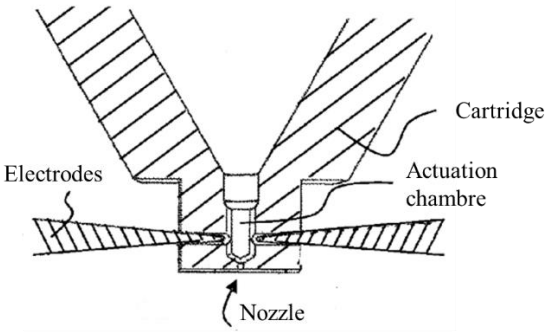


Figure 3.3- *Side-view image of cartridge demonstrating the actuation chamber.*

The position of the print head is fixed, and the substrate moves in the X, Y, and Z directions through a stepper motor controller based on the signals received from a LabView Data Acquisition module. The stage is moved to the desired locations, and the waveform generator is triggered based on the information from bitmap images obtained from a sliced CAD (Computer-Aided Design) or STL (Standard Triangle Language) file. For this, the centre-to-centre distance between droplets and frequency of jetting is set by the operator, and the substrate speed is automatically adjusted such

that droplets are successively deposited onto the desired locations. Two replaceable 20 mm x 20 mm substrates can be positioned on the stage shown in **Figure 3.4**, and they can be heated up to 800 °C using resistance heating. The temperature is set and controlled using a SHIMADEN temperature controller. In order to prevent oxidation during jetting, the system is kept inside an argon-controlled atmosphere glove box, maintaining the oxygen content under one ppm. It is known that the reaction of molten metal with oxygen disturbs the production of droplets due to oxide formation and changes in the physical properties of the newly formed oxide layer [221]. For example, oxidation of molten Sn reduces its surface tension and increases the viscosity, both of which perturb the jet break up [222]. The oxidation can also influence the droplets' size and shape [223], hence an important parameter to be well controlled.

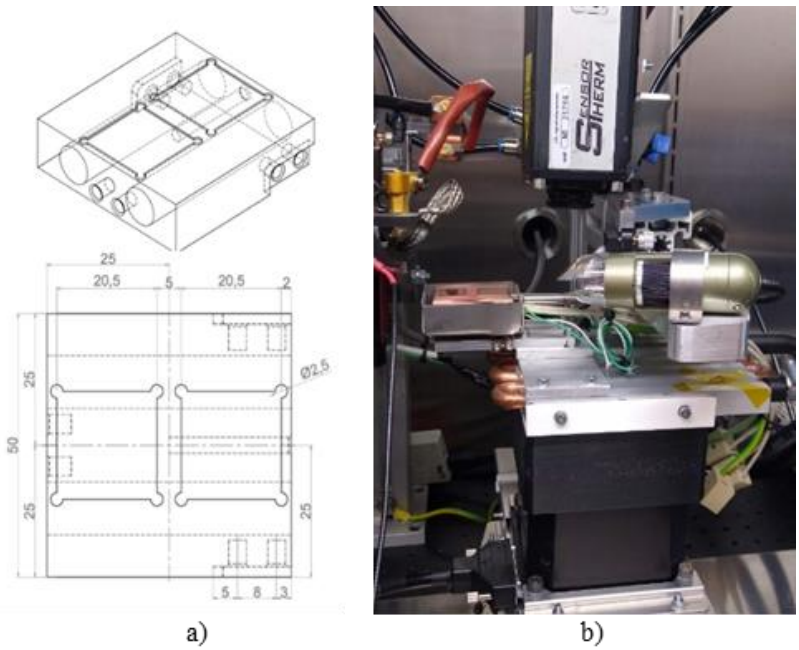


Figure 3.4*- a)3D and top view images of the MetalJet substrate holder design, b) and its integration to the MetalJet stage.*

3.1.2. Materials

The investigations in this work have been performed pure elemental metals, one of low (T < 600 °C), and two materials of high (T > 900 °C) melting point temperatures. In this regard, functional materials of Sn ($T_m = 232\ °C$), Ag ($T_m = 962\ °C$), and Cu

($T_m = 1085\ °C$) belonging to the low and high-temperature categories, respectively, were chosen. These materials are operational within the parameters of the equipment used in this work and are suitable for the main targeted applications. As it was mentioned in the introduction and literature review, the main application for the MetalJet platform is electronic devices, which require high conductivity. Ag and Cu are the most conductive elements on the earth and hence were chosen in this thesis. Ag and Cu have high melting temperatures, and the reaction between the coating inside the cartridge and these elements at temperatures above their melting point could be challenging. Consequently, Sn, which is widely used in the electronics industry and has a low melting temperature, was chosen to provide a wider range of temperatures for experiments. Pure Sn shots of grade 5N, pure Ag rods of grade 5N, and pure Cu rods of grade 5N, supplied by ESPI Metals (Oregon, USA), were used as feedstock material for jetting. Immediately before introducing the materials inside the cartridge, they were etched using 37% HCl diluted to 50% with distilled water for five minutes to remove the oxidation or surface impurities. After that, the materials were cleaned in a mixture of Isopropyl alcohol (IPA) and distilled water for one minute using ultrasonic cleaning. Finally, the materials were completely dried with N_2 gas.

1 mm thick substrates of various materials were used in this work: (1) tempered as-rolled Sn sheets of 99.9% purity, (2) tempered as-roll Ag sheets of 99.97 % purity, (3) tempered half-hard Oxygen-Free High Thermal Conductivity (OFHC) Cu sheets of 99.98 % purity, (4) tempered as-rolled Zn sheets of 99.99% purity supplied by Advent research materials (Oxford, UK). These materials were chosen because of their metallurgical compatibility and solubility with the jetting materials. The metallic substrates were polished using SiC papers grit sizes of 2500, 4000, and 15000 to remove surface oxides immediately before experiments. In one part of the study, the substrates were etched with a similar etchant used for the feedstock material to reduce the surface roughness. In both cases, the substrates were cleaned using IPA and dried with N_2 gas.

3.1.3. Temperature control, jetting pulses and frequencies, other parameters

- ***Droplet temperature control***

The material inside the cartridge should be heated following a specific pattern to reduce the risk of damage to the coating layer inside the cartridge, which can be caused by rapid heating cycles. The temperature was manually increased to 700 °C according to the graph presented in **Figure 3.5**. This temperature is above the melting point of Sn (232 °C) and is mainly used for printing structures in Sn. After that, the temperature could be adjusted through the PID control program. The temperature was increased in steps of 100 °C up to 1020 °C, and 1120 °C for Ag and Cu, respectively. The exact temperature of the melt could be obtained from the deviation between the minimum temperature at which the jetting occurred and the pyrometer readings. The minimum jetting temperature could be associated with the material's melting point. Printing at least 40°C above the melting temperature is recommended to maintain stable jetting, but higher temperatures (below the evaporation temperature) can be used for Sn and Ag. Once the actual melt temperature was obtained, the temperature was increased gradually and in steps of 100 °C to the final temperature. Cu is more susceptible to reacting with the coating material used in the cartridge, consequently, it is recommended to use the minimum jetting temperature for this material.

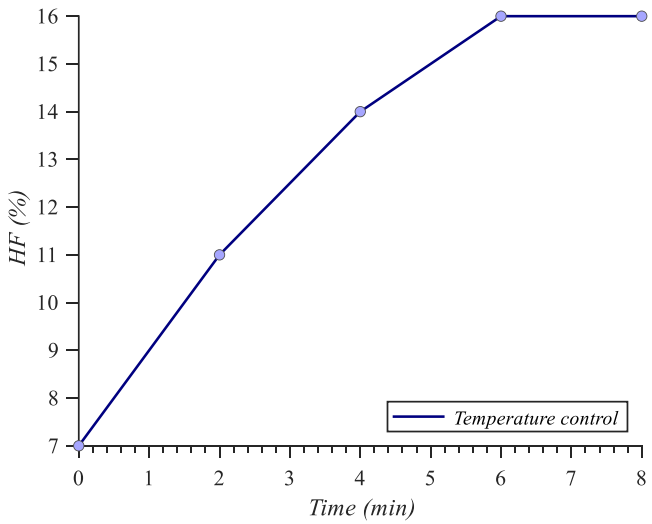


***Figure 3.5**-The manual heating setup.*

- ***Jetting pulses***

The jetting pulse (length and voltage) controls the consistency and stability of the droplet formation. The exact values are specific properties of each system and are kept constant to ensure jetting stability of each material. At first, the printhead should be initialised (purging process) to remove the possible dirt or gas bubbles which can block the metal flow or interfere with the jetting performance. Purging is also used to recover a cartridge that has become inoperative after a period of time. The initialization pulse used in this study cannot be disclosed due to the confidentiality.

The waveforms for various materials used in this study consist of a succession of two positive and negative trapezoidal pulses as demonstrated in **Figure 3.6**. In these bipolar waveforms, the voltage is ramped from an initial voltage (0) to a final voltage within a defined time (t_{rise}), creating a *positive force* to expel the molten metal from the nozzle. The same and constant voltage is applied during the so-called t_{dwell}, causing the actual drop ejection. Henceforth, the voltage is dropped to the negative final voltage within a relatively short time (t_{fall}), and it is sustained at this negative voltage for a period of time, called t_{echo}. During the negative pulse, a *negative force* is applied to the material, such that the material is sucked back into the nozzle, avoiding the ejection of residual material. Finally, the voltage goes back to zero within t_{rise} period. The jetting voltage varies for different materials. This modulation is repeated with the jetting frequency to generate multiple droplets. The details of these waveforms, including the duration and jetting voltages, for the materials used in this thesis cannot be disclosed.

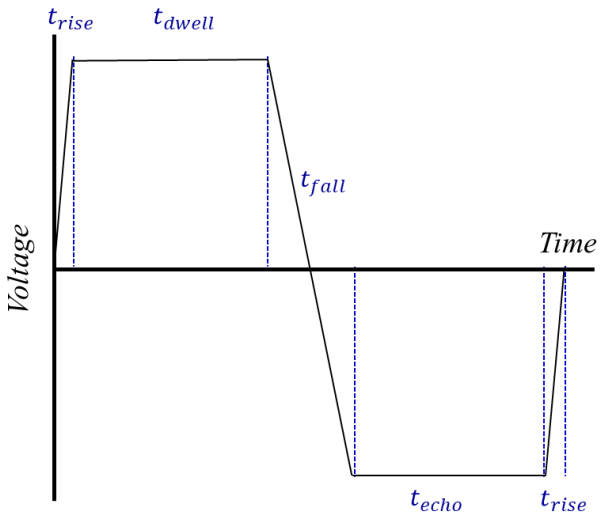


Figure 3.6- *Jetting waveforms.*

- ***Jetting frequency and speed***

The jetting frequency is adjustable from 10 to 2000 Hz but was mostly fixed to 500 Hz in the study. The jetting speed can be controlled within a narrow range for each material and cartridge and varies between 0.5 m/s and 3 m/s. The size of the nozzle, jetted material, voltage, and jetting temperature define the jetting speed.

- ***Other parameters***

It is preferable to minimize the distance between the nozzle and substrate, i.e., standoff distance, in order to reduce the in-flight cooling. Moreover, as per **Figure 3.7**, when the distance between the nozzle and substrate (h_{N-S}) increases, the deposition accuracy decreases. The deposition error (d_{error}) is originated from the lateral speed of droplets due to machining tolerance of the inner wall of nozzle, slag formation, or non-uniform coating, which causes non-uniform wetting at the orifice. In this work, the standoff distance was set to 1 mm.

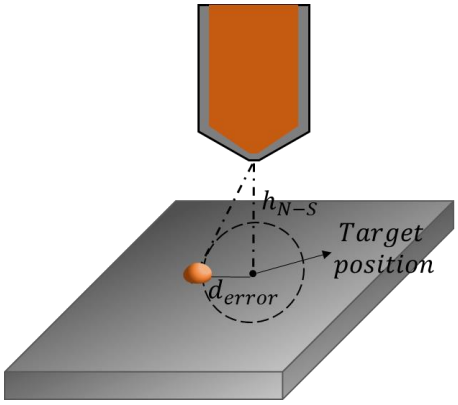


***Figure 3.7**- Schematic representation of deposition error caused by lateral speed and high standoff distances.*

3.1.4. Printing experiments

In order to investigate the morphology of individual droplets, droplet-to-substrate adhesion, droplet-to-droplet bonding, and microstructure evolution, the experimental layout presented in **Figure 3.8** was used for the particular material under investigation. The specific printing parameters used in each experiment, including the droplet material, jetting temperature, substrate material and temperature, and surface roughness, varied according to the study's objective and are described in related chapters.

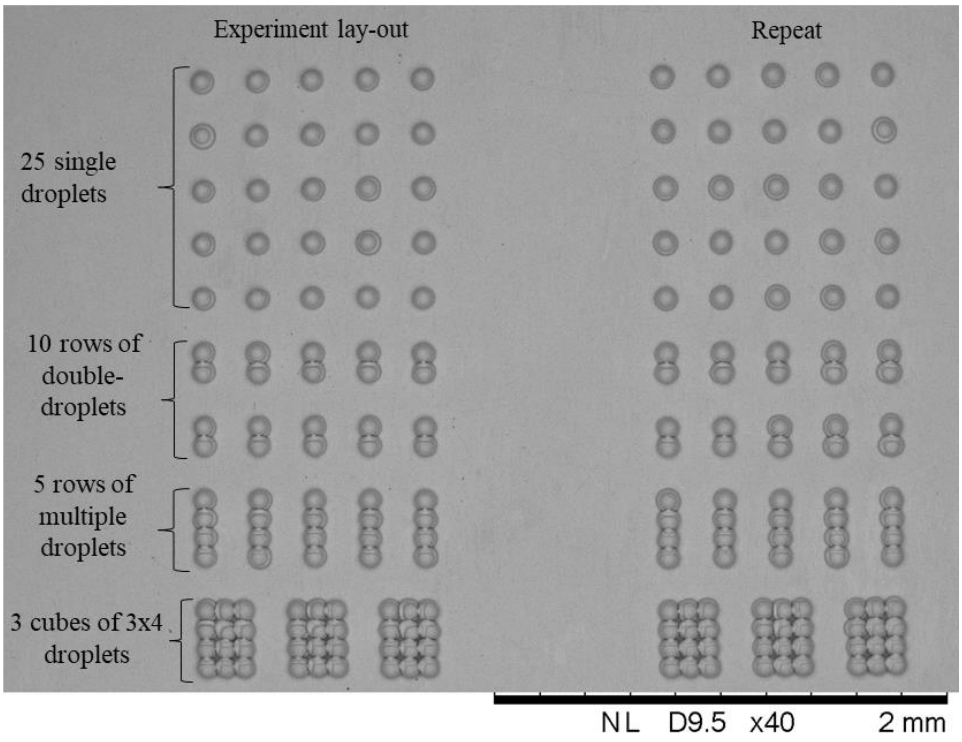


Figure 3.8- *The printing experiment layout used in this thesis to investigate the morphology of droplets, droplet-substrate, droplet-droplet bonding, and microstructure evolution. The SEM image is taken from an experiment of Ag deposition at 1040 °C onto an Ag substrate at 775 °C.*

3.1.5. Characterisation techniques

Due to the size scale and often fragile (due to a poor droplet-droplet or droplet-substrate bonding) nature of the samples printed by MetalJet, conventional material characterisation techniques used for other metal AM technologies were unsuitable. Hence, advanced characterisation techniques were applied to characterize the droplet formation, morphology of single and multiple droplets, their microstructure, the interaction between them and their interaction with the substrate at a micro to nano scale spatial resolution.

3.1.5.1. Techniques to study the droplets characteristic in flight

The formation and stability of jetting and the in-flight measurement (such as droplet radius, velocity, and trajectory) were continuously monitored by a JetXpert drop watcher (ImageXpert Inc., New Hampshire, USA) (**Figure 3.9**). In this method, a CCD camera (Charged-coupled Device) takes snapshots of subsequent drops at

regular intervals, with the output resembling static events or slow-moving droplets. The camera was triggered by the jetting pulses to capture the images. Double pulses separated by times down to 800 ns enabled the measurement of velocities at several discrete positions below the nozzle. Camera resolution could be adjusted between 1.1 and 6.1μm per pixel within a field of view of 1024 x 768 pixels. A typical example of the data obtained by the drop watcher is shown in **Figure 3.9**. The data obtained from the JetXpert camera during the droplet formation was processed using Image Processing Toolbox in MATLAB. The in-flight characteristic of droplets, such as droplet size, speed, and trajectory, were processed in situ through the ImageXpert software. A LabVIEW program, referred to as Big Data, was used to collect and calculate data from various devices and instruments which are used during MetalJet experiments. This includes data from the thermocouple, oxygen sensor, pulse parameters (jetting frequency, jetting current, and jetting voltage), RF current, printhead resistance, and Dino-Lite images. Moreover, the program read the data from the drop watcher, including the droplet speed, size, and trajectory and saved all this information in text files. These files can be further processed through MATLAB or other data analysis programs to investigate the effects of various process parameters on the droplet's characteristics.

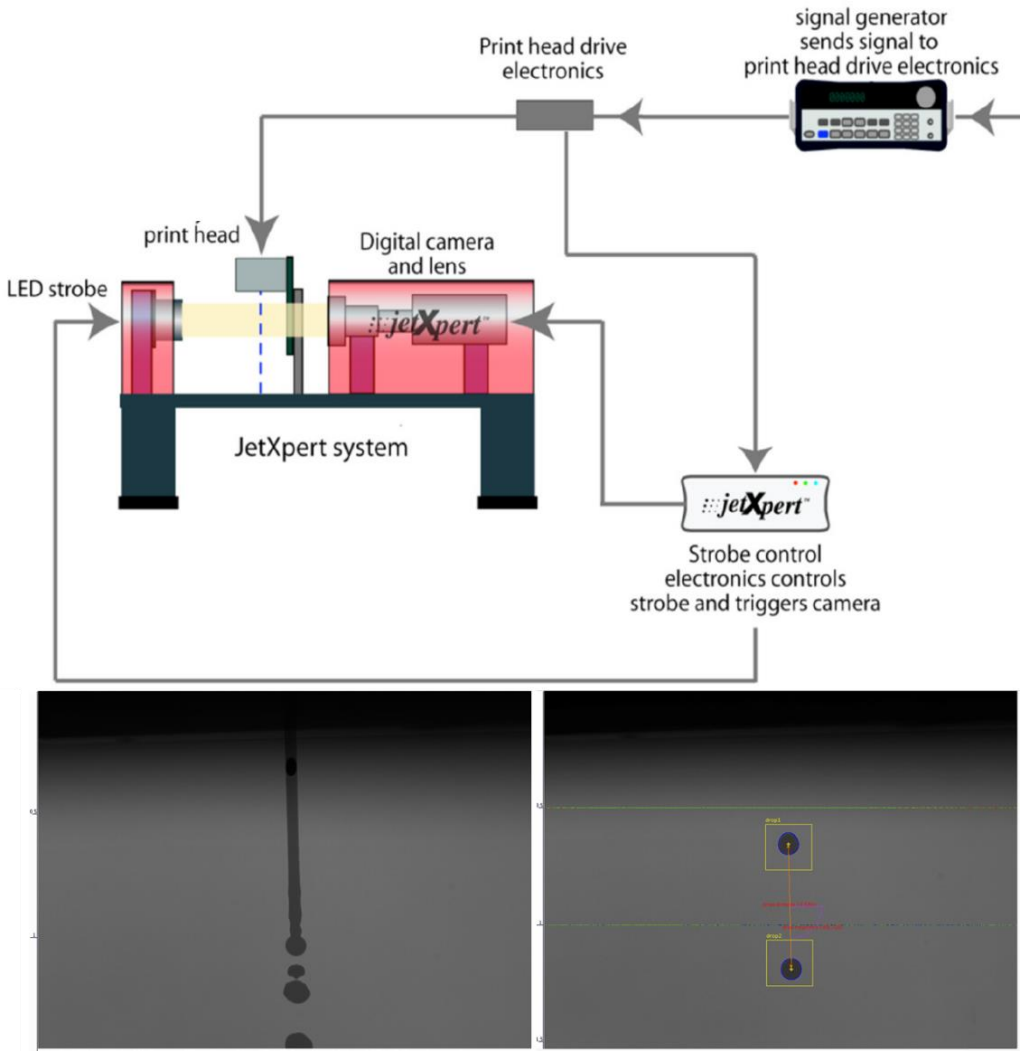


Figure 3.9- *Schematic representation of droplet formation observation through the JetXpert system. a) the set-up including the camera, printhead, LED strobe, and strobe controller, b) Data obtained from the JetXpert camera demonstrating a) a successful purge, b) double-droplet-based analysis, and c) calculated and measured information.*

3.1.5.2. Technique to investigate the surface roughness

The surface roughness of substrates was measured with an optical 3D measurement system, Alicona InfiniteFocusG4. In this technique, the topographical and colour information of the scanned surfaces are obtained from the variation of focus. The data captured from the surface is converted into 3D information and a true colour image with full depth of field through a special algorithm. The typical data obtained from the measurements are $R_a, R_q,$ and R_z. Where R_a is the average of profile height deviations

from the mean line. R_q is the quadratic average, or root mean square average of profile height deviations from the mean line. R_{zi} is the maximum peak to valley height of the profile, within a single sampling length; and R_z is the average R_{zi} value over assessment length. R_a is more commonly used when referring to surface roughness, hence this value is used as the reference in this thesis.

3.1.5.3. Techniques to study droplets' morphology

A TM3030 Scanning Electron Microscope (SEM) (Hitachi, Tokyo, Japan) with a 20 kV accelerating voltage equipped with a backscatter electron detector was used to study the droplets from the top view. A Quanta 200 3D Dual Beam FIB-SEM (FEI, Hillsboro, Oregon, USA) was used to investigate the droplets' side view at 54° and to measure their solidification contact angle at 87°-89°, using various 5-axes stages.

3.1.5.4. Techniques used to study the bonding levels

In order to study the bonding level, the droplet and substrate should be cross-sectioned. Due to the often fragile nature of MetalJet samples due to poor bonding levels between droplets, the standard specimen preparation procedures of cutting, mounting and polishing cannot be readily used. Instead, FIB (Focused Ion Beams) was used in which focused beams of Ga+ ions are rastered across the specimen surface. In this technique, the high-energy Ga+ ions strike the sample and sputter atoms from the surface without disrupting the atoms in the layers beneath (**Figure 3.10**). The advantage of this technique is that delicate features such as micropores and interfaces are not smeared or rounded, unlike in conventional mechanical polishing. A Quanta 200 3D Dual Beam FIB-SEM and a Zeiss crossbeam 550 (Oberkochen, Germany) have been used for this purpose.

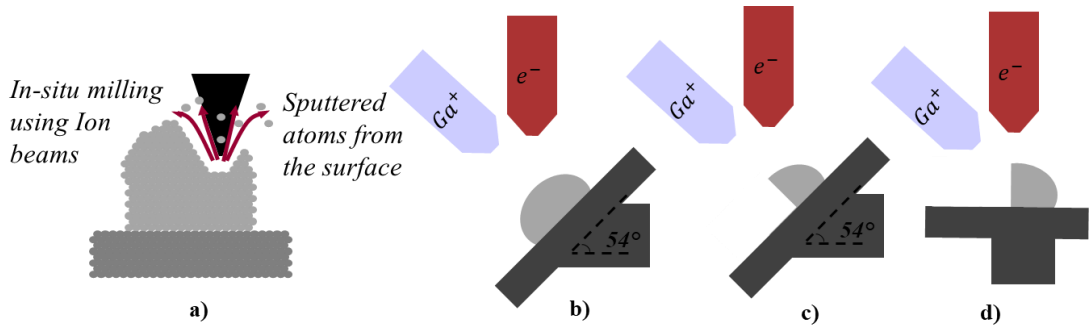


Figure 3.10- *The schematic representation of a) in-situ milling using FIB, b-d) steps used to cross-section the interface of droplets with substrates.*

Figure 3.11 demonstrates the sample preparation methodology used in this work step by step. Preliminary, a high ion current is used to remove large sections of material (**Figure 3.11** -c). The maximum current of Quanta 200 is 20 nA which can be used at this step. Zeiss 500's maximum current is 100 nA, however, 65 nA was used for the preliminary cross-sectioning since the higher current damaged the samples. As per **Figure 3.11-d**, the cross-sectioned area was inspected with the stage brought back to 0° to estimate the required dimension and current for the cleaning step. The black arrows in the image demonstrate the areas to be further polished. The refining polishing is necessary to reveal the microstructure with ion beams and for the EBSD (Electron Backscatter diffraction) characterisation. Therefore, interfaces are polished using lower currents (7 nA in both systems). Further polishing may be required at this stage with a lower current (3 nA or 1 nA), which usually depends on the material. For example, Sn (and sometimes) Cu) needed more refining polishing, whereas Ag samples were less susceptible to curtaining. Finally, the stage is brought back to 0°, and the cross-sections are etched for 60 s to 30 s using these ion beams of 3 nA or 7 nA, respectively.

It should be noted that the FIB is inherently destructive, and a long-time exposure, especially at higher currents, can damage the cross section or make the surface amorphous. Finally, secondary electrons or secondary ions generated by low-current Ga+ beams (50 pA- 0.3 nA) were picked up by detectors for imaging. The grain contrasts were captured due to the different channelling of various crystal orientations with respect to the beam. Zeiss Crossbeam system has several advantages over the FE

Quanta system, including higher currents, the possibility of inspecting the sample during the milling process, and having in-lens and EBSD detectors.

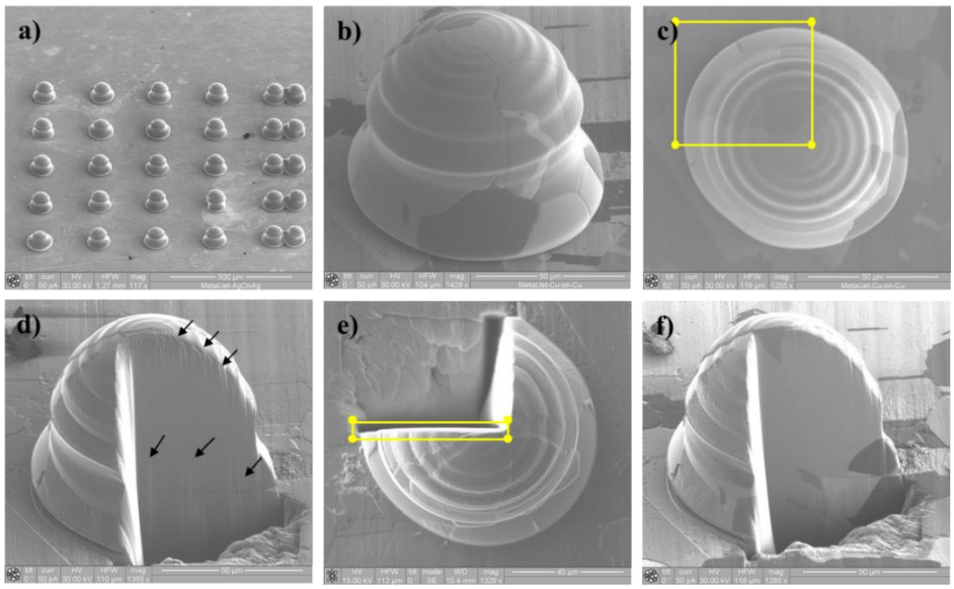


Figure 3.11*- Steps of sample preparation using FIB milling, a-b) selecting the zone, c) tilting stage to have ion beams parallel to the surface, and setting the cross-sectioning dimension, including the milling depth and beam current, d) verifying the cross-section area to identify the beam parameters for the refining step, e) cleaning the surface using low current on a small cross-section area, f) etching the sample using medium ion beam current.*

A similar protocol has been adapted to cross-section multiple droplets to investigate the inter-droplet bonding level, the only difference being the stage used in this case (**Figure 3.12**). A pre-tilted stage of 45° was used to mount the samples, enabling the ion beams to be almost parallel to the substrate. This protocol allows performing an EBSD analysis at the interface between the droplets.

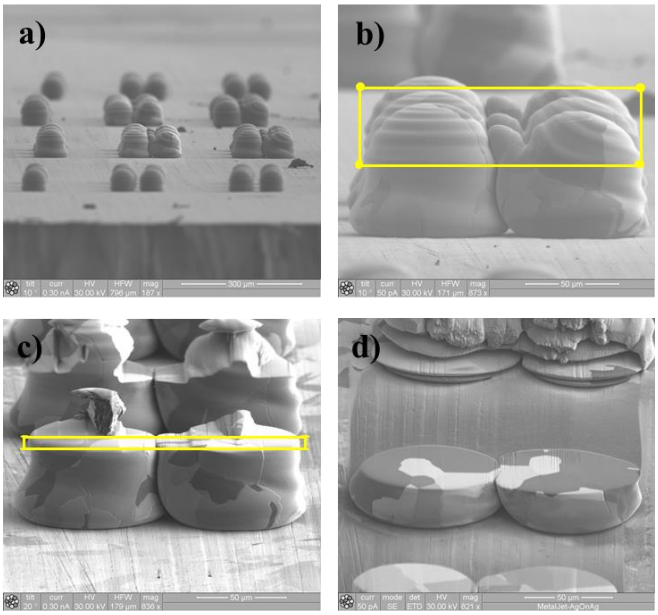


Figure 3.12*- Sample preparation steps using FIB milling, a-b) selecting the zone, c) tilting stage to have ion beams parallel to the surface, and setting the cross-sectioning dimension, including the milling depth and beam.*

A part of the characterisations presented in this work has been characterised using A xenon-plasma FIB, Helios G4 He+ pFIB (Thermofisher Scientific Inc. Massachusetts, United States). The plasma FIB enables the sectioning of larger sample zones at higher rates.

3.1.5.5. Techniques to study the microstructure

- *Crystallographic orientations and Chemical composition*

A Jeol 7100 FEG-SEM equipped with Oxford Instruments AZtec HKL Advanced Electron BackScatter Diffraction (EBSD) system (Oxford Instruments plc, Abingdon, UK) and a Zeiss crossbeam 550 (Oberkochen, Germany) equipped with an Electron Backscatter Diffraction (EBSD) were used for further microstructural observation of the prepared cross-sectioned samples. These analyses were performed on the inter-droplet interfaces based on the protocol explained in **Figure 3.12**. Moreover, some EBSD and backscattered electron analysis were performed using a xenon-plasma Focused Ion Beam (FIB), Helios G4 He+ pFIB (Thermofisher Scientific, formerly FEI) equipped with a symmetry Electron Backscatter Diffraction (EBSD) and Ultim

Max 170 Energy Dispersive X-ray (EDX) detectors (Oxford Instruments). The fast milling speed in this system enabled the lift out of an entire droplet-substrate cross-section in less than three hours, whereas a ¼ cross-sectioning requires at least 6 hours of work using the Quanta 200 system.

The procedure for the sample preparation for EBSD and EDX characterisation is shown in **Figure 3.13**. Initially, a layer of Pt (blue square in **Figure 3.13** a) is deposited along the centreline of the droplet in order to protect the lamella from potential damages due to the fast milling rate. Both sides of the droplet were sectioned using FIB (yellow squares in **Figure 3.13** b) such that a lamella attached to the substrate was created. One side and the bottom section of the lamella are removed; at this stage, the droplet is held in place from the opposite side, which has not yet been removed. The needle is inserted and welded to the lamella using Pt deposition, and the other side is removed so that the lamella can be lifted out. The lamella is welded to the crown for further polishing, which is required for EBSD characterisations.

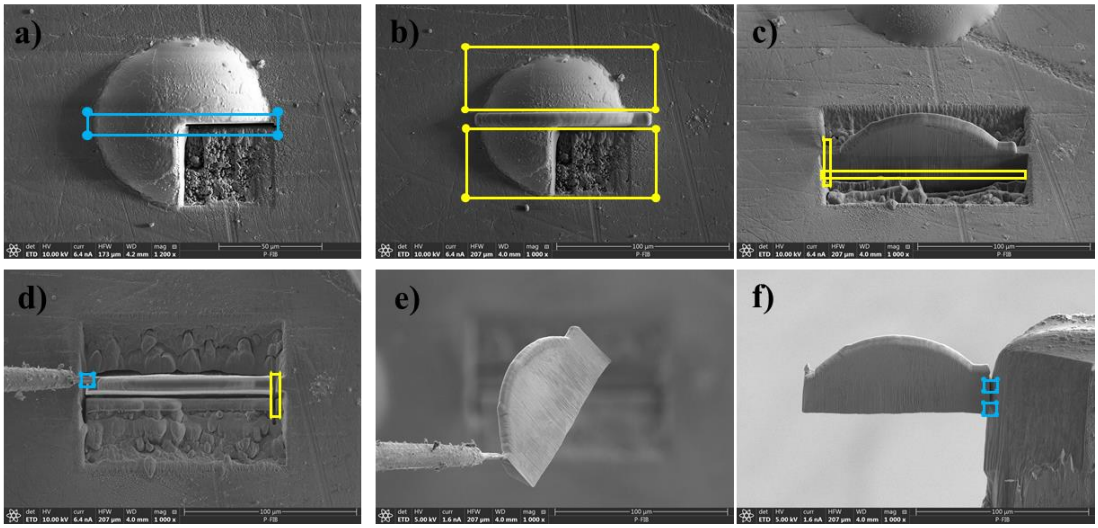


***Figure 3.13**- Steps of EBSD and EDX sample preparation using a xenon-plasma FIB, a) deposition of a Pt layer to protect the lift-out lamella, b) milling both sides of the droplets, c) milling the bottom and side section of the lamella, d) welding the needle to the lamella using Pt deposition, and milling the last portion of the lamella, e) lifting the lamella out, f) welding the lamella to the Cu crown using Pt deposition.*

- *Fine crystallographic structure:*

Transmission electron microscopy TEM has been performed on the droplet-substrate interface using a Tecnai F20 Field Emission Gun Scanning Transmission Electron Microscope (FEG-STEM) (formerly FEI) operated at 200 kV. The lamellae used for the EBSD analysis were thinned to 150 nm on the exact site of interest. The TEM was equipped with Oxford Instruments Energy Dispersive X-ray spectroscopy (EDS) with an 80 cm^2 sized windowless detector. Bright-field (BF) images and STEM EDS maps were recorded to gain high spatial resolution chemical information on zones of interest in the case of dissimilar material printing.

3.2. Computational

Firstly, the droplet's heat loss before impact was calculated using an analytical model. Secondly, a sequentially coupled thermo-mechanical model was established using a commercial FE package, ABAQUS/ standard, version 2019 (Dassault Systèmes Simulia Corp.), to simulate droplet deposition in the MetalJet process. It was assumed that the stress and deformation depended on the temperature field, whereas the temperature is not a function of the deformation response, i.e., one-way coupling. This is regarded as a realistic consideration since the displacements are small and hence, have little effect on heat generation or distribution. The thermal model predicts the temperature evolution of the droplets and substrate during the deposition process.

In this study, the phenomena of interest mainly occur in the solid phase, and the shape of the solid droplets was taken from experimental observations. Hence, the fluid dynamics of impact and spreading were not modelled. However, the effects of convective heat transfer due to the droplet motion were integrated into the modelling approach by implementing an effective thermal conductivity for the liquid metal. The droplet was considered a continuum body, and its shape was reproduced from the experimental observations. The fluid thermophysical properties were applied to the droplets' sections above the material melting point. The mechanical model provides information on the consequent residual stresses and deformations due to the thermal changes during the cooling process.

3.2.1. In-flight cooling of droplets

As droplets are detached from the nozzle, they travel 1 mm in an inert environment with a speed of 1 to 3 m/s and hence are subjected to an initial cooling before impacting the substrate. It is important to investigate the droplet's heat loss amount in this phase since this information is an essential parameter to adjust the jetting temperature. Moreover, this information is the input data for the droplet deposition and solidification model. The in-flight cooling of microdroplets was initially calculated by an analytical model in which the drag force, forced convection and conduction inside the droplet were ignored. In this model, the droplet was considered a sphere with a uniform temperature, which is a reasonable assumption since the Biot number ($Bi = h_{if}D/K \ll 1$) is small. The droplet cooling during the flight was obtained by solving the following equation:

$$\frac{4}{3}\rho c\pi r^3 \frac{dT}{dt} = -4\pi r^2\left[h_{if}(T - T_\infty] + \epsilon_{em}\sigma_{SB}(T^4 - T_\infty^4)\right] \qquad \text{(Equation 41)}$$

Where ϵ_{em} is the emissivity and equal to 0.1, σ_{SB} is the Stefan-Boltzmann constant and equal to $5.67 \times 10^{-8}\ W/m^2C^4$, and h_{if} is the convective heat transfer during the flight, which was obtained by

$$h_{if} = Nu\frac{K_{atm}}{D} \qquad \text{(Equation 42)}$$

In which $K_{atm}$is the thermal conductivity of the Argon gas in which the droplets travel. Various empirical expressions exist for the Nu number, which depends mainly on the Re number. In this thesis, the equation established by Lewis and Gauvin [224] was considered :

$$Nu = \left(2 + 0.515Re_d^{\frac{1}{2}}\right)(\vartheta_d/\vartheta_\infty)^{0.15} \qquad \text{(Equation 43)}$$

The temperature of the Argon gas was estimated to be the average of the nozzle and substrate temperature and hence varied based on the printed material. However, for each material, the Argon gas temperature was considered constant, and consequently, the thermal conductivity and kinematic viscosity of the Argon gas were constant for

each material. Equation 41 was solved using the finite difference method with a step size of 1×10^{-4} s.

In addition, a more sophisticated model was established in collaboration with the University of Warwick. In the second model, the temperature distribution in the gap between the nozzle and the substrate was calculated initially. The droplet's heat loss was calculated considering conduction and forced convection. Moreover, the equation of motion for the droplet, including the gravity and drag effects, was considered when solving the heat loss rate. These models were verified through MetalJet experimentations. Even though both models yielded close results, the output from the second model better matched the experimental results; consequently, it was used to calculate the deposition temperatures used in this thesis.

The simplified model presented in this thesis underestimated the amount of heat loss since (I) the forced convection in the droplet was ignored and (II) the Ar gas temperature was overestimated (using the average value of the nozzle and substrate temperatures). Detailed descriptions of the second model and the experimental approach and results used to validate the model are described in a manuscript under review, '*In-flight cooling and solidification of metallic microdroplets'*. For each study in this thesis, the ejection temperature, i.e., the nozzle temperature, and the deposition temperature, i.e., the droplet temperature on impact, are presented at the beginning of the relevant sections.

3.2.2. Thermal model definition

The governing equation in the thermal model constitutes the conduction between the droplet and the substrate with a general heat convection and radiation boundary condition. The droplet spreading was considered a precursor of the thermal process; however, the effects of convective heat transfer due to the droplet motion were integrated using an effective thermal conductivity for the liquid metal. The initial temperature distribution of the droplet and substrate was considered uniform. The geometry of quarter-symmetry and symmetry models to simulate single and multiple droplet deposition, respectively, is shown in **Figure 3.14**. The droplet geometry and the droplet-substrate contact angle were measured experimentally. The substrate was assumed to be sufficiently small to avoid the excessive computational cost but large

enough to capture the depth to which the heat is diffused. This is also to eliminate the constraints caused by the boundary conditions in the mechanical simulations and to guarantee that a constant temperature can be specified at the bottom surface of the substrate.

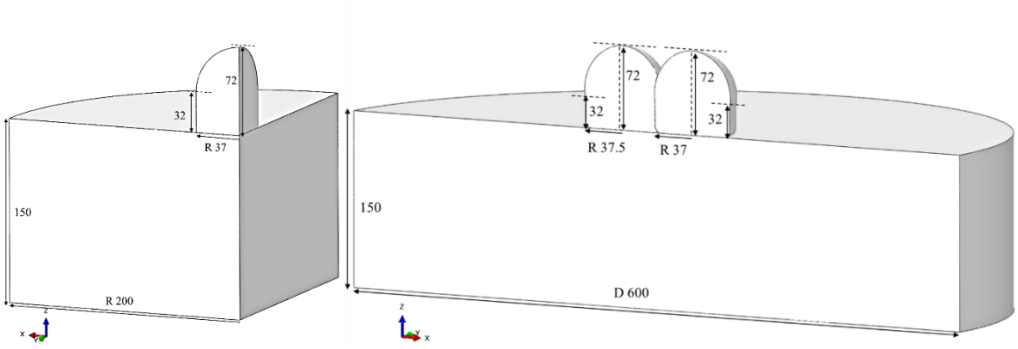


Figure 3.14*- Geometry of droplet and substrate for a) single droplet deposition and b) multiple droplet deposition.*

The transient temperature distribution throughout the domain was obtained by solving the three-dimensional heat conduction (Equation 41) in the droplet and substrate along with the appropriate initial and boundary conditions.

$$\rho c_p \frac{\partial T}{\partial t} = \frac{\partial}{\partial x}\left(k\frac{\partial T}{\partial x}\right) + \frac{\partial}{\partial y}\left(k\frac{\partial T}{\partial y}\right) + \frac{\partial}{\partial z}\left(k\frac{\partial T}{\partial z}\right) + Q \qquad \text{(Equation 44)}$$

Where k is the temperature-dependent thermal conductivity, T is the temperature, Q is the power generated per unit volume, ρ is the material density.

The forced convective heat transfer in the liquid droplet due to its motion was accounted for by the use of an effective thermal conductivity when the temperature of the metal was above its melting point using the equation suggested by Zarzalejo, et al. [184].

$$K_{eff} = c_{mf} K \qquad \text{(Equation 45)}$$

Where K is the thermal conductivity at the given temperature, K_{eff} is the effective thermal conductivity and c_{mf} is the conductivity multiplier factor, which is greater than one and is a function of the Nusselt number (Nu), the droplet height (x), and the

interface length. c_{mf} has been experimentally measured in various studies [4], [184], [196], [225] and is equal to 2.

Combined convection and radiation from the free surfaces and conduction between the droplet and substrate were considered. The convection and radiation heat exchange at the free surfaces of droplet and substrate were implemented according to Newton's law of cooling:

$$q = h\,(T - T_{\infty}) \qquad \text{(Equation 46)}$$

where T_{∞} is the ambient temperature equal to 30 °C and h is a user-defined heat transfer coefficient. To consider the effects of heat radiation but avoid the consequent computational non-linearities, a radiative and convective heat transfer coefficient was used based on the equation proposed by Mughal et al. [26]:

$$h = h_{conv} + \epsilon_{em}\sigma_{SB}(T_s + T_{\infty})(T_s^2 + T_{\infty}^2) \qquad \text{(Equation 47)}$$

where ϵ_{em} is the emissivity and equal to 0.1, σ_{SB} is the Stefan-Boltzmann constant ($5.67 \times 10^{-8}\ W/m^2C^4$) and h_{conv} is the free heat convection ($\cong 40\ W/m^2C$).

The conductive heat transfer between the droplet and substrate interfaces is defined by:

$$q_{cond} = k_c\,(T_s - T_d) \qquad \text{(Equation 48)}$$

where T_d is the droplet temperature at the interface with the substrate, T_s is the substrate temperature at the interface with the droplet, and k_c is the thermal conductance coefficient. The thermal contact property at the interface of two surfaces depends on various parameters, such as flatness, surface roughness, and hardness; and is defined by the thermal contact resistance, R_c, or the thermal conductance coefficient, k_c, which have a reciprocal relation

$$k_c = 1/R_c \qquad \text{(Equation 49)}$$

Although it is well known that this parameter has a major influence on the heat transfer between two surfaces, in previous works in the literature, it has either been arbitrarily chosen [13], [181] or neglected altogether [4], [25], [184], [191] due to the lack of information on how to estimate it. In some research, this parameter was experimentally

measured; however, the response time of temperature sensors is usually longer than the spreading time of the droplets, leading to inaccuracies in the results. Aziz et al. [192] calculated the thermal contact resistance between molten Sn droplets and a stainless-steel substrate by matching the measured surface temperature variation with an analytical solution. Their measured values varied been $10^{-6}\ m^2K/W$ and $5 \times 10^{-6}\ m^2K/W$. Similarly, Kumar et al. [35] estimated the thermal contact resistance between Al–33 wt.% Cu droplets and stainless steel at $7e^{-4}\ m^2K/W$. Trapaga et al. [181] considered several values of thermal resistance ranging between $10^{-4}\ m^2K/W$ and $10^{-6}\ m^2K/W$ for Cu droplet impinging on a Cu substrate. In this study, we have modified the relation established by Xue et al. [226] to estimate a temperature-dependent thermal resistance

$$R_c = R_a/(K\ \alpha_t) \qquad \text{(Equation 50)}$$

In which R_c is the thermal contact resistance, R_a is the surface roughness, K is the thermal conductivity, and α_t is a unitless parameter, which depends on surface tension and contact pressure and is defined in this work.

$$\alpha_t = 2\pi r\rho gx/\sigma_s \qquad \text{(Equation 51)}$$

In which ρ is the material density and σ_s is the surface tension. For the solidified material, α_t is considered constant and equal to its value at the liquidus temperature. It should be stressed that this relation is applicable only if the substrate asperities scale (R_a) is considerably smaller than the droplet height.

3.2.3. Mechanical model definition

Stress and deformation analysis were performed considering nodal temperatures, which are time and position-dependent through a sequentially coupled thermo-mechanical model. This coupling can be used when the stress or deformation field depends on the temperature field, but the temperature field can be found independently of the stress or deformation response. Full coupling is required for problems with extensive inelastic deformation occurring very rapidly. If the process is slow or plastic deformations are limited, the heat generated by the plastic deformation has time to dissipate, or the heat generation is limited, such that uncoupled analysis would be sufficient.

In the sequentially coupled heat transfer analysis in this thesis, the temperature fields from the heat transfer model were read into the stress analysis as a predefined field, i.e., they are not changed by the stress analysis solution. The isotropic elastoplastic rate-independent material definition was used, which has a relatively simple form and yields the model more efficient. Since the cooling rate in the process of interest was extremely high, and the high-temperature duration was significantly short, the creep effects were ignored. The local force equilibrium in a Lagrangian viewpoint was represented using:

$$\int_S t dS + \int_V f dV = 0 \qquad \text{(Equation 52)}$$

Where V is the volume of the body, S is the surface, f is the body force per unit volume, and t is the surface traction per unit area:

$$t = n.\sigma \qquad \text{(Equation 53)}$$

Here, σ is the Cauchy stress matrix, and n is the unit outward normal to the surface. Introducing Equation 53 into equation 52 and using the Guess theorem, the following relation is obtained:

$$\left(\frac{\partial}{\partial x}\right).\sigma + f = 0 \qquad \text{(Equation 54)}$$

In the absence of external mechanical loading (here, the stresses are only arising from differential thermal contractions and expansions), the stress equilibrium is governed by:

$$\nabla.\sigma = 0 \qquad \text{(Equation 55)}$$

The total strain tensor is governed by:

$$\epsilon = \frac{1}{2}[\nabla \mathrm{u} + (\nabla u)^T] \qquad \text{(Equation 56)}$$

Where ∇u is the spatial displacement gradient.

The constitutive mechanical law is defined by:

$$\sigma = C\epsilon^E \qquad \text{(Equation 57)}$$

Where C is the fourth-order elasticity tensor of material properties.

The total strain can be decomposed into three components:

$$\epsilon = \epsilon^E + \epsilon^P + \epsilon^{Th} \quad \text{(Equation 58)}$$

where ϵ^E is the elastic strain, ϵ^P the plastic strain and ϵ^{Th} is the thermal strain. Thermal strain, arising from differential thermal contractions and expansions, contributes to the residual stresses. These thermal stresses constitute either elastic or plastic components. The thermal strain is defined by:

$$\varepsilon^{Th} = \int_{T_{ref}}^{T} \alpha_e \, dT \quad \text{(Equation 59)}$$

In which α_e is the temperature-dependent thermal expansion coefficient, presented in **table 3.1**.

For the plastic term, the flow rule is defined by Prandtl-Reuss equations:

$$de^P = d\bar{e}^P n \quad \text{(Equation 60)}$$

In which $d\bar{e}^P$ is the equivalent plastic strain rate, and n is defined by:

$$n = {}^3\!/_2 \, \frac{S}{q} \quad \text{(Equation 61)}$$

where S is the deviatoric stress and q when the von misses yield criterion is adopted is defined by:

$$q = \sqrt{{}^3\!/_2 \; S : S} \quad \text{(Equation 62)}$$

3.2.4. Parameters and material properties

The thermo-physical properties of the material, including density, heat capacity and thermal conductivity, were considered temperature-dependent. A finite temperature range of 2 - 4 °C was considered for the solidification of pure metal, during which latent heat is released. The mechanical properties, Young's modulus, coefficient of thermal expansion, and yield stress were also considered temperature-dependent. The Poisson's ratio of Cu was assumed to be 0.35 and temperature independent. The Cu

thermo-mechanical properties ranging from room temperature to 1200 °C are listed in **Table 3.1.** The Yield strength from room temperature to 900 K is obtained from an empirical equation (temperature in K) as follows [227]:

$$\sigma_Y = 1570.8 - 14.184\,T + 5.641\,T^2 \times 10^{-2} - 1.0592\,T^3 \times 10^{-4} + 9.288\,T^4 \times 10^{-8} - 3.086\,T^5 \times 10^{-11} \quad \text{(Equation 60)}$$

The yield strength is obtained from the literature [228] for higher temperatures. Since a non-zero value for the yield strength is required by the numerical solver, a relatively small value of 0.1 MPa was used at temperatures above the solidus temperature. The Ultimate tensile strength from room temperature to 900 K is defined by an empirical equation (temperature in kelvin) [227] :

$$\sigma_U = 191.32 + 0.65.36\,T - 1.85\,T^2 \times 10^{-3} + 1.0185\,T^3 \times 10^{-6} \quad \text{(Equation 61)}$$

For higher temperatures, the yield strength is obtained from the literature [228], and the temperature-dependent flow stress of Cu is demonstrated in **Table 3.2**.The thermo-physical properties of Sn and Ag are listed in **Table 3.3** and **Table 3.4**, respectively.

Table 3.1*- Temperature-dependent properties of pure Cu.*

Temperature (°C)	**27**	**227**	**427**	**627**	**827**	**1027**	**1200**
Density (Kg/m^3)	8960	8762	8564	8366	8168	7971	7800
Surface tension (N/m)							1.28
Specific heat capacity (J/Kg °C)	385	408	425	441	464	506	520
Thermal conductivity (W/m °C)	401	386	372	359	345	331	319
Thermal expansion (1/ °C) $\times 10^{-6}$	15.4	16.9	18.5	20.1	21.9	23.7	25
Dynamic viscosity (mPa.s)						4.03	3.45
Young modulus (GPa)	125	112	98	85	72	58	4
Yield strength (MPa)	210	181	66	20	5	2	0.1
Ultimate tensile strength (MPa)	250	200	105	30	18	5	-

Table 3.2- *Temperature-dependent flow stress of Cu.*

Temp (°C)	Yield Stress (MPa)	Plastic Strain
27	210	0
27	235	0.1
27	238	0.4
27	250	0.5
227	181.5	0
227	192	0.1
227	198	0.4
227	200	0.5
427	65.93	0
427	95	0.1
427	102	0.4
427	105	0.5
627	20	0
627	25	0.1
627	29	0.4
627	30	0.5
827	5	0
827	12	0.1
827	17	0.4
827	18	0.5
1027	2	0
1027	4	0.1
1027	4.5	0.4
1027	5	0.5

Table 3.3- *Temperature-dependent properties of pure Sn.*

Temperature (°C)	**27**	**232**	**327**	**1127**
Density (Kg/m^3)	7300	6900	6850	6300
Surface tension (N/m)		0.546	0.540	0.480
Specific heat capacity (J/Kg °C)	207	210.1	211.9	233.5
Thermal conductivity (W/m °C)	66.6	56	95.7	163.2
Dynamic viscosity (mPa.s)		1.8	1.6	0.8
Kinetic viscosity $\times 10^{-7}$ (m^2/s)		2.7	2.4	1.0

***Table 3.4**- Temperature-dependent properties of pure Ag.*

Temperature (°C)	**27**	**327**	**627**	**962**	**1200**
Density (Kg/m^3)	10490	10300	10100	9600	9000
Surface tension (N/m)				1.89	1.88
Specific heat capacity (J/Kg °C)	235	245	270	297	310
Thermal conductivity (W/m °C)	428	405	380	360	340
Dynamic viscosity (mPa.s)				4.07	4
Kinetic viscosity $\times 10^{-7}$ (m^2/s)				5	4.9

3.2.5. Mesh and boundary conditions

The thermal and mechanical models utilised identical nodal locations to simplify coupling. The meshes for the single and multiple droplets are shown in **Figure 3.15**. A uniform hexahedral mesh with an element length of 1 µm was used for the droplet, resulting in 46,512 elements for a single droplet and 300,235 for the multiple droplet model. For the substrate, a non-uniform density mesh was used, with an element length of 1 µm close to the interface, where the temperature and displacement gradients are steepest, gradually increasing towards the bottom and sides. This meshing strategy resulted in a total of 96,668 elements for substrate in the single droplet model and 433,161 in the multiple droplet model. In the mechanical model, reduced integration elements were used to enhance the convergence behaviour.

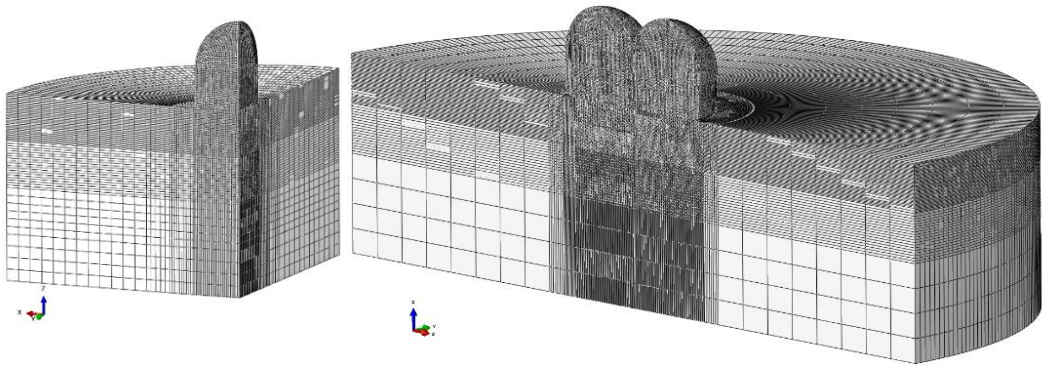


***Figure 3.15**- Initial mesh of droplet and substrate for a) single droplet deposition and b) multiple droplet deposition model.*

Uniform initial temperatures were assigned to both the droplet and substrate. The temperature at the bottom surface of the substrate was kept constant throughout the

simulation. Adiabatic conditions were applied to the symmetric surfaces of the droplet and substrate. Heat exchange was enabled at the free surfaces of droplet and substrate through the definition of convection and radiation surfaces. These were implemented according to Newton's law of cooling:

$$q = h\,(T - T^0) \qquad \text{(Equation 63)}$$

Where T_∞ is the ambient temperature and h is a user-defined heat transfer coefficient. To consider the effects of heat radiation but avoid the consequent computational nonlinearities, a combined radiative and convective heat transfer coefficient was used based on the equation proposed by Mughal et al. [229]

$$h = h_{conv} + \epsilon\sigma(T_s + T_\infty)(T_s^2 + T_\infty^2) \qquad \text{(Equation 64)}$$

where ϵ is the emissivity, σ is the Stefan-Boltzmann constant, and h_{conv} is the free heat convection from a plate, which are available in the literature.

A stress-free initial condition was considered, and symmetrical conditions ($U_x = UR_y = UR_z = 0$ at YZ plane and $U_y = UR_x = UR_z = 0$ at XZ plane for the single droplet) were applied to the symmetry planes of the droplet and substrate. The bottom surface of the substrate was constrained in all displacement and rotations. A tie constraint, i.e., perfect bonding, between the droplet and substrate was assumed, which ensures no relative motion between the contact surfaces

A transient heat transfer and a general static analysis with a time step of $10^{-9}\ s$ was used to solve the thermal and mechanical problems, respectively. The time step was chosen to effectively capture the effects of the fast cooling rate in the process. A typical thermo-mechanical simulation of a single droplet required 53 hours of CPU time, whereas the thermal simulations of multiple droplets took approximately 71 hours of CPU time.

3.2.6. Time step and solution control

A transient heat transfer and a general static analysis with a time step of $10^{-9}\ s$ was considered to solve the thermal and mechanical problems, respectively. The time step was chosen to capture the steep temperature changes due to the fast cooling and the latent heat release. It should also satisfy the requirement for convergence and the

limitation imposed by the software. A typical thermo-mechanical simulation of a single droplet requires 53 hours of CPU time, whereas the thermal simulations of multiple droplets take 71 hours of CPU time.

3.3. Summary

In order to achieve the aim and objectives of this PhD, an integrated experimental, numerical, and analytical approach was adopted. This method provides insights into the five main parameters defined in **Figure 3.2**, namely droplet formation, morphology of droplets, droplet-substrate and droplet-droplet bonding, microstructure, and residual stress evolution, as shown in **Figure 3.16**.

- The droplet formation through the MetalJet platform was investigated through high-temperature experiments (Ag) and in-situ monitoring of droplet ejection and analysis of the characteristics of droplets.
- The droplet morphology was investigated by characterising single droplets of Sn, Ag, and Cu, printed through the MetalJet platform. In addition, numerical simulations were performed to predict the temperature evolution in droplets and substrates during the deposition process. In parallel, analytical analysis through the scaling method was performed to understand the dynamics of droplets during the deposition.
- The inter-droplet bonding and the adhesion of droplets to the substrate were evaluated through characterising the interfaces. For this purpose, Cu, Sn, and Ag droplets were printed onto various substrates. In addition, numerical simulations were performed to predict the interface temperatures.
- The microstructure of printed droplets of Sn, Cu, and Ag was investigated through various material characterisation approaches, including FIB-SEM and EBSD.
- The thermomechanical simulation brought insights into the experimentally observed delamination of Cu droplets from the Cu substrate. Virtual experiments were performed to underpin conditions under which the residual stresses and risk of delamination are mitigated.

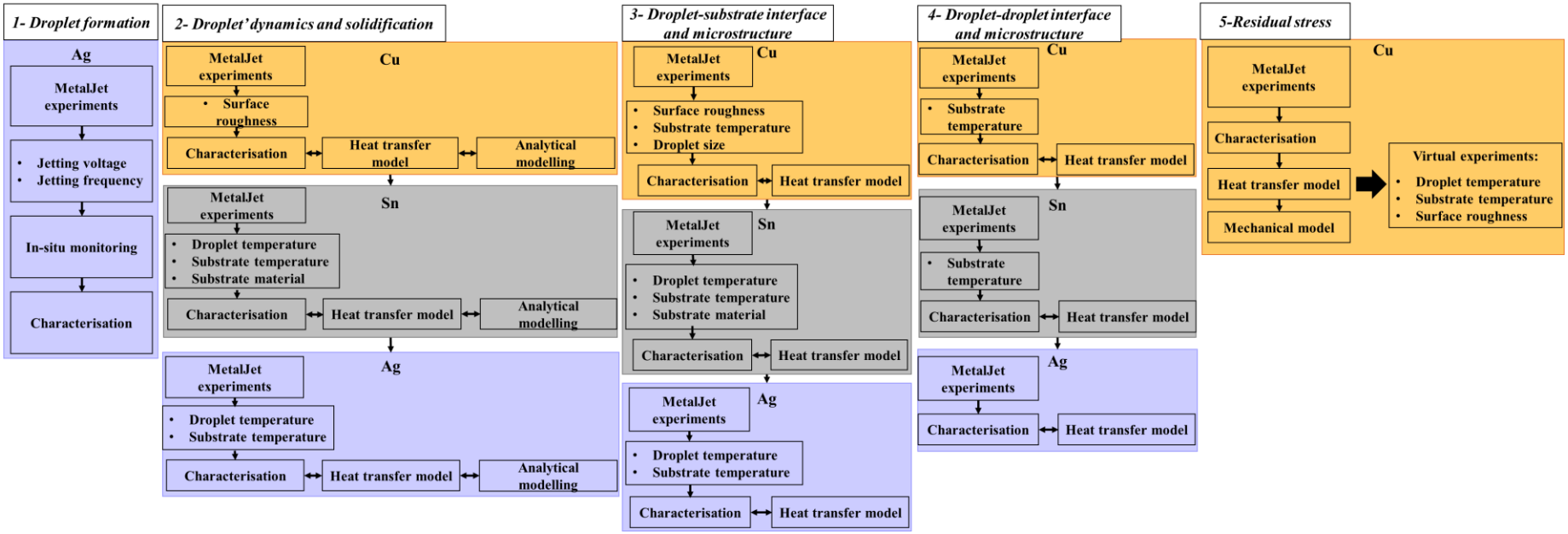


Figure 3.16- *Flowchart summarising the methodology used in the thesis.*

4. Droplet Formation in The MetalJet Process: Silver

In drop-on-demand devices, the generation of uniform, tuneable, stable, and repeatable droplets is one of the primary challenges to be addressed (**Figure 4.1**). Indeed, the resolution and consistency of printed parts rely on good control over the droplets' size, velocity, trajectory, and absence of satellite droplets. To achieve a successful and satellite-free ejection, the stream length at which the droplet breaks up should be precisely controlled. To this end, the actuation waveform, including jetting voltage, dwell time, echo time, and jetting frequency, should be carefully tuned. Moreover, material properties such as viscosity, surface tension and density, the geometry of the printhead, and in particular, the nozzle diameter and the bore length, control the formation of the droplets. This challenge has been widely studied in the inkjet printing processes [92], [94]. With the recent emergence of DoD-MJ, limited investigations have addressed the formation of metallic droplets. However, these studies are concerned with the formation of millimetre-size metallic droplets [21], [75], [95], [96].

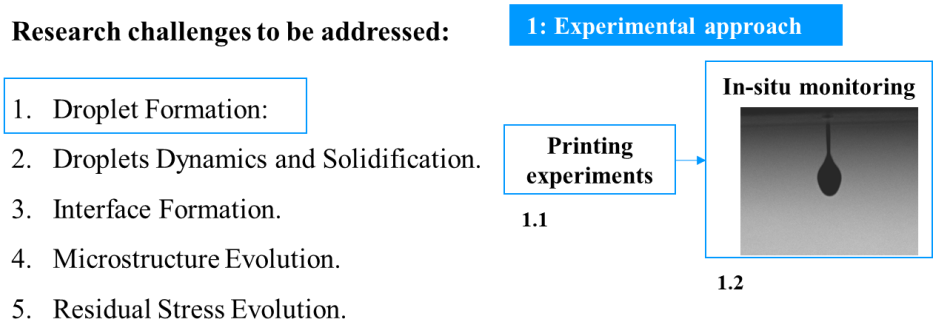


***Figure 4.1**- The first challenge to be addressed in this thesis referring to Figure 52.*

The major differences between ink jetting and metal jetting are the higher density (~ 10 times), lower viscosity, and significantly higher surface tension of liquid metals (20 - 30 times higher), all of which makes metal jetting more challenging. Higher pressures are required to create a sufficient momentum in the liquid metal that overcomes the surface tension at the orifice level and eject droplets. Furthermore, droplets are more prone to break into satellite droplets due to the low viscosity of liquid metal compared to common inks. The satellite droplets may be deposited to undesired locations on the substrate, but also, they can be retracted to the nozzle plate, disturbing the jetting trajectory or droplet size. Hence, it is imperative to gain knowledge on the margins of printability and physics of droplet formation in the DoD-MJ technology to avoid the formation of satellites and control the droplet properties.

To the best of the author's knowledge, stable generation of micro metallic droplets remains unaddressed in the current state of the art, consequently, it is the main motivation for the study presented in this chapter. Here, the formation of droplets under various jetting conditions, including jetting pulses and frequencies, was studied. The in-situ drop formation, particularly, the tail breaking behaviour, droplet speed, radius, and trajectory, were investigated using the JetXpert camera. The tail breaking is important because (I) it influences the drop characteristic such as speed, (II) it contributes to the cleanliness of the nozzle after each ejection, (III) more importantly, it controls the formation of satellite, all of which dictates the repeatability of the process. The droplet formation in the MetalJet platform for low melting materials does not pose technical issues due to their relatively low surface tension (0.54 N/m) and viscosity (1.83 mPa/s). On the other hand, the droplet formation of Cu is challenging

due to the relatively higher surface tension (1.28 N/m), viscosity (4.03 mPa/s), and high melting temperature (1084 °C). Moreover, the chemical reaction between the coating inside the cartridge and molten Cu was reinforced when exploring the extreme ranges of jetting waveforms. All of which made the investigations of droplet ejection impossible for this material. As the mechanism of droplet formation is experimentally investigated, and due to the high costs and limited number of cartridges available during the PhD, this topic has been investigated only for Ag. Ag is a high-temperature and non-reactive metal with relatively high surface tension (1.89 N/m) and viscosity (4.07 mPa/s). Consequently, the ejection of uniform droplets for this metal is complicated. Yet, due to its vast application in the electronic industry, printing pure Ag is of great interest and hence studied in this chapter.

4.1. Mechanism and sequences of droplet ejection

Figure 4.2 illustrates the droplet formation and tail breaking sequences for a typical droplet generation event when the jetting parameters were tuned. As a result of the actuation pulse, the fluid was pushed out of the nozzle and subsequently stretched (0 – 120 µs). The length of the stream increased continuously in this step. After that, the ligament length did not increase anymore; instead, the head became rounder, and the tail thinned (140 µs) until the stream was broken at the nozzle exit (140-160 µs) due to the Rayleigh–Plateau instability. At this stage, single droplets are formed if the ligament merges with the head. Alternatively, the thinned ligament may pinch-off at the neck of the ligament and creates a satellite droplet.

The surface tension of molten metal plays an essential role in the pinch-off process since it causes the tail to retract or separate. It is also possible that the free tail breaks at several points and forms multiple satellite droplets. In the presented jetting issue here, the second pinch-off occurred at the neck of the ligament (160 µs) but the satellite droplet caught up with the main droplet and integrated into it (160 – 180 µs). This observation can be explained by the numerical modelling of the jetting process. It has been shown that the tail speed is higher than the head if the actuation pulse is finely tuned [86]. The alignment of jetting and droplet trajectories is critical when satellites are formed, otherwise, the satellites are not able to merge with the main droplet.

Eventually (t >180 µs), the droplet kept oscillating until the fluctuations were dampened, and a nearly spherical droplet was formed.

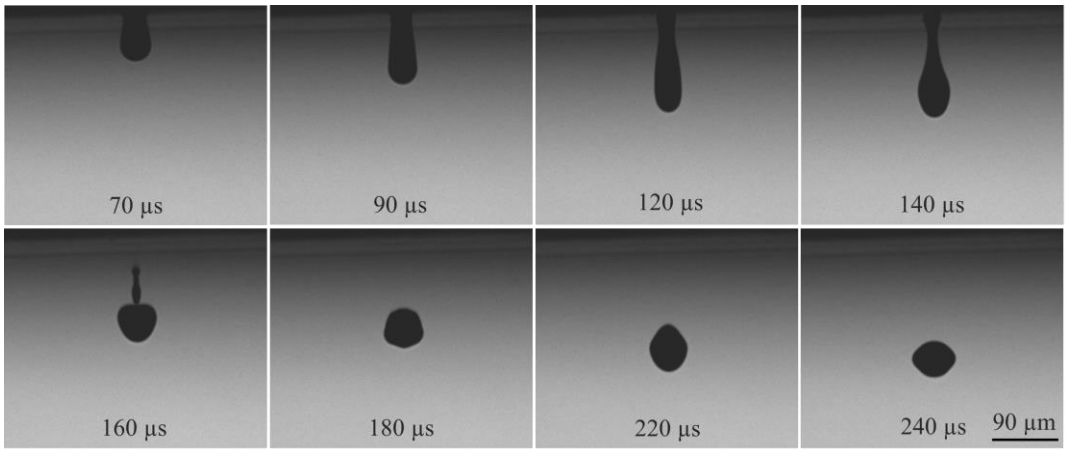


***Figure 4.2**- Various stages of droplet formation demonstrating the formation of satellite free Ag microdroplets at 1020 °C with a frequency of 250 Hz and jetting voltage of 5 V.*

In order to produce satellite-free and uniform spherical droplets presented in **Figure 4.2**, the actuation pulse should be carefully optimised. In the MetalJet system, an MHD actuator is used, where the force to push the material out of the nozzle is provided by Lorentz force using two permeant magnets and a variable electrical pulse, $\overrightarrow{f_{MHD}} = \vec{J} \times \vec{B}$. Hence the intensity of the jetting force is set by the current density ($\vec{J}$), i.e., jetting voltage. The exerted force varies as a function of the viscosity and surface tension, both of which are temperature-dependent properties of the molten liquid. The jetting force should be adequate to overcome the surface tension at the orifice. Besides, it controls the volume of ejected material as well as its velocity, which should be carefully optimised such that the stream is broken into satellite-free droplets of the desired diameter. Other actuation characteristics, such as the dwell and echo times, influence the droplet ejection and must be carefully tuned.

4.2. Effects of jetting voltage on breakup length and droplet formation

The effects of pulse amplitude on droplet formation for liquids of similar properties (Oh number) are demonstrated in **Figure 4.3**. Here, Ag droplets at 1020 °C were ejected with a frequency of 500 Hz, using similar jetting pulses but with amplitudes of 4.5 V, 5 V, and 5.5 V. The optimal jetting voltage for Ag was known to be 5 V from

the previous experiments (not included in this thesis). 4.5 V and 5.5 V were chosen to explore the extreme limits of consistent jetting and to investigate the influence of jetting voltage on the characteristics of droplets. It was observed that jetting voltages outside this interval resulted in no jetting or spraying. At the lower jetting voltage, the ligament pinched off close to the nozzle, and the single satellite droplet was retracted to the nozzle. In this case, the tail end velocity was not high enough to catch with the main droplet; such a scenario may affect the cleanness of the nozzle and the consequent jetting events. At jetting voltage of 5 V, which is the optimal jetting voltage for the presented liquid, the column was broken up at a similar time scale, however, it was relatively longer at the pinch-off. A single satellite droplet was formed, which quickly merged with the main droplet to form a single droplet.

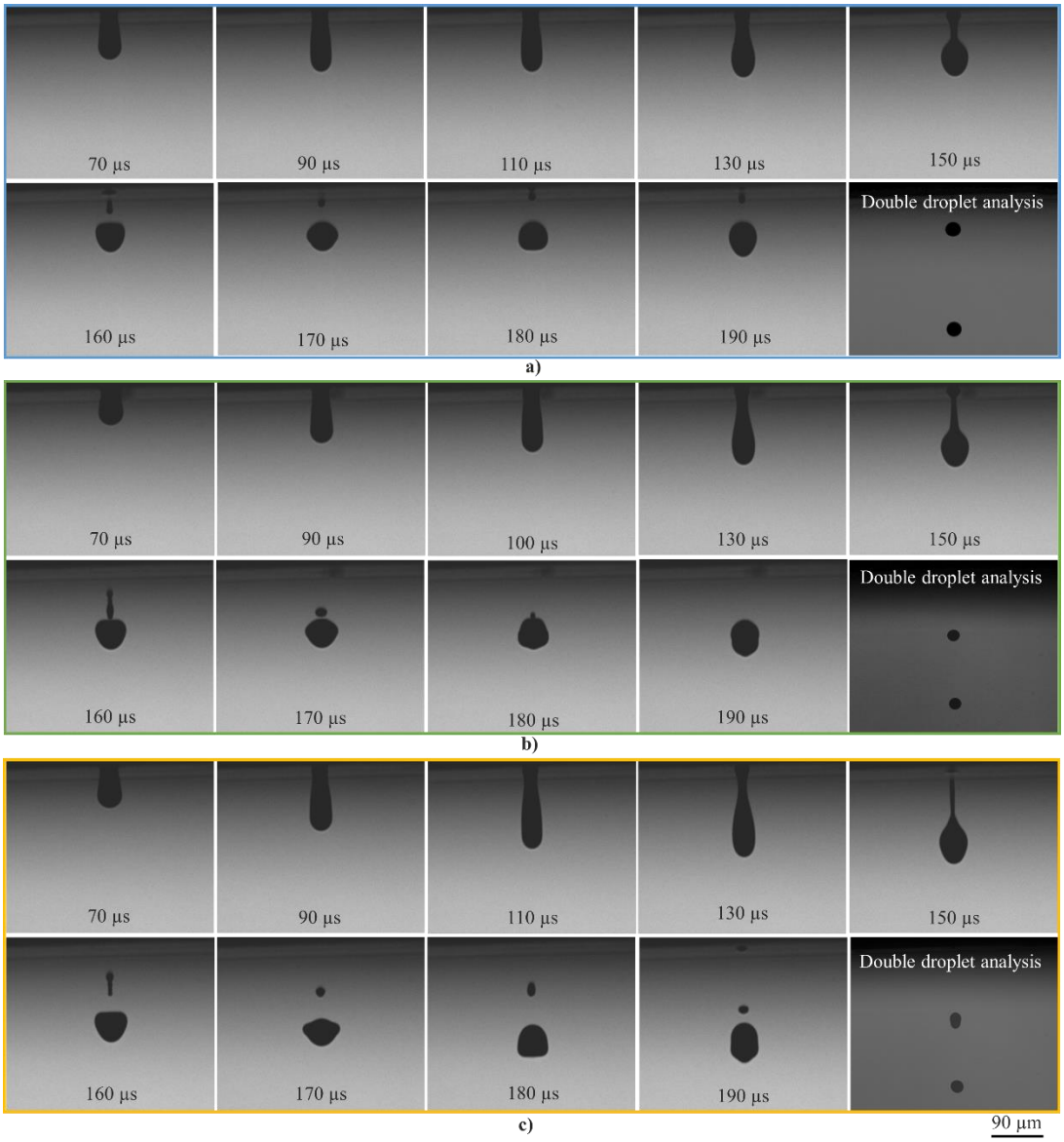


Figure 4.3*- Various stages of droplet formation for Ag at 1020 °C with a jetting frequency of 500 Hz a) jetting voltage of 4.5 V showing the retraction of satellite droplet to the nozzle, b) jetting voltage of 5 V showing the formation of uniform and satellite-free droplets, and c) jetting voltage of 5.5 V showing the formation of single satellite droplets.*

When the jetting voltage was increased to 5.5 V, the tail of the ejected material became more extended and thinner before the breakup. A single satellite droplet was formed at the pinch-off, but it could not catch the main droplet due to their considerable relative speed. Consequently, both main and satellite droplets flew down and were deposited onto the substrate. It has also been shown in the literature that high voltage

amplitudes cause longer ligaments, which are more prone to several pinch-off and the formation of satellite droplets [100]. It is noteworthy that in all the cases presented here, the pinching occurred in two positions, just below the orifice and above the bulbous head of the ligament. It has been shown that such a breakup is more prone to the formation of satellite droplets [230], with the head and tail velocities being the main controlling parameters. Whereas a single pinch-off at the top of the ligament is less prone to create satellite droplets, hence more favourable.

The droplet head position, which is the distance between the bottom tip of the stream and the exit of the nozzle, is mapped in time for various jetting voltages, as demonstrated in **Figure 4.4**. These curved are obtained by measuring the stream length obtained from the JetXpert camera using Image Processing Toolbox in MATLAB (as described in the methodology section). This information is critical in setting the jetting velocity and, consequently, the speed of droplets in-flight. It is seen that the breakup length increased as the jetting voltage increased under identical conditions. This finding is consistent with those of Wang et al. [231] and Zhao et al. [232], who found longer streams at the breakup of metal and ink-based liquids in DoD devices. In other words, the droplet size is expected to increase as the jetting voltage increases. Moreover, it is seen that the slope of these graphs increases initially, implying that the stream was thinning and stretching vertically due to the acceleration effects. This is followed by a gradual decrease in the slope, indicating a declaration due to surface tension effects, where the stream head curvature increased and formed a rounder shape.

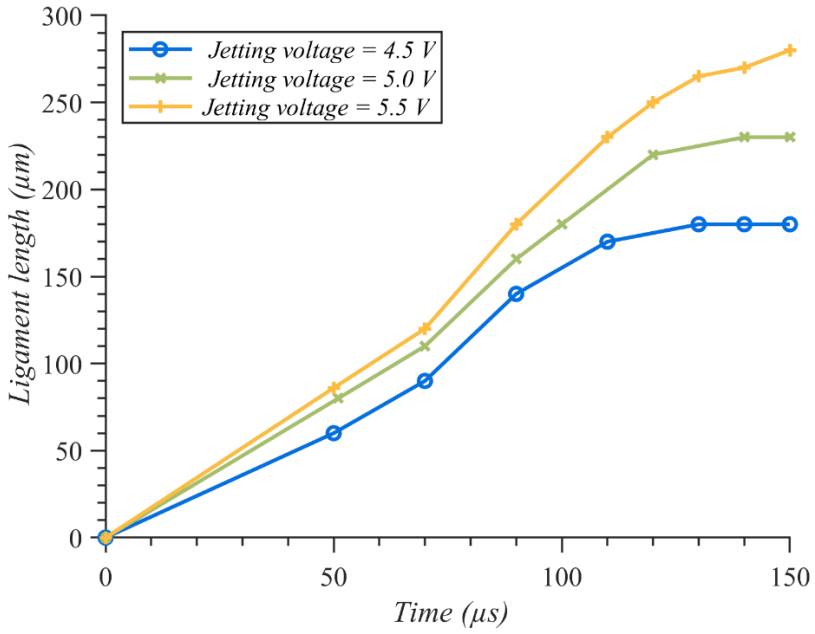


***Figure 4.4**- Ligament length of Ag at 1020 °C from the nozzle in time for various jetting voltages.*

It is also noted that breakup occurred at 150 µs regardless of the amplitude of the jetting pulse, leading to the conclusion that the pinch-off time is controlled by the pulse duration and not the pulse amplitude. Moreover, the jetting temperature influences the pinch-off time due to the variation of surface tension with temperature since the higher surface tension values have proven to promote an earlier droplet breakup [74]. The ligament velocity is equal to the slope of the stream trajectory, which increases as the jetting voltage increases. Accordingly, the jetting velocity was 1.2 m/s at 4.5 V, increasing to 1.7 m/s at 5.5 V. The linear increase of the ejection velocity by voltage amplitude corroborates the findings of a great deal of the previous work in inkjet printing [233]. The speed of individual droplets formed from these streams followed a similar trend and was faster at higher voltages. The We_j, which is obtained from the jetting velocity and the nozzle diameter ($We_j = \rho V_j^2 D_n/\sigma$), increases as the jetting voltage increases. These findings indicate that the breakup time is independent of the We_j, which is contrary to that of Beck et al. [95], who found that the breakup time decreased with increasing We_j for molten Sn droplets in a pneumatic actuator.

As suggested in state of the art [8] and due to the independency of the Oh number from the velocity, this number is traditionally used to evaluate the printability of liquid metal. The Oh number, which only depends on the liquid's physical properties and the nozzle's geometry, controls the capillary-driven pinch-off of a fluid stream and the Rayleigh-Plateau instability of an infinite jet. The former sets the detachment from the nozzle, and the latter plays an essential role in forming the satellite droplets. The nozzle diameter in this study was 54 µm, so the Oh number was equal to 0.005 for all the cases. The We_j was plotted against the Oh number as demonstrated in **Figure 4.5** a. The We_j number was 0.78, 1.22, and 1.56 for the jetting voltage of 4.5 V, 5.0 V, and 5.5 V, respectively. The We_j vs. Re number is demonstrated in **Figure 4.5** b for the same cases. Interestingly, these data differ from the printability map established by Derby [9], where jetting of inks was limited to the Oh number in the range of 0.1 to 1.

The set of data in this thesis did not match the printability zone for metallic droplets suggested by Sukhotskiy et al. [75] either, where the printability range was limited to $We_j > 5$. It can be said the current printability criteria are limited to a set of specific materials or the nozzle size and a global printability criterion is missing in state of the art. In order to establish a criterion for the formation of satellite-free droplets, the speed and length of ligament should also be considered, on which the material properties, nozzle geometry, and jetting force play an essential role.

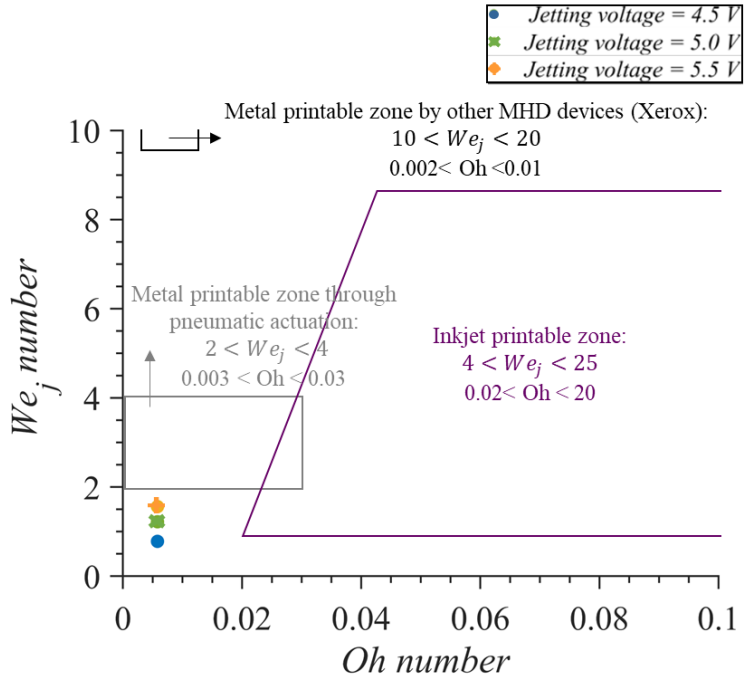


***Figure 4.5**- Droplet formation map based on dimensionless numbers a) Jetting We and Oh numbers, b) Jetting We and Re number.*

4.3. Effects of jetting voltage on droplets characteristics

The droplets oscillate after the pinch-off until the motion is dampened and a nearly spherical shape is formed. It was noted that this process was faster at lower voltages due to the lower jetting speeds and the consequent lower initial kinetic energies of droplets. Once the droplets were spherical, their in-flight characteristics could be measured using the JetXpert stroboscopic camera (**Figure 4.6**). The measurements, such as droplet diameter, velocity, and trajectory, were performed at distances below the nozzle where the droplets were spherical. For example, in **Figure 4.6**, the first droplet was 500 µm below the nozzle, and the second droplet was 530 µm apart from the first droplet.

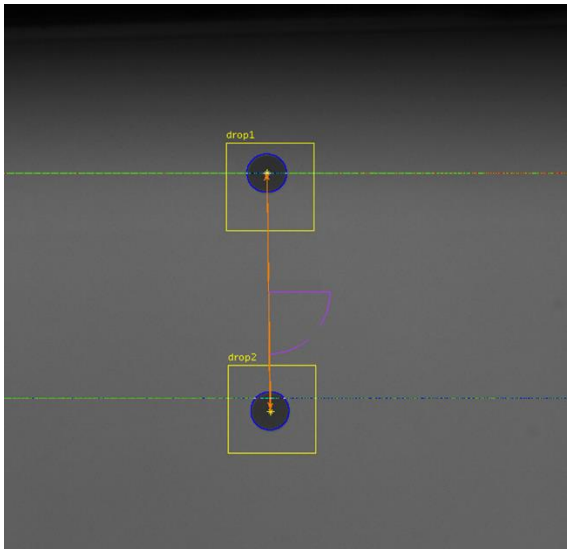


***Figure 4.6**- In-flight droplet characteristics measurement using the JetXpert camera.*

The droplets' sizes set the printed parts' accuracy and resolution when manufacturing via metal jetting. This is due to the voxel-by-voxel definition of objects printed through this process. As mentioned in the literature review, one of the main applications of MetalJet is the micro-electronics and the accuracy of deposition onto precise locations plays an essential role in the performance of final printed objects. Moreover, the droplets should be identical in shape and size during the jetting to maintain precision. The diameter of droplets ejected with various jetting voltages was measured using the JetXpert camera for events of 150 droplets. As demonstrated in **Figure 4.7 a-c**, the droplets' diameters were almost identical over 150 ejections for each scenario with standard deviations of 0.09 µm, 0.23 µm, 0.29 µm for jetting voltages of 4.5 V, 5.0 V, and 5.5 V, respectively. As expected, the droplets' diameters increased as the jetting voltages increased, where the average diameters were 42.37 µm, 44.11 µm, and 45.79 µm for 4.5 V, 5.0 V, and 5.5 V, respectively. This is in agreement with the findings of Feng et al. [100] and Ma et al. [101], who demonstrated that higher voltages yielded larger solder droplets using piezoelectric DoD actuators. Droplets ejected at the jetting voltage of 5.0 V were collected at 10 cm below the nozzle, as demonstrated in **Figure 4.7 d**. At such distances, the molten droplets were cooled below the liquidus temperature and impinged on the substrate in the solid state. The collected droplets were mounted on a carbon tape for SEM characterisations. As

observed in **Figure 4.7 e**, these droplets were uniform in diameter and had a spherical shape.

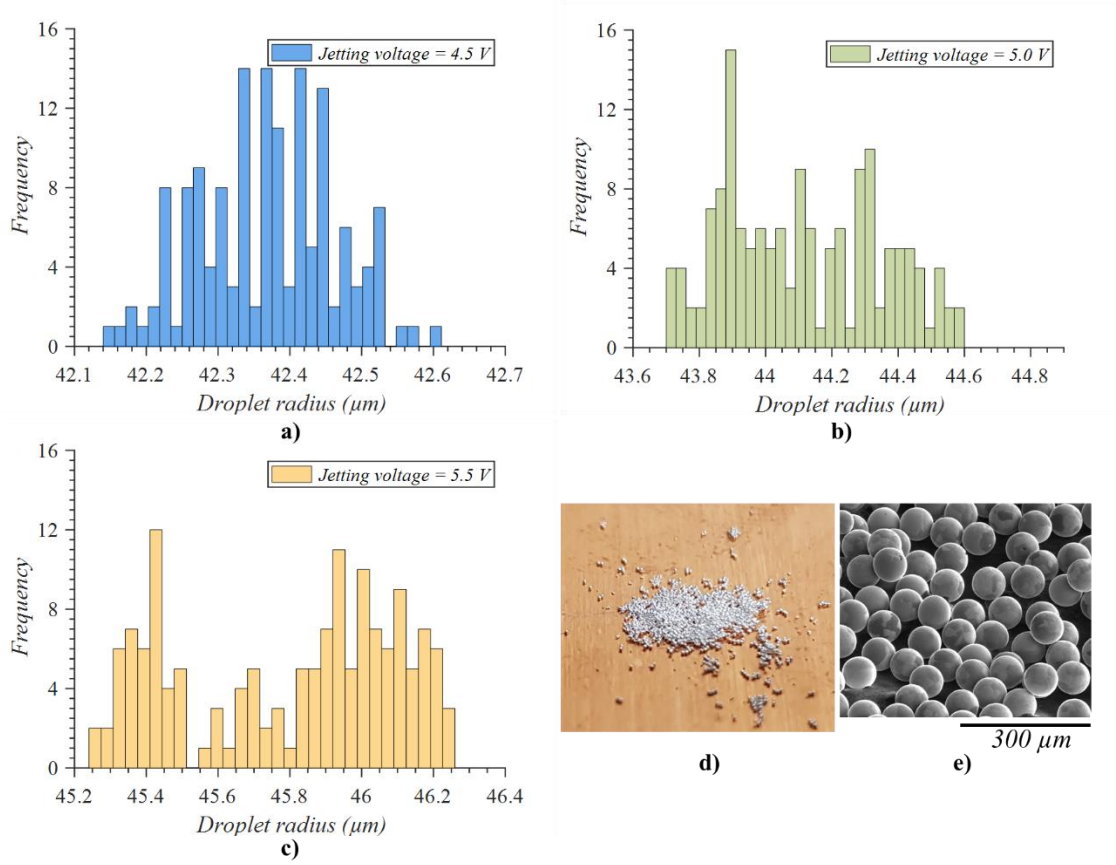


***Figure 4.7**- Distribution of droplets' diameter of droplets for events of 150 ejections with various jetting voltages **a)** 4.5 V, **b)** 5V, **c)** 5.5 V, **d)** in-flight solidified Ag droplets with the jetting voltage of 5.0 V, collected at 10 cm below the nozzle, **e)** SEM image of the droplets presented in d.*

The characteristics of individual droplets after they were detached from the jetting stream and their oscillations were dampened are demonstrated in **Figure 4.8** for various jetting voltages for events of 150 droplets. It can be seen that the individual droplet's speed increased as the jetting voltage increased. The average droplet speed was 0.36 m/s, 1.02 m/s, 1.59 m/s for jetting voltages of 4.5 V, 5.0 V, and 5.5. V, respectively. It was also seen that the jetting was stable, where for 150 droplets studied in this study, the speed variation was minimal, with a standard deviation of 0.009 m/s, 0.008 m/s, and 0.004 m/s at 4.5 V, 5.0 V, and 5.5. V, respectively. The droplet

trajectory, the angle between the nozzle plate and the trajectory of consecutive droplets, was 89.97°, 90.02°, 89.95° at 4.5 V, 5.0 V, and 5.5 V, respectively, indicating an excellent perpendicular jetting. More importantly, the angular deviation was 0.05°, 0.02°, and 0.01° for the respective jetting voltages. The angular deviation ($\sigma_{angular}$) causes the mis-displacements in the deposition location, leading to printing inaccuracy. The mis-displacement also depends on the standoff distance (d_{N-S}) and is defined by $\sigma_{deposition} = \sigma_{angular} \times d_{N-S}$. In MetalJet, the standoff distance is 1 mm for the printing experiments. Accordingly, for the optimised jetting voltage of 5 V in the case of Ag, the deposition inaccuracy is estimated 0.35 µm due to trajectory deviation.

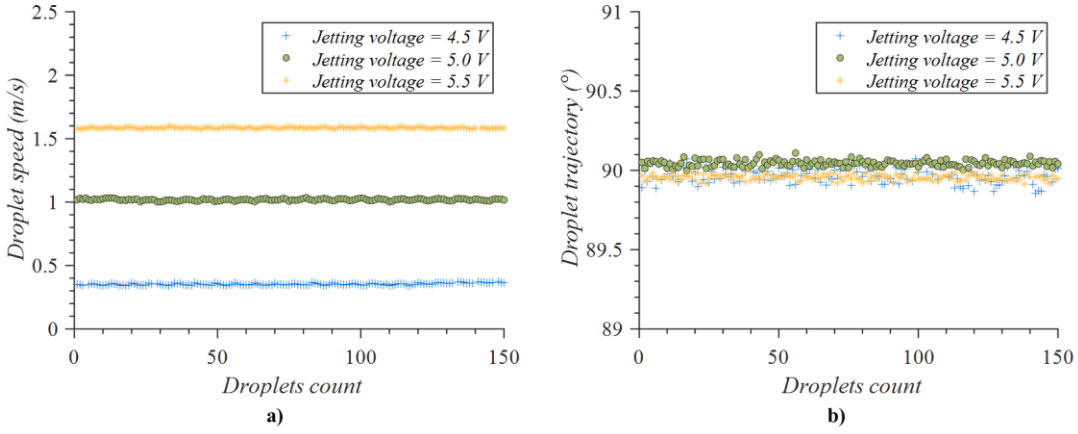


***Figure 4.8**- Characteristics of individual droplets in-flight for various jetting voltages a) droplets speed and b) trajectory of droplets.*

Figure 4.9 demonstrates the relation between the jetting voltage and the droplets' radii and speeds for Ag droplets ejected at 1020 °C at various jetting frequencies. It was found that the jetting frequency did not influence the droplet formation characteristics. This finding is consistent with that of Verkouteren et al. [234], who showed that at frequencies of 10 Hz to 10,000 Hz, the droplet velocity and mass were not varied by the jetting frequency. More importantly, the droplet size increased up to 9 % on average as the jetting voltage increased from 4.5 V to 5.5 V, while the jetting speed increased to 77 % in the same interval. Even though the jetting voltage can be considered a strong tool to control the droplet's speed, its flexibility margin is limited.

The main reason is the satellite formation due to a slight deviation from the optimised jetting voltage. In this experiment, satellites were formed at both 4.5 V and 5.5 V. At V < 4.5 V; there was not adequate force to expel the droplets from the nozzle and at V > 5.5 V, and droplets were sprayed from the nozzle in random directions in an uncontrolled manner. The linear increase of droplet velocity with the jetting voltage in this study corroborates the earlier finding in ink jetting processes [94]. A similar relation stands for the droplet volume and jetting voltage.

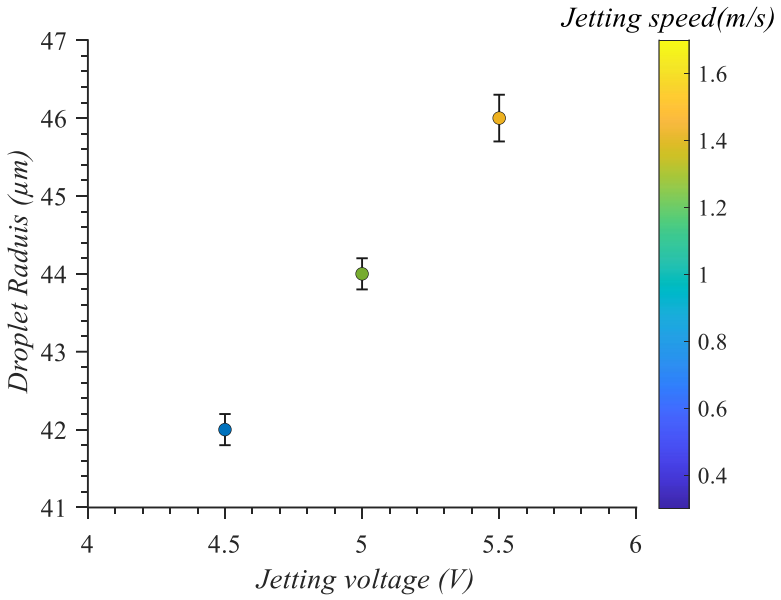


***Figure 4.9**- Droplet's radius and speed variation as a function of jetting voltage for Ag at 1020 °C. The error bars represent the maximum and minimum values.*

Comparing the results to the literature review shows that the droplet formation sequences and behaviour in piezoelectric actuators and MHD have similar trends. In both techniques, if push-pull pulses are used, the time at which the stream is pinched at the nozzle depends on the waveform duration and not the amplitude of the jetting. This can also influence the droplet size, as the longer pulse duration increases the volume of material ejected from the nozzle before the breakup. Furthermore, it was observed that in piezoelectric [100], [101], [235], [236], and the MHD actuator used in this thesis, the droplet size was also influenced by the jetting voltage. Similarly, the droplet speed increases as a function of jetting voltage for both actuation methods [94], [235].

According to this study, we define seven categories for droplet ejection:

1. Stable and satellite-free droplet formation.
2. No ejection: when the force is not sufficient to create an adequate motion in the molten material and eject a droplet.
3. Hide and seek mode: a meniscus bulges out of the nozzle, but the momentum is insufficient to overcome the surface tension at the orifice, and the material is retracted back.
4. Satellite formation (mode I): when the droplet and one satellite droplet are formed during the pinch-off, but the satellite is retracted to the nozzle (**Figure 4.3** a).
5. Satellite formation (mode II): when the droplet and one satellite droplet are formed, but the satellite is merged with the main droplet (**Figure 4.3** b).
6. Satellite formation (mode III): the droplet and one satellite droplet are formed, but the satellite is not retracted to the nozzle, nor can it catch the main droplet (**Figure 4.3** c).
7. Spraying: when only satellite droplets are sprayed from the nozzle in various directions.

4.4. Summary

The formation of uniform and consistent droplets is the primary challenge to address in the DoD processes. Although this topic has been widely studied for aqueous fluids used in inkjet printers, only a few works are available in the literature investigating the droplet formation of metallic droplets. To the best of the author's knowledge, the generation of metallic microdroplets through MHD actuator devices is missing in the literature. To fill the gap in the knowledge, this chapter provided insight into the mechanism of microdroplet formation for a high-temperature metallic material (Ag). Furthermore, the effects of the jetting voltage and frequency on the ejection mechanism and the characteristics of droplets in flight were investigated. The main finding of this research can be summarized in the following points:

- The characteristics of droplets obtained from stroboscopic photography demonstrated high reproducibility of droplet formation in the MetalJet system.

Droplets were uniform in shape and size, and their trajectories were perpendicular to the nozzle.

- Satellite-free droplets were formed when the optimal jetting voltage was used, and deviation from the optimal value caused the formation of satellite droplets. The satellite droplets resulted from one or several breakups in the free ligament, forming multiple smaller and slower droplets than the main droplet.
- The breakup length and, consequently, the droplet size increased as the jetting voltage increased. In contrast, the breakup time was independent of the jetting voltage and is expected to be controlled by waveform properties such as dwell time.
- The jetting and droplet speeds increased as the jetting voltage increased.
- Comparing the results obtained in this chapter with the literature about inkjet printing droplet formation using piezoelectric actuators, it was observed that jetting voltage effects on droplet characteristics are similar. In other words, the droplet size and velocity increase with the jetting voltage in both techniques.

5. Droplet Dynamics and Solidification in The MetalJet Process: Copper, Tin, and Silver

Due to the droplet-by-droplet nature of fabrication in MetalJet, a comprehensive understanding of the individual droplets' behaviour on deposition, including the morphology, is one of the second steps to be addressed. Droplets' morphology results from the simultaneous spreading and solidification of molten droplets as they impact on the substrate. Despite extensive research on droplet spreading in isothermal conditions [109], metallic droplets' spreading and solidification mechanisms at medium and high temperatures, particularly at a micro-scale, are still exclusive. This chapter investigates the spreading and solidification of single Sn, Ag, and Cu droplets using an integrated computational, analytical, and experimental approach, as demonstrated in **Figure 5.1**. This brings insight into the influencing parameters that define the droplets' morphology and provides the required elements to control them in the context of DoD-MJ. The morphology of individual droplets on deposition is a key element since it defines the inter-droplet space required during the printing

process. Moreover, it influences the resolution and the surface roughness of the final printed object, hence should be thoroughly investigated.

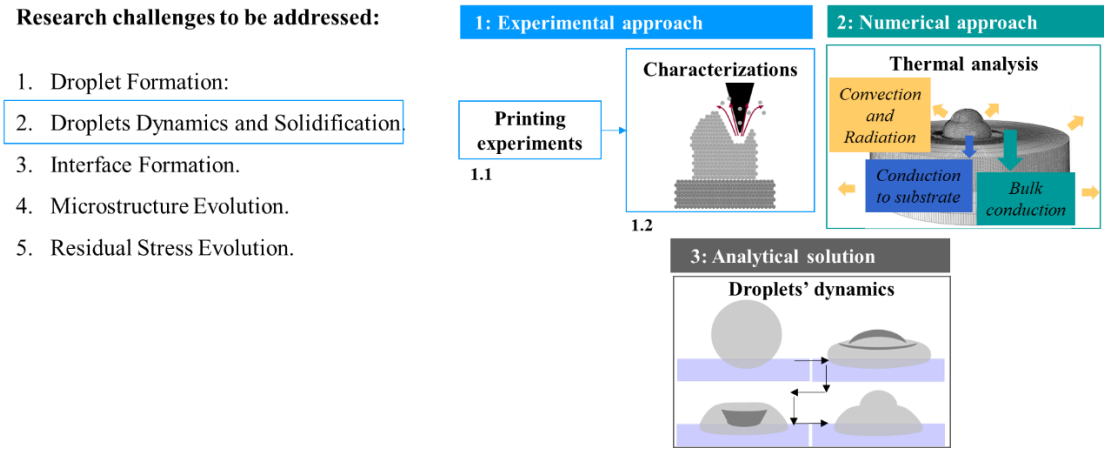


Figure 5.1- *The second challenge in DoD-MJ and the methodology implied in this thesis to address it, referring to Figure 52.*

5.1. Model verification

In order to provide verification of the numerical model used in this work, in particular, the proposed relation for the thermal resistance coefficient and effective thermal conductivity multiplier, pure Sn (grade 5N) droplets with various droplet/substrate temperatures were deposited on Sn substrates. Sn was chosen for these validation studies since its low melting point provides the condition of substrate melting, which could be used to validate the proposed model.

A FIB secondary ion image of a cross-sectioned Sn droplet deposited at 655°C onto an Sn substrate at 50°C is shown in **Figure *5.2* a.** The droplet-substrate interface, indicated by the black arrows, is partially visible, implying that the substrate did not melt during droplet deposition in this zone. The droplet-substrate interface is partially visible, the white line indicated by the black arrows, indicating that the substrate did not melt during droplet deposition in this zone. In this case, ~ 14 µm of the contact line is melted, and ~ 25 µm is not melted. As per **Figure *5.2* b**, the length of the melted interface has increased for the Sn droplet deposited at 755°C onto an Sn substrate at 50°C. In this case, the droplet melted the contact surface up to a radius of ~ 26 µm and

only ~ 9 µm remained un-melted. As the deposition temperature was increased to 955°C (**Figure *5.2* c)**, the entire Sn substrate interface was melted. Alternatively, the interface of an Sn droplet at 655°C deposited onto an Sn substrate at 100 °C was investigated. In **Figure *5.2* d**, the interface is partially visible, implying partial substrate melting. Here, the molten droplet melted the contact surface up to a radius of ~ 28 µm from the droplet centre, but an annulus of ~ 18 µm remained un-melted. In the un-melted zone, the grains within the droplet nucleated at the interface with the substrate. Whereas in the melted section, common grains formed from the inner zone of the substrate.

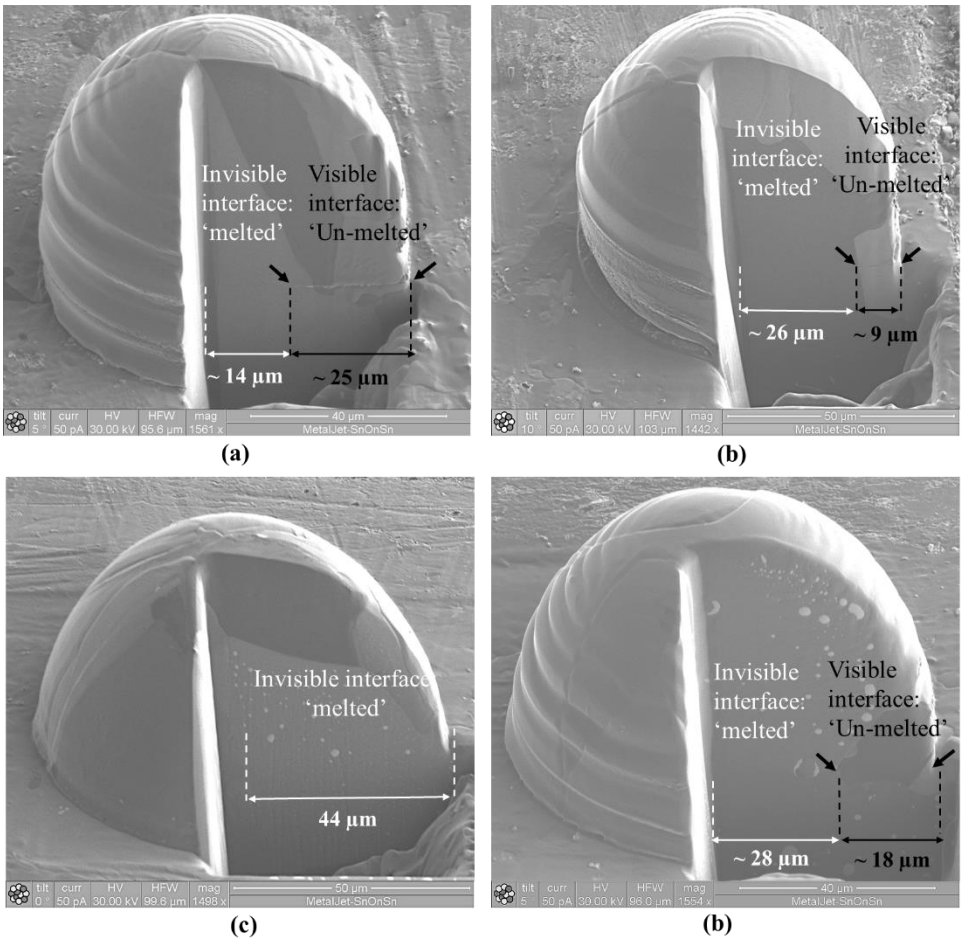


Figure 5.2- FIB-SEM cross-section of individual Sn droplets deposited on an Sn substrate **a)** $T_{drop} = 655\ °C$ and $T_{substrate} = 50\ °C$ indicating partial remelting of the substrate interface, and **b** $T_{drop} = 755\ °C$ and $T_{substrate} = 50\ °C$ indicating partial remelting of the substrate interface, **c)** $T_{drop} = 955\ °C$ and $T_{substrate} = 50\ °C$ indicating complete remelting of the substrate interface, and **d)** $T_{drop} = 655\ °C$ and $T_{substrate} = 100\ °C$ indicating partial remelting of the substrate interface.

The four scenarios shown in **Figure *5.2*** were simulated using the thermal FE model. In **Figure 5.3 a-d**, three locations on the surface of the substrate were chosen, two of which correspond to the warmest and coldest nodes. These nodes are below the droplet's centre and edge, respectively. The third node is where the substrate temperature reaches the melting point of Sn. From this location toward the droplet's edge, the substrate temperature remains below the melting point of Sn. As illustrated in **Figure 5.3 a** when $T_{droplet} = 655\,°C$ and $T_{substrate} = 50\,°C$, the interface temperature remains below the melting point of Sn up to a periphery of 25 μm from the droplet's edge during the droplet cooling and solidification. The un-melted interface is 12 μm and 3 μm from the droplet's edge as the droplets temperature increase to 755 °C (**Figure 5.3 b)** and 955 °C (**Figure 5.3 c)**, respectively, with the substrate at 50 °C. **Figure 5.3 d** demonstrates the interface temperature evolution when $T_{droplet} = 655\,°C$ $T_{substrate} = 100\,°C$. It is seen that the interface below the droplet centre exceeds the melting temperature of Sn, the same behaviour is observed up to a periphery of 28 μm from the centre."

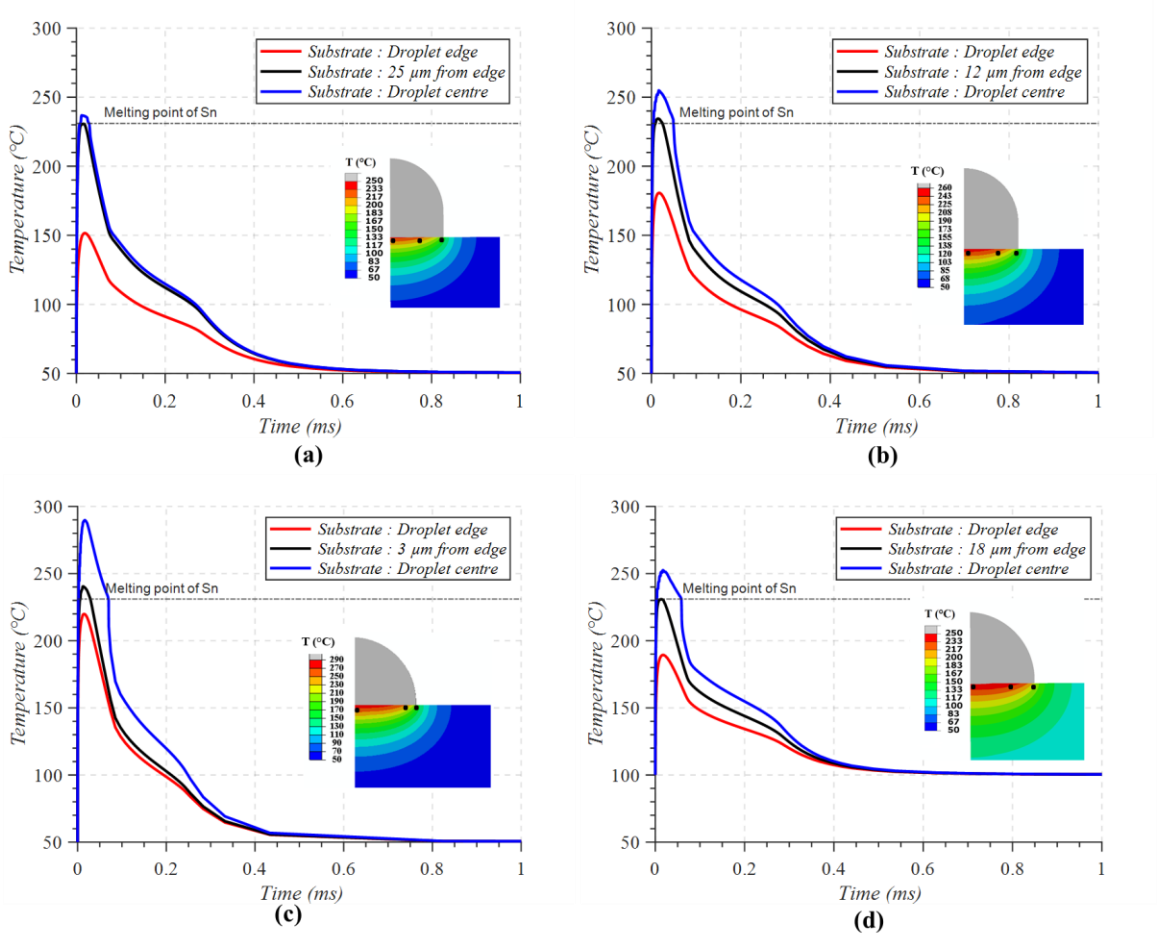


Figure 5.3- *Sn substrate temperature evolution at the interface of an Sn droplet when:* ***a)*** $T_{drop} = 655\ °C$ *and* $T_{substrate} = 50\ °C$ *for nodes below the droplet centre, 25 µm from the droplet edge, and the droplet edge,* ***b)*** $T_{drop} = 755\ °C$ *and* $T_{substrate} = 50\ °C$ *for nodes below the droplet centre, 12 µm from the droplet edge, and the droplet edge,* ***c)*** $T_{drop} = 955\ °C$ *and* $T_{substrate} = 50\ °C$ *for nodes below the droplet centre, 3 µm from the droplet edge, and the droplet edge, and* ***d)*** $T_{drop} = 655\ °C$ *and* $T_{substrate} = 100\ °C$ *for nodes below the droplet centre, 18 µm from the droplet edge, and the droplet edge.*

5.2. Morphology of individual copper droplets

DoD-MJ is a very interesting technology in the electronic industry because of the flexibility and versatility it offers in fabricating micro-electronic components. The primary materials to be printed using this technology should possess the electrical and thermal properties required in this industry. Surpassed only by Ag, Cu has the highest electrical conductivity among metals, and it is a highly ductile material. Cu is

relatively inexpensive when compared to its metallic competitors, such as Ag and Au, and it has excellent thermal conductivity. It is also relatively resistant to oxidation at room temperature. These properties make Cu an interesting metal in the DoD-MJ process. However, despite a great interest in the direct printing of Cu, it has been scarcely investigated in the state of art due to the challenges related to its high melting temperature (1085°C) and challenges related to its printability due to its high surface tension and viscosity [237]. Moreover, slag formation due to the possible reaction of Cu with oxygen or the metal used in the cartridge can block the nozzle. The main objective of this section is to better understand the MHD metal deposition of Cu, further explain the experimental observations, and investigate the morphology of droplets. This is achieved through an integrated experimental and computational approach. For this purpose, single Cu droplets at 1120 °C were ejected onto a Cu substrate kept at 500 °C using MetalJet and were characterised. The motivation for this set of parameters was jetting stability at this specific temperature, and the maximum reachable substrate temperature was 500 °C when these experiments were performed. It was noted that at lower substrate temperatures, the adhesion to the substrate was limited, such that characterisation was not feasible. The ejected droplets in this study were uniform and had an average diameter of ~80 μm. In parallel, a computational model was established to predict the thermal evolution of the droplets and substrate. The intensive computational effort to simulate the spreading dynamics of the droplet was avoided by utilising the experimentally observed droplet morphology and implementing this into a 3D FE thermo-mechanical model. However, the convective effects in the liquid droplet were still considered by applying a modified thermal conductivity for the liquid metal. The thermal resistance between the droplet and substrate, and temperature-dependent material properties were also considered. It is considered that this combined experimental and 3D thermo-mechanical modelling approach provides a sufficiently accurate and computationally efficient method of investigating the MetalJet process to achieve the aims of the study.

5.2.1. Droplet's spreading and solidification

As the Cu droplets make contact with the substrate, they spread and solidify, forming ripples on the droplet's periphery, as can be seen in the FIB-SEM images in **Figure 5.4**. Ripples have also been reported in previous works [13], [133], however, in this study, the striations are more widespread. It is likely that the droplets solidified practically instantly at the moment of impact in the bottom portion (yellow dashed double arrow) such that the solidification rate was greater than the spreading rate, leaving no ridges. Whilst in the top portion (yellow double arrow), where solidification was slower, the droplet oscillated, spread and recoiled. If solidification occurs during this oscillation, the observed ripples are frozen into the droplet's surface. The results from the computational thermal analysis of a single droplet cooling on a substrate are used to support this argument.

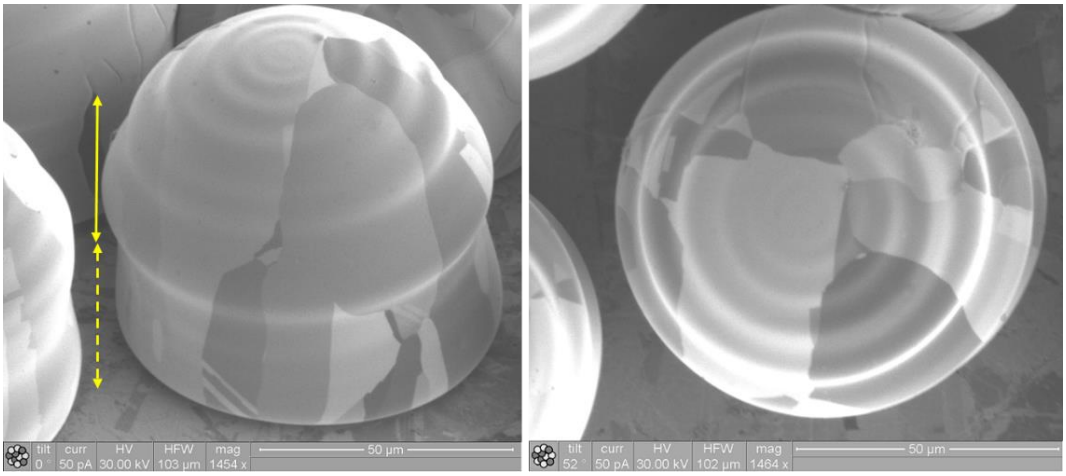


***Figure 5.4**- Morphology of single Cu droplet deposited on a Cu substrate, forming ripples on their periphery during the solidification: **a)** side view, **b)** top view.*

The ejected droplets cooled in-flight and were deposited at 1090 °C on the substrate. According to the thermal profile of a single Cu droplet at 1090 °C deposited onto a 500 °C Cu substrate in **Figure *5.5*-a:c**, solidification initiates at the interface, where the droplet is in direct contact with the cooler substrate. Indeed, conduction with the substrate, which acts as a heat sink, is the dominant mode of cooling. The solidification

front moves upwards through the droplet, and in less than 50 µs after the impact, the entire droplet solidifies. After 1 ms, the droplet reaches steady-state, i.e., the droplet temperature is uniform and equal to the substrate temperature. This is faster than the time interval before the deposition of the second droplet using a jetting frequency of 500 Hz, which is equal to 2 milliseconds. Comparing the experimental results versus the computational results, the ridges observed in **Figure 5.4** follow the solidification planes predicted by the numerical simulation (**Figure 5.5**). As per the droplet temperature evolution in **Figure 5.5 d**, the material freezes practically instantly at the interface when it contacts the cooler substrate, whilst remaining liquid in the top section.

Solidification in the uppermost sections is slower for two reasons: (1) cooling through convection and radiation is negligible compared with cooling through conduction with the substrate and (2) the release of latent heat during solidification. Towards the bottom of the droplet, the latent heat energy is invested in heating the substrate and has a minor influence on the droplet's cooling speed. Contrarily, in the top section of the droplet, cooling is slowed by the release of the latent heat of solidification. Indeed, the computational modelling proves that the presence of more ridges at the top sections of the droplet is due to the differential solidification rates.

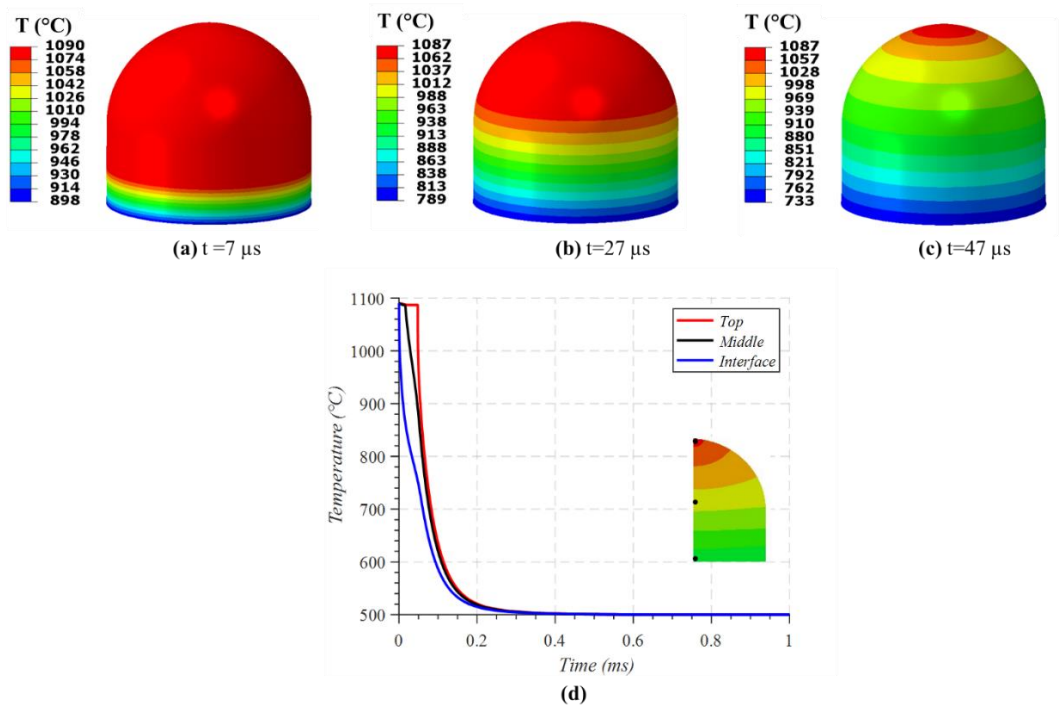


Figure 5.5*- 3D profile temperature whilst single droplet cooling, taken at a real-time of a) t=7 µs, b) t=27 µs, c) t=47 µs, d) temperature evolution of nodes in the top, middle, and interface of the droplet.*

It is proposed that the various observations in the literature regarding droplet ripples can be attributed to the use of different droplet and substrate materials, droplet size, and droplet initial temperatures. All of these factors will affect the rate of solidification and/or frequency of oscillation of a droplet, which in turn affects whether, and where the oscillatory movement of the droplet will be 'frozen in'. For example, in [17] and [30], the wavelength of stirations on the surface of droplets decreased bottom up, such that there were no ridges on the top section of droplets. Three factors contribute to the contradictory observation regarding the pattern of these ridges in the mentioned literature and this study. Firstly, these findings were reported for Al and Al-alloy droplets printed onto a Ni substrate. The Cu substrate and Cu droplets used in this study have a higher thermal conductivity than the Ni substrate and Al droplets, inducing a faster solidification, in particular close to the interface.

Secondly, the size of the droplets in those studies was 1.5 mm in diameter. The smaller droplets in this study dissipate their thermal energy into the substrate at a higher rate.

Thirdly, in our research, droplets were deposited just above their melting point, whereas in previous studies, the liquid metal was superheated to 100 °C or 200 °C above the melting point. These three facts result in a slower cooling rate in those studies, which in turn leads to simultaneous progress of solidification front into the oscillating liquid, hence the formation of ripples in the bottom sections. In the top section, with the slower rise of the solidification front, the viscosity damped oscillations and left no striation trace behind. In our study, the solidification time was faster than one oscillation interval in the bottom section where no ripple was formed. Striations were formed only in the top section, where solidification is relatively slower, based on the explained mechanism.

5.2.2. Effects of surface roughness on droplet's morphology

The effects of surface roughness on the deposition characteristics of the droplet have been studied in the literature due to its importance in many biological and industrial processes. The objective of these studies, which were mainly focused on the isothermal conditions, was to evaluate the final morphology of droplets deposited onto structured surfaces [238]–[240]. These studies have shown that surface heterogeneities govern the dynamic behaviour of the droplet and lead to contact angle hysteresis. In this section, effect of surface roughness on the droplet's morphology in a non-isothermal condition, i.e., simultaneous spreading and solidification, is studied. For this purpose, Cu droplets at 1120 °C were ejected onto Cu substrates at 775 °C, which were polished using SiC papers with grit sizes 2500 and 4000. The surface roughness was measured with an optical 3D measurement system, Alicona InfiniteFocusG4, and the average height deviations from the mean value, i.e., R_a, were equal to 0.01 µm and 0.1 µm.

The first information obtained from **Figure 5.6** is the influence of the roughness on the spreading of the contact line at higher surface roughness. The surface irregular heterogeneities acted as pinning sites and produced asymmetric local deformation, leading to an irregular final morphology compared to the droplet deposited at lower surface roughness. It is very likely that the rugged features on the surface act as micro-capillary bridges, preventing the contact line from de-pining and receding from the

roughness features. These results are accentuated due to the high surface tension of Cu, for which makes the recoiling of the molten material more complicated. The interface of Cu droplets printed on a Cu substrate solidified almost instantly (< 10 µs) due to the high thermal conductivity of Cu. As a results, the droplet printed on a rougher surface froze in-place before receding from the irregularities in the surfaces.

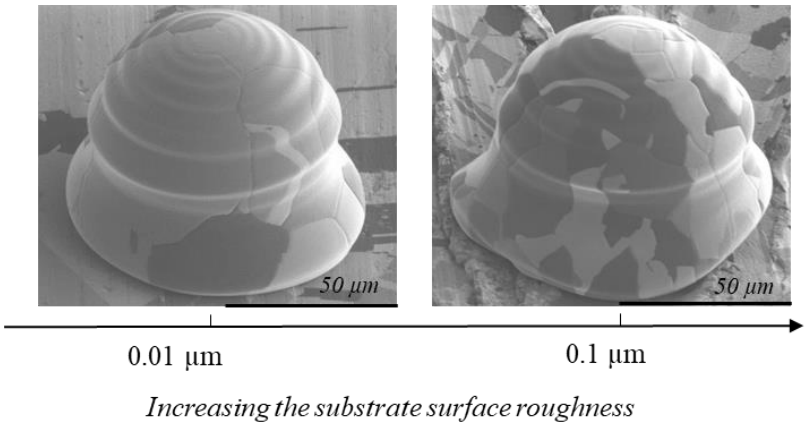


Figure 5.6- *Effect of surface roughness on Cu droplet morphology.*

Besides the irregularities in the morphology of individual droplets, the higher surface heterogeneities create an issue regarding the repeatability of droplet morphologies, as shown in **Figure 5.7**. The irregular droplet shapes may eventually cause pores and gaps between droplets since the inter-droplet distances cannot be kept constant during printing. Moreover, the liquid metal cannot enter the irregular solidification ripples and fill the pores. Both of which decrease the density and properties of printed parts. Due to the undesired effects caused by rougher surface roughness, this parameter was kept constant throughout the thesis, and the substrates were etched or polished with fine SiC papers of grit sizes 4000.

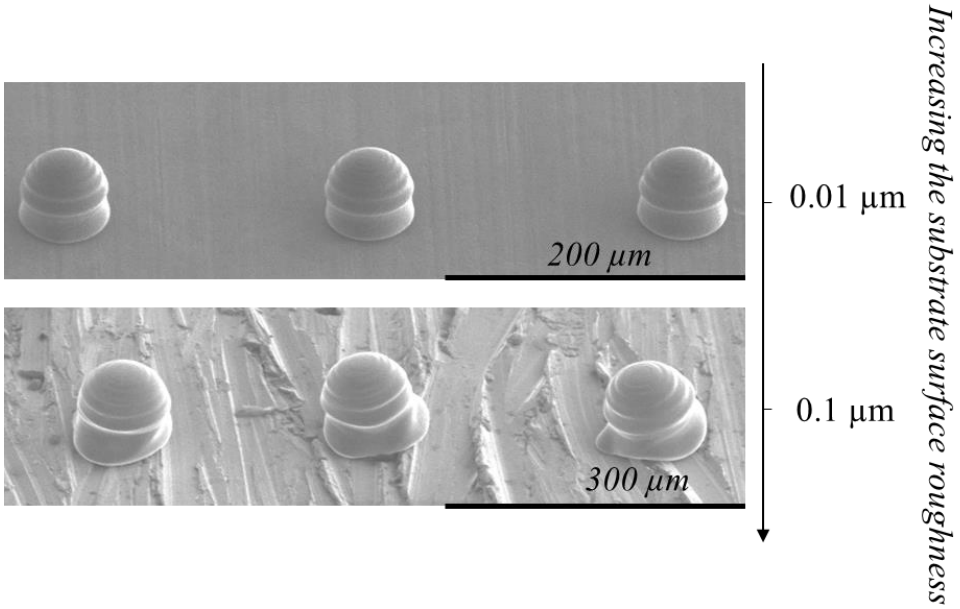


Figure 5.7*- Effect of surface roughness on the repeatability of droplet morphology.*

5.3. Morphology of individual tin droplets

Sn, with a melting temperature of 232 °C, is an interesting metallic element for DoD-MJ investigations since it provides a wide range of jetting temperatures. The lower melting temperature of Sn compared to Cu solves the previously mentioned issues associated with the slag formation at the nozzle level due to the reaction of molten material with the coating inside the cartridge. Moreover, the solidification period of Sn droplets can be extended by maintaining the substrate temperature at temperatures close to its melting point. In addition, Sn has a good printability thanks to its relatively lower surface tension. It also has a good compatibility with many metals, providing a wide range of substrate materials. Consequently, Sn was chosen in this section to provide insight into the spreading and solidification during printing metallic microdroplets using DoD-MJ. This brings the necessary elements to optimise the jetting and deposition parameters involved in producing consolidated 3D prints. For this purpose, single Sn microdroplets at low We numbers with various temperatures were deposited onto substrates of various temperatures and materials using the

bespoke MetalJet platform. The deposits were characterised to correlate their quality to the printing parameters. In parallel, a FE model was used to predict the temperature evolution of the droplets and substrate during solidification and cooling. These simulations allowed the investigation of features of the process beyond the resolution available to experimental analysis. Finally, the time scales of the droplets' oscillation and damping were calculated using analytical methods to provide information on the dynamics of droplet spreading.

The four principal phases during the impact and spreading of a metallic microdroplet onto a substrate are schematically presented in **Figure 5.8**. At the early stage of impact, i.e., the kinematic phase, the contact diameter increases with time, regardless of the wettability between the droplet and the substrate. In the context of metallic microdroplets at a low We number, this stage has a short duration of only several microseconds (less than 10 μs). In the spreading stage, which usually lasts a tenth of a microsecond, the contact line is pushed outward radially, and a rim lamella is formed on the periphery of the contact line (**Figure 5.8 b**). Once the contact line is reached its maximum extent, the surface forces act against the further spreading of the droplet, and the contact line starts to recede. Here, the dynamic contact angle (θ_d) is smaller than the equilibrium contact angle (θ_e). It has been shown numerically and experimentally that, as in the kinematic phase, wettability does not play a role in the spreading phase [112], [116]. In the first two stages, the liquid motion is dominated by inertia forces. The contact line of the retracted droplet ($\theta_d > \theta_e$) advances during the relaxation phase, and the dynamic contact angle decreases. During this phase, which usually lasts longer than the previous ones, wettability becomes an influential parameter, and it will be determined if the droplet will continue to recoil and oscillate or rebound. The liquid motion in the droplet decelerates at the wetting phase until a steady contact diameter is obtained. The contact angle is equal to the equilibrium contact angle in the non-reactive wetting, and the steady contact angle in the reactive wetting.

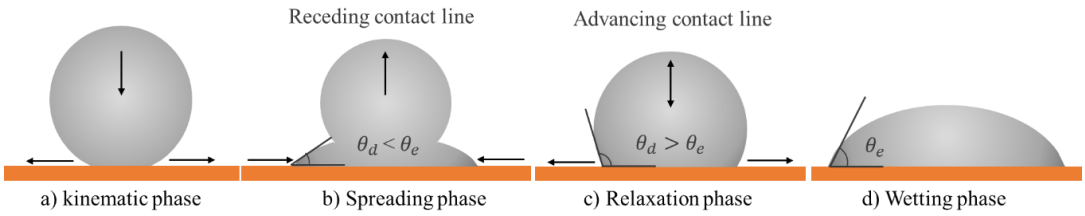


***Figure 5.8**- Schematic representations of droplet impact and spreading timeline, and dynamic contact angle evolution.*

Droplet spreading is controlled by the jetting speed (V), initial diameter (D), density (ρ), dynamic viscosity (μ), surface tension (σ) of the droplet, and the wettability of the substrate, which manifests as the contact angle (θ). These parameters can be organised into dimensionless numbers, of which Weber (We) and Ohnesorge (Oh) are the most important to characterise the spreading dynamics for the low impact speed microdroplet. The We number ($We = \rho V^2 D/\sigma$) determines the driving force for droplet spreading onto the substrate. For We>1, the spreading is mostly impact-driven, while for We<1, it is capillarity-driven, which means the interfacial forces play the deterministic role in driving the spreading process. On the other hand, the Ohnesorge number ($Oh = \frac{\mu}{\sqrt{\rho\sigma D}}$) determines the resistance force. The resistance force is mostly the viscosity for high Oh numbers, while for lower Oh numbers, it is the inertia.

The specific set of parameters used in this section is presented in **Table 5.1**. The minimum ejection temperature used in this study is 670 °C, which is the minimum working temperature in the MetalJet system (detailed in chapter 3). The maximum jetting temperature for Sn was 1000 °C, and jetting at higher temperatures caused slag formation at the nozzle level and deterioration of the jetting stability. The deposition temperature is calculated based on the method explained in section 3.2.1. The room temperature, medium, and high (12 °C below the melting point of Sn) substrate temperatures were chosen to investigate the effects of the substrate temperature. The room temperature substrate provides the conditions for the fastest solidification rate. Whereas keeping the substrate just below the melting point of the Sn permits investigating the droplet's dynamics in the wetting phase. Indeed, the higher substrate temperature results in a slower cooling rate in a droplet due to a limited heat transfer

to the substrate, which is proportional to the temperature gradient between the droplet and the substrate. An intermediate substrate temperature was chosen to provide the minimum sample size for the investigation. Finally, Sn, Zn, and Cu were chosen for substrate materials due to their metallic compatibility with Sn droplets.

***Table 5.1**- Specific set of parameters used to investigate the Sn droplets' final morphology.*

		Ejection temperature	Deposition temperature	Substrate temperature	Substrate material
1. Effects of **droplet** temperature on droplet morphology	1	670 °C	651 °C	130 °C	Cu
		850 °C	822 °C		
		1000 °C	964 °C		
2. Effects of **substrate** temperature on droplet morphology	2	670 °C	647 °C	30 °C	Cu
			651 °C	130 °C	
			654 °C	220 °C	
3. Effects of substrate **material** on droplet morphology	3	670 °C	647 °C	30 °C	Cu
					Sn
					Zn

5.3.1. Effect of superheat temperature

The morphologies of Sn droplets jetted at 670 °C, 850 °C, and 1000 °C onto a Cu substrate at 130 °C (the first row in **Table 5.1**) are shown in **Figure 5.9 a-c**. The mushroom shape of the lower temperature droplets changed to an ovoid shape as the droplet temperature increased. At the same time, horizontal solidification ripples were present on the peripheries of droplets in all cases. The temperature evolution of the droplet during impact and solidification is calculated by the FE thermal model (**Figure 5.9 d)** and is compared against the oscillation and damping periods. In this study, We number is in the range of 0.76 to 0.81, and Oh number is ≅ 0.002. Hence the capillary forces are the main driver for the spreading, and the inertia is the resistance force. For such conditions, the oscillation and damping periods are analytically obtained by **Equations 62** and **63** [120] and the results are demonstrated in **Figure 5.9 e**):

$$t_{osc} = 2.3\sqrt{\rho x^3/\sigma} \qquad \text{(Equation 65)}$$

$$t_{damp} = 0.035\frac{x^2}{\vartheta} \qquad \text{(Equation 66)}$$

Where ϑ is the kinetic viscosity and x is the height of the liquid droplet.

After impact, the superheated droplets freely spread on the substrate based on the mechanism explained in **Figure 5.8**. The local solidification at the interface, which arrests the contact line and impedes further spreading, occurred during the relaxation phases (**Figure 5.8 c**). The pinning of the contact line occurs when the droplet's temperature at the interface (shown with dashed lines in **Figure 5.9 d**) dips below the solidification temperature of Sn.

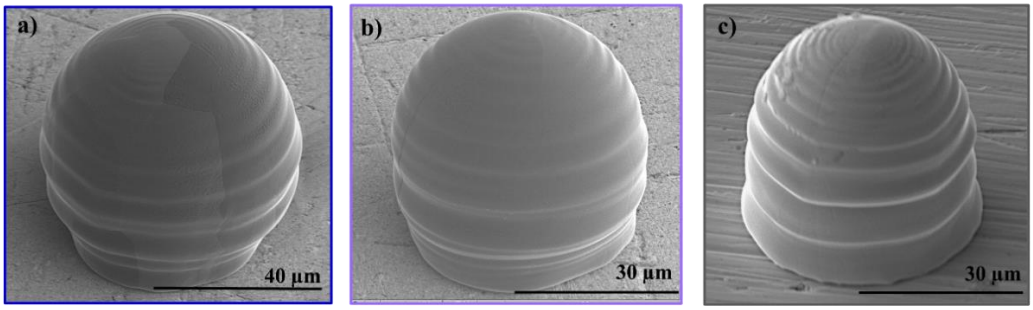


Figure 5.9*- Morphology of individual Sn droplets deposited onto a copper substrate at 130 °C, for droplets ejected at temperatures* ***a)*** *670 °C,* ***b)*** *850 °C,* ***c)*** *1000 °C.*

According to the FE numerical simulations, solidification at the interface occurs after only 33 µs from the droplet's impact onto the substrate for an initial droplet temperature of 670 °C. The time before solidification at the interface increases as the initial droplet temperature increases; at 850 °C and 1000 °C, it occurs at 42 µs and 47 µs, respectively. After that, droplets continue to oscillate until they completely solidify, as indicated by the temperature at the top of the droplet in **Figure 5.9 d**. The time for the droplet to completely solidify is longer than the predicted oscillation period for all cases (**Figure 5.9 e**). This prediction is supported by the experimental evidence of ripples on the droplets, which formed when the oscillations were frozen in place. The appearance of ripples also shows that there was not enough time for the oscillations to be damped by the viscous effects prior to droplet solidification. This is

consistent with the damping period being longer than the solidification time, as predicted in **Figure 5.9 e**.

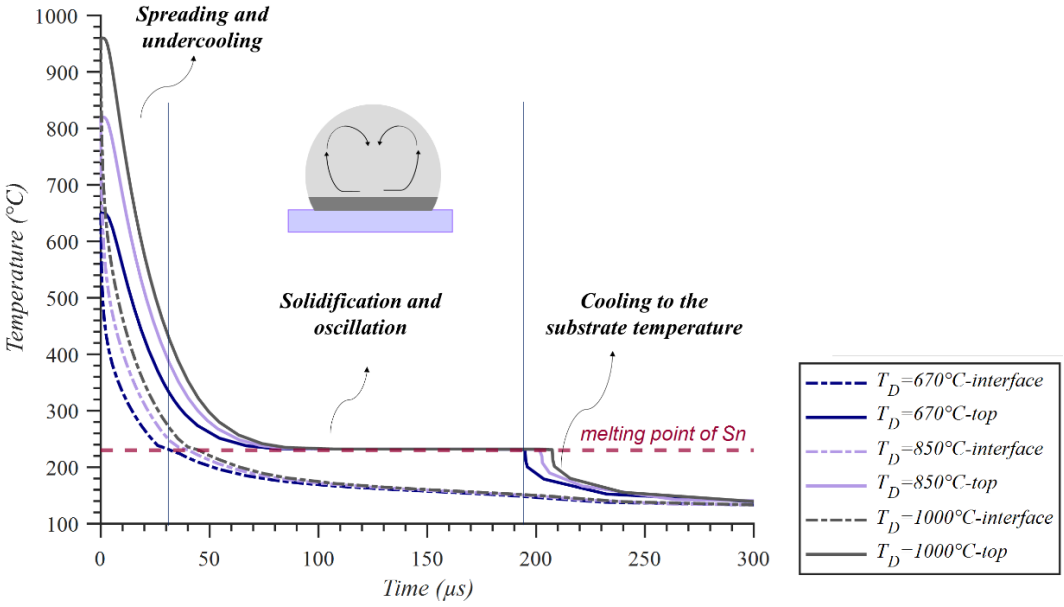


Figure 5.10- *Cooling curves at the central nodes in the interface and top of the droplets when deposited with various superheat temperatures.*

The spacings between the ripples at the top section of the droplets are smaller, which is due to the decreasing time of oscillation (**Figure 5.9 e**) and the slower solidification front motion (**Figure 5.9 d**). The oscillation period decreases since the effective (liquid) radius decrease with time. Based on the numerical simulations, the bottom of the droplet, at the interface with the substrate, cools down at the highest rate, while the top of the droplet is the last part to solidify. The interval between frozen ripples is a product of the speed at which the solidification front moves upwards and the oscillation period of the remaining liquid. Since they decrease toward the top of the droplet, the wavelength between ripples is shorter in the experimental observation.

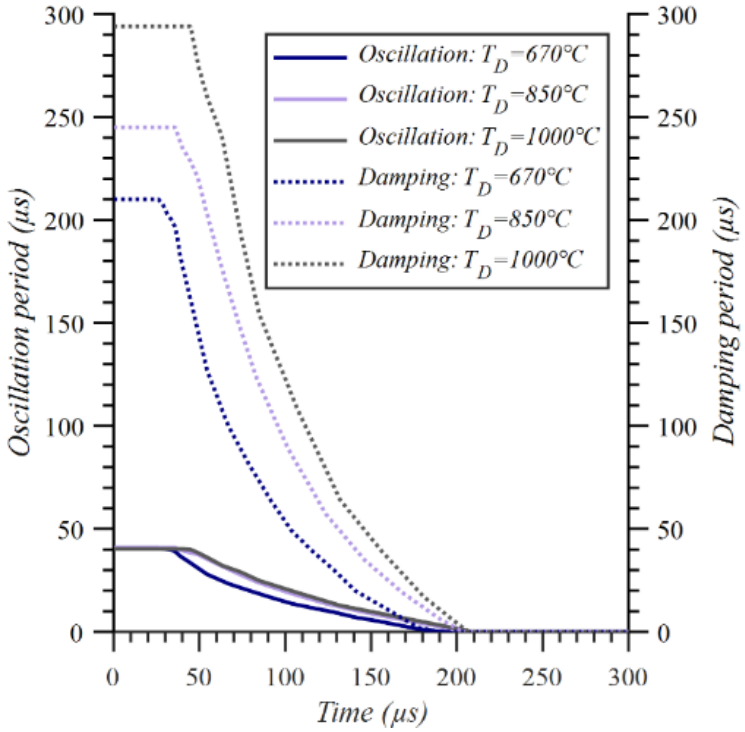


Figure 5.11- *Evolution of oscillation and damping periods for the droplets when deposited with various superheat temperatures.*

Figure 5.12 shows the solidification contact angle for various droplet temperatures, experimentally measured from 15 droplets per condition. This angle corresponds to the dynamic contact angle at which the droplet motion has been frozen by solidification. It was observed that the solidification contact angle decreased as the temperature increased. Depending on the superheat temperature, the solidification likely occurred between the relaxation and wetting phases.

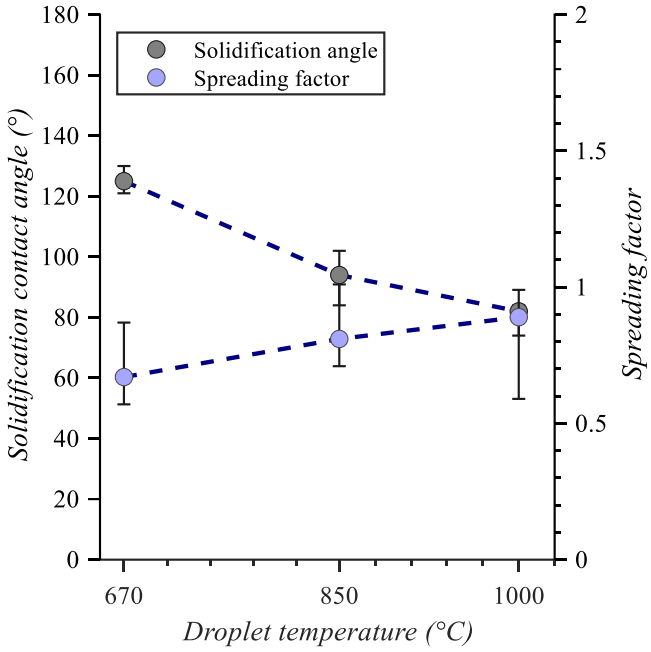


***Figure 5.12**- The spreading factor and solidification contact angle as a function of initial droplet temperature for substrate at 130 °C. The error bars represent the standard deviation.*

For higher droplet temperatures, this process was delayed, which resulted in a smaller solidification angle. In the context of DoD-MJ, a solidification angle of 90° or less is desired, such that no voids or gaps form between adjacent droplets. Another critical parameter in the droplet deposition is the spreading factor (S_{max}), which is the ratio of the maximum diameter (D_{max}) to the initial diameter of the droplet ($S_{max} = D_{max}/D_0$).

The spreading factor is an essential piece of information in droplet-based 3D printing since it defines the required overlap between droplets to build consistent parts. The spreading factor (**Figure 5.12**) increased monotonically with the droplet temperature, which is attributed to two main factors. Firstly, the lower surface tension of Sn at higher temperatures. Secondly, and more importantly, the prolonged local solidification at the interface for higher droplet temperatures. As in the wetting phase, the latter allows the droplet to spread further before the contact line is arrested. This also provided more time for a smaller contact angle.

5.3.2. Effect of initial substrate temperature

The second row in **Table 5.1** presents the three undercooling temperatures ($\Delta T = T_m - T_s$) investigated in this section, where T_m is the melting temperature of the droplet and T_s is the substrate temperature. As demonstrated in **Figure 5.13**, the final shape of a droplet with the same initial deposition temperature (670 °C) varies significantly based on the substrate temperature.

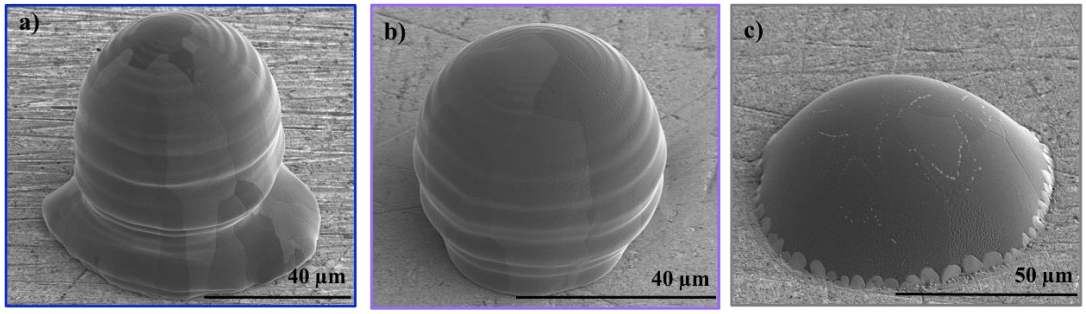


***Figure 5.13**- Morphology of individual molten Sn droplets at 670 °C onto a Cu substrate with an initial temperature of **a)** 30 °C, **b)** 130 °C, and **c)** 220 °C.*

The cooling curves at a central node in the droplet at the interface and droplets top in **Figure 5.14** are presented to explain the variation in the morphology of droplets as a function of substrate temperature. At a low substrate temperature (30 °C), concurrently with the outward spreading of the contact line (stage b in **Figure 5.8**), the molten material in the close vicinity of the substrate froze and formed a "solid crust". In this case, the solidification was very rapid (**Figure 5.13 a),** such that the contact line was pinned before further spreading. The molten material in the upper sections pulled back due to the surface tension. Moreover, oscillations in the upper section during solidification left the familiar ripples on the surface of the droplet. With an increase of substrate temperature to 130 °C (**Figure 5.13 b)**, the local solidification period increased, which provided time for the droplet to reach the relaxation phase (**Figure 5.8 c**) before the contact line was pinned by solidification. Similar to the droplet with the lower substrate temperature, the molten material in the top section oscillated and solidified in a layer-by-layer fashion from the bottom to the top. At the substrate temperature close to the melting point of the droplet, i.e., 220 °C (**Figure 5.13c**), the

local solidification was sufficiently slow (70 µs) to enable the droplet to enter the wetting stage (**Figure 5.8 d**) before the contact line was pinned due to solidification. It is seen that the influence of the initial substrate temperature on the cooling rate of the droplet is more significant than the initial droplet temperature. The time required for the droplet to completely solidify increased significantly with the substrate temperature from 114 µs to 572 µs, i.e., more than four folds for a temperature increase from 30 °C to 220°C.

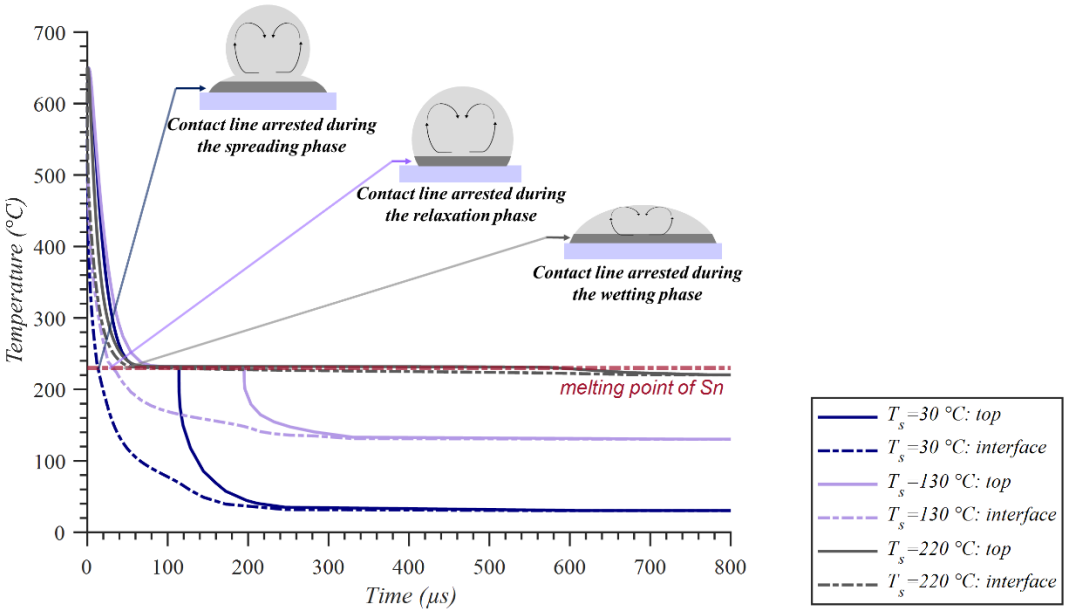


***Figure 5.14**- Cooling curves at the central nodes in the interface and droplet top deposited on the substrate at various temperatures.*

Another important piece of information in **Figure 5.13** is the evolution of ripples' formation on the surface of the droplets at various substrate temperatures. The evolution of oscillation and damping periods with time for the various substrate temperatures are presented in **Figure 5.15**. Even though the solidification speed was lower at higher substrate temperatures (130 °C compared to 30 °C), the ripples on the peripheries were almost alike in **Figure 5.13 a** and **b.** This can be explained by the longer oscillation period for higher substrate temperatures (**Figure 5.15)**, which is indeed a consequence of slower solidification. However, as per **Figure 5.13 c**, the

droplet's surface was completely smooth after the solidification of the molten droplets at the elevated substrate temperature. The main reason for such behaviour is that for the 220 °C substrate, the bulk solidification period was longer than the damping period (**Figure 5.14** and **Figure 5.15)**; such that the viscosity dampened the oscillations before they froze in place.

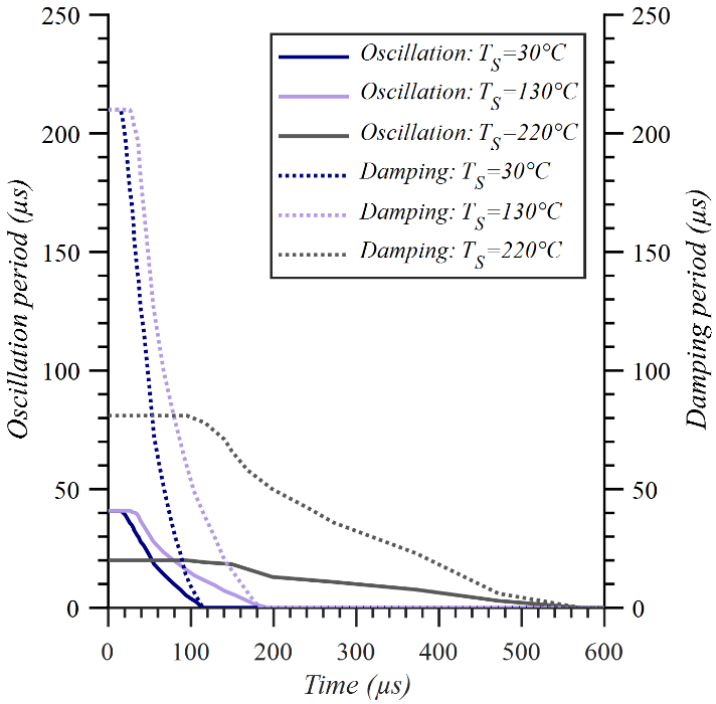


Figure 5.15- *Evolution of oscillation and damping periods for the droplets when deposited with various undercooling temperatures.*

The spreading factor and solidification contact angle as a function of the substrate temperature are shown in **Figure 5.16**. The spreading was halted by local freezing very quickly (14 µs) at low substrate temperatures (30 °C). Consequently, a ring lamella was frozen in place, and a large surface area was pinned to the substrate. This accounts for the apparently anomalous results at the lower temperature in **Figure 5.16**. At the intermediate substrate temperature, the surface area was relatively smaller since the local solidification occurred later, allowing the droplet to recoil after the initial spreading phase. Higher substrate temperatures, close to the melting point of Sn,

delayed the solidification process such that the droplet had enough time to enter the wetting phase, with increased spreading and decreased contact angle compared with the results at the intermediate temperature.

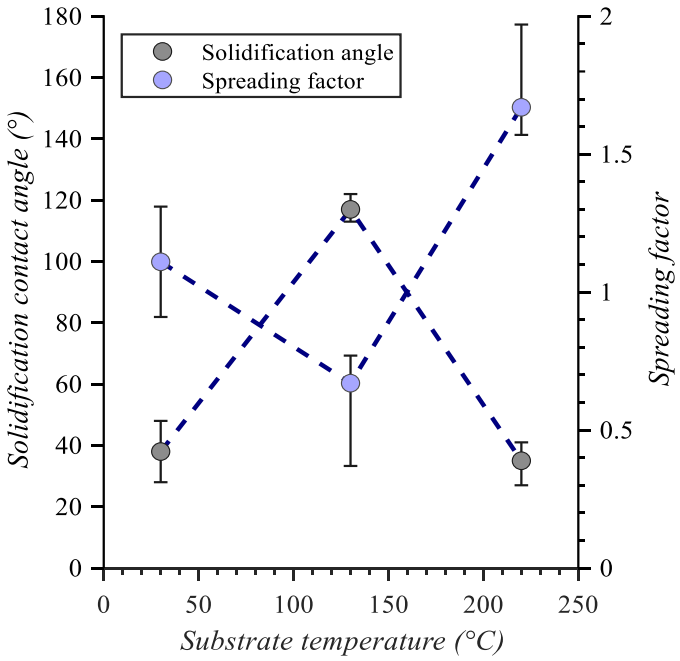


Figure 5.16- *The spreading factor and solidification contact angle as a function of initial substrate temperature for droplets jetting at 670 ℃. The error bars represent the standard deviation.*

5.3.3. Effect of substrate material

The side views of individual Sn droplets deposited with an initial temperature of 670 °C onto Cu, Zn, and Sn substrates at 30 °C (the third row in **Table 5.1**) are presented in **Figure 5.17 a-c**. The influence of the substrate material on the final shape of droplets is more pronounced than that of the substrate or droplet's initial temperatures. As shown in **Figure 5.17 a-b**, the contact line of an Sn droplet on an Sn substrate solidified during the relaxation phase instead of the spreading phase for the Cu substrate, despite their identical droplet and substrate temperatures. Both substrates are wettable by Sn, however, their dissimilar morphologies upon deposition arise from the different thermal properties of the substrates.

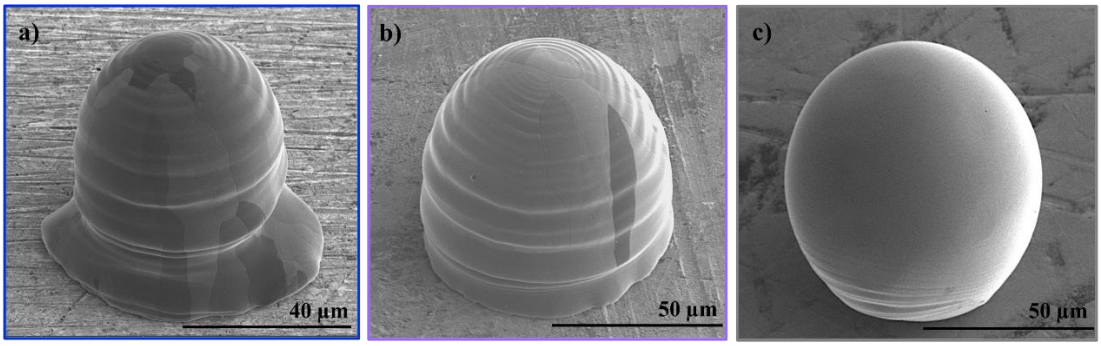


Figure 5.17- *Morphology of individual molten Sn droplets at 670 °C deposited onto* ***a)*** *Cu,* ***b)*** *Sn, and* ***c)*** *Zn substrates at 30°C.*

Figure 5.18 demonstrates the notable influence of the substrate thermal properties on the cooling behaviour of droplets. The thermal conductivity of Cu is almost six times higher than Sn at room temperature. Consequently, the local solidification at the interface of a Cu substrate occurs faster (14 µs) than an Sn substrate (71 µs), leading to an altered contact line arrest and, subsequently, different morphologies. During the experiments, it was observed that most liquid Sn droplets did not adhere to the Zn substrate but were instead bouncing off. The wettability of the substrate by the droplets profoundly influences the deposition behaviour in this regard. If the substrate is not wettable by the droplet, it can lead to a receding break up, which was observed during the deposition of Sn on Zn, **Figure 5.17 c**. Generally, the initial spreading is fast and independent of the substrate's wetting properties. Consequently, it is only during the relaxation phase, where the droplet starts recoiling and oscillating, that de-wetting can potentially occur [20]. It has been proposed that re-bouncing is a violent form of droplet oscillation [28] that happens so fast that droplets bounce off the substrate. Solidification also plays an essential role in a rebound from the substrate. According to the study by Kim et al. [28] regarding the recoil of Sn droplets from a non-wetting surface, the bouncing off phenomenon potentially occurs when the solidification time at the interface is longer than the oscillation period.

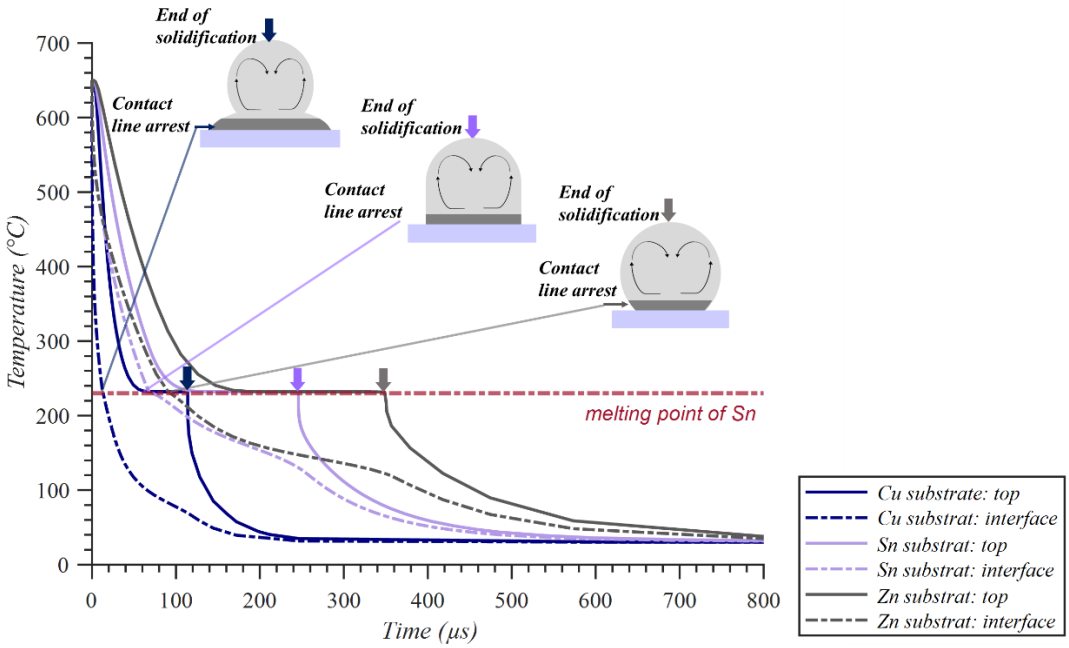


***Figure 5.18**- Cooling curves at the central nodes in the interface and droplet top deposited on various substrates.*

According to **Figure 5.18** and **Figure 5.19**, the contact line arrests 93 μs after the impact on the Zn substrate, while the initial oscillation period is 54 μs, which explains the re-bouncing of droplets in this case. Unlike the cases for the other substrates, when depositing on Zn, the droplet's surface was smooth at the top, since the viscosity was able to dampen the liquid oscillations prior to solidification **Figure 5.18** and **Figure 5.19.** The slow solidification is ascribed to the small droplet-substrate contact area due to the poor wetting and the lower heat conductivity of Zn compared to Cu.

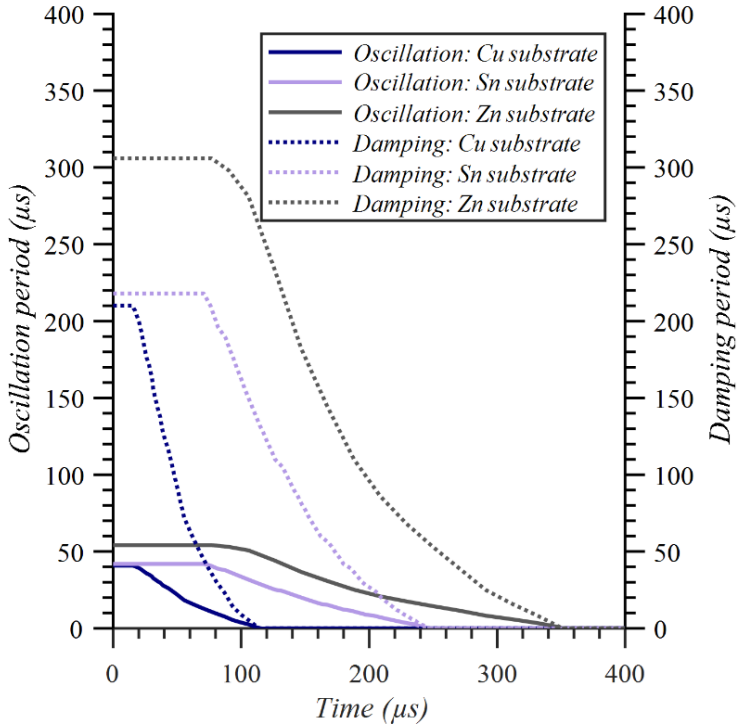


Figure 5.19*- Evolution of oscillation and damping periods for droplets deposited on various substrates.*

The interfacial solidification period for the droplet on the Zn substrate was relatively long, and the droplet likely had enough time to spread fully before it solidified. However, as per **Figure 5.20**, the solidification contact angle was more than 90°, confirming that Zn is not wettable by Sn. The droplet had pinned to the Sn substrate during the wetting phases, also the solidification contact angle was 86° on average, which is greater than the equilibrium contact angle. However, the value being less than 90° proves that the substrate is wettable by the droplet. The spreading factor was lower than the unit value for the Zn substrate since the droplet pulled back due to the poor wettability, while it was more than one for the Sn substrate. The contact angle and spreading factor on the Cu substrate were discussed in 3.2.2.

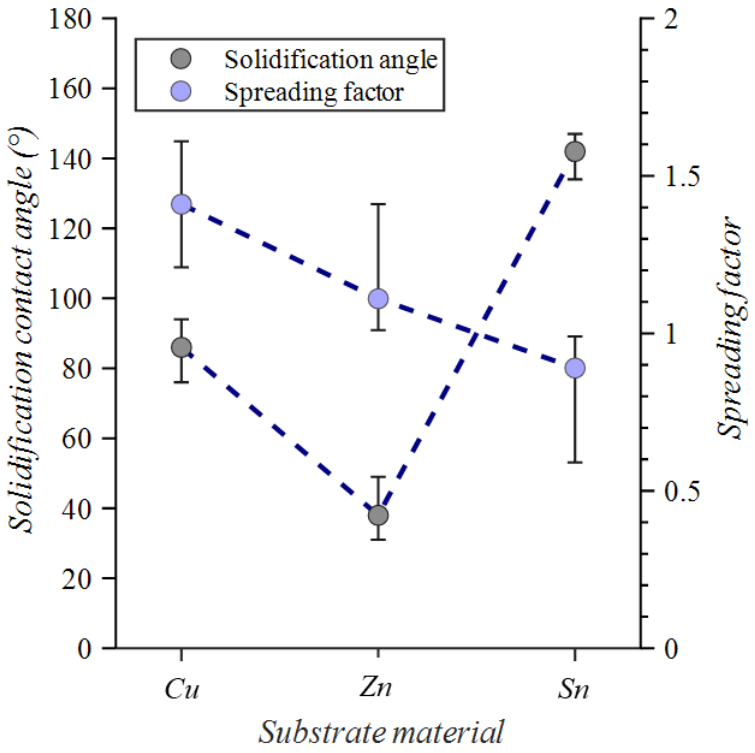


Figure 5.20- *The spreading factor and solidification contact angle as a function of the substrate material for droplets jetted at 670 ℃ onto substrates at 30 ℃. The error bars represent the standard deviation.*

5.4. Morphology of individual silver droplets

Ag is the most conductive metal and has the potential to be used in the electronic industry for radio frequency identification antennas, touch screens, printed circuit boards, and flexible/ wearable electronics. Ag is widely used as the catalyst for many processes [241], [242] and has been proven beneficial in electrochromic and energy storage devices [243]. Moreover, Ag is regarded as one of the most effective alternatives to antibiotics; hence, medical devices such as breathing tubes, catheters, artificial bones, and scaffolds are sometimes coated with Ag to fight against infections [244]. Silver ions penetrate the cell walls of bacteria without injuring mammalian cells, thus destroying the chemical and structural bonds essential for the bacteria's survival and growth. Ag is ductile and lustre, so it is widely used for jewellery and in

micro-electronics devices such as smartphones, which can be bent into narrow spaces without breaking. These reasons make Ag an interesting metal in DoD deposition processes, however, due to its high melting temperature (962 °C) the research in the field has been mainly restricted to nano particle ink jetting technologies to date.

The main issue with the Ag nanoparticles suspensions inks is the lower electrical conductivity compared to the bulk material because of the residual solvent or the presence of pores between the sintered nanoparticles [105], [245]. Moreover, the printed parts usually suffer from an undulating surface morphology, surface defects, internal cracks, and voids [53]. Furthermore, inkjet printing of high-aspect-ratio structures is still challenging. Therefore, printing the Ag nanoparticles is mainly restricted to 2D printing, due to the spreading dynamics of low viscosity inks used in inkjet processes. The pre-processes, such as ink formulation and nanoparticle synthesis [246], as well as postprocessing, such as sintering [247], are inevitable aspects of nanoparticle inkjet printing, which cause extra complications, time, and costs for this technology. Ag does not oxidize in air; however, it reacts with the hydrogen sulphide in the air and creates a silver sulphide layer which is not very conductive. Recent studies have discovered that Ag nanoparticles have toxic effects on various mammalian cell lines, which causes severe doubts about the uptake of the technology in medicine [248].

The most straightforward solution to overcome the mentioned challenges related to the printing of highly conductive Ag structures with high aspect ratio and resolution is the DoD-MJ. However, most metal jetting techniques are limited to low melting temperature metals such as Sn and Al. The current high-temperature metal jetting techniques in the literature are limited to the large droplet size (hundreds of microns) [21], [237], which impede achieving the high resolutions required for electronic applications. Moreover, these techniques are restricted by the low jetting frequencies due to the use of pneumatic actuators. To the best of the author’s knowledge, only one research work has overcome the barriers of printing high-temperature microdroplets [11], where an MHD actuator was used to print Ag droplets of less than 100 micrometres at 500 Hz. Despite the significant progress, the printed Ag structures in

their study suffered from a lack of consolidation between droplets, which is detrimental to the electrical conductivity. Therefore, there is a need to bridge the gap and propose a technical solution that enables printing Ag structures with acceptable properties. In addition, there is also a great interest in studying the interplay between the spreading and solidification of Ag droplets. Despite the extensive research on the droplets dynamics at the isothermal depositions [114], [249] and for low-melting temperature droplets [136], [216], the spreading and solidification mechanisms of metallic droplets at high temperatures, in particular at a micro-scale, is still unclear from the literature.

In this study, the MetalJet platform was used to investigate the feasibility of printing fully consolidated 3D structures in Ag. To this aim, the spreading and solidification of individual Ag droplets ejected at various temperatures onto Ag substrate at various substrate temperatures, presented in **Table 5.2**, are studied through an integrated computational, analytical, and experimental approach. The set of parameters corresponds to the minimum and maximum jetting temperatures for Ag using the MetalJet platform, which are 1040 °C and 1200 °C. At temperatures above 1200 °C, Ag reacts with the coating inside the cartridge and produces vapour, destabilising the jetting process. Additionally, an intermediate temperature of 1120 °C was investigated. The substrate temperatures were kept constant at room temperature, with a maximum substrate temperature (775 °C), and an intermediate temperature (400 °C).

***Table 5.2**- Specific set of parameters used to investigate the Ag droplets' final morphology deposited onto Ag substrates.*

1. Effects of **droplet** temperature

2. Effects of **substrate** temperature

	Ejection temperature	Deposition temperature	Substrate temperature
1	1040 °C	1025 °C	25 °C
	1120 °C	1105 °C	
	1200 °C	1185 °C	
2	1040 °C	1025 °C	400 °C
	1120 °C	1108 °C	
	1200 °C	1188 °C	
3	1040 °C	1030 °C	775 °C
	1120 °C	1110 °C	
	1200 °C	1190 °C	

5.4.1. Droplet's dynamic and solidification

The sequences of droplet spreading since it impacts on the substrate, which is an interplay between the inertia and surface tension forces, is demonstrated schematically in **Figure 5.21**. During the early stages of spreading, mainly driven by the droplet's inertia, the descending bulk of material pushes the fluid near the substrate radially outwards and forms a rim at the contact line **Figure 5.21 a-d**. The rim continuously grows while the droplet's top remains unchanged with a spherical cap shape. As depicted in **Figure 5.21 a-f**, the apex continuously descends until it breaks into the rim and creates a hole inside it. At this stage, the droplet starts recoiling, and the apex region, in the centre of the droplet, turns into a strong jet which rises. The possible de-wetting and bouncing off could occur in this period if the substrate is not wettable by the droplets. The capillarity effects soon force the apex (jet) downwards **Figure 5.21 g-i.**

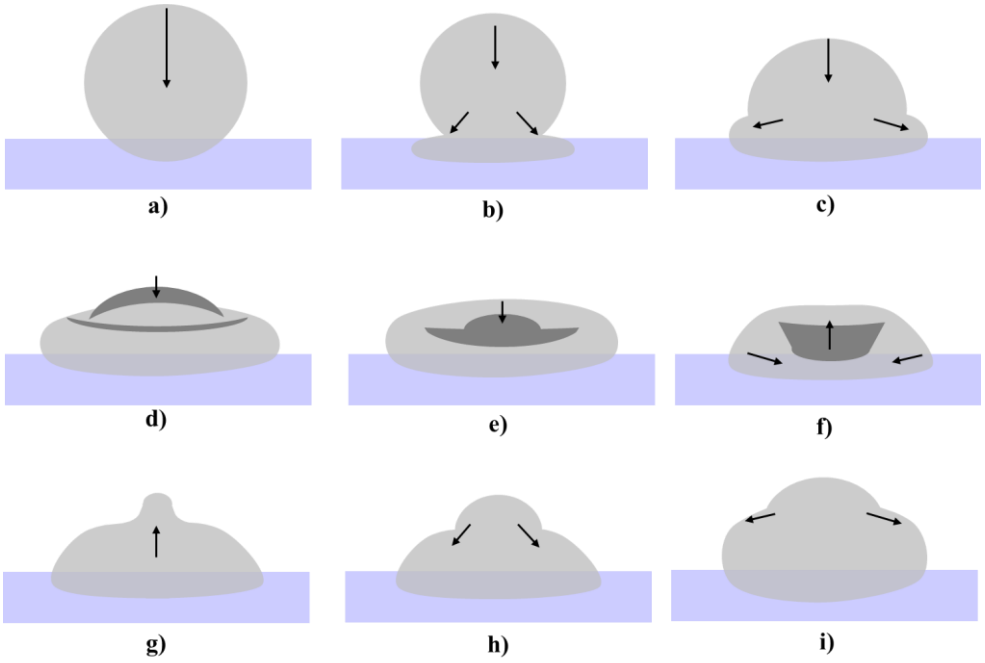


***Figure 5.21**- Schematic representations of impact and spreading evolution of Ag microdroplets.*

The morphology of individual droplets ejected at temperatures of 1200 °C, 1120 °C, and 1040 °C onto the substrate at 775 °C (the first group in **Table 5.2**) is demonstrated in **Figure 5.22** a-c. It is seen that the shape of droplets changes remarkably as a function of the initial droplet temperature. Whereas the droplet at higher temperature has a rounder shape, the droplet at lower temperature has a hat-like morphology. The morphology of the droplets in **Figure 5.22** is a consequence of an interplay between droplet dynamics and solidification.

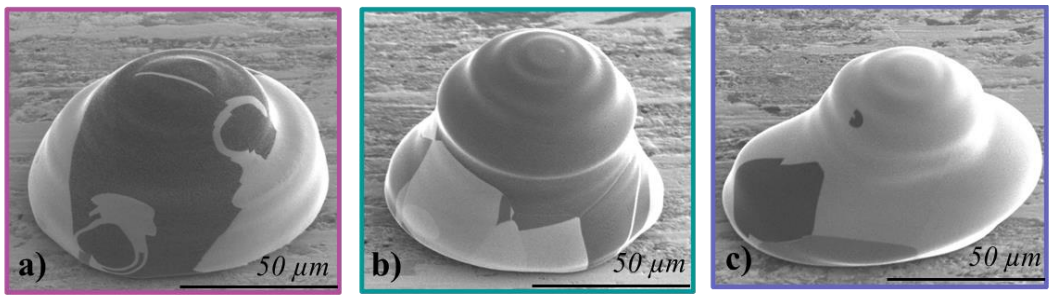


***Figure 5.22**- Morphology of individual Ag droplets for various droplet temperatures a) 1200 °C, b) 1120 °C, c) 1025 °C deposited onto an Ag substrate at 775 °C.*

The gradual solidification height in time, obtained from the numerical simulation, and the estimated ripple distance from the analytical analysis are demonstrated in **Figure 5.23**. It is seen that droplets deposited on the substrate at 775 °C fully solidified in 36.6 µs, 40.4 µs, and 43.7 µs when ejection temperatures were 1040 °C, 1120 °C, and 1200 °C, respectively. These periods correspond to the sequences **h** to **i**, in **Figure 5.21.** Another interesting observation from **Figure 5.22** is the presence of solidification ripples on the surface of these droplets. The solidification ripples result from the droplet's oscillatory motion coinciding with the solidification front moving from the interface to the droplet's top. The solidification rate obtained from the computational simulation and the oscillation period obtained from the theoretical scaling analysis can explain the formation of such ripples. The ripple distance, i.e., the distance between the peak of each of two consecutive waves, is a product of the oscillation period multiplied by the solid front speed.

The solidification ripples on the periphery of droplets deposited at 775 °C and their interval decreased as the solidification front elevated. The graph in **Figure 5.23** correctly predicts the absence of solidification ripples in the bottom section of the droplet at 1040 °C and the formation of these ripples in the top section. The accordance is attributed to the interval distance being higher than the solidified height at the initial stage and the opposite correlation in the top section. The computational and analytical results also match the experimental results for droplets at 1200 °C, where ripples were predicted all over the droplet with a narrower wavelength on the top section. The results, however, indicate a similar trend for the droplet at 1120 °C, while from experimental observation, no ripples were observed on the bottom section, identical to the droplet at 1040 °C. This signifies that the solidification speed may be faster than our computational results.

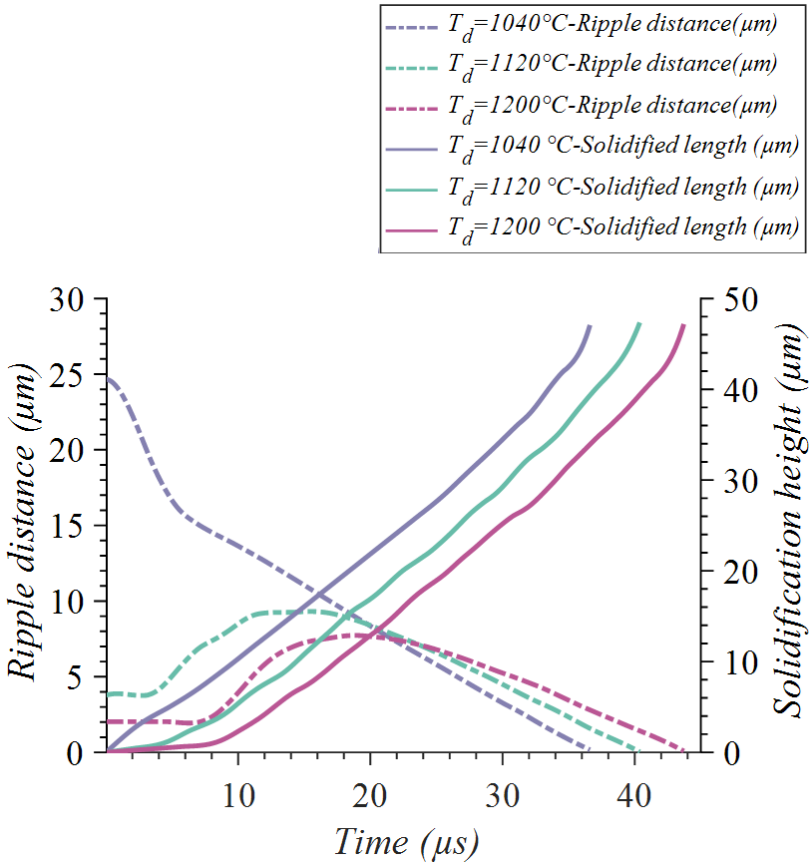


Figure 5.23- *Droplets' solidification timeline based on simulation and analytically predicted ripple distances based on the droplets dynamics for various droplet temperatures deposited onto an Ag substrate at 775 °C.*

Figure 5.24 demonstrates the morphology of droplets ejected at temperatures of 1200 °C, 1120 °C, and 1040 °C onto the substrate at 400 °C (the second group in **Table 5.2**). Droplets with a higher initial temperature have a sharper cap shape compared to the spherical cap at the substrate of 775 °C. On the other hand, droplets ejected at 1040 °C have a toroidal shape.

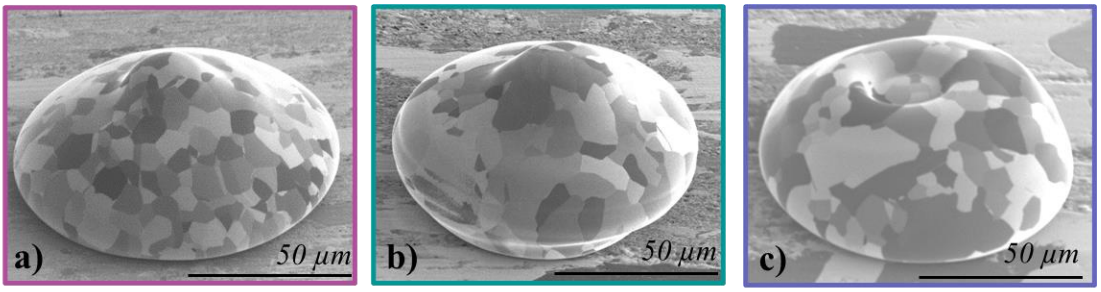


Figure 5.24- *Morphology of individual Ag droplets for various droplet temperatures a) 1200 °C, b) 1120 °C, c) 1025 °C deposited onto an Ag substrate at 400 °C.*

The gradual solidification height in time, obtained from the numerical simulation, and the estimated ripple distance from analytical analysis is demonstrated in **Figure 5.25**. The solidification period for droplets deposited onto the substrate at 400 °C is shorter and is equal to 13.9 μs, 15.1 μs, and 16.4 μs when ejection temperatures are 1040 °C, 1120 °C, and 1200 °C, respectively. These periods correspond to the sequences f to g in **Figure 5.21**, which signifies droplets freeze in place at these frames before they complete the spreading to an equilibrium state. There is no solidification ripple in the periphery of droplets deposited onto the medium substrate temperature in **Figure 5.24**. The expected ripple distance for the tested scenarios obtained for the simulations in **Figure 5.25** is considerably larger than the droplet's solidification height at medium substrate temperatures. Consequently, no ripples can be observed in these cases. In other words, the solidification speed of the droplets on 400 °C substrates are too fast compared to the speed of the ripple formation.

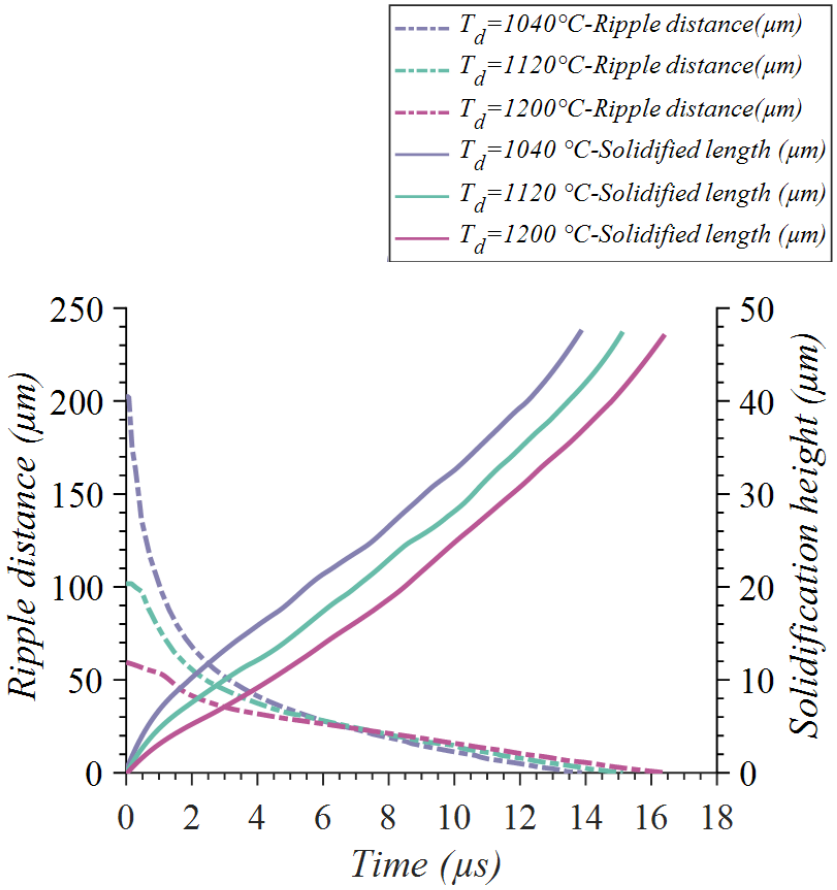


Figure 5.25- *Droplets' solidification timeline based on simulation and analytically predicted ripple distances based on the droplets dynamics for various droplet temperatures deposited onto an Ag substrate at 400 °C.*

Figure 5.26 demonstrates the morphology of droplets ejected at temperatures of 1200 °C, 1120 °C, and 1040 °C onto the substrate at 25 °C (the third group in **Table 5.2**). It is seen that these droplets have a toroidal shape regardless of the ejection temperature. The solidification period for droplets of 1040 °C, 1120 °C, and 1200 °C deposited to a room-temperature substrate is 9.2 µs, 10.1 µs, and 10.9 µs, respectively. It is notable that the solidification period decreases significantly as the substrate temperature decreases, and interestingly, the ejection temperature becomes less influential. The similarity of droplet morphologies at low-temperature substrates stems from the latter. Droplets with various initial temperatures deposited onto the substrate at 25 °C freeze to the substrate at frame f in **Figure 5.21.** Despite the similarities between the

morphology of the droplet ejected at 1040 °C onto a substrate at 400 °C and the droplets deposited onto the room temperature substrate, they are distinguishable by the smaller inner diameter of the toroid in the former. The slower solidification rate in this case provides more time for the apex to rise and to narrow the hole caused by the surface tension forces.

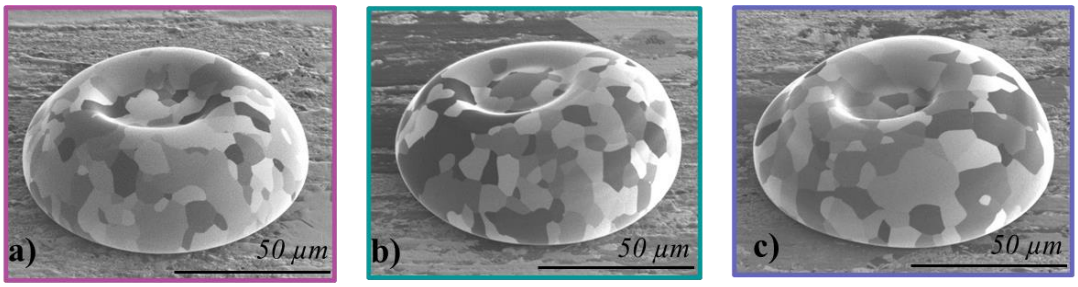


Figure 5.26*- Morphology of individual Ag droplets for various droplet temperatures a) 1200 °C, b) 1120 °C, c) 1025 °C deposited onto an Ag substrate at 25 °C.*

The gradual solidification height in time, obtained from the numerical simulation, and the estimated ripple distance from the analytical analysis are demonstrated in **Figure 5.27**. Similar to the substrate at medium temperature, the expected wavelength of the ripples is considerably larger than the droplet's height at low substrate temperature. Consequently, no ripples can be observed in these cases. As an example, for the droplets with the initial temperature of 1120 °C on the substrate at 25°C, the expected ripple distance in five microseconds after deposition is 33 µm, whereas 24 µm of the droplet's height has already solidified at this time (24 µm liquid). In such a case, the oscillatory motion of the droplet will not be frozen in place due to the droplet's fast solidification rate. In other words, the solidification speed of the droplets on 25 °C and 400 °C substrates is too fast compared to the speed of the ripple formation.

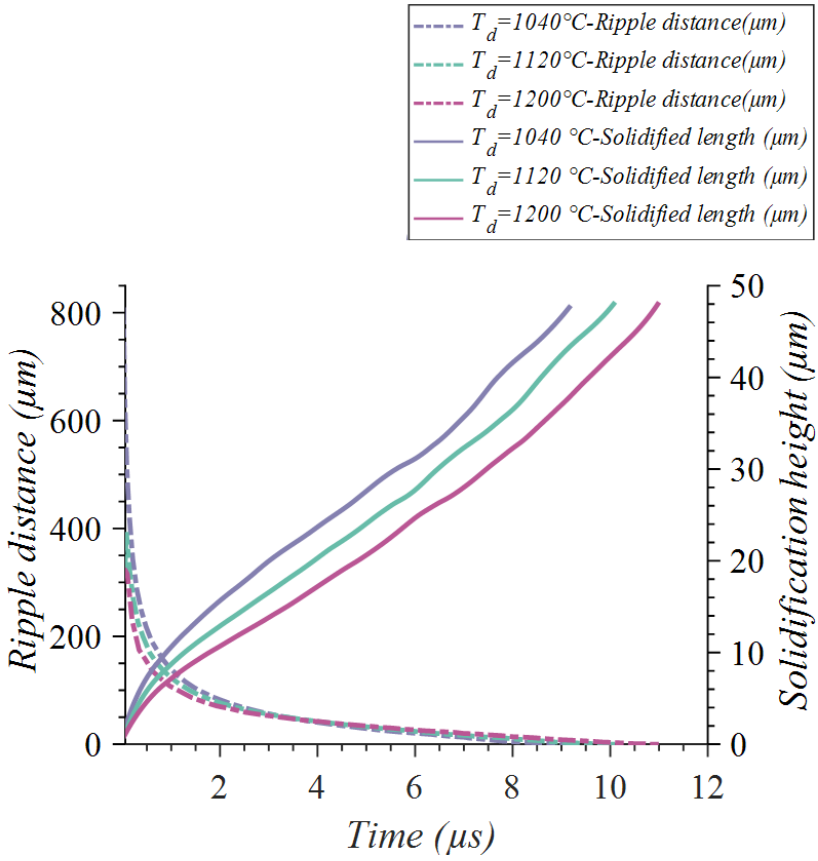


Figure 5.27- *Droplets' solidification timeline based on simulation and analytically predicted ripple distances based on the droplets dynamics for various droplet temperatures deposited onto an Ag substrate at 25 °C.*

The solidification period and spreading sequence during which the contact line was halted are summarized in **Table 5.3** for all the simulated cases.

***Table 5.3**- The solidification period of Ag droplets deposited to Ag substrates at various droplet and substrate temperatures and the spreading sequence during which the contact line was halted.*

Substrate temperature (°C)	Ejection temperature (°C)	Solidification period (µs)	Contact line arrest in spreading sequence
775	1040	36.6	h
	1120	40.4	h
	1200	43.7	i
400	1040	13.9	f
	1120	15.1	g
	1200	16.4	g
25	1040	9.2	f
	1120	10.1	f
	1200	10.9	f

5.5. Summary

In DoD printing processes, 3D parts are fabricated through the deposition of individual droplets onto designated locations according to a CAD file. Fully dense structures could be obtained if the spreading and solidification of droplets are controlled to enhance the precision of the process. For instance, the spacing between droplets must be attentively optimised at the first step, for which predicting the final morphology of droplets on the substrate after the solidification is essential. In this chapter, the dynamics of droplets from impact to solidification, which set the final shape of droplets, were studied for Sn, Ag, and Cu through an integrated computational, analytical, and experimental approach.

It was found that the substrate material is the most influential parameter in setting the droplets' morphology since its wetting and thermal properties are critical to the droplets' dynamics and solidification, respectively. First, the substrate should be wettable by the liquid metal droplets, otherwise, droplets most likely bounce off from the substrate on deposition. Moreover, the substrate's thermal properties define the rate of heat exchange between the droplet and substrate and consequently determine the time and position of the contact line arrest alongside the solidification rate.

Furthermore, it was shown that the droplet and substrate initial temperatures also play an essential role in the droplet's solidification rate and the contact line arrest, with the substrate temperature being more influential since it acts as a heat sink. Droplets at higher temperatures, containing higher thermal energies, deposited onto substrates with low thermal conductivity and maintained at higher temperatures undergo a slower heat dissipation into the substrate.

The study presented in this chapter enabled understating the underlying physics of droplets dynamics and solidification in the context of DoD-MJ for Cu, and Ag. This knowledge can be extended to new materials, in order to predict the morphology of droplets on solidification. Moreover, the numerical tools developed in this thesis can be used to optimise the process parameters for new materials such that the desired quality is met.

The specific outcomes of the study are listed as follows:

- Cu droplets deposited just above their melting point were practically instantly solidified upon impact onto the substrate. The solidification rate at the droplet's bottom section was faster than one oscillation period, as observed by a ripple-free morphology. Whereas on the top area of the droplet, with a slower solidification rate due to the latent heat effects, solidification ripples were formed.
- Sn droplets on a medium temperature Cu substrate were pinned to the substrate during the early stage of the relaxation phase when the contact line was not fully advanced. Consequently, a higher solidification contact angle was obtained, leading to potential inter-droplet voids in the printed parts.
- Ripples forming on the Sn droplet's periphery during solidification disappeared at elevated substrate temperatures. The high substrate temperature, close to the melting point of Sn, induces long solidification periods, such that the viscosity effects damp the oscillations before they freeze in place. Furthermore, the delayed solidification provided enough time for the droplet to enter the wetting phase, lead to a higher spreading factor and a decreased contact angle compared with the results at the intermediate temperature.

- The Sn droplets wetted the Cu and Sn substrates. In contrast, the Zn substrate demonstrated poor wettability, leading to potential droplet rebound upon impact, making it impossible to print a consistent part onto a Zn substrate.
- The high thermal conductivity of Ag and micron-order size of the droplets provided the opportunity of observing the toroidal morphology of solidified droplets on an Ag substrate for the first time. Droplets ejected at various temperatures shared similar toroidal morphologies with no solidification ripple at room and medium substrate temperatures, both of which were caused by extremely high solidification rates. In comparison, the droplet deposited on higher substrate temperatures had a more common cap-like shape.

6. Formation of Droplet- Substrate Interface and Microstructure: Copper, Tin, and Silver

The quality of the printed parts by DoD-MJ is mainly dictated by two factors, namely the droplet-to-substrate adhesion and inter-droplet bonding. These parameters influence the mechanical performance and structural integrity of the manufactured components. Hence, it is imperative to study the interface/interphase formation at both levels attentively. The main objective of this chapter was to underpin the mechanisms of the droplet to substrate bonding for Cu, Sn and Ag droplets deposited on various substrate materials and under various process conditions. To investigate the bonding, the interfaces of individual droplets with the substrate were characterised, and the experimental observations were analysed with the aid of computational simulations as demonstrated in **Figure 6.1**. The numerical results provided information not accessible with the experimental set-up, including the droplet and substrate temperatures' evolution and the maximum substrate temperature uptake during deposition.

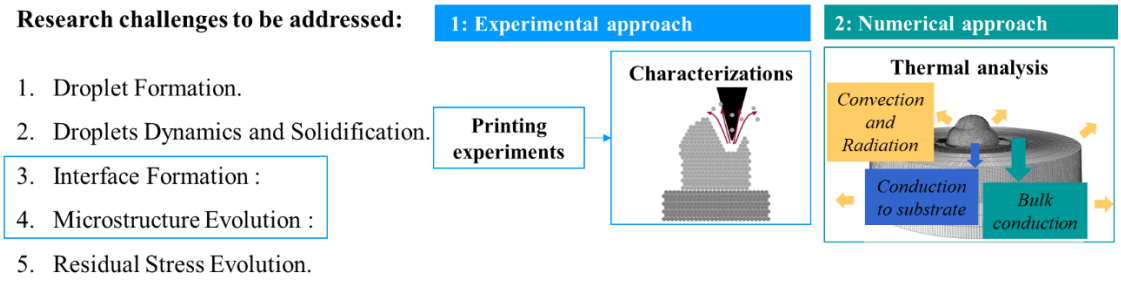


Figure 6.1- *The third and fourth challenges in DoD-MJ and the methodology implied in this thesis to address it, referring to Figure 52*

There are three bonding mechanisms during droplet deposition: (I) physical adsorption, where two surfaces are joined together through the weak van der Waals forces, (II) strong metallurgical bonding through melting the substrate, and (III) diffusion of atoms between the substrate and the droplet, leading to epitaxial growth or formation of an intermetallic (IM) layer in dissimilar materials. The properties of both the droplet and the substrate, i.e., their chemical composition, microstructure, and temperature-dependent diffusive phenomena, which takes place at the interface, dictate the level of bonding. Therefore, a high substrate temperature, a similar chemical composition or good compatibility between the droplet and the substrate, and an oxide-free substrate surface favour a more robust adhesion.

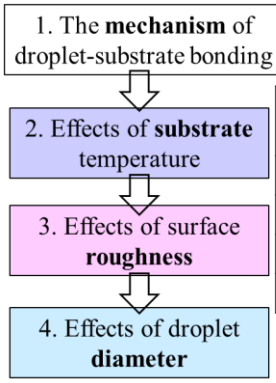
The bonding level in substrate melting is the strongest, hence being more favourable. However, a considerable energy level is required for this type since the substrate acts as a heat sink because of its significant mass difference from the microdroplets. Another bonding mechanism, so-called mechanical interlocking, is counted for thermal spraying processes, which is created by localized plastic deformation at the interfaces [250]. This type of bonding is achieved only if the droplet's speed exceeds a critical impact velocity, moreover, the strength of adhesion is usually weaker compared to chemical bonding. In most DoD-MJ technologies, the droplet speed is roughly 100 to 500 times less than the critical speeds for interlocking, consequently, this bonding mechanism is not considered in the current thesis.

6.1. Adhesion of Cu droplets to a Cu substrate

Individual Cu droplets were deposited onto Cu substrates using the parameters presented in **Table 6.1** through the MetalJet platform, and the interfaces were characterised using the protocol explained in chapter 3. In parallel to the experimental investigation, the temperature evolution of the droplets and substrate was calculated using the FE model presented in Chapter 3. The motivation for this set of parameters was the stability of jetting at this specific jetting temperature. Initially, the maximum stage temperature had been limited to 500 °C, which was upgraded according to the intermediate results through the thesis to accommodate for the maximum temperature of 750 °C. It was noted that at substrate temperatures below 500 °C, the adhesion of Cu droplets to the Cu substrate was limited, such that characterisation was not feasible (droplets were peeled-off from the substrate during the manipulation). The maximum substrate temperature was chosen based on the limitation is the system, including the highest temperature the stage and the printhead can stand. The working distance during printing experiments is usually 1 mm, so the permanent magnets in the printhead may lose their magnetic properties if exposed to higher temperatures from the substrate throughout the printing process. Moreover, the stage holder and printhead surrounding are made of Al (melting temperature ~ 670 °C). Consequently, the rational decision was made to limit the stage heating to 800 °C.

The droplets in this study were uniform, with an average diameter of ~ 80 μm in sets one to three in **Table 6.1** and ~ 60 μm in the fourth set. The variation in the droplet size originated from the difference in the nozzle's diameter used in the experiment. In the MetalJet system, the nozzle diameter mainly defines the droplet size. Slag formation at the nozzle level, which in turn varies the nozzle diameter, can also lead to a droplet size variation. The substrates were polished to obtain the surface roughness of $R_a = 0.01\ \mu m$ and $R_a = 0.10\ \mu m$. The surface roughness sets the thermal resistance between the droplet and substrate (Equation 47), influencing the heat transfer from the liquid droplets to the substrate.

Table 6.1*- specific set of parameters used for evaluating the adhesion of Cu droplets to the Cu substrates.*



	Ejection temperature	Deposition temperature	Substrate temperature	Surface roughness	Droplet diameter
1	1130 °C	1090 °C	500 °C	0.01 µm	80 µm
2			500 °C-750 °C	0.01 µm	80 µm
3			750 °C	0.01 µm-0.1 µm	80 µm
4			750 °C	0.01 µm	60 µm-80 µm

6.1.1. The mechanism of droplet-substrate bonding

In the cross-sectional view of a single droplet shown in **Figure 6.2**, the interfacial line between the droplet and the substrate is clearly visible. It was also observed that the droplet was only loosely attached to the substrate, confirming the absence of substrate melting to form a fusion (metallurgical) bond between the droplet and substrate. A similar issue was reported in [11] for Ag droplets deposited onto a Cu substrate. Moreover, there was no sign of a preferential grain orientation due to a potential epitaxial growth at the interface, consequently, no interdiffusion has occurred. Also, a gap can be seen between the droplet and substrate at the droplet's edge, which is indicative of distortion of the droplet due to residual stresses (this is marked in **Figure 6.2 b** by a double-headed arrow). However, what was not clear without further investigation is whether the residual stress caused delamination at the interface or whether it is the lack of bonding at the interface resulting in no constraint from the substrate to residual stress-induced deformation. Another feature observed in **Figure 6.2** is that the droplet had a polycrystalline microstructure with large grains compared to the size of the droplet, such that each droplet consists of ~ 8 to 14 grains. The large grain size suggests heterogeneous nucleation over the substrate surface. The heterogeneous nucleation is attributed to the imperfections on the substrate caused by polishing, yielding the initial nucleation sites. Also, the surface defects provide the condition for adequate undercooling in the absence of impurities in the deposited droplet. However, the low crystallites suggest a low nucleation rate resulting from a

small undercooling. The latter can be attributed to the poor contact at the interface. It was also observed that the grains were directed from the substrate interface toward the droplet's top, indicating a directional heat flux.

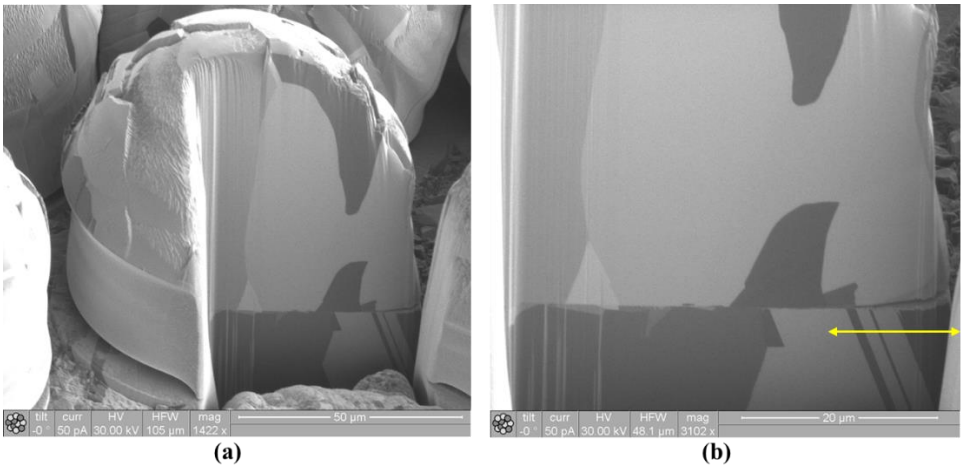


***Figure 6.2**- FIB-SEM cross-section of individual Cu droplet deposited on a Cu substrate showing **a)** droplet's polycrystalline microstructure with large grains, **b)** absence of substrate remelting or diffusion at the interface, and droplet delamination in the edges.*

The cross-sectional views of the droplet and substrate's thermal profile obtained by numerical simulations in **Figure 6.3 a-c** show the substrate heating from contact with the droplet. It can be seen that the affected area of the substrate is quite local to the contact site, which is not surprising given the small mass of the droplet and hence the amount of thermal energy available for transfer to the substrate. The substrate temperature reached a maximum value of 760 °C at the central point of the interface, which is far below the melting point of Cu (1084°C). This temperature is also below the required temperature to promote the diffusion of Cu atoms between the two surfaces [251], particularly as this level of high temperature was maintained only for a few tens of microseconds. Consequently, metallic bonds did not form at the interface, and droplets were attached to the substrate through physical adsorption (physisorption), in which the droplet's molecules are attracted towards the substrate's

molecules by weak Van der Waals forces. This explains the poor droplet-to-substrate bonding observed in the experimental results.

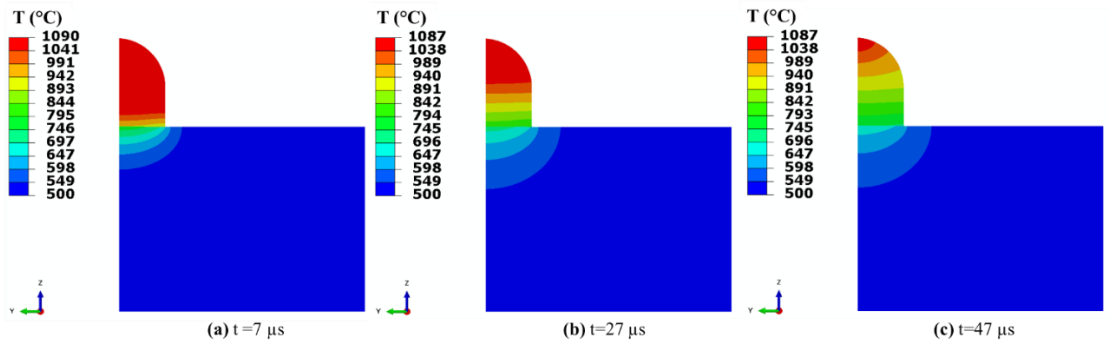


***Figure 6.3**- Cross-sectional profile views of temperature during single droplet deposition, taken in real-time of **a)** t=7 µs, **b)** t=27 µs, **c)** t=547 µs after deposition.*

Various process parameters contribute to the bonding level in the case of similar material deposition. The next sections discuss the effect of the substrate temperature, droplet size, and surface roughness on the bonding level. The droplet's temperature is also a contributing factor, however, due to the challenges involved with the ejection of Cu, this parameter has not been included in the current study.

6.1.2. Effects of substrate temperature on the droplet-substrate bonding

Based on the knowledge obtained from the study in section 6.1.1, the most plausible solution to enhance the bonding level between droplets and substrate was to increase the substrate temperature. Preheating the substrates to improve the adhesion of droplets is a common practice in thermal spraying technologies [5], [252]. To this aim, the stage heater in the MetalJet platform was upgraded to account for further heating, up to 800 °C, the maximum temperature the stage can tolerate. Droplets under the same conditions (second line in **Table 6.1**) were deposited on substrates at 500 °C and 750 °C and were FIB cross-sectioned to evaluate the bonding level.

The droplet interface with the substrate at 750 °C in **Figure 6.4** demonstrates that the preheating was insufficient to promote substrate melting. According to the numerical simulations, the maximum substrate temperature was 920 °C in this case, which confirms the experimental observations. However, it seems crystal grains grew in epitaxy with the substrate closer to the droplet centre. An EBSD analysis was necessary to confirm this hypothesis but scanning the cross-section zone was impossible due to the geometry of the samples.

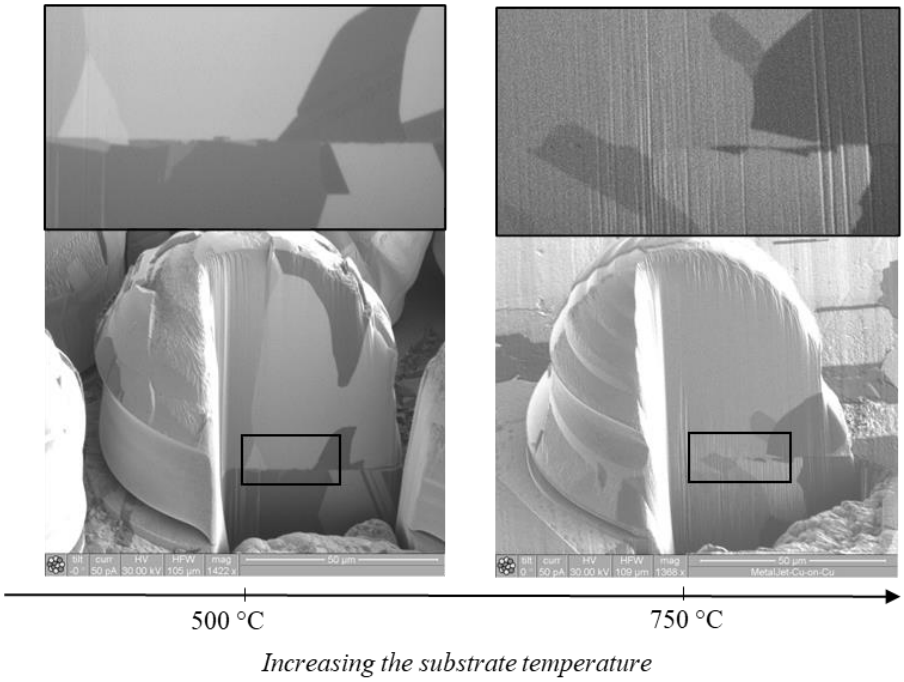


Figure 6.4*- Cross-section of individual Cu droplets deposited at 1090 °C onto Cu substrates at 500 °C and 750 °C to investigate effects of the substrate temperature on droplet-substrate. The inset presents the close-up of the interface indicated in the black box.*

Nevertheless, increasing the initial substrate temperature had a visible influence on the solidification contact angle and the spreading factor, which were 0.95 and 1.09 for the substrates at 500 °C and 750°C, respectively. The solidification period was more extended for droplets deposited at higher substrate temperatures. Consequently, the contact line was pinned to the substrate at a later stage of spreading, leading to a higher

spreading factor and a narrower contact angle. These results can be somewhat discouraging, however, there is still room for further progress to improve the bonding at the interface. In future investigations, a substrate with a lower thermal conductivity can be chosen such that the heat dissipation to the large substrate volume is decreased. In such cases, higher interfacial temperatures can be expected.

6.1.3. The effects of surface roughness on the droplet-substrate bonding

The role of surface roughness on droplet adhesion to the substrate is scarcely investigated to date. To study the effects of the surface roughness on the droplet-substrate bonding, droplets at the same conditions (the third line in **Table 6.1**) were printed on substrates polished using SiC papers with grit sizes 2500 and 4000. The surface roughness was measured with an optical 3D measurement system, Alicona InfiniteFocusG4, and the average height deviations from the mean value, i.e., R_a, were equal to 0.01 µm and 0.1 µm.

The first information obtained from **Figure 6.5** is the influence of the roughness on the spreading of the contact line at higher surface roughness. The surface irregular heterogeneities acted as pinning sites and produced asymmetric local deformation, leading to an irregular final morphology compared to the droplet deposited at lower surface roughness. It is very likely that the rugged features on the surface act as micro-capillary bridges, preventing the contact line from de-pining and receding from the roughness features. In fact, the contact line is set to motion only if the micro-capillary bridges are separated from the surface. This happens by necking and rupturing or through depinning and receding from each roughness feature. Despite various studies on this topic [240] [253], the complete mechanism of de-pining is still not known. In the current thesis, the pinning of molten Cu in the heterogonies of the substrate is accentuated due to the high surface tension of the material.

The metallurgical bonding through substrate melting was not obtained in either case in **Figure 6.5** due to the low temperatures at the interfaces. Moreover, based on to the numerical simulations results, the roughness had a deteriorating impact on the substrate temperature uptake during the deposition. The maximum substrate

temperature was 920 °C when $R_a = 0.01\ \mu m$, whereas, for the rougher surface, it was only 766 °C. The effect of surface roughness on the bonding level was evaluated by performing a manual tape peel test. Standard tape tests (ASTM standard - D3359-09) are commonly used in nanoparticle-printed electronics [8] and thermal spraying technologies [248]. The SEM observations evidenced the increase in the bonding level at higher surface roughness after the test.

The majority of the droplets (14 / 15 in the first experiment and 11/ 15 in the second) deposited on the smoother surface were peeled off. In contrast, only a few numbers of droplets (6 / 15 and 7 / 15 in the first and second trials, respectively) were removed from the rougher surface. Without a standard quantitative measurement, it cannot be concluded that increasing surface roughness enhances substrate adhesion. The results obtained from the tape peel test can be misleading since the tape was manually inserted and removed. However, the considerable difference in the tape peel-off test cannot be ignored. The better adhesion of droplets to the rougher surface can be attributed to the surface tension-related forces acting along the bases of the capillary bridges during the spreading. The interlocking of droplets to these heterogeneities during the solidification could create a relatively stronger bond. As discussed in section 5.2.2, due to the undesired effects of surface roughness on droplet morphology, this parameter is kept constant in this thesis and R_a equal to 0.01 µm is used for the experiments.

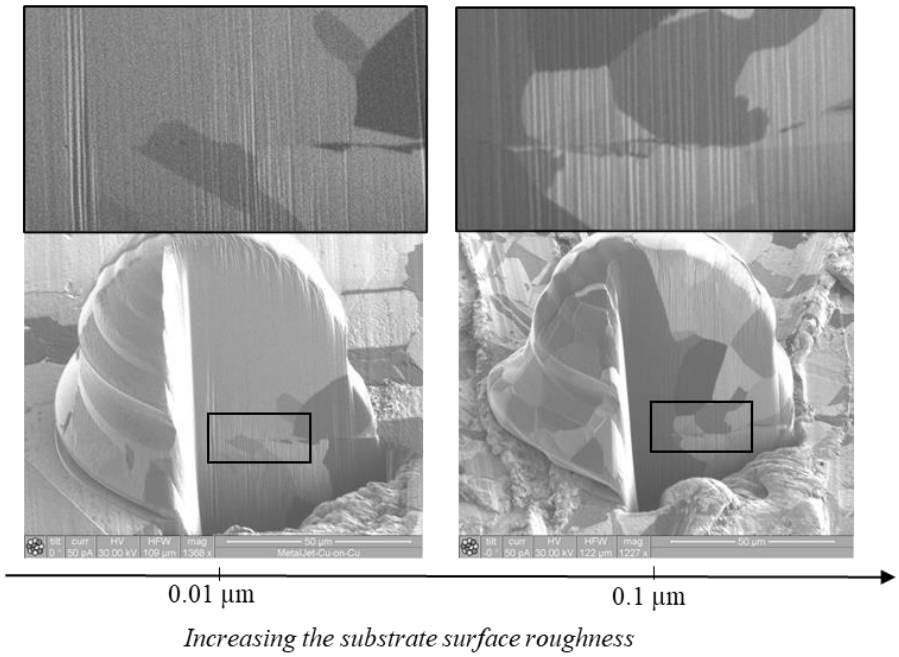


Figure 6.5- *Effect of surface roughness ($R_a = 0.01$ µm and $R_a = 0.1$ µm) on the droplet-substrate bonding for deposition of Cu droplet on Cu substrate at 750 °C. The inset presents the close-up of the interface indicated in the black box.*

6.1.4. Effects of droplet size on the droplet-substrate bonding

The effect of the droplet size on the bonding level was investigated by the ejection of droplets of 60 µm and 80 µm in diameter at the same deposition conditions (the fourth line in **Table 6.1**). The difference in the droplet size is related to the variation in the nozzle diameter. Larger droplets contain more initial thermal energy ($\propto r^3$), in this case, the larger droplets had 2.4 times higher thermal energy. Moreover, they could release higher latent energies upon solidification ($Q = mL$), consequently, it is expected that larger droplets create a more robust adhesion to the substrate. It is noted that the in-flight cooling and convection heat exchange are supposed to be higher for larger droplets due to larger surface areas, however, their influences remain negligible. The FIB-SEM cross-sectional views of these droplets are illustrated in **Figure 6.6**. As expected, neither case attained the metallurgical bonding through substrate melting. However, these findings are somewhat limited to the unquantified FIB-SEM

observations, and adhesion strength cannot be compared between them. It is important to point out that the contact line of the smaller droplets was arrested faster, leading to a smaller contact area with the substrate. Therefore, the heat flux and the maximum substrate temperature are expected to vary compared to the larger droplet.

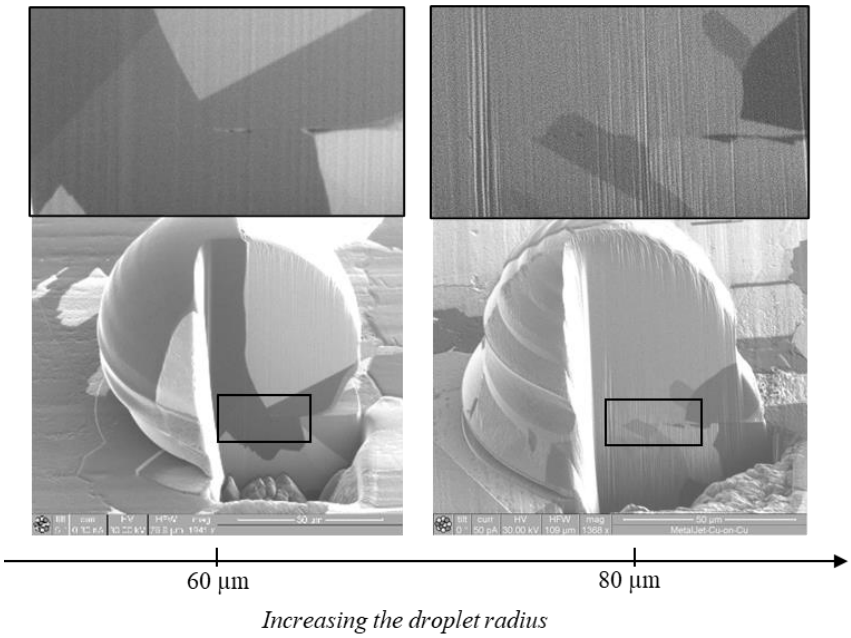


Figure 6.6- *Effect of droplet size of 60 µm and 80 µm in diameter on the droplet-substrate bonding for deposition of Cu droplet on Cu substrate at 750 °C. The inset presents the close-up of the interface indicated in the black box.*

6.2. Adhesion of Sn droplets to various substrates

The low melting point of Sn provided the possibility of investigating the effects of a wider range of process parameters, mainly the ejection temperature on the droplet-substrate bonding. Moreover, diffusion bonding between dissimilar materials could be evaluated since the material could be held in the liquid state for more prolonged periods using the preheated substrate. In this section, the effects of superheating temperature and substrate temperature on the droplet adhesion to the substrate were evaluated for Sn droplets deposited on a Cu substrate. Moreover, the bonding level

and mechanism of Sn droplets to various substrates (Sn, Cu, and Zn) were investigated. The specific set of parameters used in this section is presented in **Table 6.2**. The minimum ejection temperature used in this study is 670 °C, the minimum working temperature in the MetalJet system (detailed in chapter 3). The maximum jetting temperature for Sn was 1000 °C, and jetting at higher temperatures caused slag formation at the nozzle level and deterioration of the jetting stability. The room temperature, medium, and high (12 °C below the melting point of Sn) substrate temperatures were chosen to investigate the effects of the substrate temperature. Finally, Sn, Zn, and Cu were chosen for substrate materials due to their metallic compatibility with Sn droplets. Due to the low melting point of Sn (232 °C), the interface of the Sn substrate was expected to melt during the deposition of superheated Sn droplets to create strong metallurgical bonding. Cu (1084 °C) is a high-temperature material; consequently, bonding through remelting is not expected to occur in this case. However, according to the literature, bonding through diffusion could be envisaged. Zn has a medium melting temperature (419.5 °C) and a higher diffusivity rate than Cu. As a result, it is interesting to investigate the bonding between Sn and Zn in the context of the DoD-MJ process. The integrated experimental and numerical approach used to assess the bonding of the individual droplets to the substrate was mentioned in Chapter 3.

***Table 6.2**- Specific set of parameters used for evaluating the adhesion of Sn droplets to various substrates.*

		Ejection temperature	Deposition temperature	Substrate temperature	Substrate material
1. Effects of **droplet** temperature	1	670 °C	651 °C	130 °C	Cu
		850 °C	822 °C		
		1000 °C	964 °C		
2. Effects of **substrate** temperature	2	670 °C	647 °C	30 °C	Cu
			651 °C	130 °C	
			654 °C	220 °C	
3. Effects of substrate **material**	3	670 °C	647 °C	30 °C	Cu
					Sn
					Zn

6.2.1. Effects of droplet temperature

The FIB secondary ion images of the cross-sectioned interfaces of Sn droplets jetted at various temperatures onto a Cu substrate at 130 °C in **Figure 6.8 a-c** demonstrate the formation of intermetallic layers at the droplet-substrate interface at all conditions. Two types of intermetallic (IM) layers at the interface of liquid Sn and solid Cu are formed [254]–[257], which is predicted by the Sn-Cu phase diagram and is schematically presented in **Figure 6.7**. Initially, the liquid Sn reacts with the Cu substrate to form a layer of $\eta - Cu_6Sn_5$ as per:

$$6Cu + 5Sn \rightarrow Cu_6Sn_5 \qquad \text{(Equation 66)}$$

Cu atoms diffuse from small grains to larger grains; thus, the initial thin layer transforms into coarsened Cu_6Sn_5 scallops during the ripening process. In the following stage, it is thought that the Cu atoms react with the initial Cu_6Sn_5 layer to form $\epsilon - Cu_3Sn$ (**Equation 65**). This reaction is slower since it is solid-state rather than solid-liquid diffusion. The Cu_3Sn grows in time, forming a layer thick enough to impede further diffusion of Cu in the Cu_6Sn_5.

$$Cu_6Sn_5 + 9Cu \rightarrow 5Cu_3Sn \qquad \text{(Equation 67)}$$

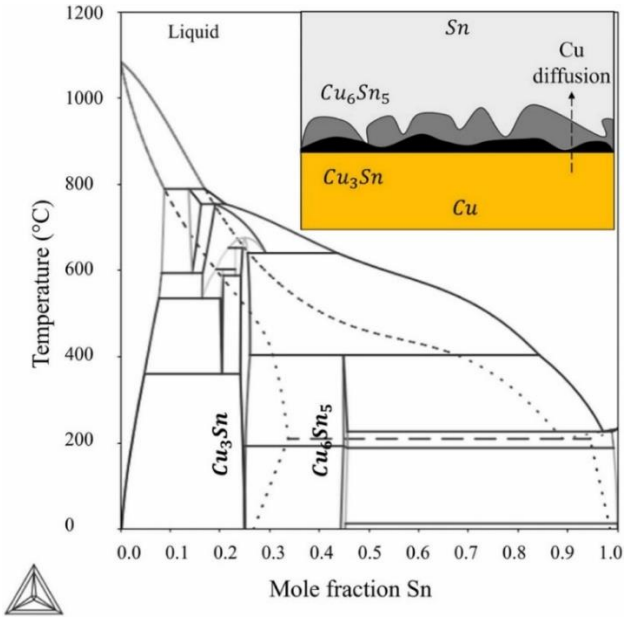


Figure 6.7- *Thermo-Calc generated Sn-Cu phase diagram and schematic representation of Cu atom diffusion into liquid Sn to form intermetallic layers.*

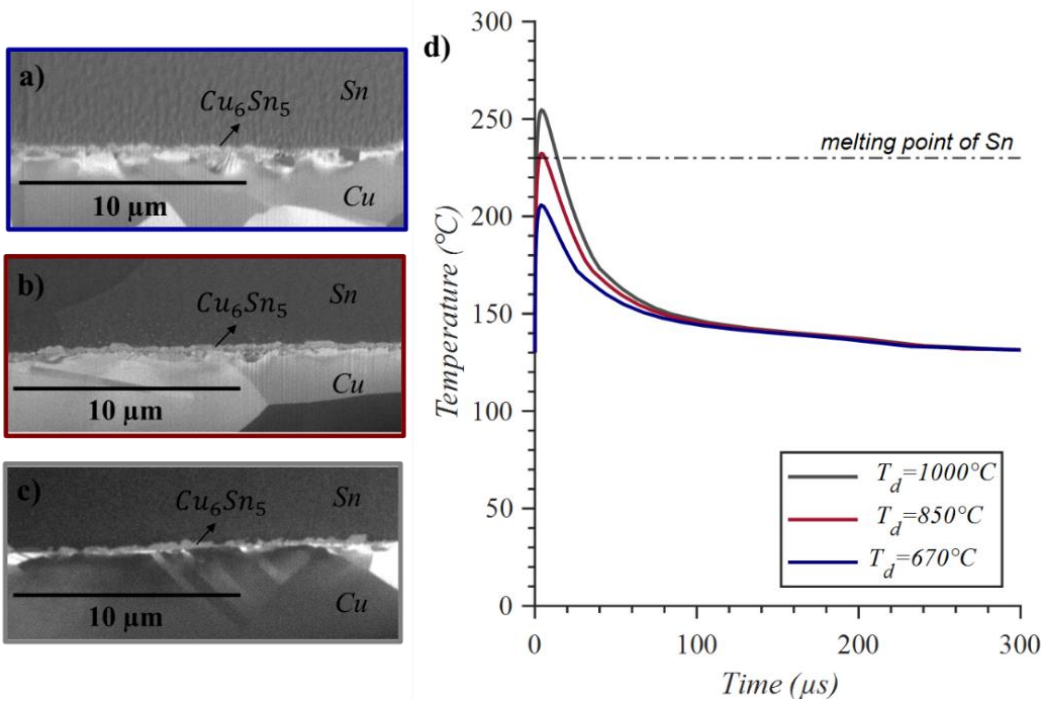


Figure 6.8- *FIB-SEM cross-sections of the interfaces for droplets deposited at* ***a)*** *=670 °C,* ***b)*** *850 °C, and* ***c)*** *1000 °C onto a Cu substrate at 130°C showing the formation of IM layers with various consistency,* ***d)*** *the substrates temperature evolution at the interface during the solidification and cooling of droplets.*

For the droplets deposited at 670 °C, the IM layer (**Figure 6.8 a**) was neither thick nor consistent. The integrity and thickness of this layer improved as the droplet temperature increased (**Figure 6.8 b-c**). Where the average IM layer thickness was 0.29 µm, 0.36 µm, and 0.39 µm with a standard deviation of 0.15 µm, 0.13 µm, and 0.06 µm for 670 °C, 850 °C, and 1000 °C droplets, respectively, hence, improved bonding levels at higher jetting temperatures can be assumed. As per **Figure 6.8 d**, the maximum substrate temperature at the interface was higher at more elevated jetting temperatures. However, the period of time at which these temperatures are maintained lasted less than a hundredth of a microsecond. This explains the negligible variation of IM layer thicknesses since the diffusion varies as a function of time and temperature [32].

6.2.2. Effects of substrate temperature

The FIB-SEM cross-sectional views of the interfaces for droplets deposited at 670°C onto a Cu substrate at various temperatures are demonstrated in **Figure 6.9 a-c** The temperature at the droplet-substrate interface and the duration at elevated temperature were not sufficient to promote the diffusion of the Cu atoms into the liquid Sn at $T_{substrate} = 30$°C. As a result, the bonding level was very poor (as evidenced by the droplets peeling off the substrate during handling samples after printing). Increasing the substrate temperature to 130°C resulted in a thin and non-consistent IM layer at the interface of 0.29 µm on average. At more elevated temperatures, close to the melting point of Sn, the IM layer grew to 1.8 µm on average (with a standard deviation of 0.32 µm) through coarsening of the Cu_6Sn_5 scallops. Moreover, a layer of Cu_3Sn (0.39 µm) formed due to there being sufficient temperature and time for this reaction. This would be expected to increase the strength of bonding at the interface. The temperature evolution at the interface in **Figure 6.9 d** demonstrates that the maximum temperature obtained for the substrate at elevated temperature was 287°C against 120°C for the substrate at room temperature. Once the steady temperature, i.e., the temperature at which the substrate was kept, was obtained, the diffusion process

continued with a higher rate for higher substrate temperature. Moreover, cooling of the substrates from elevated to room temperature extended the diffusion time in these cases.

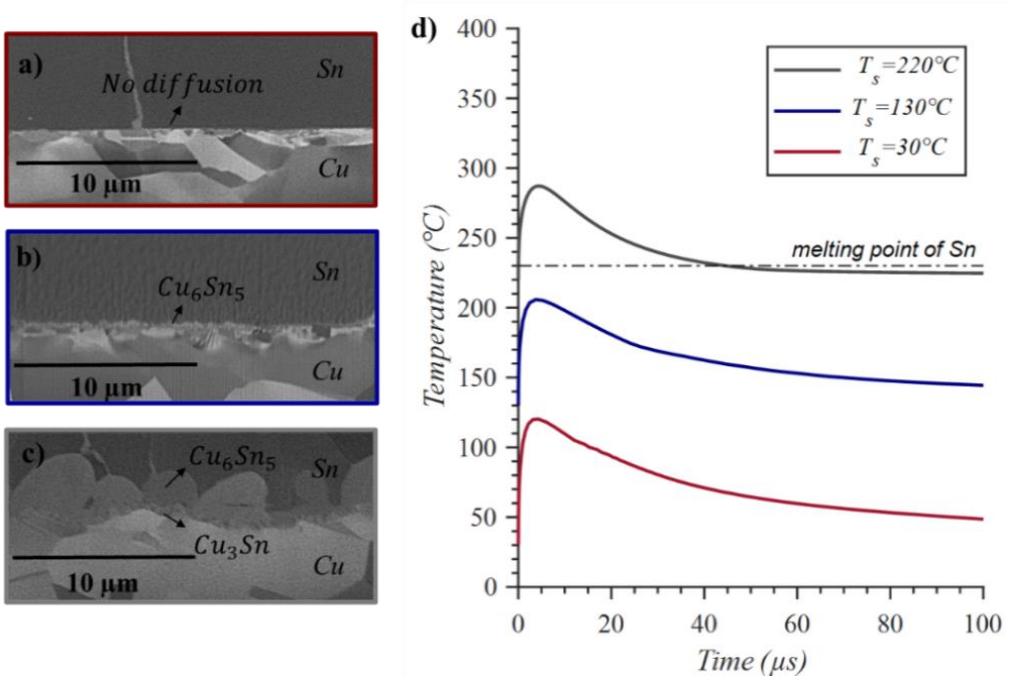


***Figure 6.9**- FIB-SEM cross-sections of the interfaces for droplets deposited at 670°C onto a Cu substrate at **a)** 30°C, **b)** 130°C, and **c)** 220°C, showing the formation of IM layers with various thicknesses, d) the substrates temperature evolution at the interface during the solidification and cooling of droplets.*

6.2.3. Effects of substrate material

The FIB-SEM cross-sections of the interfaces for Sn droplets at 670 °C deposited onto substrates of various materials at 30 °C are shown in **Figure 6.10 a-c**. As previously explained (section 4.2.2), Cu atoms did not diffuse significantly into the liquid Sn droplets due to the low interfacial temperatures. However, a superheated Sn droplet may be expected to form a strong bond to an Sn substrate through substrate melting. However, the droplet and substrate are not fused (**Figure 6.10 c**), and the separation at the interface is clearly visible (white line), which indicates the absence of substrate melting. From the numerical simulations, the interfacial temperature reaches the highest value of 228°C for the Sn substrate at the droplet centre (**Figure 6.10 d**), which

is below the melting point of Sn. Hence a strong metallurgical bonding through melting cannot be expected. The low interfacial temperature is attributed to the thermal resistivity, which in turn is related to the surface roughness. As for the Zn substrate, no diffusion was observed despite the high diffusion rate of Zn atoms into the liquid Sn, which is higher than the inter-diffusion rate of Sn itself or the Cu diffusion rate. According to simulation results, the Zn substrate is heated only to 140°C during the droplet deposition, which is assumed not to be high enough to promote bonding through diffusion (similar to the Cu substrate, which was only heated to 120°C). The lower substrate temperatures reached by the Cu and Zn are attributed to their higher heat capacity compared to Sn. Consequently, no diffusion or melting is expected, as the melting point of Zn is 419.5°C. As observed experimentally, the droplets only weakly adhered to the Zn and Cu substrates through what can be attributed to van der Waals forces (physical adsorption).

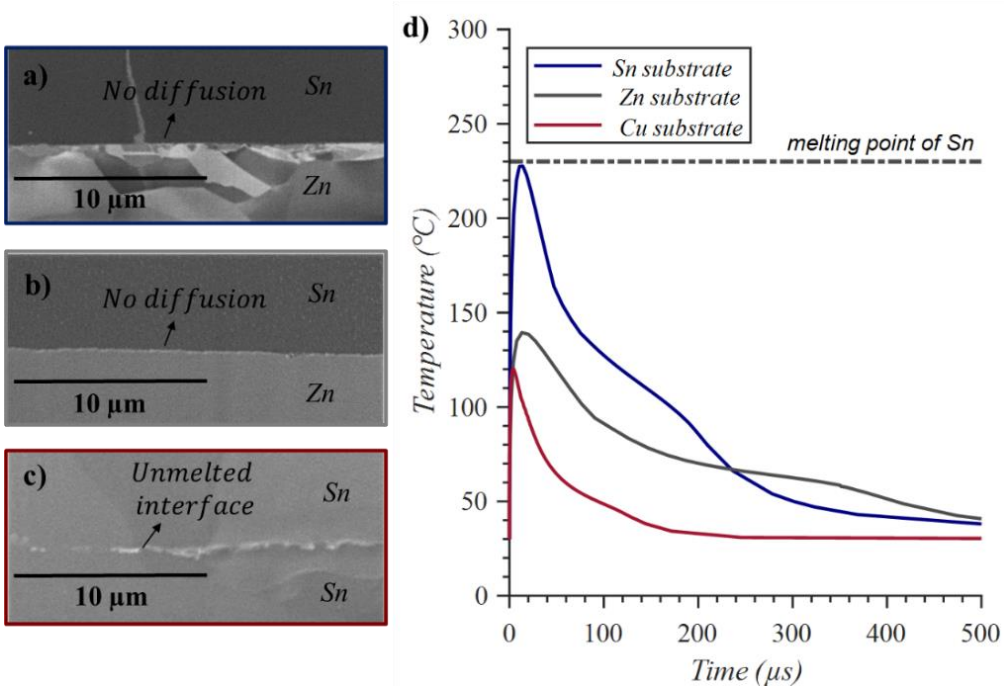


***Figure 6.10**- FIB-SEM cross-sections of the interfaces for droplets deposited at 670 °C onto **a)** Cu, **b)** Sn, and **c)** Zn substrates at 30 °C, **d)** the substrates temperature evolution at the interface during the solidification and cooling of droplets.*

6.3. Adhesion of Ag droplets to an Ag substrate

In this section, the effects of superheating temperature and substrate temperature on the droplet adhesion to the substrate were evaluated for Ag droplets deposited onto Ag substrates. The specific set of parameters used in this section is presented in **Table 6.3**. The minimum ejection temperature used in this study is 1040 °C, the minimum ejection temperature for Ag. The maximum jetting temperature for Ag was 1200 °C, and jetting at higher temperatures caused slag formation at the nozzle level and deterioration of the jetting stability. The room temperature, medium, and high (maximum temperature in the MetalJet platform) substrate temperatures were chosen to investigate the effects of the substrate temperature. The integrated experimental and numerical approach used to assess the bonding of the individual droplets to the substrate was mentioned in Chapter 3.

***Table 6.3**- Specific set of parameters used for evaluating the adhesion of Sn droplets to various substrates.*

1. Effects of **droplet** temperature

2. Effects of **substrate** temperature

	Ejection temperature	Deposition temperature	Substrate temperature
1	1040 °C	1025 °C	25 °C
	1120 °C	1105 °C	
	1200 °C	1185 °C	
2	1040 °C	1025 °C	400 °C
	1120 °C	1108 °C	
	1200 °C	1188 °C	
3	1040 °C	1030 °C	775 °C
	1120 °C	1110 °C	
	1200 °C	1190 °C	

6.3.1. High substrate temperatures

The FIB-SEM image of the droplet-substrate interfaces for droplets ejected at 1040 °C, 1120 °C, and 1200 °C onto the substrate at 775 °C and the substrate temperature evolution during the deposition obtained from the numerical simulations are demonstrated in **Figure 6.11**. The visible interface for the droplet ejected at 1040 °C indicated that the substrate melting had not occurred in this condition. This was

confirmed through numerical simulations where the maximum substrate temperature was 920 °C during the deposition. The grain contrast at the droplet interface at 1120 °C revealed the formation of refined grains in this area zone with a thickness of ~2 µm.

The numerical simulation results show that the droplet's solidification rate was very high, and the contact line froze in less than tens of microseconds. At first glance, the grains with the size of 200 nm to 1.5 µm in this layer can be attributed to the high rates of thermal cycles, which promote a higher nucleation rate with insufficient time for the nucleus to grow. However, a closer observation makes it more probable that the thin layer is an epitaxial layer. The epitaxial growth from the substrate is also reported in thermal spraying [258] and L-PBF processes [259].

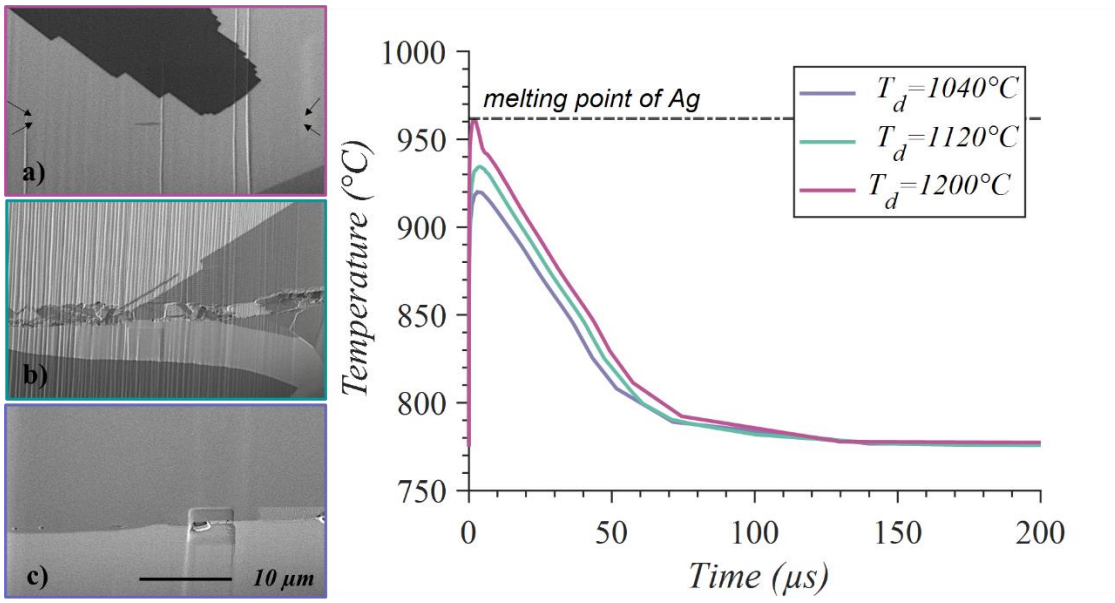


Figure 6.11*-The interface of Ag droplets deposited at a) 1200 ℃, b) 1120 ℃, and a) 1040 ℃ onto the Ag substrate at 7750 ℃ and the substrate temperature evolution at the centre of droplets obtained from the numerical simulations.*

Indeed, heterogeneous nucleation and epitaxial growth could occur during the solidification of metal droplets on a surface. The epitaxial growth is a special form of

crystal growth mechanism, during which the formation of nucleation sites is hindered [260]. Its occurrence mainly depends on various factors, including lattice mismatch, substrate crystalline structure [258], orientation, and external factors such as pressure and temperature [261]. The physical mechanism of both processes is the same and related to the diffusion and adhesion of liquid atoms to the nuclei or substrate surface. If most liquid atoms diffuse to the nuclei or melt interface, the droplet's solidification is governed by heterogeneous nucleation. Otherwise, liquid atoms condense on the substrate without nuclei formation, and epitaxial growth occurs. The epitaxial growth can only occur if the epitaxial grains grow fast enough such that nuclei do not have enough time to form on the substrate surface [260].

For the droplet under analysis, an epitaxial front has rapidly grown in the vicinity of the substrate, which is the first impact point. However, its growth was soon overcome by growing nucleated clusters in the top section of the droplet. In the thermal spraying process, the droplets with the epitaxial zone at the interface showed higher fracture strength compared to the polycrystalline zones [258]. Hence, a better droplet-substrate bonding is expected for the droplet at 1120 °C. Finally, by increasing the ejection temperature to 1200 °C, a strong metallurgical bonding through substrate melting was obtained. The numerical results demonstrate that the substrate temperature reached the melting point of Ag at this temperature, which is in good agreement with the experimental observations.

6.3.2. Medium substrate temperatures

The interface between the droplets ejected at 1040 °C, 1120 °C, and 1200 °C onto the substrate at 400 °C is demonstrated in **Figure 6.12**. The interface is clearly visible in all cases, indicating the lack of substrate melting. The maximum substrate temperature obtained from the numerical simulation was 756 °C, 778 °C, and 803 °C for these cases, respectively, which is well below the melting point of Ag. Consequently, a strong droplet-substrate bonding is not expected. One interesting aspect of the data in **Figure 6.12** is the microstructure of the droplets, which is more refined compared to the droplets deposited on the substrate at 775 °C. This is attributed to the faster cooling

rates during the solidification process. The cooling rates of droplets at 400 °C substrate was ~ 10 to 12 °C/µs, while it was ~ 3.5 °C/µs for the droplets deposited on the substrate at 775 °C.

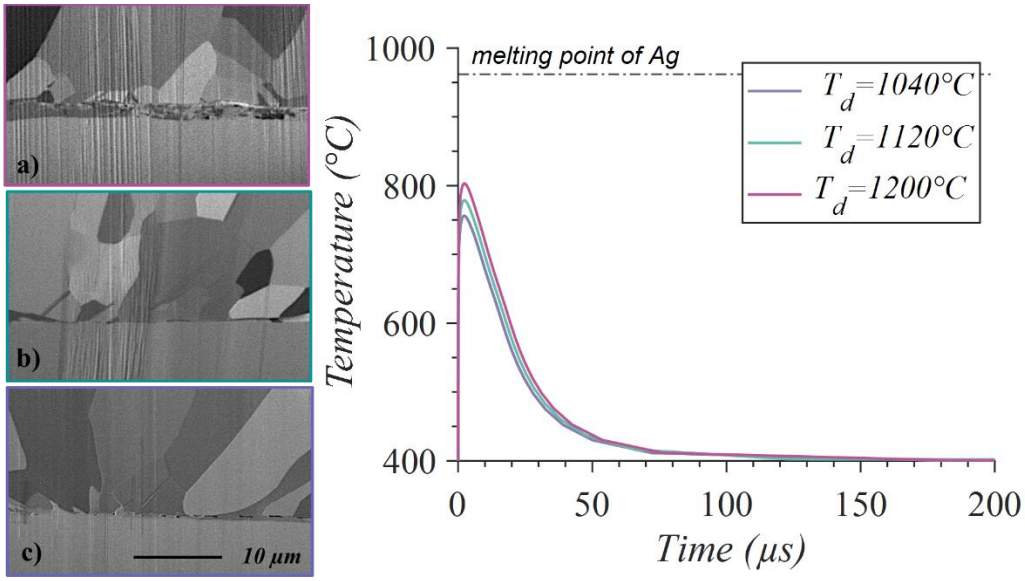


Figure 6.12- *The interface of Ag droplets deposited a) 1200 ℃, b) 1120 ℃, and a) 1040 ℃ onto the Ag substrate at 400 ℃ and the substrate temperature evolution at the centre of droplets obtained from the numerical simulations.*

What stands out in **Figure 6.12** is the refined layer at the interface of the droplet at 1200 °C, similar to the droplet at 1120 °C on the substrate at 775°C (**Figure 6.11**). However, the InLens (secondary electron detector within column) image of this zone, shown in **Figure 6.13** reveals that the refinement has taken place in the substrate, not the droplet. This layer resembles a grain refinement due to recrystallization, which is regularly observed at the interface of droplets in thermal spraying processes [262], [263]. Dynamic recrystallization is usually classified into rotational and migrational mechanisms related to the plastic deformation and annealing in the cooling regime after adiabatic heating [263]. Neither of these explanations can be responsible for the recrystallization at the substrate interface in this study since the droplets are gently

deposited on the substrate at the speed of 1-3 m/s. In contrast, droplets impact on the substrate with speeds as high as 300 m/s in thermal spraying processes.

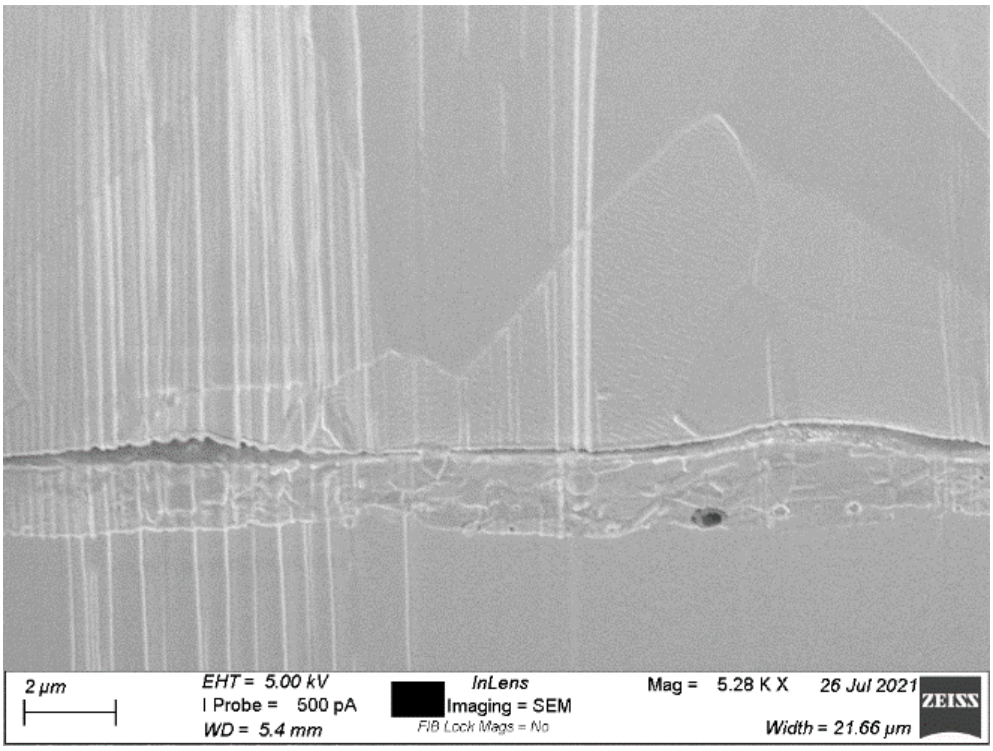


Figure 6.13*- The recrystallization of the substrate interface during the deposition of Ag droplet at 1200 ℃ on a substrate at 400 ℃.*

Moreover, according to the numerical simulation results, the elevated temperature in these zones remains only for tens of microseconds, hence, there is not enough time for annealing. In recent years, it has been discovered that the refined grains observed in L-PBF, EBM, and DED processes can be indeed attributed to recrystallization (also called in-situ recrystallization) [264]–[267]. Rapid heating and cooling cycles during liquid metal deposition result in thermal strains and eventually lead to dislocations, mainly accumulated at the interface. These dislocations contain free energy that is not entirely released during the process. Consequently, the rearrangement of these dislocations from low dislocation density regions leads to recrystallization, and finally new sub-grain formation. During the so-called in-situ recrystallization, the nucleation via coalescence of sub-grains occurs at temperatures as low as 65% of the melting

temperature [265]. According to the numerical simulations in **Figure 6.12**, the substrate temperature in this case has been above this threshold for tens of microseconds.

It is apparent from **Figure 6.13** that the droplet-substrate bonding is relatively poor, and the droplet is already delaminated from the substrate. The high milling rates are partially responsible for such delamination, but it is evident that the bonding was not strong enough to resist the stresses produced during the process. What is not clear without further investigation is whether the recrystallization has played a role in inducing the poor bonding or whether it can enhance the mechanical properties of the material.

6.3.3. Low substrate temperature

The interface between the droplets ejected at 1040 °C, 1120 °C, and 1200 °C onto the substrate at 25 °C is demonstrated in **Figure 6.14**. Similar to the substrate at 400°C, the visible interface between the droplet and substrate signifies a lack of bonding in the zone. This is attributed to the low substrate temperature, as evidenced by the numerical simulation results. This was confirmed by the droplets peeling off the substrate while handling samples after printing. The solidification rate of droplets deposited onto the room temperature substrate was ~16 - 23 °C/µs, which is 1.5 to 2 times higher than the solidification rate at 400 °C substrate. As a result, grains are generally more refined for all ejection temperatures. In particular, fine equiaxed grains are observed at the interface, followed by fine directional columnar grains in the top section of the droplets. All of which is attributed to the considerable thermal gradient between the liquid metal droplet and the substrate and fast cooling rates. The micron-sized grain exhibiting twins stands out from the data presented in **Figure 6.14**.

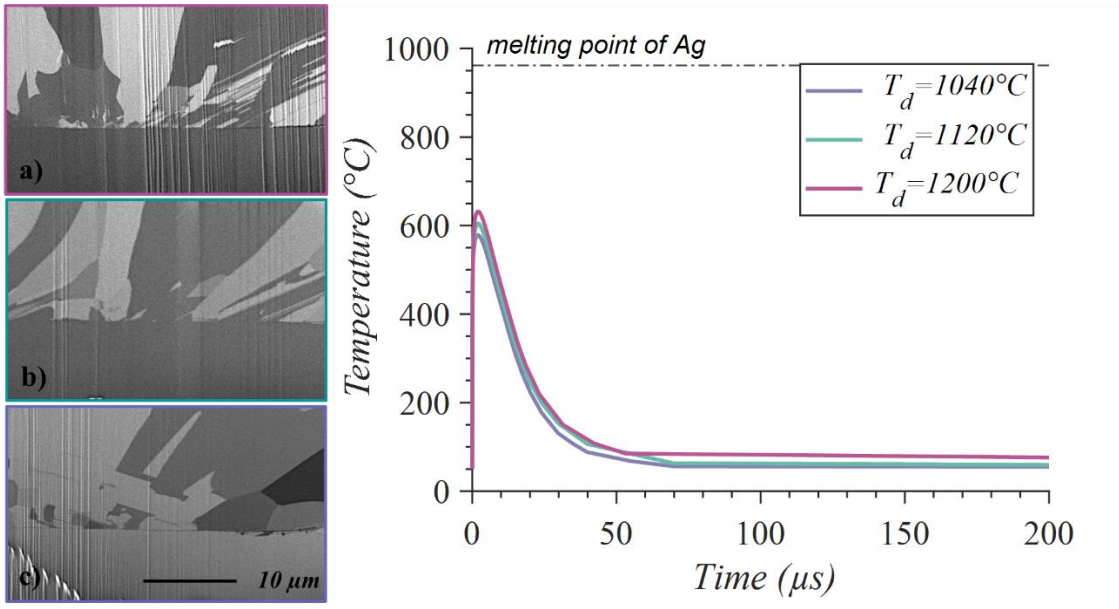


***Figure 6.14**- The interface of Ag droplets deposited at a) 1200 ℃, b) 1120 ℃, and a) 1040 ℃ onto the Ag substrate at 25 ℃ and the substrate temperature evolution at the centre of droplets obtained from numerical simulations.*

Generally, two possibilities exist for the formation of twins after high strain rate deformation. Twinning results from high strain rate deformation and can occur directly or shortly after shock loading or annealing during migrational recrystallization [263]. In the AM processes, the twin formation could be attributed to the occurrence of the growth accident theory during recrystallization. In this theory, twin boundaries form at a migrating grain boundary due to a stacking fault energy. The formation of twins reduces the energy of growing grain boundaries [265]. Indeed, rapid thermal cycles cause plastic deformation and an increase in the dislocation density, which in turn leads to a higher resistance to the motion of dislocation. This process activates the cross-slip deformation and twining. [268]. Previous studies have shown that twins can contribute to better mechanical properties by increasing the material's ductility [268], [269], fatigue, and corrosion resistance [270]. Even though the lower substrate temperature results in a poor bonding level, the in-situ formation of interesting metallurgical phenomena such as twining and recrystallization opens up new opportunities, which merit further investigations.

6.4. Summary

The interfaces formed during the deposition of low to high-temperature materials (Sn, Ag, and Cu) using the MetalJet process at the droplet-substrate and the droplets' final microstructure were investigated in this chapter. Process parameters such as the substrate material, droplet temperature, substrate temperature, and surface roughness were varied to investigate their effects on the bonding level and microstructure. It was understood that the substrate properties are the most influential element in setting the bonding levels, mainly due to the significant mass difference between the substrate and microdroplets. The choice of the substrate material, which defines the wetting conditions, chemical compatibility with the droplets, and substrate's thermal properties, is the most critical parameter in this regard. After that, the initial temperature of the substrate is the parameter to be attentively selected for each material. The substrate temperature should be high enough to promote an adequate level of bonding. Substrate melting can be achieved in the case of similar material printing or if the substrate material has a lower melting temperature than the droplet material.

Diffusion bonding, another form of strong bonding, could be obtained if the substrate temperature is maintained at high enough temperatures for an adequate period of time. Computational modelling was required to choose the optimal substrate and droplet temperature for each set of materials. Furthermore, it was shown that the droplet temperature, surface roughness and droplet size influence the interfacial temperatures, hence the bonding levels. However, their effects remain somehow limited compared to the effects of substrate properties.

The numerical model developed in the thesis can be used to predict the process parameters required to obtain a strong metallurgical bonding between the droplet and substrate of various materials. This is a useful tool to expand the palette of materials used in the context of DoD-MJ. For this purpose, the thermophysical properties of materials of interest are the required input to the model. Moreover, the knowledge obtained concerning the influence of substrate wettability is essential to choose the substrate materials such that they the printability requirement. Overall, the work

presented here can be used to study the interface formation for the MetalJet process and is scalable to be used in the context of any metal droplet deposition process.

The specific outcomes of the study are listed as follows:

- Strong bonding between the Cu droplets and Cu substrates could not be achieved with the system's current configuration. This is mainly attributed to the high thermal conductivity of Cu, the maximum initial substrate temperature (limited to 800 °C), and the low initial droplet temperature. The latter cannot be varied due to the jetting stability issues at higher temperatures for this material.
- A robust metallurgical bonding through substrate melting was not realised for superheated Sn droplets deposited onto room temperature Sn, Cu and Zn substrates. The reason is that substrates quickly absorb the thermal energy of the microdroplets without a significant increase in the interface's temperature.
- One of the noteworthy outcomes of this research was demonstrating a strong adhesion of droplets to the substrate at temperatures considerably below the melting point of the substrate's material through diffusion bonding. For example, in the case of Sn droplets deposited onto a Cu substrate kept at 220 °C, intermetallic layers of Cu_6Sn_5 and Cu_3Sn were formed at the droplet-substrate interface, providing an adequate level of bonding.
- It was shown that a robust metallurgical droplet-substrate bonding could be achieved for Ag droplets deposited onto an Ag substrate if the optimised process parameters obtained from the numerical simulations were used. The substrate remelting occurred for droplets ejected at 1200 °C onto a substrate kept at 775 °C. Droplets ejected at 1120 °C onto high substrate temperatures are also expected to have strong adhesion to the substrate due to the formation of an epitaxial layer in the vicinity of the substrate. It is known from thermal spraying processes that the formation of such epitaxial layers enhances the fracture strength.

7. Formation of Droplet- Droplet Interface and Microstructure: Copper, Tin, and Silver

The bonding between the droplets mainly defines the mechanical performance and structural integrity of fabricated components through DoD-MJ. In addition, microstructure evolution during the successive deposition of droplets plays an essential role in defining the properties of printed parts. The main objective of this chapter was to provide insights into the interface formation between adjacent droplets and investigate the final microstructure of multiple droplets. To this end, the interface between Cu, Sn, and Ag droplets deposited on similar and dissimilar substrate materials was investigated. This was achieved through the characterisation of the interface of successive droplets printed through the MetalJet platform and analysing of the experimental observations with the aid of computational simulations.

It was seen that the bonding mechanism between adjacent droplets is similar to the droplet-substrate bonding in the case of similar material deposition. The remelting of the inter-droplet interface is essential to ensure a strong metallurgical bonding, which in turn results in high structural integrities. In addition, the microstructure of the

second droplets differs from the first droplets due to the variation in the thermal fluxes during the depositions of these droplets.

7.1. Copper inter-droplet bonding

In order to evaluate the inter-droplet bonding, the top section of two droplets deposited successively with a frequency of 500 Hz and a centre-to-centre distance of 75 µm was removed and imaged to investigate inter-droplet bonding. As observed in **Figure 7.1**, the microstructure of the second droplet ($droplet_2$) is quite different to the first droplet ($droplet_1$). The vertical columnar grains observed in $droplet_1$, were replaced by larger grains directed toward the interface in $droplet_1$. Moreover, it seems the neighbouring droplets shared grains at their interface, even though the borders of the droplets were visible at the interface between them.

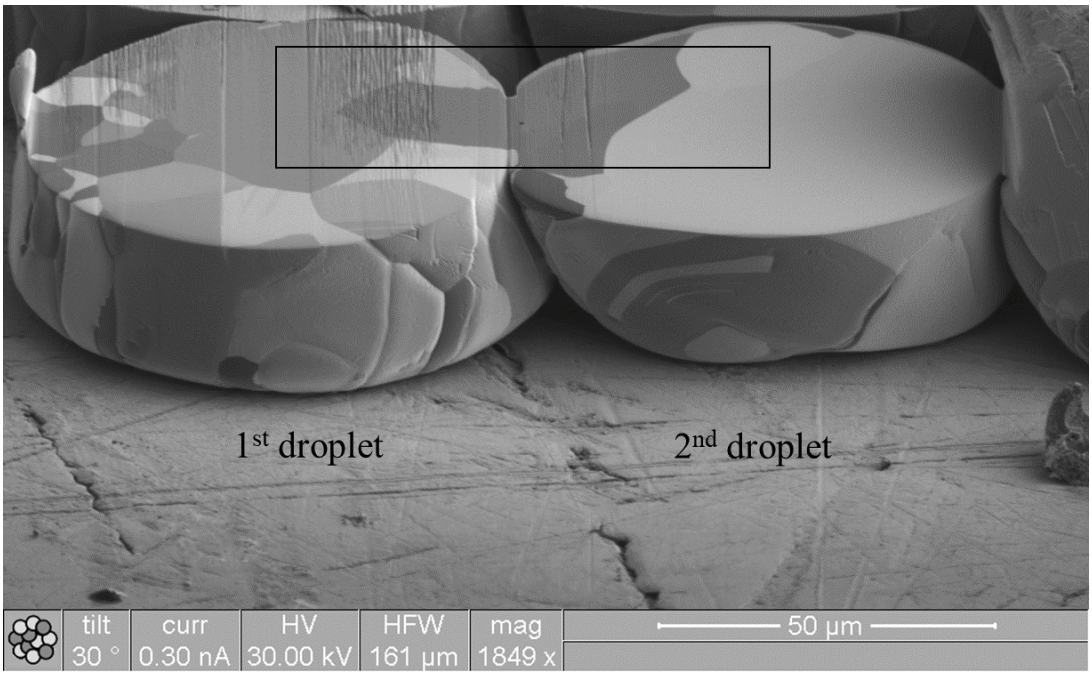


***Figure 7.1**: FIB-SEM cross-section of two successively deposited droplets demonstrating the lack of remelting at the interface between droplets, and various grain structures for the first and the second droplet.*

To clarify this observation, an EBSD analysis was conducted in the zone indicated with the black square in Figure **7.1**. The inverse pole figure map (IPF) in the transversal direction (X) of the cross-sectioned sample is shown in **Figure 7.2**. The IPF is a colour-coded representation of the crystallographic orientation of each scanned pixel with respect to a particular spatial coordinate. Here, the X direction corresponds to the heat flux direction at the inter-droplet interface zone. It is confirmed that $droplet_2$ does not melt $droplet_1$ at their interface to from common grains. Moreover, the crystal orientations of interfacial grains are dissimilar, which indicates the absence of epitaxial growth, hence inter-diffusion has not actually happened at the interface as previously thought. Despite the random grain orientation at the interface of the droplets and substrate, low-angle grain boundaries at the interface between droplets were observed.

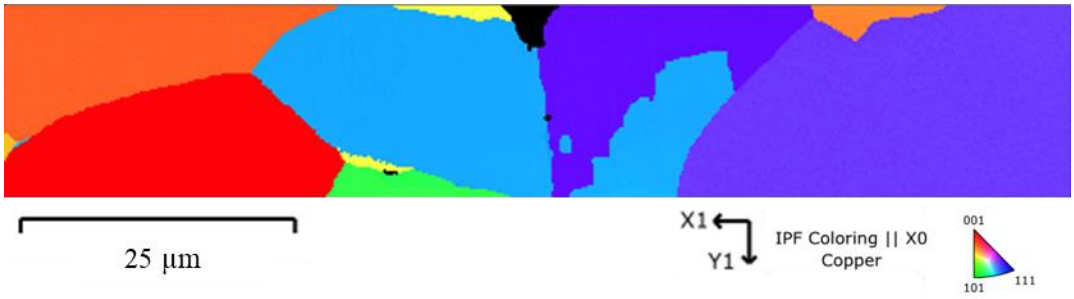


Figure 7.2- *EBSD IPF-X map of two successively deposited droplets in the region highlighted in figure 103 indicating the absence of epitaxy at the interface between droplets.*

Cross-sectional views of the temperature profile within the droplets and the substrate during the cooling of the second droplet are demonstrated in **Figure 7.3 a:c**. $Droplet_2$ loses heat through contact with the substrate and the preceding droplet, which have already cooled down to the substrate's pre-set temperature. $Droplet_2$ solidifies in a layer-by-layer fashion, bottom-up and side-to-side. During cooling, $droplet_2$ reheats the substrate, $droplet_1$, and also the substrate in contact with $droplet_1$. $Droplet_1$ is entirely reheated to some extent, however, the interface with $droplet_2$ is where the highest temperature is attained (**Figure 7.3 d**). It is also seen that the top section of the interface of the droplets is heated to the highest value of 833 °C, while closer to the

substrate interface, the maximum temperature is 825°C. Indeed, in the top segment, the energy transformed into $droplet_1$ through the interface is uniquely invested in heating this zone, whereas in the bottom section, this energy is split into heating the substrate and $droplet_1$.

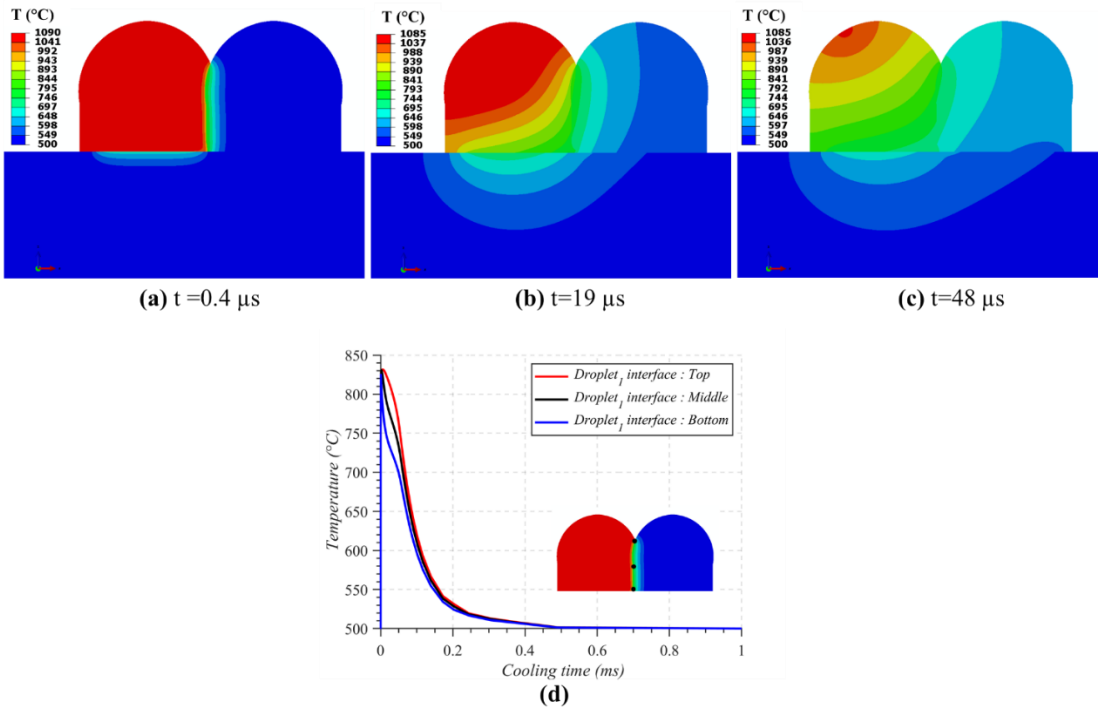


Figure 7.3- *Cross-section profile views of temperature whilst second droplet solidification, taken at a real-time of* ***a)*** *t=0.4 µs,* ***b)*** *t=19 µs,* ***c)*** *t=48 µs,* ***d)*** *temperature evolution of various nodes at* $droplet_1$*'s interface with* $droplet_2$ *in the bottom, middle, and top sections.*

During the cooling of the second droplet, the substrate temperature reaches the highest value of 763 °C at the interface with $droplet_2$ while this value was 766 °C at the interface with $droplet_1$ during cooling of the first droplet. This slight difference is due to the inter-droplet heat exchange during the cooling of $droplet_2$. Also, as depicted in **Figure 7.4**, the cooling rates of the first and second droplets at the central node are slightly different. The faster cooling of $droplet_2$ is justified by its increased contact with colder surfaces.

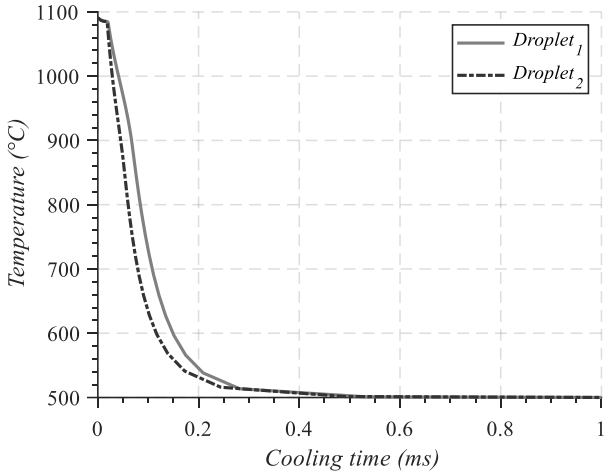


***Figure 7.4**- Temperature evolution of nodes at the centre of droplets during the deposition of $droplet_1$ and $droplet_2$.*

The thermal resistance at the interface between the droplets is lower than that at the substrate interface due to the surface roughness dissimilarity. The surface of solidified droplets is smoother compared to the surface of polished substrates. Although the $droplet_1$'s surface is not perfectly flat due to the solidification ripples, it does not induce a significant contact resistance at the droplets' interface since the molten droplet can spread in between the ridges and fill the gaps. Contrarily, the microscale and nanoscale asperities present on the substrate surface act as a thermal exchange barrier because they cannot be filled with liquid metal due to its high surface tension. In addition, the bottom segment of the droplets, where two droplets come into contact, is ripple-free. Consequently, the interface between droplets reaches a higher temperature of 833 °C, compared to 763 °C at the substrate interface. This is possibly the reason for the formation of elongated grains with low-angle boundaries at the inter-droplet interface compared to the heterogonous grains at the droplet-substrate interface.

7.1.1. Effects of substrate temperature on inter-droplet bonding

Due to the insufficient inter-droplet bonding, the system was upgraded to provide the possibility of preheating the substrate to the maximum temperature of 800 °C. Droplets at the same deposition conditions as in the previous section were deposited

on the substrate at 750°C to investigate the influence of higher substrate temperatures on inter-droplet bonding. The FIB-SEM cross-section in **Figure 7.5** shows that grains in the second droplets are nucleated in continuation with the initial droplet (grain-sharing). However, similar to the substrate at 500 °C, the border between droplets is visible at the interface. Further EBSD analysis was required to confirm this hypothesis.

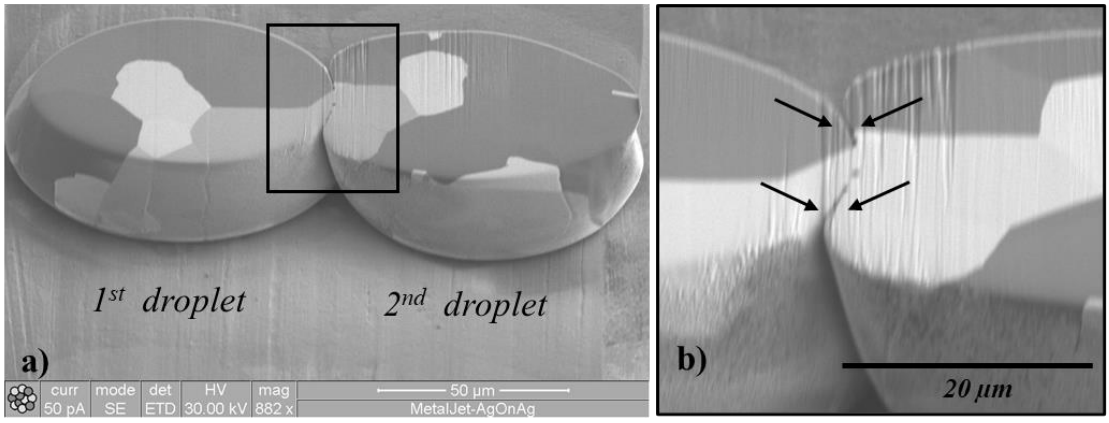


***Figure 7.5**- FIB-SEM cross-section of two successively deposited Cu droplets onto a Cu substrate at 750 °C, EBSD IPF-X map over the cross-sectioned area.*

Figure 7.6 demonstrates the IPF-X map from the EBSD scan conducted on the cross-sectioned area presented in Figure **7.5**. Surprisingly, the grains at the interface of droplets share the same crystal orientation, where the solidifying metal assumes a crystallographic orientation identical to that of the adjoining droplet at the interface. The epitaxial growth signifies that the conditions for an inter-diffusion were present at the interface. Indeed, the focused heat source provided by the molten droplet and a steep temperature gradient parallel to the built direction (X-direction) contributed to the epitaxial crystal growth with the orientation of the previously deposited droplet. The epitaxial growth has also been observed in the "epitaxial laser metal forming" [271], thermal spraying [272] and DED processes [273].

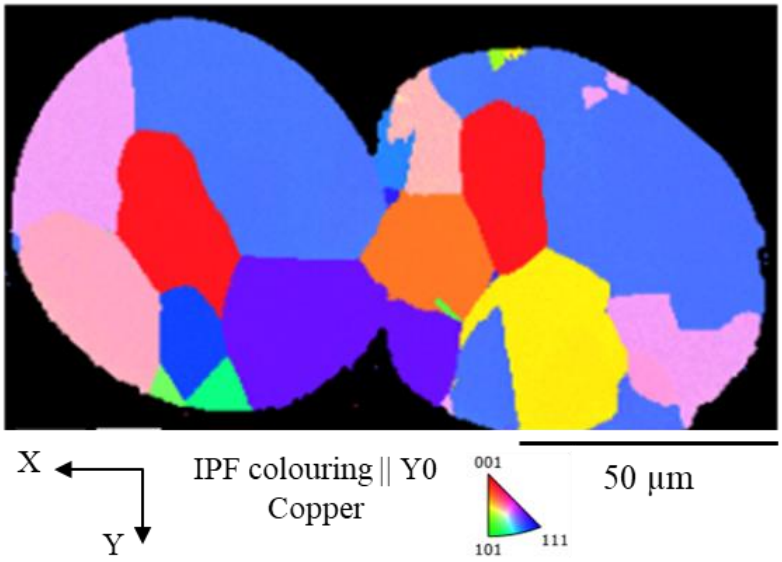


***Figure 7.6**- EBSD IPF-X map of two successively deposited droplets shown in Figure **7.5** indicating an epitaxial growth from the interface of the previously deposited droplet.*

A second EBSD scan was performed on the second pair of droplets deposited at the same condition to confirm the results. It can be seen in **Figure 7.7** that the crystal orientation of the second droplet is almost identical to that of the previously deposited droplet, signifying the epitaxial growth of the grains at the inter-droplet interface. The epitaxial growth of the solidification from the interface is in contrast with the previously discussed results at lower substrate temperatures, where new grains nucleated from the interface of the substrate. This signifies that the condition for such growth has been only provided at higher substrate temperatures.

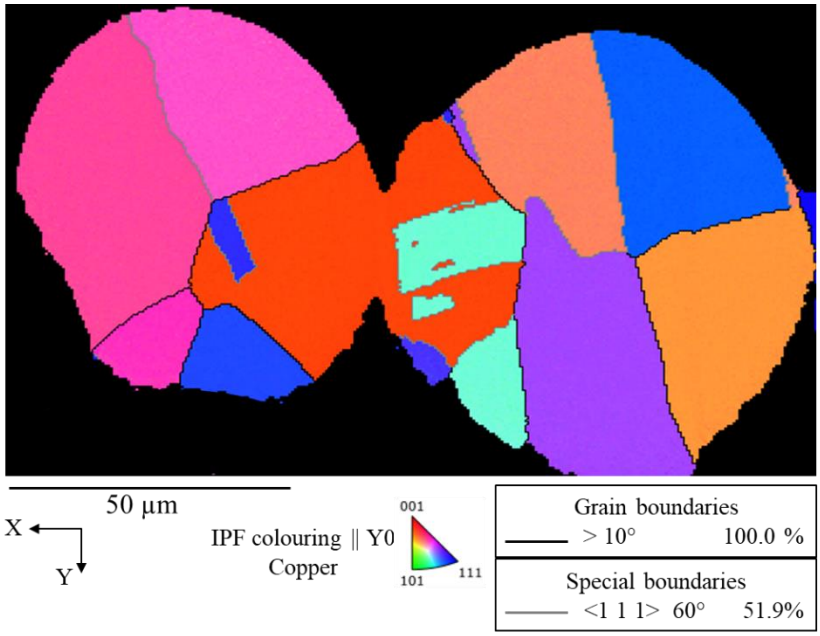


***Figure 7.7**- EBSD-IPF-X map two successively deposited droplets with highlighted grain boundaries and special boundaries indicating twin boundaries at the inter-droplet interface.*

The partially remelted dendrites at the interface have served as the nuclei for directional crystal growth along the dominant thermal gradient direction. What stands out from **Figure 7.7** is the presence of some regions which resembled twin boundaries, including those close to the interface between droplets. The data analysis using AZtecCrystal was performed to observe the grain boundaries and the results confirmed that some of the grain boundaries are Sigma 3, <111> 60°. These twin boundaries are shown in grey, and other grain boundaries in black. No grain boundary between the previously deposited droplet and the new deposit is perceptible, and the interface between droplets consists of a single large grain. This is expected to provide a stronger bonding at the droplets' interface. These results corroborate the findings of Juang et al. [274] and Liu et al. [275], which showed that direct bonding of <111> oriented Cu surfaces were feasible at lower temperatures. It was discussed that the surface diffusion coefficient of <111> oriented Cu surfaces is three to four orders of magnitude faster compared to the standard surfaces.

7.2. Tin inter-droplet bonding

It was shown that the mechanism of substrate-droplet bonding at the dissimilar material deposition is through diffusion. This section investigates the mechanism of inter-droplet bonding for such conditions. For this purpose, the top section of two Sn droplets deposited successively with a frequency of 500 Hz and a centre-to-centre distance of 55 µm was removed and imaged. From the side-view FIB-SEM image of droplets in **Figure 7.8 a,** it seems that necking has occurred. The second droplet has solidified from the contact area with the first droplets and substrate, as evidenced by the solidification ripples grown vertically and horizontally. The FIB-SEM image of the cross-section in **Figure 7.8 b** demonstrates that the interface between droplets was entirely remelted, hence, a strong bonding is expected. Moreover, columnar grains of tens of micrometre parallel to the heat transfer direction are observed in both droplets. Numerical simulation results presented in **Figure 7.8 c** confirm that the temperature exceeded the material's melting point at the droplets' interface. It is also seen that the remelting depth was ~12 µm from the interface to the first droplet. In order to visualize the numerical results, the first droplet's borders are highlighted in white, and the border of the second droplet, including the remelting zone, is highlighted in black. A good agreement between computational results and experimental work is observed.

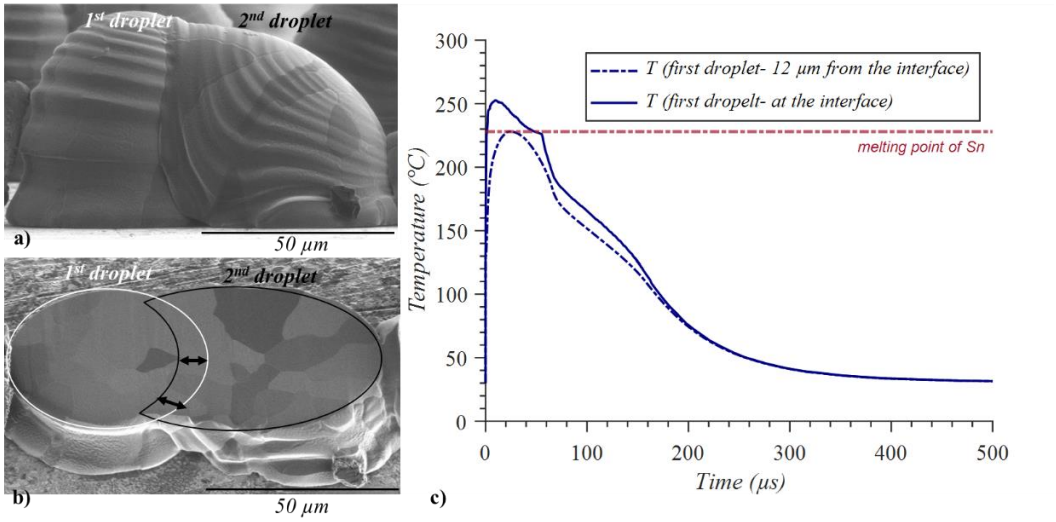


Figure 7.8*- a) FIB-SEM image of two successively deposited Sn droplets ejected at 670 °C on a Cu substrate at 30 °C, b) FIB-SEM image of the cross-section demonstrating a strong inter-droplet bonding through remelting, b) temperature evolution of a central node at* $droplet_1$*'s interface with* $droplet_2$.

The droplet-substrate bonding at low substrate temperatures was insufficient, such that droplets were easily peeled off from the substrate. Hence, it was necessary to increase the substrate temperature, even though a strong metallurgical inter-droplet bonding was obtained at lower temperatures. Thus, the effects of higher substrate temperature on inter-droplet adhesion should be investigated. To this aim, droplets at the same condition were deposited onto the substrate at 130 °C. The side view image of the successively deposited droplets in **Figure 7.9** a demonstrates necking between the droplets. **Figure 7.9** b shows that the interface between droplets was remelted with a larger remelting depth compared to the low-temperature substrate. According to the numerical simulations, 25 µm from the interface was remelted in the first droplets, which agrees with the experimental observations. One striking piece of information was the grain microstructure in **Figure 7.9**, which differs remarkably from the one in **Figure 7.8**. While the droplets at 130 °C consist of very few large grains, many refined columnar grains were observed in droplets deposited at 30 °C substrates. The larger grain at high substrate temperature is attributed to the slower cooling rate, whereas high-temperature gradient and fast solidification rates triggered fine grains at low substrate temperature.

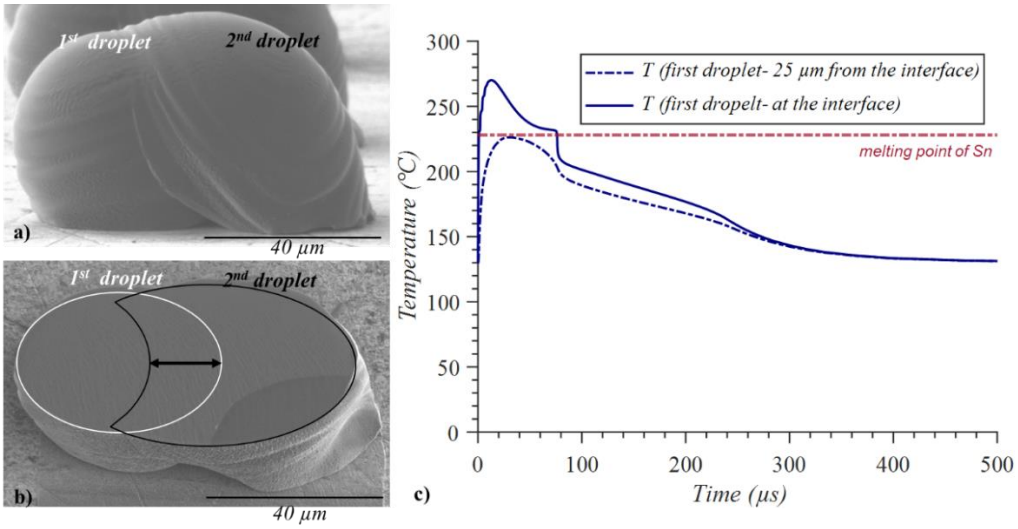


Figure 7.9*- a) FIB-SEM cross-section of two successively deposited Sn droplets ejected at 670 °C on a Cu substrate at 130 °C, demonstrating a strong inter-droplet bonding through remelting, b) temperature evolution of a central node at* $droplet_1$*'s interface with* $droplet_2$*.*

7.3. Silver inter-droplet bonding

The results in section 6.1.3, regarding the deposition of Ag droplets at 1200 °C on an Ag substrate at 775 °C showed that the substrate interface was melted during the deposition of droplets, and a strong metallurgical bonding was obtained. Consequently, a good inter-droplet bonding is expected since the temperature at the interface exceeds the material's melting point, according to the numerical results. To evidence it, the interface between two droplets was cross-sectioned vertically, as shown in **Figure 7.10**. It is seen that the interface was entirely remelted, and no pore or void is observed in the contact zone. However, the inter-droplet void at the substrate is observed, where the second droplet could not fill the space between the curved surface of the initial droplet and the substrate. The high surface tension of Ag and the contact line pinning to the substrate at immensely high rates contributed to this observation.

What can be seen in **Figure 7.10** is the formation of a unique large grain, which can be attributed to several factors. (I) Droplets did not experience a high-temperature gradient (187 °C) due to the high temperature of the substrate. (II) the interfaces were

fully remelted during the deposition of droplets, hence, there is not a large number of nucleation sites for the formation of fine grains. In the earlier investigation by Simonelli et al. [11], the lack of remelting between Ag microdroplets on a Cu substrate at 500 °C caused low structural integrity and a low density in the printed parts. The droplets were not necking in their study, and inter-droplet pores were present in the cross-sectioned areas. Interestingly, there is no sign of so-called cold laps, previously reported in DoD-MJ processes [61], [143], [200]. Cold laps are formed as a result of liquid metal not being able to fill the space between the solidification ripples, leaving inter-droplet pores at the interfaces.

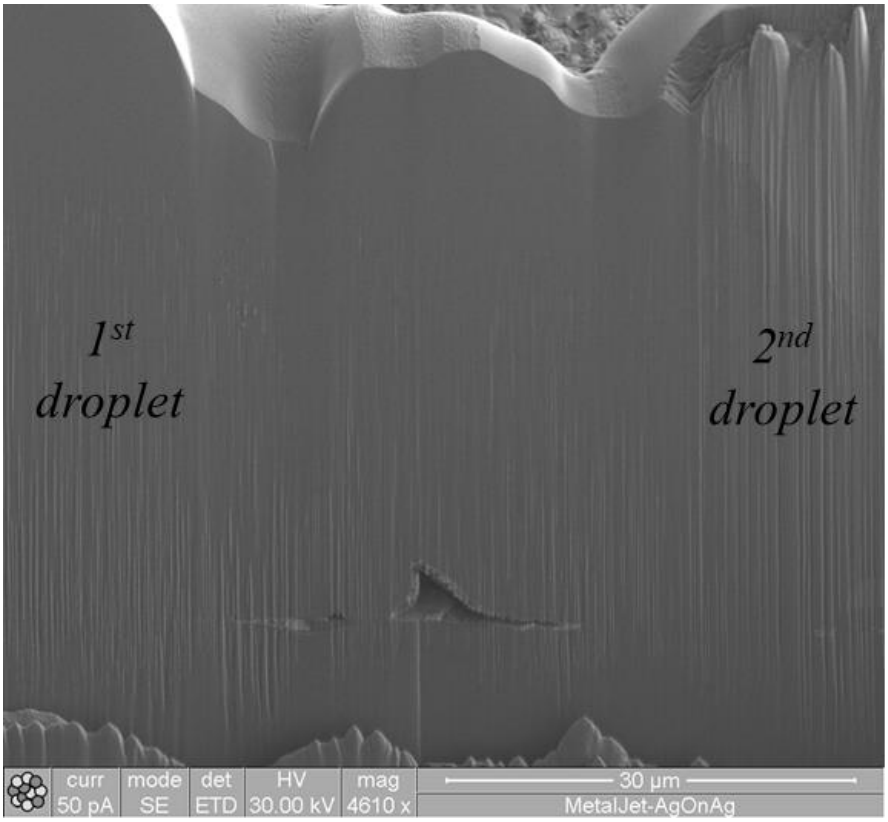


***Figure 7.10**- FIB-SEM vertical cross-section of two successively deposited Ag droplets at 1200 ℃ on an Ag substrate at 775 ℃, demonstrating a strong inter-droplet bonding through remelting.*

A 3D structure was printed at the same deposition conditions to evaluate the inter-droplet bonding in the normal direction to the substrate. **Figure 7.11** b shows FIB ion

channelling contrast images of the cross-section between three layers. The interface between these layers is remelted, therefore, a strong bonding is expected. Even though these results are very encouraging, the 3D structure in **Figure 7.11** a is not fully packed due to the unfilled space between droplets. These gaps result from simple linear voxel by voxel deposition strategy and are expected to improve by staggered deposition strategy and optimal inter-droplet spacing. The further increase of the substrate temperature to 775 °C in the current study enabled the eradication of the previously-reported [11] lack of consolidation between Ag droplets. Supplementary investigations on optimising the printing strategies are required to improve parts' aspect ratio and density. Yet, this study is a clear step toward directly printing high-temperature metallic 3D parts of high integrity.

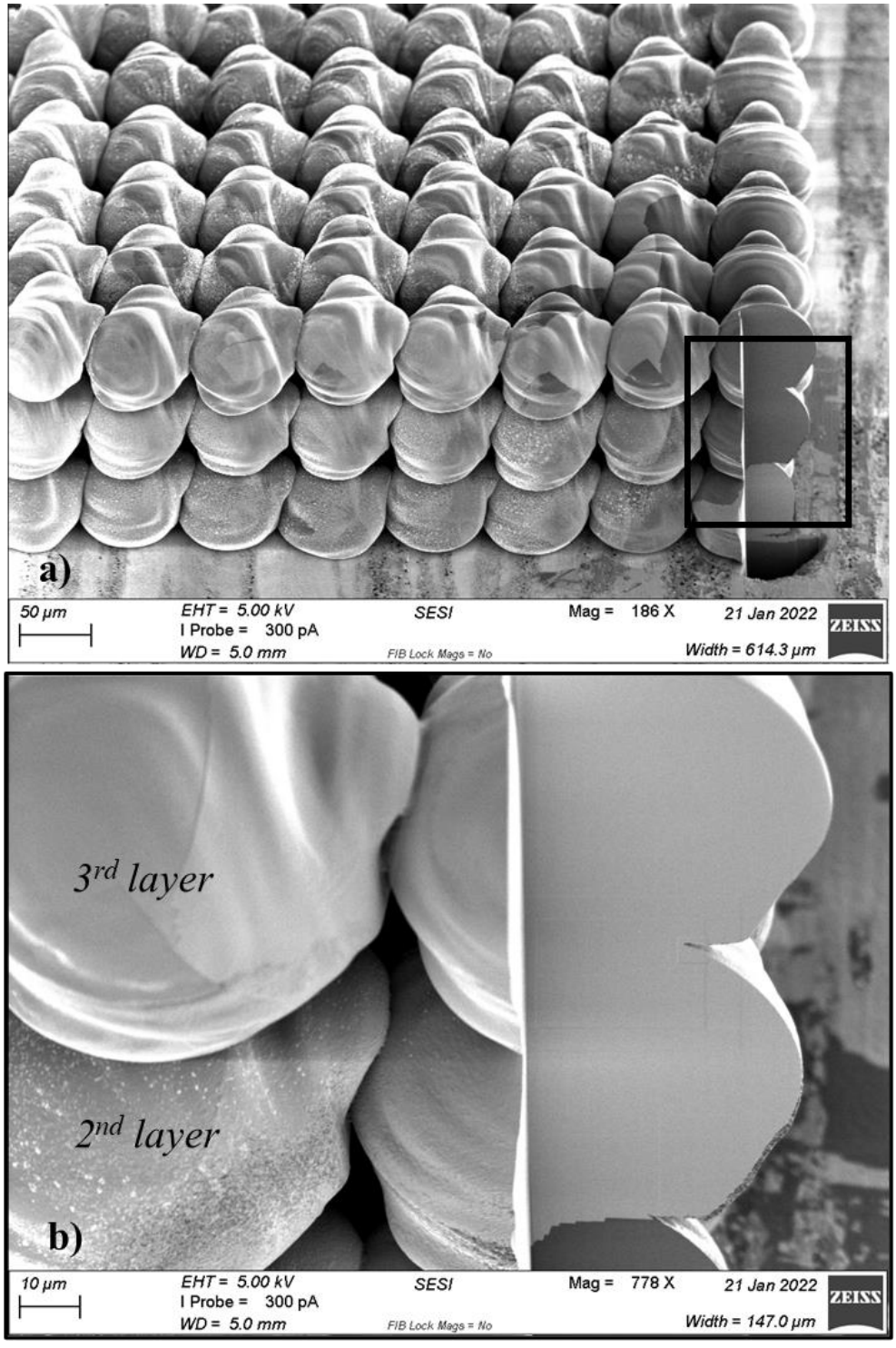


Figure 7.11- *a) FIB-SEM image of a 3D structure in Ag at 1200 ℃ on an Ag substrate at 775 ℃, b) cross-section of the zone highlighted with a black square, demonstrating a strong inter-droplet bonding through remelting.*

7.4. Summary

The interfaces formed during the deposition of low to high-temperature materials (Sn, Ag, and Cu) using the MetalJet process at the droplet-droplet level and the final microstructure were investigated in this chapter. It was demonstrated that the interface formation between droplets requires fewer initial thermal energies than that of droplet and substrate, which could be attributed to three factors: (I) the surface of previously deposited are smoother than the substrate, and hence the thermal resistivity is lower at the inter-droplet interfaces, (II) the surface of droplets are oxide-free, whereas the etched/ or polished substrate could still react with the oxygen in the short time before the installation of the substrate inside the glove box, and (III) the grain structure, size, and direction of the surface on which the liquid material is deposited has a critical role in the diffusion of atoms and consequently epitaxial growth.

The developed numerical brought understanding to the experimental observation for the materials under investigation in this thesis. The verified model can be used to predict the process parameters required to obtain a strong metallurgical bonding between the droplets of new materials. This is a valuable tool to expand the palette of materials used in the context of DoD-MJ. For this purpose, the thermophysical properties of materials of interest are required. Moreover, the model can be used to predict the necessary process parameters to acquire a strong bonding in 3D since the underlying physic of bonding at the interfaces is similar. Overall, the work presented here can be used to study the inter-droplet interface formation for the MetalJet process and is scalable to be used in the context of any metal droplet deposition process.

The specific outcomes of the study are listed as follows:

- Even though a strong droplet-to-droplet bonding through remelting or epitaxial growth at the droplets' interface was not achieved for the Cu material deposited onto a substrate at 500 °C, the numerical results showed the higher interfacial temperatures in this zone provide a better level of bonding compared to the droplet-substrate bonding. The FIB-SEM images also confirmed this, where elongated grains with low-angle boundaries were observed at the inter-droplet interface.

- Furthermore, the higher temperature at the interface between the Cu droplets deposited onto a Cu substrate at 750 °C provided the condition for an epitaxial crystal growth with the orientation of the previously deposited droplet. Hence, a more robust level of bonding is expected under this condition.
- A strong inter-droplet bonding for low-temperature metal (Sn) was obtained regardless of the substrate temperature due to the ejection temperature being three times higher than the material's melting point. Furthermore, it was observed that the depth of remelting was increased at higher substrate temperatures.
- Interestingly, the microstructure of the dual Sn droplets at higher temperatures consisted of very few large grains, whereas many refined columnar grains were observed in droplets deposited onto substrates at lower temperatures. The variation between the cooling rates, direction and level of temperature gradients led to these observations.
- It was reported that for the first time, the fabrication of fully dense parts with high structural integrities on high-temperature metal could be obtained. This was possible due to the strong inter-droplet bonding through the remelting at the droplet interface of Ag material deposited onto an Ag substrate at high temperatures.

8. Residual Stress Evolution in the MetalJet Process: Copper

Residual stresses and stress gradients are of great importance in all manufacturing processes since they affect mechanical performances, structural stabilities, and the lifetime of fabricated parts. If the residual stresses are too high, they cause failure, even at small loads. An inherent issue of the DoD-MJ processes is the generation of thermal stresses during the solidification and cooling of droplets at successive deposition. Warping, delamination, cracking, and dimensional tolerance losses are the main detrimental effects of the thermally residual stresses in the process. Although some levels of warping can be tolerated for some specific applications, direct printing of functional parts does not tolerate warping or delamination. Several mechanisms contribute to the evolution of residual stresses during the deposition process, which must be fully understood at the first step in order to control them.

As demonstrated in **Figure 8.1**, this chapter uses a sequentially coupled thermomechanical modelling to explain the physical mechanism of residual stress generation during the metal deposition process. The modelling results are used to explain the experimentally observed delamination at the interface of the Cu droplets

with the Cu substrates. Furthermore, an effort was made to indicate solutions to rectify these issues through virtual experiments, hence providing a basis for a more targeted experimental investigation. **Table 8.1** summarizes the set of parameters used in this study.

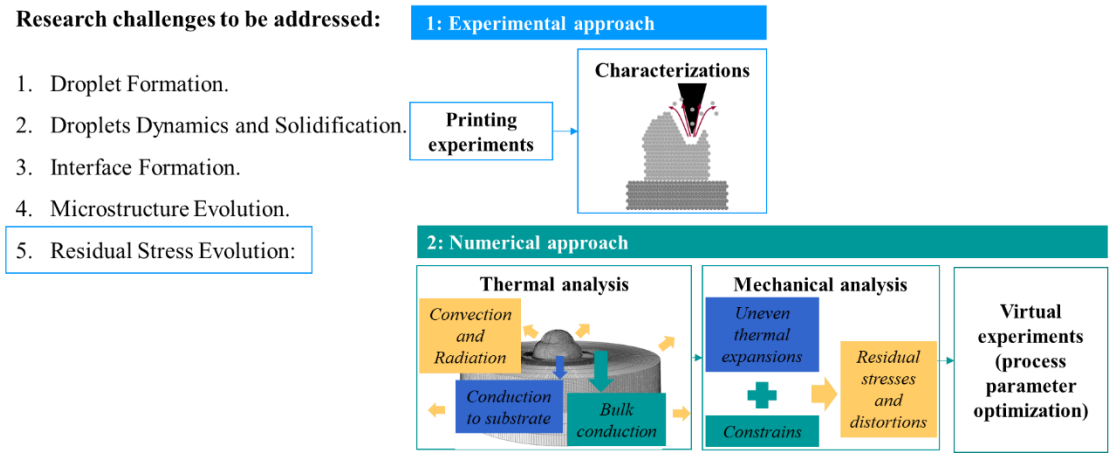


***Figure 8.1**- The fifth challenge in DoD-MJ and the methodology implied in this thesis to address it, referring to Figure 52.*

***Table 8.1**- Specific set of parameters to investigate the residual stresses evolution during the solidification of Cu droplets on Cu substrates.*

1. The **mechanism** of residual stress generation during droplet deposition
2. Effects of **substrate** temperature
3. Effects of droplet **temperature**
4. Effects of surface **roughness**

	Ejection temperature	Deposition temperature	Substrate temperature	Surface roughness	Droplet temperature
1	1130 °C	1090 °C	500 °C	0.01 µm	1090 °C
2			30 °C-800 °C	0.01 µm	1090 °C
3			750 °C	0.01 µm-0.1 µm	1090 °C
4			750 °C	0.01 µm	1090 °C-1690 °C

8.1. Residual stress generation during a single droplet deposition

The non-uniform temperature distribution in the droplet on cooling and between the droplet and substrate results in differential thermal contractions and, consequently,

transient residual stress. A high gradient of residual stresses at the substrate-droplet interface can cause the separation of the droplet from the substrate, i.e., delamination. This was experimentally observed in the deposition of Cu droplets onto a Cu substrate with the process parameters mentioned in the first line of **Table 8.1**. The cross-sectional SEM images of a single droplet, where 16 µm and 20 µm from the edge were removed, are shown in **Figure 8.2 a-b**, respectively. The droplet seems to be detached from the substrate in **Figure 8.2 a**, while in **Figure 8.2 b**, it is partially bonded to the substrate in the central region and de-bonded at the edges. In **Figure 8.2 c**, further material was removed to a depth of 45 µm from the edge. It is seen that the de-bonded region at the edge was persistent. In general, it seems the droplet is lifted from the substrate at the free edges, and the separation subsequently propagates toward the centre of the droplet. The source of such phenomenon is probably the residual stresses; hence, it is essential to understand how they develop in order to mitigate their consequences.

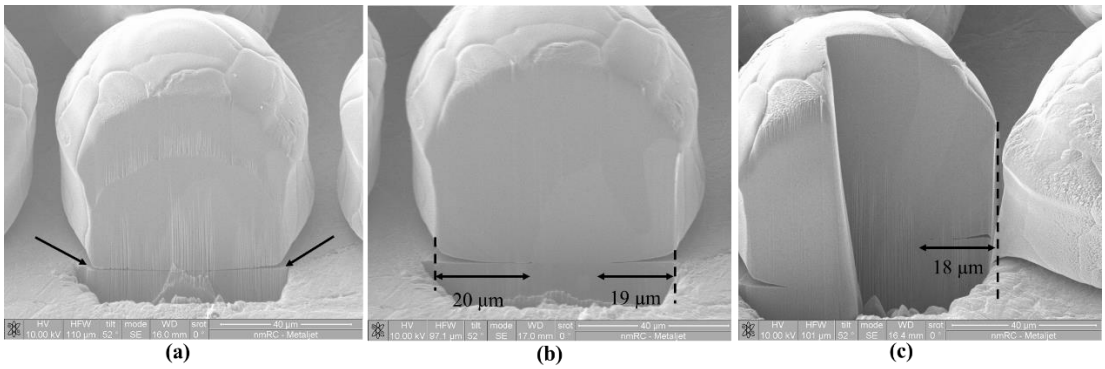
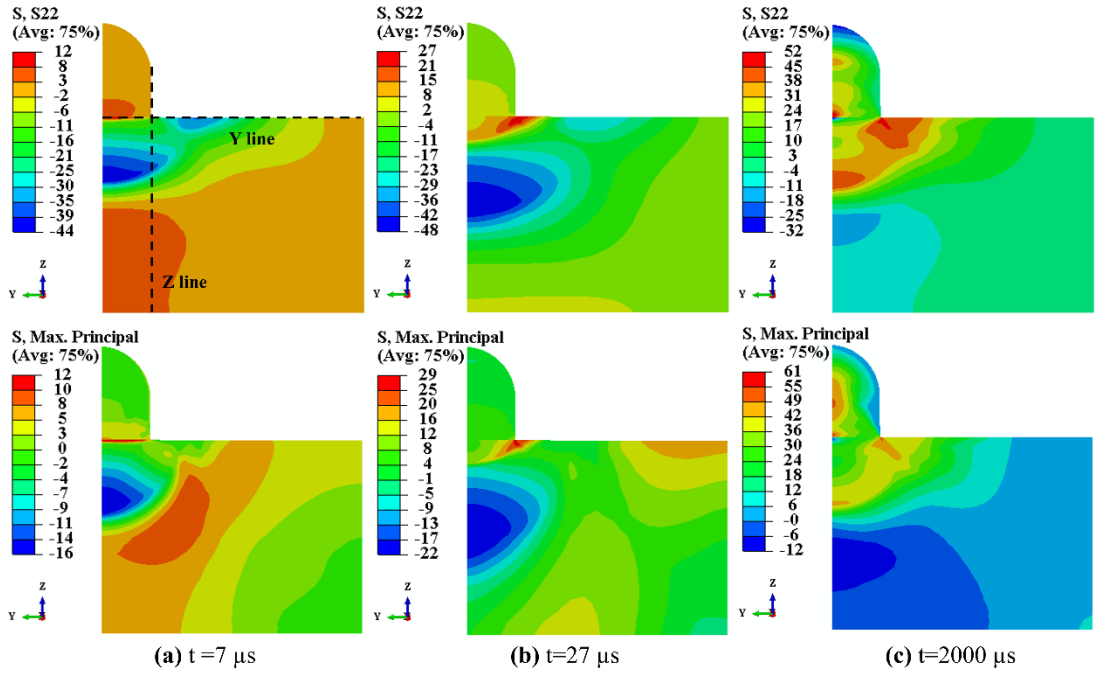


Figure 8.2*- SEM cross-section of individual Cu droplet after FIB milling of :* ***a)*** *16 µm,* ***b)*** *20 µm,* ***c)*** *45 µm from the edge showing the partial delamination of the droplet from the substrate.*

Figure 8.3 a-c illustrates the transversal (σ_{yy}) and maximum principal stress fields in the droplet and substrate on the Y-Z plane at various time frames (refer to the timelines in Figure **6.3**). As soon as the high-temperature droplet is deposited onto the relatively cooler substrate, it starts to solidify in the interface region, and tensile stresses develop in the droplet, resulting from the substrate constraining the thermal contraction due to cooling. The substrate, however, experiences an initial phase of heating due to the

thermal exchange with the high-temperature droplet, until it reaches a maximum temperature and then cools down to the temperature at its bottom face (500°C).

These heating and cooling cycles occur alternatively in different zones of the substrate. Initially, the top portion of the substrate is heated up to the maximum temperature; this hot region is constrained from a free expansion by the relatively colder portion of the substrate at the bottom, which leads to compressive stresses in this area. Subsequently, the substrate, along with the droplet, cool down to the pre-set temperature. In this phase, the tensile stresses are developed in the top portion of the substrate while the bottom portion is under compression. The cool-down to ambient temperature is not discussed in this study since the droplet and substrate temperatures are already uniform at this stage, thus, the further induced residual stresses are not critical. It should be noted that due to the assumed condition of perfect bonding, strain values are equal at the interface, while they are not necessarily continuous because of the temperature gradient at the interface.



(a) t =7 µs **(b)** t=27 µs **(c)** t=2000 µs

Figure 8.3- *σ_{yy} and $\sigma_{Max\ pricncipal\ stress}$ fields (MPa) in the Y-Z plane whilst first droplet cooling at real-time of **a)** t=7 µs, **b)** t=27 µs, and **c)** t=2000 µs after deposition.*

The cross-sectional views of the droplet's deformation (µm) in the Y direction at various times are depicted in **Figure 8.4 a -c**. For better visualisation, the distortion

was exaggerated by a factor of 20. As the droplet cooled down bottom-up, it underwent uneven thermal contractions. At only 7 µs from droplet deposition (**Figure 8.4 a**), the solidified material close to the interface contracted, particularly at the periphery of the droplet. Concurrently, the substrate interface, which was bonded to the droplet, experienced an expansion as a result of the droplet's heat dissipation into the substrate. As the cooling continued to the top layers of the droplet, the contraction zones expanded. It can be seen in **Figure 8.4 c** that the droplet shrank in the Z and radial directions, where the maximum deformation in Y-direction was 0.63 µm at the steady-state.

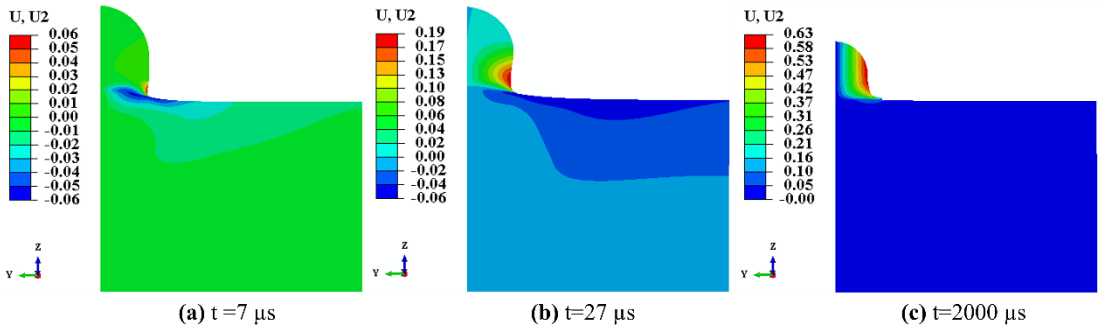


***Figure 8.4**- Droplet's deformation in µm in Y direction exaggerated 20 times at **a)** 7 µs, **b)** 27 µs, **c)** 2000 µs after deposition.*

Figure 8.5 schematically describes the edge delamination process, which is likely to occur during the early stages of solidification, where only a thin layer of the droplet in the vicinity of the interface has solidified. The bending moments created due to uneven contraction and expansion in these regions act as a driving force to lift the droplet at its edges. This happens only if the bending forces are greater than the adhesion forces. As the heat transfer proceeds, these interfacial cracks propagate from the droplet's edges toward the centre.

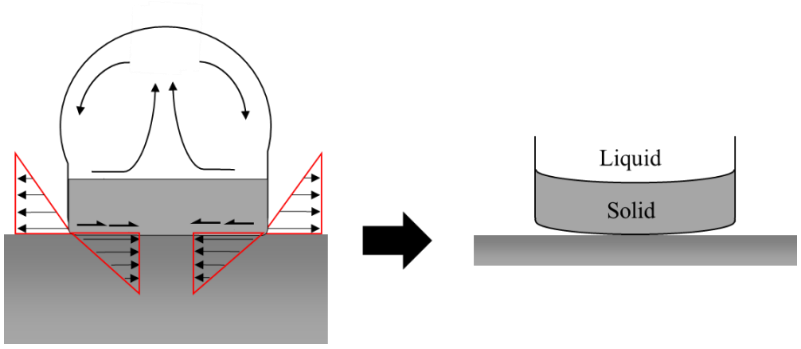


***Figure 8.5**- Schematic representation of the residual stresses in the droplet and substrate during the early stage of solidification, yielding to edge curling.*

In order to quantify the likelihood of delamination, the maximum principal stress to temperature-dependent yield strength ratio is used in this study. Similar criteria are used in other processes, such as laser-assisted AM technologies [276]–[278], thin films [279], and thermal spraying [280], [281]. Delamination is likely to occur when the longitudinal residual stress value is higher than the room temperature yield strength and close to the ultimate tensile strength. In the case under investigation in this study, this ratio at the Y and Z lines indicated in Figure **8.3** are shown in **Figure 8.6 a-b.** Here, if this ratio is greater than one, the magnitude of the principal stress exceeds the metal's yield strength, and it is assumed that delamination is likely to occur. It is seen that the failure limit at the interface of droplet and substrate is attained at only 27 µs after the droplet deposition. These results can explain the experimental observation in Figure **8.2**.

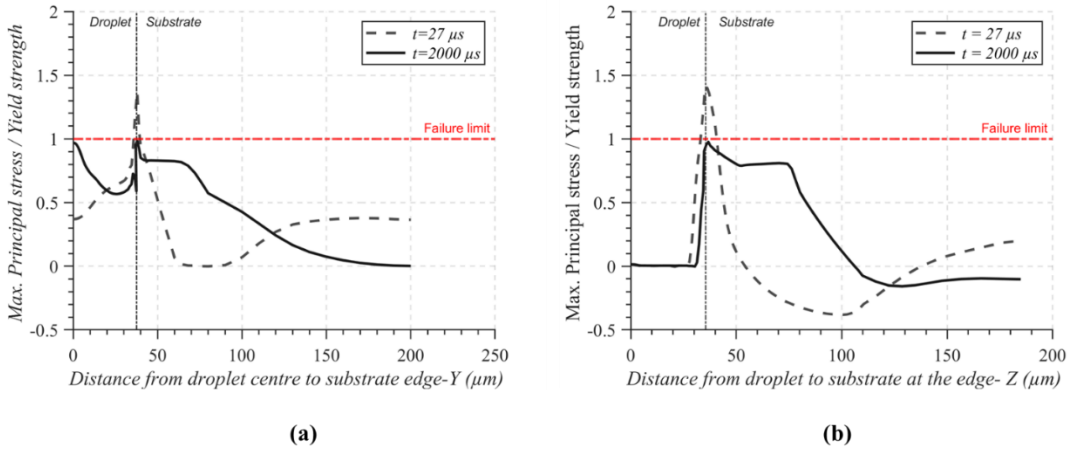


***Figure 8.6**- The maximum principal stress to temperature-dependent yield strength ratio in **a)** the radial path at the interface of droplet and substrate (Y line shown in Figure 11), **b)** droplet and substrate thickness at the edge (Z line shown in Figure 11).*

8.2. Effects of various process parameters on residual stresses

In this section, the effects of three process parameters, which are assumed to be the most influencing ones concerning residual stress evolution, are investigated through sets of virtual experiments. The objective is to provide solutions to resolve the previously explained residual stresses-related issues in the MetalJet process.

8.2.1. Effect of initial substrate temperature

The lowest substrate temperature, i.e., room temperature, the maximum substrate temperature before the system upgrade (500 °C) and the highest substrate temperatures (800 °C) after the upgrade were simulated to investigate the effects of substrate temperature in residual stress evolution. The second line in **Table 8.1**. Results will be compared against the substrate at 800 °C, which will only be achievable by modifying the system. The average cooling rate of the droplet increases as the substrate temperature decreases, where it is 7.92×10^3 °C /ms for $T_{substarte} = 30$ °C versus 8.64×10^2 °C/ms for $T_{substarte} = 800\ °C$ (**Figure 8.7** a). The interface temperature reached only 462 °C when the substrate was at 30 °C, while it raised to 941°C for the substrate at 800 °C (**Figure 8.7** b). It was shown in Section 6.1.1 that substrate preheating improved the droplet-substrate bonding, however, a strong metallurgical bonding through substrate fusion was not possible at this temperature.

The maximum principal stress to temperature-dependent yield strength ratio for various substrate temperatures at time frames, which corresponds to similar temperatures at the interface, is shown in **Figure 8.7** c-d. It is seen that by increasing the substrate's initial temperature from 30 °C to 800 °C, residual stresses at the interface are significantly reduced. Moreover, at 800 °C, the residual stresses at the critical zones remain below the failure limit. This suggests that delamination is less likely to occur at higher substrate temperatures. A similar effect has been reported in the literature for other conventional manufacturing and AM processes, such as welding, thermal spraying [282], micro casting [38], DED [276], and L-PBF processes [283]. In DoD-MJ, increasing the initial substrate temperature has the twofold benefit of improving the bonding and reducing the residual stresses, both of which reduce the risk of delamination.

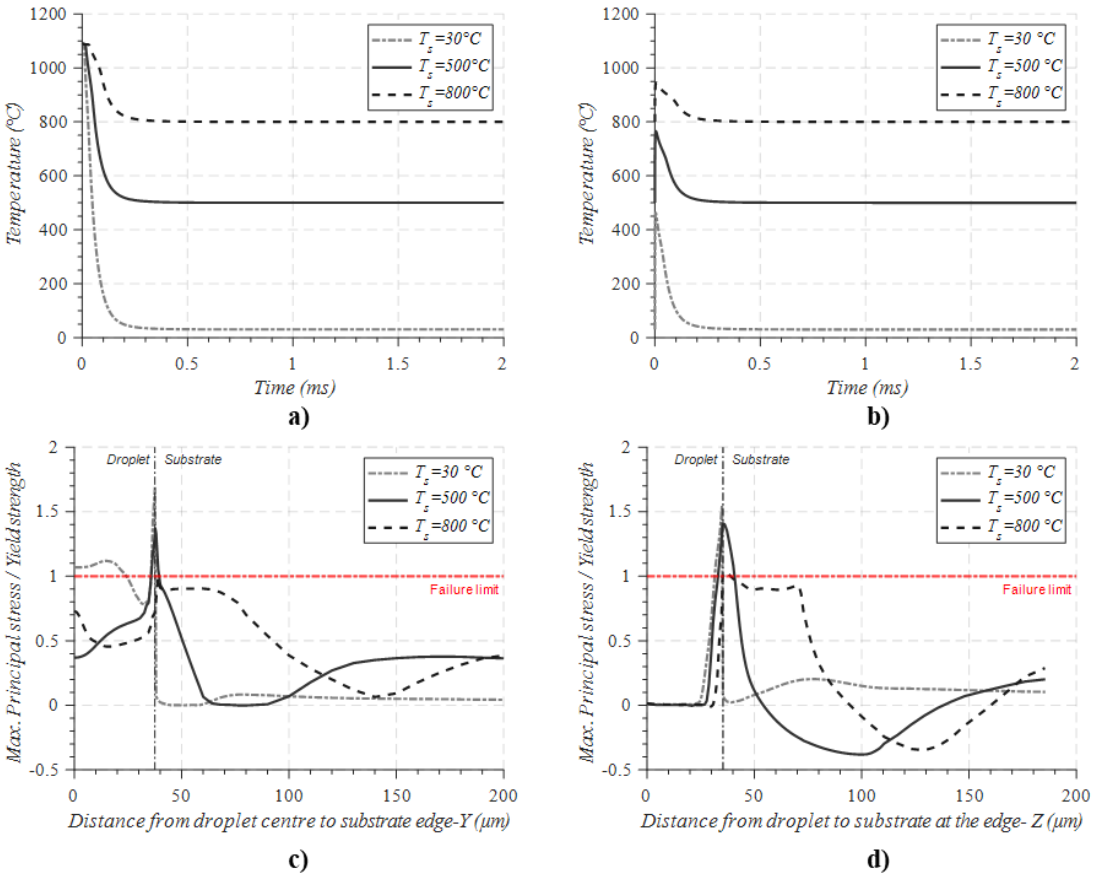


***Figure 8.7**- Temperature evolution for various substrate temperatures at **a)** the central node in the droplet, **b)** substrate interface. Maximum principal stress to temperature-dependent yield strength ratio for various substrate temperatures at time frames corresponding to similar interfacial*

*temperatures in **c)** the radial path at the interface of droplet and substrate (Y line shown in Figure 115), **d)** droplet and substrate thickness at the edge (Z line shown in Figure 115).*

8.2.2. Effect of initial droplet temperature (superheat)

The droplets deposited at higher temperatures contain higher initial thermal energies, which proved to be beneficial for promoting stronger adhesions to the substrates. In this section, the effect of higher droplet temperatures on residual stress evolution is investigated. It was noted that increasing the droplet temperature could cause challenges at the ejection level, in particular for high temperature materials such as Cu. Yet, computational modelling provides the possibility of investigating this process parameter virtually. The process parameters used in this study are presented in the third line of **Table 8.1**. The droplet cooling and substrate heating curves considering three different initial droplet temperatures are shown in **Figure 8.8** a-b. By increasing the droplet temperature from 1090 °C to 1390 °C, and 1690 °C, the maximum interfacial temperature increased from 756 °C to 820 °C and 903 °C, respectively. Therefore, it is more likely to form a strong bonding.

It was seen that by the increase of the $T_{substrate}$ in a step of 300 °C, the interfacial temperatures were increased 182 °C, whereas interface temperature was increased 64 °C when $T_{droplet}$ was increased 300 °C. Increasing the particle temperature is reported to improve the bonding level during thermal spray coating processes [5]. These curves are parallel to each other with an initial offset related to the different onset temperatures, implying that the droplet cooling rates are similar in these scenarios. It is seen that a considerable increase in superheat temperature has a slight influence on the cooling rate, which matches the results of Liu et al. [284]. They studied the effects of superheat temperature on the cooling speed of Ni droplets of 5 mm impacting onto a Cu substrate. It was understood that droplets with high superheat temperatures had higher cooling rates before the onset of the solidification. While after the solidification, droplet cooling was not much influenced by its initial temperature. Similar cooling rates could suggest that the final residual stress fields and amplitude should be similar for these cases. However, as seen in **Figure 8.8**, the likelihood of delamination decreases as the superheat temperature increases. This counterintuitive

result can be explained by the fact that the higher the droplet temperature, the higher the temperature to which the substrate is heated.

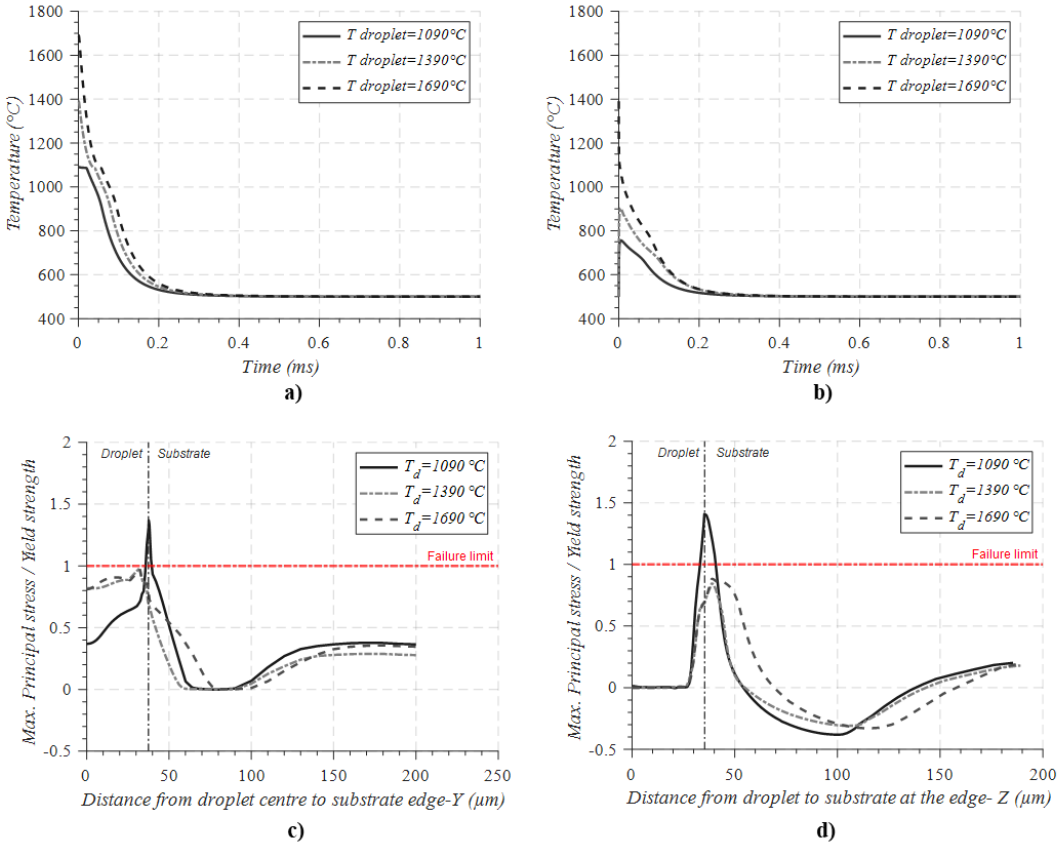


Figure 8.8*- Temperature evolution during droplet deposition considering different superheat temperatures for a node* ***a)*** *at the centre of the droplet and* ***b)*** *at the interface of the substrate with the droplet.*

8.2.3. Effect of surface roughness

It was seen in section 6.1.1 that the heterogeneities in the surface acted as pinning sites and caused local deformation in the droplet interface, which were frozen in place during the solidification. As a result, droplets were interlocked to the substrate and were more resistant to peeling than the droplets deposited on smoother surfaces. In this section, the residual stress evolution during the solidification of Cu droplets deposited onto substrates with various roughness (The fourth line in **Table 8.1**) is

discussed. It is acknowledged that these simulations do not take into account the spreading of droplets, hence only effects of surface roughness on the heat exchange and its consequent thermal stresses are considered. **Figure 8.9 a** displays the temperature evolution of a node in the centre of a droplet for substrates with surface roughness (R_a) values of 0.1 µm and 0.01 µm, which are the typical values for the substrates used in the MetalJet experiments. These two are compared against an ideal case where there is a perfect contact between the droplet and substrate, i.e., no thermal resistance. It is seen that the surface roughness impacts the efficiency of heat conduction between the droplet and the substrate. For a rougher surface, the droplet cools at a lower rate; consequently, the extent and amplitude of substrate heating are lower. **Figure 8.9 b** depicts the temperature evolution of the substrate at the interface for the same conditions. It is observed that even for a perfect contact condition, the substrate's temperature is considerably increased, but it does not rise to its melting point. If the surface roughness of the substrate is reduced by a factor of ten, the interfacial substrate temperature increases by 24%. As already discussed, a higher interfacial temperature is crucial in improving the bonding, hence the importance of utilising finely polished substrates. Moreover, inhomogeneous crystal growth at the interface could potentially be reduced by using a substrate with fewer defects.

Due to the slower cooling rate caused by higher thermal resistance, the residual stresses developed during the cooling and solidification process were lower for the rougher surface. However, the effectiveness of this strategy in lowering the magnitude of the residual stresses was limited. More importantly, regardless of the magnitude of residual stresses, all cases had a stress concentration zone at the interface. The maximum principal stress to temperature-dependent yield strength ratio for various surface roughness at Y and Z lines (shown in **Figure 8.3**) at similar temperatures are demonstrated in **Figure 8.9 c-d.** It is seen that for a rougher surface, the failure limit is also attained at the vicinity of the interface, indicating possible delamination in all cases.

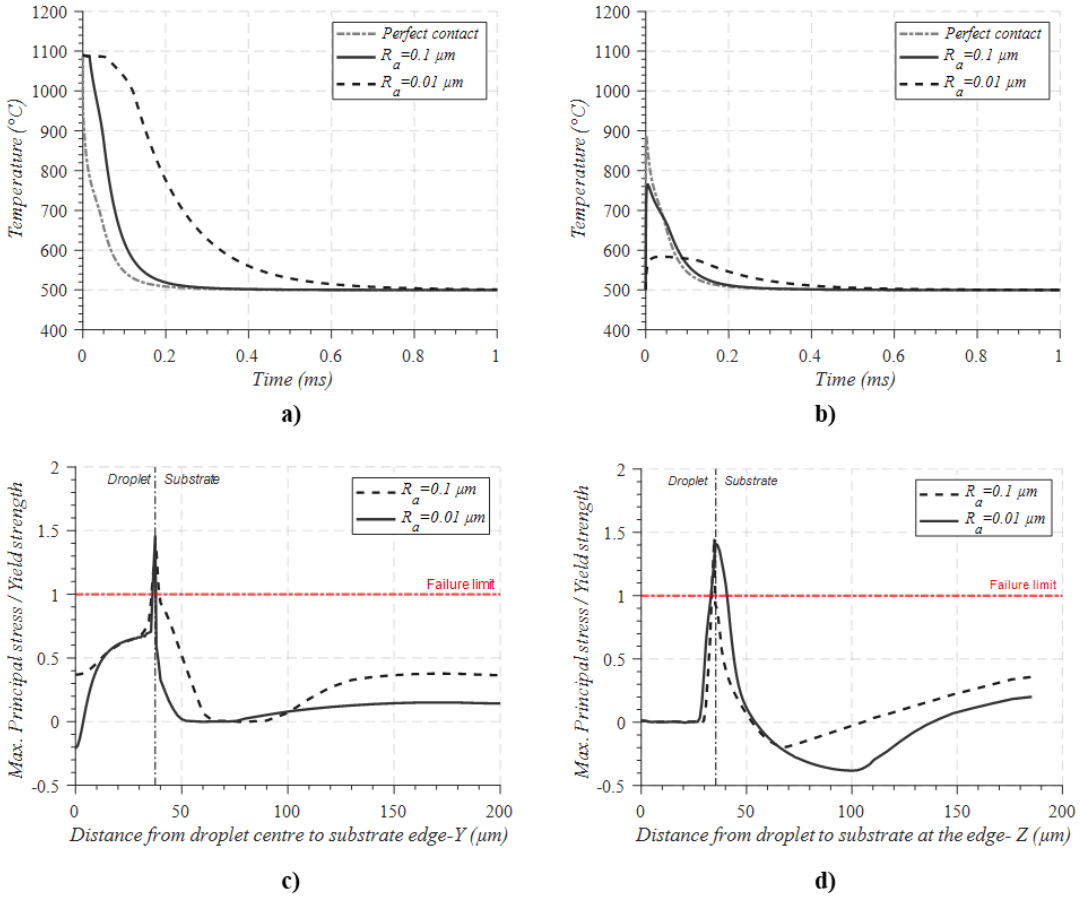


***Figure 8.9**- Temperature evolution during droplet deposition considering different substrate roughness for a node **a)** at the centre of the droplet, **b)** at the interface of the substrate with the droplet. Maximum principal stress to temperature-dependent yield strength ratio for various substrate roughness in **c)** the radial path at the interface of droplet and substrate (Y line shown in Figure 115), **d)** droplet and substrate thickness at the edge (Z line shown in Figure 115.*

8.3. Summary

In this chapter, thermomechanical FE modelling was used to provide insights into the mechanism of residual stress generation during the deposition of single droplets. The numerical results were interpreted to understand the origin of the experimentally observed delamination at the interface of Cu droplets deposited onto a medium-temperature substrate. Further numerical efforts were made to evaluate the effects of various process parameters in mitigating the level of these thermal stresses and

rectifying the undesirable delamination. The specific results can be summarized as follow:

- Residual stresses were developed due to steep temperature gradients during the deposition and cooling. Uneven contraction and expansion in the vicinity of the interface likely lifted the droplet at its edges. Due to the high magnitude of thermal stresses at the droplet-substrate interface, which exceeded the elastic limits of the material, residual-stress-induced delamination occurred.
- Substrate preheating to elevated temperatures was the most effective strategy for mitigating the residual stresses at the interface of droplets and substrates. Increasing the initial substrate temperature is also beneficial to enhancing the level of bonding, consequently, it is an effective strategy for improving the quality of printed parts.
- Despite slower cooling rates for surfaces with a higher roughness, this strategy was ineffective in lowering the magnitude of residual stresses developed during the deposition process.

9. Implications of the Developed Knowledge

This chapter demonstrates the implications of the knowledge obtained from the previous chapters in printing functional parts through the MetalJet platform. Moreover, the rationales for the studies presented in each chapter are discussed, and the general trends and understandings are compared with what is available in the literature. Furthermore, the impact of these studies on printing structures that meet the requirements for the specific applications is discussed. It is also explained how the knowledge obtained from this thesis can be applied to developing new materials using the MetalJet platform. Finally, the limitations of the system and the challenges that may slow down the progress of the technology are highlighted.

Generally speaking, the thesis has shown the major roles of droplet formation, solidification and dynamics of droplets, interface formation, microstructure, and residual stresses in the context of drop-on-demand metal additive manufacturing. The findings provide insight into the effects of various printing process parameters on these aspects. Furthermore, these results underpinned the optimal process conditions under which the 3D structures produced with this technology can exhibit reliable integrity and consistency. The applicability of the knowledge obtained by this study was

demonstrated through the successful printing of defect-free 2D and 3D structures presented in **Figure 9.1**.

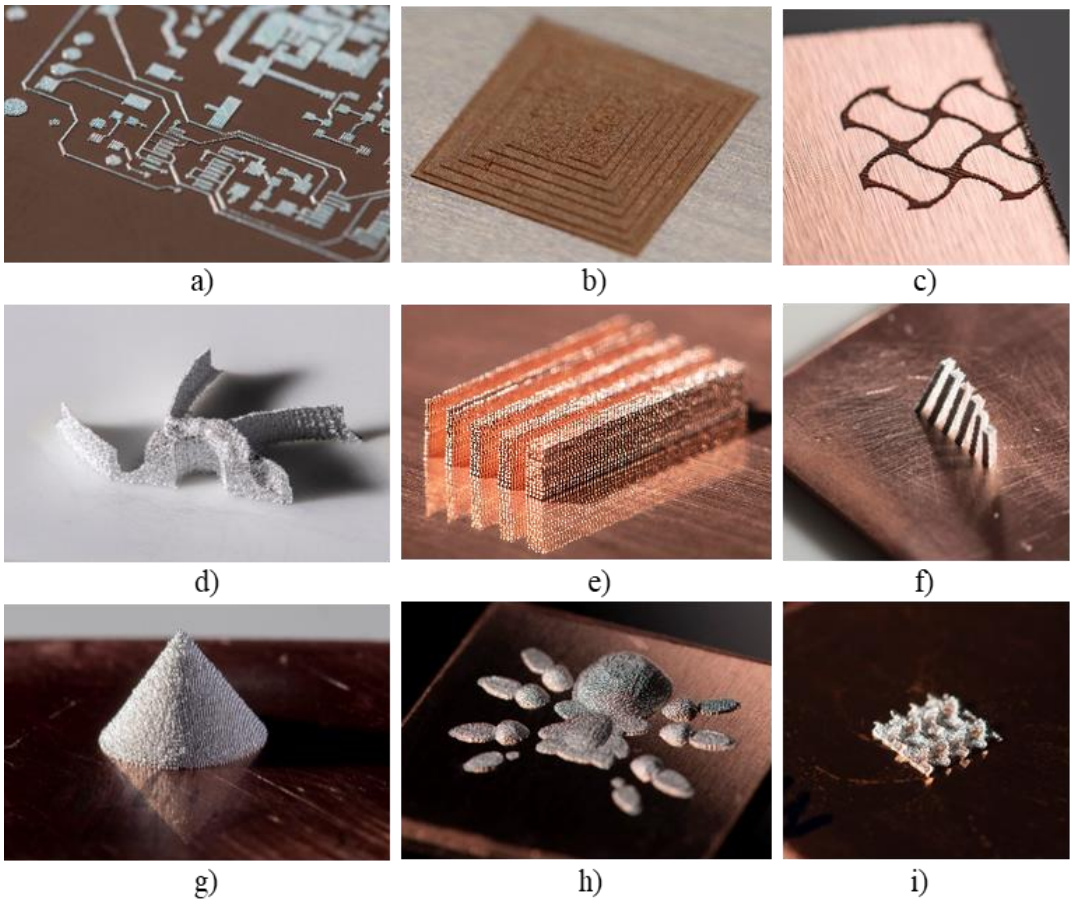


Figure 9.1*-Demonstration of MetalJet capacity in printing 2D and 3D defect-free structures: a) an electronic circuit in Sn on a Cu substrate, b)a pyramid in Cu on a Cu substrate, c) a 2D honeycomb pattern in Cu on a Cu substrate, d) Ag propeller on an alumina substrate, e) Cu walls of various thicknesses on a Cu substrate, f) Ag overhang pillars on a Cu substrate, g) an Sn cone on a Cu substrate, h) Boris spider in Sn on a Cu substrate, i) a lattice structure in Ag on a Cu substrate.*

As depicted in **Figure 9.2**, the five main research challenges that need to be thoroughly investigated in this technology are (I) the mechanism of droplet formation to ensure consistent and uniform satellite-free droplets, (II) droplet dynamics and solidification, which determine the final morphology of deposited droplets, (III) the mechanism of interface formation, which defines the level of bonding at droplet-substrate and droplet-droplet interfaces, (IV) microstructure evolution, which sets the mechanical

properties of printed structures, and (V) residual stress evolution, which can lead to undesired warping or delamination at the interfaces.

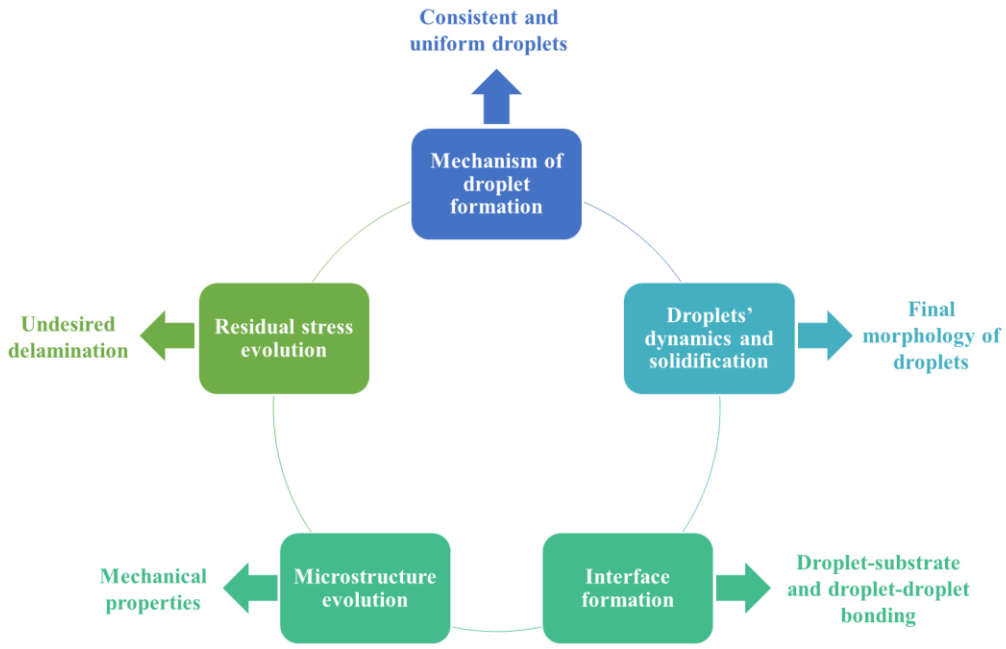


Figure 9.2*- The graphical abstract demonstrating the five principal elements involved in the metal jetting processes.*

9.1. Implications of droplet formation investigation in 3D printing through DoD-MJ

Understanding the mechanism of droplet generation, the factors that control it, and in-situ monitoring of droplets' characteristics in-flight are essential for two main reasons:

(I): Suppressing the formation of undesired satellite droplets is one of the primary challenges in all DoD processes since their trajectories are difficult to be controlled or predicted. Consequently, these satellites are scattered in random locations (**Figure 9.3** a), which deteriorates the geometry and precision of printing. Moreover, they result in variations in the main droplet's size (**Figure 9.3** b), causing overlapping or voids between droplets and eventually failing the print. Finally, satellite droplets can also interfere with the in-situ monitoring of droplets' characteristic in flight.

Investigating the mechanism of droplet formation in Chapter 4, it was understood that the free ligaments detached from the nozzle were pinched off at the thinned neck, and satellite droplets were formed regardless of the jetting voltage. However, the satellites, developed at the optimal jetting voltage, could merge into the main droplet due to their correct relative speed. It was also seen that increasing the actuation voltage led to higher inertia within the liquid stream; consequently, the satellite droplets could not coalesce into the faster main droplets. These results are consistent with the findings of a great deal of the previous work in metal [75], [100], [101] and ink-based [94], [232] DoD devices, which reported the appearance of satellite droplets with an increase in jetting voltage.

(II): In-situ monitoring of the droplets, which provides information about their size, speed, and trajectory, is crucial in choosing the spacing distance between droplets to avoid staircasing (**Figure 9.3 c**) or inter-droplet gaps (**Figure 9.3 d**). Furthermore, the speed of droplets should be known and synchronised with the motion of the stage such that droplets are deposited at pre-defined locations at the correct time. Finally, deviation of the droplets' trajectory is unfavourable since droplets will be deposited onto the substrate with an offset from the locations obtained from the CAD file (**Figure 9.3 e)**.

The in-situ stroboscopic measurements presented in Chapter 4, demonstrated high reproducibility in forming uniform droplets in size and shape, with a perpendicular trajectory to the nozzle in the MetalJet platform. Furthermore, it was seen that the size and speed of individual droplets increased linearly with the jetting voltage, which corroborates the previous observations in the literature [100], [231], [236]. It is known that droplets' size is mainly controlled by the length of the fluid column at the breakage [285], [286], and the higher jetting voltages induce longer streams.

These results provided insight into the mechanism of metallic microdroplet generation at high temperatures (>1000 °C) for the first time and the effects of various jetting voltages on it, which were the primary objective of Chapter 4. Nevertheless, it is acknowledged that the effects of other important parameters, such as waveform (rise and dwell times) [62], [232], droplet material [75], and temperature (both of which influence viscosity and surface tension), reported to be influential in other DoD

devices, are yet to be understood. Given that investigating these aspects of the process experimentally is challenging due to its associated high costs, numerical modelling can be an alternative tool for this purpose.

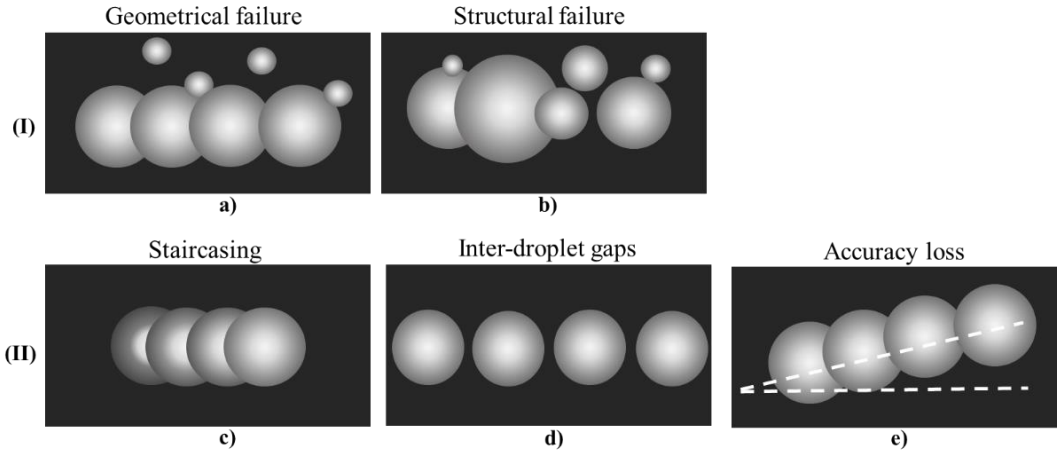


Figure 9.3*- (I) Issues related to the formation of satellite droplets a) geometrical failure due to deposition of satellite droplets in undesired locations, b) structural failure due to the non-uniform size of droplets. (II) The necessity of in-situ monitoring to avoid c-d) staircasing and inter-droplet gaps due to the small and large overlap between droplets, respectively, both related to the lack of information about the droplet size, e) the inaccuracy in the droplet deposition due to the misalignment of droplet trajectory.*

9.2. Implications of droplet morphology investigation in 3D printing through DoD-MJ

Providing insights into droplet dynamics and solidification, which define the final shape of the droplets, and understanding the factors that control them, were presented in Chapter 5. This investigation is important for several reasons:

(I): The maximum droplet spreading defines the optimal spacing between the droplets such that there is neither a gap between droplets nor staircasing (**Figure 9.4 a-b)**. This study demonstrated that the final morphology of droplets, including the spreading factor and solidification contact angle, resulted from an interplay between the spreading and solidification mechanisms. Whereas the wettability of the substrate by the molten droplet was key in the droplet's dynamics and contact line motion, the substrate thermal properties and temperature were critical in the contact line arrest and

solidification behaviour. Spreading was predicted to increase with the increase in droplet temperature, which is in agreement with results previously reported in the literature [42], [120].

Furthermore, the predicted increase in spreading factor with increase in substrate temperature, observed in Section 5.2, supports findings in other studies [31], [32], [192]. However, the theoretical models used in these studies did not match the experimental observations in this thesis due to the reactive nature of wetting in the current research, which influences both the maximum spreading factor and the solidification contact angle. Moreover, the results presented in this section evidenced the more influential role of the substrate's temperature in defining the spreading factor compared to the droplet's temperature due to the significant difference in their masses.

(II): Inter-droplet voids, which in turn lead to lower relative densities, potentially form if the solidification contact angle is > 90°, as demonstrated in **Figure 9.4 c**. High solidification contact angles were observed when the substrates were not wettable by the droplets and also when the solidification halted the contact line during the early stages of the relaxation phase. Porosity formation due to these reasons has been reported in the literature for millimetre-sized droplets of pure Al [13], [61] and Ag microdroplets [11]. Moreover, higher solidification contact angles, i.e., lower spreading factors, generate higher surface roughness (**Figure 9.4 c)**, which is detrimental to the deposition of the next layer of droplets. On the other hand, the precision of the printed part decreases for droplets with a high spreading factor, as shown in **Figure 9.4 d**. In Chapter 5, it was discussed that long solidification periods resulted in contact line arrest during the wetting phase if there is a good wettability between droplet and substrate. This scenario, which resulted in a high spreading factor, occurred when the substrate temperature was slightly below the melting point of the deposited material.

(III): Newly deposited molten droplets can unlikely fill the areas between ripples on the peripheries of previously deposited droplets (**Figure 9.4 e)**, creating voids and increasing the thermal resistance at the droplets' interfaces. It was demonstrated that slow cooling rates, such that the solidification period is longer than the damping period, prevent the formation of such striations. High substrate temperatures or a

limited heat transfer between the droplet and substrate, i.e., substrate material with a low thermal conductivity, provides such conditions. Results reported by Yi et al. [61] suggested that droplets deposited onto substrates with low thermal conductivities had a smoother surface, which is in agreement with the findings in this thesis. However, the claim that solidification ripples could not be improved by controlling the temperature parameters is refuted by the results presented in the current study.

With the integrated numerical, analytical and experimental approach used in Chapter 5, it was understood how the droplets' final morphology is formed for Sn, Ag, and Cu. The knowledge obtained can be extended to other materials to obtain the required information regarding the spreading, solidification, and damping periods while avoiding costly and time-consuming experiments. Nevertheless, it is acknowledged that this method does not predict the exact morphology of droplets in the DoD-MJ process, for which extensive computational efforts are needed and were out of the scope of the thesis.

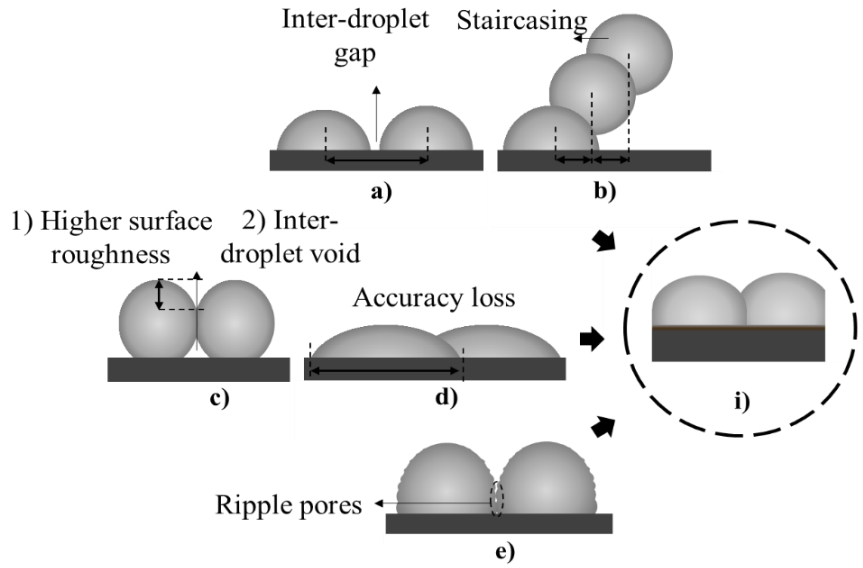


Figure 9.4- a) *Inter-droplet gap and* ***b)*** *droplet staircasing due to overlapping misadjustment,* ***c)*** *high surface roughness and inter-droplet void due to high solidification contact angle,* ***d)*** *loss of accuracy due to over-spreading of droplets,* ***e)*** *pores due to lack of fusion formed at mating surfaces when ripples are present,* ***f)*** *droplet delamination due to the poor droplet-to-substrate bonding.*

9.3. Implications of interface formation investigation in 3D printing through DoD-MJ

Understanding the mechanism of interface formation, evolution of microstructure during the DoD-MJ processes, and the factors that control them were discussed in Chapter 6 and Chapter 7, and are essential for the following reasons:

(I): The consistency of printed parts through DoD-MJ processes strongly depends on the droplet-to-substrate bonding. The bonding should be robust enough to withstand the thermal stresses generated during solidification and cooling. Otherwise, droplets may delaminate from the substrate (**Figure 9.5** a). It was shown that a strong metallurgical bonding could be obtained if the temperature at the interface of the droplet and substrate exceeded the melting point of the substrate material. Whereas substrate melting for low melting point metals was feasible, forming such metallurgical bonding for high-temperature metals is more challenging or impossible. This is due to the system's limited capacity to provide adequately high initial droplet and substrate temperatures. Similarly, weak adhesion to the substrate has been reported in the literature for superheated Pt microdroplets deposited onto a Pt substrate [42] and Ag microdroplets deposited onto a Cu substrate [11]. These observations can be explained by the considerable mass difference between the microdroplets and the substrate, where the substrate acts as a heat sink and rapidly absorbs the droplet’s thermal energy.

Furthermore, it was demonstrated that preheating the substrate is an effective strategy to enhance droplet-substrate bonding and increasing the superheat temperature can slightly improve the adhesion. These results reflect those of Schmaltz et al. [4] and Jafari et al. [193], who investigated the effects of the substrate and droplets’ initial temperatures on remelting depth in the microcasting process. Similarly, the adhesion strength of particles deposited on higher temperature substrates was improved in thermal spraying processes [252], [287], [288]. It was also demonstrated, for the first time, that printing on dissimilar materials provides the possibility of diffusion bonding below the melting point of the substrate material. For such bonding, the substrate should be wettable by liquid droplets to allow them to spread. Additionally, it should

possess a high diffusion coefficient to facilitate the diffusion of atoms into the droplet to form an intermetallic layer at the interface.

(II): The bonding between droplets sets the structural integrity and consistency of printed parts in the DoD-MJ processes. Lack of consolidation between droplets causes the inter-droplet interfaces to be inherently weaker compared to the bulk material. Delamination or crack propagation is more likely to occur in these weakened regions, which could eventually lead to the failure of the part during the printing process or under external loading conditions (**Figure 9.5 b**). It was shown that strong inter-droplet bonding is achievable through remelting the interface of the previously deposited droplets if the temperature at the inter-droplet interface exceeds the melting point of the printed material.

It was also seen that inter-droplet interface formation requires less initial thermal energy than the droplet-substrate interface formation, which could be attributed to three reasons: (1) the surface of the previously deposited droplets is smoother than the substrate, and hence the thermal resistivity is lower at the inter-droplet interfaces, (2) the surface of droplets is oxide-free, whereas the etched or polished substrates can still react with oxygen in the short time before installation of the substrate inside the glove box, and (3) the grain structure, size, and direction of the surface of previously deposited droplets, which facilitates the diffusion of atoms between surfaces. Consequently, epitaxial growth made the inter-droplet interface formation possible at lower initial thermal energies.

Furthermore, and consistent with the literature [61], [145], [220], it was seen that increasing the initial droplet and substrate temperatures enhances the inter-droplet bonding level. Previous research in the literature [141], [145], [214] reported the so-called heat accumulation issue in other DoD-MJ processes, which was aggravated by increasing the jetting frequency (as low as 5 Hz) and led to bulging and an eventual loss of dimensional accuracy. However, the findings of the current thesis indicated that this is not an issue in the MetalJet process. This is attributed to the rapid solidification of the microdroplets in the MetalJet process, which is faster than the maximum rate of deposition (500 Hz).

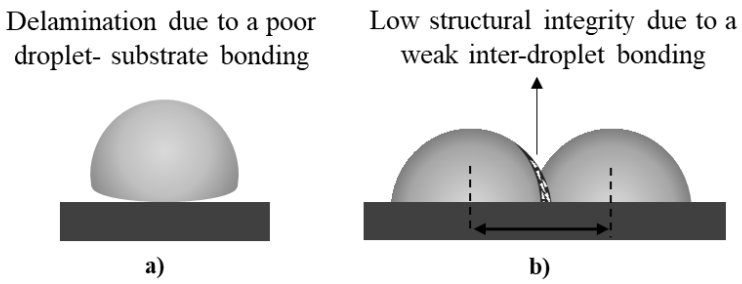


Figure 9.5*- a) delamination of a single droplet from the substrate due to a poor adhesion, b) crack propagation at the droplets' interface due to the lack of bonding.*

9.4. Implications of microstructure investigation in 3D printing through DoD-MJ

The final properties and serviceability of components are mainly defined by the capability of obtaining a target solidification structure (planner, cellular, dendritic columnar, or dendritic equiaxed) and grain size. Fine equiaxed structures are usually more favourable due to their strength, ductility superiority, and isotropic mechanical properties. In contrast, columnar grain structures tend to reduce the tensile strength of the parts. It is essential to understand the mechanism of microstructure evolution to be able to control it. In this thesis, it was shown that the solidification rates and thermal gradient, mainly dictated by the substrate temperature and properties, largely determined the solidification structure of droplets. Low substrate temperatures yielded an epitaxial layer at the vicinity of the interface, and columnar grains in the direction of the thermal gradient in the upper section of the droplet. On the contrary, larger equiaxed grains were obtained at higher substrate temperatures.

These results are in agreement with observations from other metal AM technologies, such as DED [289], EBM [265] L-PBF [208]. The microstructure in these technologies typically consists of epitaxially grown grains near the substrate or the previously deposited layer, followed by columnar grains, and eventually coarser equiaxed grains near the topside. This thesis also demonstrated that rougher substrates resulted in grain refinement since the surface heterogeneities acted as nucleation sites for the grain growth. Even though these results are encouraging, it is noted that using rougher surfaces can only improve the properties of the first layer, which is in direct contact with the substrate.

Furthermore, it was observed, for the first time, that the diffusion of atoms from the substrate to the droplets resulted in a more refined microstructure, even for substrates at elevated temperatures. Indeed, the intermetallic particles could diffuse to the upper sections of droplets, act as nucleating agents, and trigger heterogeneous nucleation. These observations indicate a mechanism operating in MetalJet that resembles the grain-refining technology used in other metal AM technologies to encourage a columnar to equiaxed transition (CET) of the structure [43], [208], [290]. Consequently, it is observed that diffusion between the substrate and droplets has a twofold impact on DoD-MJ processes. First, it enhances droplet-substrate bonding. Secondly, it leads to a more refined grain structure and, eventually, better mechanical properties.

Interestingly, in Section 6.1.3, the in-situ formation of twin boundaries during the deposition of high-temperature metal onto substrates at low temperatures was reported. Indeed, the recrystallization, triggered by plastic strains, led to twin boundary multiplication. The high thermal gradients between droplets and substrates or previously deposited droplets resulted in high residual stresses and provided the required mechanical deformation for the onset of recrystallization. Enhancing the mechanical properties of parts by incorporating twin boundary grains using special thermomechanical processing strategies, referred to as Grain boundary engineering, has been gaining attention in recent years in L-PBF [270] and DED [291] processes. This thesis demonstrated that in-situ grain boundary engineering could be obtained through the MetalJet platform under large thermal gradients between droplet and substrate or previously deposited droplets. Nevertheless, it is acknowledged that the bonding level at the interfaces aggravates under these conditions, which is detrimental to the structural integrity of parts. It is noted that these observations open up new opportunities, which merit further investigations.

9.5. Implications of residual stresses investigation in 3D printing through DoD-MJ

The mechanism of residual stress evolution in the MetalJet process was investigated in Chapter 8. This is essential because their detrimental effects, such as warping, delamination, cracking, and dimensional tolerance losses, cannot be mitigated without

this knowledge. It was understood that residual stress-induced delamination at the interface occurred due to the steep thermal gradients and uneven thermal compression and expansion for droplets of high-melting material deposited onto medium-temperature substrates. The numerical efforts were made to evaluate the effects of various process parameters in mitigating the level of these thermal stresses and rectifying the undesirable delamination.

It was demonstrated that preheating the substrate was an effective strategy for reducing the level of thermal stresses. Indeed, preheating the substrate to higher temperatures decreased the thermal gradient between the droplet and substrate and lowered the level of residual stresses. The physical mechanism of stress generation in DoD-MJ is similar to Thermal Spraying [292], DED [210], and microcasting [213] processes. Consistent with the results in this thesis, substrate preheating is used to decrease the residual stresses in the above mentioned processes [38], [276].

9.6. The implication of the current study in developing new materials and the system's limitations

Metal jetting is expected to enable the direct and digital manufacturing of complex structures while eliminating the pre- or post-printing treatments required in other metal AM techniques. In order to reach this target, this thesis aimed to comprehensively understand the role of various process parameters involved in five principal aspects of the process in this technology to optimise them effectively. This task was accomplished for three low- and high-temperature metals: Sn, Ag, and Cu, which are used for the potential applications envisaged for MetalJet, i.e., electronic devices.

In simple words, this thesis provides the knowledge for the system users to choose the process parameters, including the jetting waveforms, droplet temperature, substrate temperature, substrate material, and surface roughness for these three materials, such that the printed part meets the quality requirements. The required quality may vary based on the target application. Whereas a strong metallurgical bonding is required for an electronic circuit to ensure high electrical conductivity, a loose bonding is preferred for other applications, such as catalysts. The integrated numerical and experimental approach adopted for this study permits the expansion of this knowledge for developing new materials and provides the basis for choosing the process parameters

for them. Overall, the study performed in this thesis represents a step forward in the direct metal printing of high-resolution functional multi-material components.

During the course of this PhD, some limitations and challenges with the MetalJet platform were observed. It was seen that despite the capacity of the system to reach 2000°C, slag formation between the coating inside the cartridge and the molten metal (Cu) at the nozzle level can prevent the jetting. This is due to the reaction between Cu and the coating at an elevated temperature. Hence, it is expected that all conductive metals may not be printable through the system. Moreover, cartridges have a limited life duration and should be replaced after several experiments. Given the high costs of these cartridges due to the complicated manufacturing route, this limits the number of experiments and can slow down the progress of the technology.

Furthermore, the oxygen content should be maintained below two ppm, particularly for high-temperature materials, which add extra costs and maintenance issues for running the system. The specific design of the actuation chamber and the position of electrodes result in the formation of uniform droplets in a controlled manner since the actuation is applied to a precise volume of material close to the orifice. However, the direct contact of the electrodes with molten metal through the chamber can lead to leakage from the electrodes if the precise tolerances in the manufacturing process are not met.

10. Conclusions and Recommendations for Future Research

The PhD aimed to provide a comprehensive understanding of various aspects of drop-on-demand metal jetting through the MetalJet system. This was achieved by defining five main axes of studies, including droplet formation, droplet dynamics and solidification, interface formation, microstructure, and residual stress evolution, and investigating them through an integrated numerical, experimental, and analytical approach. Finally, the knowledge obtained throughout this PhD was successfully employed to print 2D and 3D objects through MetalJet

The main findings of this research are as follows:

- The capability of the MetalJet platform to produce uniform microdroplets in shape and size with a perpendicular trajectory to the nozzle was demonstrated. Moreover, the mechanism of droplet formation through a magnetohydrodynamic actuator was explained.
- Effects of the jetting voltage and frequency on the droplet formation and the characteristics of droplets in flight were investigated. Based on these findings, the

DoD generation was categorized into seven regimes, from no droplet ejection to spraying, which is mainly controlled by the jetting voltage.

- It was shown that liquids with high surface tensions are prone to one or several breakups in the neck of the free ligament, which forms satellite droplets. If the jetting voltage is not optimal, the satellite droplets are relatively slower than the main droplet and cannot merge into it. The breakup length and, consequently, the droplet size alongside the droplet speed increased as the jetting voltage increased. In contrast, the breakup time was shown to be independent of the jetting voltage and is expected to be controlled by waveform properties such as dwell time.
- The final morphology of droplets, which resulted from an interplay between the spreading and solidification mechanisms, was investigated through an integrated analytical and numerical approach for Sn, Ag, and Cu.
- It was shown that the desired droplet morphology with a solidification contact angle of ~90 degrees was obtained when the contact line was arrested between the relaxation and wetting phases. Furthermore, undesirable solidification ripples can be avoided if the solidification period is long enough such that the viscosity effects can dampen the oscillations before they freeze in place. The hybrid FE and analytical approach developed in this thesis can be used to identify a suitable processing window for each material.
- Conditions to obtain strong droplet-substrate bonding were investigated through FE modelling of the solidification process during the droplet deposition. It was shown that realising a robust metallurgical bonding through substrate melting for high melting materials is challenging and requires extensive substrate preheating for high-temperature metals. One of the noteworthy outcomes of this research was demonstrating a strong adhesion of droplets to the substrate at temperatures considerably below the melting point of the substrate's material through diffusion bonding.
- It was also demonstrated that the interface formation at the droplet-droplet level requires fewer thermal energies than at the droplet-substrate level due to smoother, oxide-free conditions, the grain structure, size, and direction of as-deposited droplets.

- A strong inter-droplet bonding for low-temperature metal was obtained, and the depth of remelting was increased at higher substrate temperatures. Furthermore, the microstructure of the dual droplets at higher temperatures consisted of very few large grains. In contrast, refined columnar grains were observed in droplets deposited onto the substrate at lower temperatures.
- The substrate material and temperature were shown to be the most influential element in setting the droplets' morphology and defining the level of bonding. Whereas droplet temperature, surface roughness, and droplet size also influence the bonding level, their effects remain somehow limited.
- Results from the thermomechanical model developed in this thesis showed that residual stresses were generated due to steep temperature gradients during the deposition and cooling. Uneven contraction and expansion in the vicinity of the interface lifted the droplets of high melting point material at its edges. The residual-stress-induced delamination is likely to happen due to a high magnitude of thermal stresses at the droplet-substrate interface.
- Substrate preheating to elevated temperatures was the most effective strategy for mitigating the residual stresses at the interface of droplets and substrates.

The knowledge obtained from this work can be used to establish a scientific basis for selecting the process parameters to produce consistent 3D structures that meet the desired quality. The outcomes have the potential to pave the path towards the direct metal printing of high-resolution functional multi-material components.

10.1. Recommendation of Future Work

DoD-MJ is a nascent AM technology at an early stage of development, and its full potentials are yet to be explored. The work performed in this thesis has contributed to understanding various aspects of the process, including droplet formation, interface formation, evolution of microstructure, and residual stress development. Even though the aim and objectives of this PhD were met, some areas were still not addressed in this thesis. Indeed the knowledge obtained through the course of the PhD, the

challenges, and the limitations faced are beneficial in defining the directions for future work.

10.1.1. Process and modelling

- In Chapter 4, the formation of microdroplets in the MHD process presented in this thesis was experimentally probed, which provided a basic understanding of the sequence and mechanism of droplet generation. However, a thorough understanding of this process and its underlying physics is only feasible through the numerical modelling of droplet ejection. This knowledge is essential to optimise the current waveforms at the first step, and more importantly, to expand the list of printable materials by the system.
- The five principal elements involved in the metal jetting process were investigated for three metallic elements, Sn, Ag, and Cu. The integrated analytical, numerical, and experimental approach established in this thesis can be used to choose the process parameters of new metallic elements and alloys, such as Al, Ni, Au, Sn-Ag, Ag-Si, Au-Si, Sn-Ag-Cu, and Ag-Au-Cu. Furthermore, the unique fabrication approach of DoD-MJ offers an unprecedented degree of freedom to the in-situ development of new alloys from elemental materials. Finally, DoD-MJ provides the possibility of multi-metal printing with unmatched accuracy and precision compared to other metal AM methods due to its drop-by-drop deposition capacity.
- The studies performed in the thesis were limited to single-layer deposition, while in reality, the droplets' curved surface can influence the dynamics and solidification of droplets and the consequent developed residual stresses in the following layers. In future, the presented model can be upgraded to account for this effect by incorporating the previously calculated temperature, stress, and plastic strain fields in the subsequent analysis step.
- In chapter 7, it was shown that strong metallurgical bonding between Cu droplets could not be obtained, and increasing the initial substrate temperature to the maximum level was not an effective solution. As an alternative strategy, substrate materials with lower thermal conductivities, such as ceramics, which limit the fast heat dissipation from the droplet, could be used. However, it is essential to coat their surface with a thin layer (nano-micro) of a compatible

metallic material to overcome the challenges related to their poor wettability with liquid metals. Furthermore, solutions such as increasing the temperature of droplets in-flight by applying a laser pulse or direct application of a laser pulse onto the substrate (pre or post-heating) can be envisaged. Including a laser source in the glove box requires further modifications to the system, but it can also open new opportunities for selective microstructure modifications.

10.1.2. Characterisation

- The microstructure of single and multi-droplets printed through the MetalJet platform was investigated in chapter 6 and Chapter 7. It was explained that there is a correlation between the mechanical properties and the final microstructure of parts. However, the quantitative measurement of the mechanical properties of the components printed through this technology is missing. Even though conventional mechanical performance measurements fail to fulfil this task, methods such as micro tensile testing of samples prepared by FIB-milling can be explored. This method can also be used to quantify the bonding level at the interfaces.
- The sequentially coupled thermomechanical model developed in this thesis provided insight into the mechanism of residual stress evolution in the process. However, the quantitative measurement of residual stresses of printed droplets and parts is missing, and XRD measurement (not presented in this thesis) failed to answer this question accurately. As an alternative solution, residual stresses can be obtained from the deflection of microcantilevers during FIB layer removal and a simple FE model to calculate the residual stresses from the deflections.

Reference

[1] I. Gibson, D. Rosen, and B. Stucker, *Additive manufacturing technologies: 3D printing, rapid prototyping, and direct digital manufacturing, second edition*. Springer New York, 2015.

[2] ASTM- Designation: F2792 − 12a, "Standard Terminology for Additive Manufacturing Technologies," doi: 10.1520/F2792-12A.

[3] T. Mukherjee, J. S. Zuback, A. De, and T. DebRoy, "Printability of alloys for additive manufacturing," *Sci. Reports 2016 61*, vol. 6, no. 1, pp. 1–8, Jan. 2016, doi: 10.1038/srep19717.

[4] K. S. Schmaltz, L. J. Zarzalejo, and C. H. Amon, "Molten droplet solidification and substrate remelting in microcasting Part II: Parametric study and effect of dissimilar materials," *Heat Mass Transf.*, vol. 35, pp. 17–23, 1999.

[5] C.-J. Li, G.-J. Yang, and C.-X. Li, "Development of Particle Interface Bonding in Thermal Spray Coatings: A Review," *J. Therm. Spray Technol.*, vol. 22, pp. 192–206, 2013, doi: 10.1007/s11666-012-9864-9.

[6] J. Luo, W. Wang, W. Xiong, H. Shen, and L. Qi, "Formation of uniform metal traces using alternate droplet printing," *Int. J. Mach. Tools Manuf.*, vol. 122, pp. 47–54, Nov. 2017, doi: 10.1016/J.IJMACHTOOLS.2017.05.004.

[7] T. Y. Ansell, "Current Status of Liquid Metal Printing," *Manuf. Mater. Process.*, 2021, doi: 10.3390/jmmp5020031.

[8] M. Meda, P. Mehta, C. Mahajan, B. Kahn, and D. Cormier, "Magnetohydrodynamic liquid metal droplet jetting of highly conductive electronic traces," *Flex. Print. Electron*, vol. 6, p. 35002, 2021, doi: 10.1088/2058-8585/ac0fee.

[9] Y. Dou, J. Luo, L. Qi, H. Lian, and J. Huang, "Drop-on-demand printing of recyclable circuits by partially embedding molten metal droplets in plastic substrates," *J. Mater. Process. Technol.*, vol. 297, p. 117268, Nov. 2021, doi: 10.1016/J.JMATPROTEC.2021.117268.

[10] Q. Liu and M. Orme, "High precision solder droplet printing technology and the

state-of-the-art," 1999.

[11] M. Simonelli *et al.*, "Towards digital metal additive manufacturing via high-temperature drop-on-demand jetting," *Addit. Manuf.*, vol. 30, Dec. 2019, doi: 10.1016/J.ADDMA.2019.100930.

[12] E. M. Debbi, S. Puri, A. G. Athey, and B. P. Chalmers, "Liquid Phase 3D Printing: How This New Technology Can Help Bring 3D Printing to the Operating Room," *Curr. Rev. Musculoskelet. Med.*, 2022, doi: 10.1007/s12178-022-09758-3/Published.

[13] H. Li, P. Wang, L. Qi, H. Zuo, S. Zhong, and X. Hou, "3D numerical simulation of successive deposition of uniform molten Al droplets on a moving substrate and experimental validation," *Comput. Mater. Sci.*, vol. 65, pp. 291–301, 2012, doi: 10.1016/j.commatsci.2012.07.034.

[14] J. Huang, L. Qi, J. Luo, L. Zhao, and H. Yi, "Suppression of gravity effects on metal droplet deposition manufacturing by an anti-gravity electric field," *Int. J. Mach. Tools Manuf.*, 2019, doi: 10.1016/j.ijmachtools.2019.103474.

[15] J. Huang, L. Qi, J. Luo, and X. Hou, "Insights into the impact and solidification of metal droplets in ground-based investigation of droplet deposition 3D printing under microgravity," *Appl. Therm. Eng.*, vol. 183, pp. 1359–4311, 2021, doi: 10.1016/j.applthermaleng.2020.116176.

[16] J. Huang, L. Qi, J. Luo, K. Zhang, and L. Yang, "A ground-based work of droplet deposition manufacturing toward microgravity: Fine pileup of horizontally ejected metal droplets on vertical substrates," *J. Manuf. Process.*, vol. 66, pp. 293–301, Jun. 2021, doi: 10.1016/J.JMAPRO.2021.03.062.

[17] P. M. Solyankin *et al.*, "Single Free-Falling Droplet of Liquid Metal as a Source of Directional Terahertz Radiation," *Phys. Rev. Appl.*, vol. 10, p. 34033, 2020, doi: 10.1103/PhysRevApplied.14.034033.

[18] J. W. Priest, C. Smith, and P. Dubois, "Liquid Metal Jetting for Printing Metal Parts," in *Solid Freeform Fabrication Proceedings, University of Texas at Austin, TX*, 1997, pp. 1-10.

[19] A. Amirzadeh, M. Raessi, and S. Chandra, "Producing molten metal droplets smaller than the nozzle diameter using a pneumatic drop-on-demand generator," *Exp. Therm.*

Fluid Sci., vol. 47, pp. 26–33, May 2013, doi: 10.1016/J.EXPTHERMFLUSCI.2012.12.006.

[20] S. Zhong, L. Qi, J. Luo, H. Zuo, X. Hou, and H. Li, "Effect of process parameters on copper droplet ejecting by pneumatic drop-on-demand technology," *J. Mater. Process. Technol.*, vol. 214, no. 12, pp. 3089–3097, Dec. 2014, doi: 10.1016/J.JMATPROTEC.2014.07.012.

[21] S. I. Moqadam, L. Mädler, and N. Ellendt, "A High Temperature Drop-On-Demand Droplet Generator for Metallic Melts," *Micromachines*, vol. 10, 2019, doi: 10.3390/mi10070477.

[22] K. Yamaguchi, K. Sakai, T. Yamanaka, and T. Hirayama, "Generation of three-dimensional micro structure using metal jet," *Precis. Eng.*, vol. 24, no. 1, pp. 2–8, Jan. 1999, doi: 10.1016/S0141-6359(99)00015-X.

[23] I. H. Karampelas *et al.*, "Drop-on-Demand 3D Metal Printing," *Tech Connect Briefs*, vol. 4, pp. 153–155, 2017.

[24] Z. Luo, X. Wang, L. Wang, D. Sun, and Z. Li, "Drop-on-demand electromagnetic printing of metallic droplets," *Mater. Lett.*, vol. 188, pp. 184–187, Feb. 2017, doi: 10.1016/J.MATLET.2016.11.021.

[25] V. Sukhotskiy, P. Vishnoi, I. H. Karampelas, S. Vader, Z. Vader, and E. P. Furlani, "Magnetohydrodynamic Drop-on-Demand Liquid Metal Additive Manufacturing: System Overview and Modelling," in *Proceedings of the 5th International Conference of Fluid Flow, Heat and Mass Transfer (FFHMT'18)*, 2018, doi: 10.11159/ffhmt18.155.

[26] N. Gilani, N. T. Aboulkhair, M. Simonelli, M. East, I. Ashcroft, and R. J. M. Hague, "Insights into drop-on-demand metal additive manufacturing through an integrated experimental and computational study," *Addit. Manuf.*, vol. 48, p. 102402, Dec. 2021, doi: 10.1016/J.ADDMA.2021.102402.

[27] N. Gilani, N. T. Aboulkhair, M. Simonelli, M. East, I. A. Ashcroft, and R. J. M. Hague, "From impact to solidification in drop-on-demand metal additive manufacturing using MetalJet," *Addit. Manuf.*, vol. 55, p. 102827, Jul. 2022, doi: 10.1016/J.ADDMA.2022.102827.

[28] M. V. RASA, R. BERKHOUT, W. P. J. CLASSENS, C. M. VAN, H. GENUCHTEN, and E. V. KUZNETSOV, “Device for ejecting droplets of a fluid having high temperature,” US 2011/0233239 A1, 2013.

[29] D. Zhang, L. Qi, J. Luo, H. Yi, X. Hou, and H. Li, “Geometry control of closed contour forming in uniform micro metal droplet deposition manufacturing,” *J. Mater. Process. Technol.*, vol. 243, pp. 474–480, May 2017, doi: 10.1016/J.JMATPROTEC.2017.01.007.

[30] R. De Ruiter, P. Colinet, P. Brunet, J. H. Snoeijer, and H. Gelderblom, “Contact line arrest in solidifying spreading drops,” *Phys. Rev. FLUIDS*, vol. 2, p. 43602, 2017, doi: 10.1103/PhysRevFluids.2.043602.

[31] M. V Gielen, R. De Ruiter, R. B. J. Koldeweij, D. Lohse, J. H. Snoeijer, and H. Gelderblom, “Solidification of liquid metal drops during impact,” *J. Fluid Mech*, vol. 883, p. 32, 2019, doi: 10.1017/jfm.2019.886.

[32] F. Tavakoli, S. H. Davis, and H. P. Kavehpour, “Spreading and Arrest of a Molten Liquid on Cold Substrates,” *Langmuir*, vol. 30, p. 52, 2014, doi: 10.1021/la5017998.

[33] G. Martouzet, L. Jørgensen, Y. Pelet, A.-L. Biance, and C. Barentin, “Dynamic arrest during the spreading of a yield stress fluid drop,” *Phys. Rev. Fluids*, vol. 6, p. 44006, 2021, doi: 10.1103/PhysRevFluids.6.044006.

[34] A. Gholijani, C. Schlawitschek, T. Gambaryan-Roisman, and P. Stephan, “Heat transfer during drop impingement onto a hot wall: The influence of wall superheat, impact velocity, and drop diameter,” *Int. J. Heat Mass Transf.*, vol. 153, p. 119661, Jun. 2020, doi: 10.1016/J.IJHEATMASSTRANSFER.2020.119661.

[35] A. Kumar, S. Ghosh, and B. K. Dhindaw, “Simulation of cooling of liquid Al-33 wt.% Cu droplet impinging on a metallic substrate and its experimental validation,” *Acta Mater.*, vol. 58, pp. 122–133, 2009, doi: 10.1016/j.actamat.2009.08.063.

[36] M. Pasandideh-Fard, S. Chandra, and J. Mostaghimi, “A three-dimensional model of droplet impact and solidification,” *Int. J. Heat Mass Transf.*, vol. 45, no. 11, pp. 2229–2242, May 2002, doi: 10.1016/S0017-9310(01)00336-2.

[37] Y. Z. Zheng, Q. Li, Z. H. Zheng, J. F. Zhu, and P. L. Cao, “Modeling the impact, flattening and solidification of a molten droplet on a solid substrate during plasma

spraying," *Appl. Surf. Sci.*, vol. 317, pp. 526–533, Oct. 2014, doi: 10.1016/J.APSUSC.2014.08.032.

[38] R. K. Chin, J. L. Beuth, and C. H. Amon, "Thermomechanical modeling of molten metal droplet solidification applied to layered manufacturing," *Mech. Mater.*, vol. 24, no. 4, pp. 257–271, Dec. 1996, doi: 10.1016/S0167-6636(96)00037-3.

[39] R. K. Chin, J. L. Beuth, and C. H. Amon, "Successive Deposition of Metals in Solid Freeform Fabrication Processes, Part 1: Thermomechanical Models of Layers and Droplet Columns," *J. Manuf. Sci. Eng.*, vol. 123, 2001, doi: 10.1115/1.1380199.

[40] D. Attinger, Z. Zhao, and D. Poulikakos, "An Experimental Study of Molten Microdroplet Surface Deposition and Solidification: Transient Behavior and Wetting Angle Dynamics," *J. Heat Transfer*, vol. 122, no. 3, pp. 544–556, Aug. 2000, doi: 10.1115/1.1287587.

[41] S. Haferl and D. Poulikakos, "Experimental investigation of the transient impact fluid dynamics and solidification of a molten microdroplet pile-up," *Int. J. Heat Mass Transf.*, vol. 46, no. 3, pp. 535–550, 2003, doi: 10.1016/S0017-9310(02)00289-2.

[42] H. Merrow, J. D. Beroz, K. Zhang, U. P. Muecke, and A. J. Hart, "Digital metal printing by electrohydrodynamic ejection and in-flight melting of microparticles," *Addit. Manuf.*, vol. 37, p. 101703, 2021, doi: 10.1016/j.addma.2020.101703.

[43] N. T. Aboulkhair, M. Simonelli, L. Parry, I. Ashcroft, C. Tuck, and R. Hague, "3D printing of Aluminium alloys: Additive Manufacturing of Aluminium alloys using selective laser melting," *Progress in Materials Science*, vol. 106. Elsevier Ltd, p. 100578, 01-Dec-2019, doi: 10.1016/j.pmatsci.2019.100578.

[44] L. E. Murr *et al.*, "Metal Fabrication by Additive Manufacturing Using Laser and Electron Beam Melting Technologies," 2012.

[45] F. I. Azam, A. Majdi, A. Rani, K. Altaf, T. V. V. L. N. Rao, and H. A. Zaharin, "An In-Depth Review on Direct Additive Manufacturing of Metals," doi: 10.1088/1757-899X/328/1/012005.

[46] D. D. Gu, W. Meiners, K. Wissenbach, & R. Poprawe, and R. Poprawe, "Laser additive manufacturing of metallic components: materials, processes and mechanisms," doi: 10.1179/1743280411Y.0000000014.

[47] Y. Zhang *et al.*, “Additive Manufacturing of Metallic Materials: A Review,” *J. Mater. Eng. Perform.*, vol. 27, doi: 10.1007/s11665-017-2747-y.

[48] M. Yakout, M. A. Elbestawi, and S. C. Veldhuis, “A Review of Metal Additive Manufacturing Technologies,” *Solid State Phenom.*, vol. 278, no. November, pp. 1–14, 2018, doi: 10.4028/www.scientific.net/ssp.278.1.

[49] M. Vaezi, P. Drescher, and H. Seitz, “Beamless Metal Additive Manufacturing,” *Materials (Basel).*, vol. 13, no. 922, 2020, doi: 10.3390/ma13040922.

[50] D. Günther, B. Heymel, J. Franz Günther, and I. Ederer, “Continuous 3D-printing for additive manufacturing,” *Assem. Autom.*, vol. 33, pp. 307–311, 2013, doi: 10.1108/RPJ-08-2012-0068.

[51] K. Black, P. Chalker, and J. C. Sutcliffe, “Additive manufacturing components and methods,” 01-Aug-2018.

[52] Y. Sui and C. A. Zorman, “Review-Inkjet Printing of Metal Structures for Electrochemical Sensor Applications,” *J. Electrochem. Soc.*, 2020, doi: 10.1149/1945-7111/ab721f.

[53] J. Vaithilingam *et al.*, “3-Dimensional inkjet printing of macro structures from silver nanoparticles,” *Mater. Des.*, vol. 139, pp. 81–88, Feb. 2018, doi: 10.1016/J.MATDES.2017.10.070.

[54] M. Zeng and Y. Zhang, “Colloidal nanoparticle inks for printing functional devices: emerging trends and future prospects,” *J. Mater. Chem. A*, 2019, doi: 10.1039/c9ta07552f.

[55] K. Black, J. Singh, D. Mehta, S. Sung, C. J. Sutcliffe, and P. R. Chalker, “Silver Ink Formulations for Sinter-free Printing of Conductive Films,” *Sci Rep*, 2016, doi: 10.1038/srep20814.

[56] S. B. Walker and J. A. Lewis, “Reactive Silver Inks for Patterning High-Conductivity Features at Mild Temperatures,” *J. Am. Chem.Soc*, vol. 134, p. 40, 2012, doi: 10.1021/ja209267c.

[57] Y. Yokoyama, K. Endo, T. Iwasaki, and H. Fukumoto, “Variable-size solder droplets by a molten-solder ejection method,” *J. Microelectromechanical Syst.*, vol. 18, no. 2,

2009, doi: 10.1109/JMEMS.2008.2011154.

[58] D. Zhang, L. Qi, J. Luo, H. Yi, and X. Hou, “Direct fabrication of unsupported inclined aluminum pillars based on uniform micro droplets deposition,” *Int. J. Mach. Tools Manuf.*, vol. 116, pp. 18–24, May 2017, doi: 10.1016/J.IJMACHTOOLS.2017.01.001.

[59] M. Suter, E. Weingärtner, and K. Wegener, “MHD printhead for additive manufacturing of metals,” *Procedia CIRP*, vol. 2, pp. 102–106, Jan. 2012, doi: 10.1016/J.PROCIR.2012.05.049.

[60] M. Meda, V. Sukhotskiy, and D. Cormier, “Pinhole Formation in Printed Electronic Traces Fabricated viaMolten Metal Droplet Jetting,” *Electronics*, 2021, doi: 10.3390/electronics10131568.

[61] H. Yi, L. Qi, J. Luo, D. Zhang, H. Li, and X. Hou, “Effect of the surface morphology of solidified droplet on remelting between neighboring aluminum droplets,” *Int. J. Mach. Tools Manuf.*, vol. 130–131, no. August, pp. 1–11, 2018, doi: 10.1016/j.ijmachtools.2018.03.006.

[62] Y. Yokoyama, K. Endo, T. Iwasaki, and H. Fukumoto, “Variable-size solder droplets by a molten-solder ejection method,” *J. Microelectromechanical Syst.*, vol. 18, no. 2, pp. 316–321, 2009, doi: 10.1109/JMEMS.2008.2011154.

[63] H. Yi, L. Qi, J. Luo, and N. Li, “Hole-defects in soluble core assisted aluminum droplet printing: Metallurgical mechanisms and elimination methods,” *Appl. Therm. Eng.*, 2019, doi: 10.1016/j.applthermaleng.2018.12.013.

[64] D. Zhang, L. Qi, J. Luo, H. Yi, W. Xiong, and Y. Mo, “Parametric mapping of linear deposition morphology in uniform metal droplet deposition technique,” *J. Mater. Process. Technol.*, vol. 264, pp. 234–239, Feb. 2019, doi: 10.1016/J.JMATPROTEC.2018.08.048.

[65] Y. Chao, L. Qi, Y. Xiao, J. Luo, and J. Zhou, “Manufacturing of micro thin-walled metal parts by micro-droplet deposition,” *J. Mater. Process. Technol.*, vol. 212, no. 2, pp. 484–491, Feb. 2012, doi: 10.1016/J.JMATPROTEC.2011.10.015.

[66] M. Ma and H. Zhang, “An experimental study of pneumatic extruding direct writing deposition-based additive manufacturing,” *Int. J. Adv. Manuf. Technol.*, 2018, doi:

10.1007/s00170-018-1998-6.

[67] M. Fang, S. Chandra, and C. B. Park, “Building three-dimensional objects by deposition of molten metal droplets,” *Rapid Prototyp. J.*, vol. 14, no. 1, pp. 44–52, 2007, doi: 10.1108/13552540810841553.

[68] T. Metz, G. Birkle, R. Zengerle, and P. Koltay, “StarJet: Pneumatic Dispensing of Nano- to Picoliter Droplets of Liquid Metal,” in *Proceedings of the IEEE International Conference on Micro Electro Mechanical Systems (MEMS)*, 2009, pp. 43–46, doi: 10.1109/MEMSYS.2009.4805314.

[69] T. Metz, W. Streule, R. Zengerle, and P. Koltay, “StarTube: A Tube with Reduced Contact Line for Minimized Gas Bubble Resistance,” *Langmuir*, vol. 24, 2008, doi: 10.1021/la801194j.

[70] N. Lass, L. Riegger, R. Zengerle, and P. Koltay, “Enhanced Liquid Metal Micro Droplet Generation by Pneumatic Actuation Based on the StarJet Method,” *Micromachines 2013, Vol. 4, Pages 49-66*, vol. 4, no. 1, pp. 49–66, Mar. 2013, doi: 10.3390/MI4010049.

[71] B. Gerdes *et al.*, “Analysis of the metallic structure of microspheres produced by printing of aluminum alloys from the liquid melt,” 2018, doi: 10.1088/2053-1591/aaf3bf.

[72] A. Tropmann *et al.*, “Pneumatic dispensing of nano- to picoliter droplets of liquid metal with the StarJet method for rapid prototyping of metal microstructures,” *Microfluid. Nanofluidics 2011 121*, vol. 12, no. 1, pp. 75–84, Jul. 2011, doi: 10.1007/S10404-011-0850-1.

[73] N. Gilani, N. T. Aboulkhair, M. Simonelli, M. East, I. Ashcroft, and R. J. M. Hague, “Insights into drop-on-demand metal additive manufacturing through an integrated experimental and computational study,” *Addit. Manuf.*, p. 102402, Oct. 2021, doi: 10.1016/J.ADDMA.2021.102402.

[74] V. Sukhotskiy *et al.*, “Magnetohydrodynamic Drop-on-Demand Liquid Metal 3D Printing,” in *Proceedings of the 28th Annual International Solid Freeform Fabrication Symposium*, 2017.

[75] V. Sukhotskiy, K. Tawil, and E. Einarsson, “Printability regimes of pure metals using

contactless magnetohydrodynamic drop-on-demand actuation," *Phys. Fluids*, vol. 33, no. 5, p. 053303, May 2021, doi: 10.1063/5.0050354.

[76] C. Willem Visser, R. Pohl, C. Sun, G.-W. Römer, B. Huis in, and D. Lohse, "Toward 3D Printing of Pure Metals by Laser-Induced Forward Transfer," *Adv. Mater.*, vol. 27, 2015, doi: 10.1002/adma.201501058.

[77] P. Serra and A. Piqué, "Laser-Induced Forward Transfer: Fundamentals and Applications," *Adv. Mater.*, 2018, doi: 10.1002/admt.201800099.

[78] M. Zenou, A. Sa'ar, and & Z. Kotler, "Laser jetting of femto-liter metal droplets for high resolution 3D printed structures," *Sci. Rep.*, vol. 5, p. 17265, 2015, doi: 10.1038/srep17265.

[79] N. Gorodesky *et al.*, "Improving Compactness of 3D Metallic Microstructures Printed by Laser-Induced Forward Transfer," *crystals*, vol. 11, 2021, doi: 10.3390/cryst11030291.

[80] S. Winter, M. Zenou, and Z. Kotler, "Conductivity of laser printed copper structures limited by nano-crystal grain size and amorphous metal droplet shell," *J. Phys. D. Appl. Phys.*, 2016, doi: 10.1088/0022-3727/49/16/165310.

[81] M. Zenou, A. Sa, Z. Kotler, M. Zenou, Z. Kotler, and A. Sa, "Laser Transfer of Metals and Metal Alloys for Digital Microfabrication of 3D Objects Laser Transfer," *Small*, vol. 11, no. 33, 2015, doi: 10.1002/smll.201500612.

[82] A. Reiser *et al.*, "Multi-metal electrohydrodynamic redox 3D printing at the submicron scale," *Nat. Commun.*, vol. 10, no. 1, pp. 1–8, Dec. 2019, doi: 10.1038/s41467-019-09827-1.

[83] R. Merz, "Shape Deposition Manufacturing," Technischen Universität Wien, 1994.

[84] R. Merz, F. B. Ramaswami, K. Terk, and M. Weiss, "Shape Deposition Manufacturing."

[85] A. Da Silva, J. Frostevarg, J. Volpp, and A. F. H. Kaplan, "Additive Manufacturing by laser-assisted drop deposition from a metal wire," *Mater. Des.*, vol. 209, p. 109987, Nov. 2021, doi: 10.1016/J.MATDES.2021.109987.

[86] A. J. Hart, J. D. Beroz, and H. Maghsoodi, “DISCRETE DEPOSITION OF PARTICLES,” US 9 , 937 , 522 B2, 2018.

[87] Sulzer Metco, “An Introduction to Thermal Spray,” 2013.

[88] Y. Xie *et al.*, “Strengthened Peening Effect on Metallurgical Bonding Formation in Cold Spray Additive Manufacturing,” *J. Therm. Spray Technol.*, vol. 28, 2019, doi: 10.1007/s11666-019-00854-4.

[89] Y. Zou, “Cold Spray Additive Manufacturing: Microstructure Evolution and Bonding Features,” *Acc. Mater. Res*, 2021, doi: 10.1021/accountsmr.1c00138.

[90] J. Chang, M. Chi, T. Shen, and Z. Liang, “A comprehensive study on the droplet formation processes and its influencing factors of a tubular piezoelectric print head,” *J. Adhes. Sci. Technol.*, 2019, doi: 10.1080/01694243.2019.1699286.

[91] B. He, S. Yang, Z. Qin, B. Wen, C. Zhang, and G. Key, “The roles of wettability and surface tension in droplet formation during inkjet printing,” *Sci Rep*, 2017, doi: 10.1038/s41598-017-12189-7.

[92] B. Derby, “Inkjet Printing of Functional and Structural Materials: Fluid Property Requirements, Feature Stability, and Resolution,” *Annu. Rev. Mater. Res.*, vol. 40, 2010, doi: 10.1146/annurev-matsci-070909-104502.

[93] N. Reis and B. Derby, “Ink Jet Deposition of Ceramic Suspensions: Modeling and Experiments of Droplet Formation,” *MRS Online Proc. Libr.*, vol. 624, no. 1, pp. 65–70, 2000, doi: 10.1557/PROC-624-65.

[94] Y. Liu and B. Derby, “Experimental study of the parameters for stable drop-on-demand inkjet performance,” *Phys. Fluids*, vol. 31, p. 32004, 2019, doi: 10.1063/1.5085868.

[95] V. A. Beck *et al.*, “A combined numerical and experimental study to elucidate primary breakup dynamics in liquid metal droplet-on-demand printing,” *Phys. Fluids*, vol. 32, p. 112020, 2020, doi: 10.1063/5.0029438.

[96] N. N. Watkins, E. S. Elton, P. H. Paul, J. R. Jeffries, and A. J. Pascall, “Experimentally probing the extremes of droplet-on-demand printability via liquid metals,” *Phys. Fluids*, vol. 33, p. 121301, 2021, doi: 10.1063/5.0076594.

[97] Z. Zhou *et al.*, “High-throughput characterization of fluid properties to predict droplet ejection for three-dimensional inkjet printing formulations,” *Addit. Manuf.*, vol. 29, p. 100792, Oct. 2019, doi: 10.1016/J.ADDMA.2019.100792.

[98] R. Bernasconi, S. Brovelli, P. Viviani, M. Soldo, D. Giusti, and L. Magagnin, “Piezoelectric Drop-On-Demand Inkjet Printing of High-Viscosity Inks,” 2021, doi: 10.1002/adem.202100733.

[99] H. S. Zuo, H. J. Li, L. H. Qi, J. Luo, S. Y. Zhong, and H. P. Li, “Effect of wetting behavior on generation of uniform aluminum droplets obtained by pneumatic drop-on-demand technique,” *J. Mater. Process. Technol.*, vol. 214, no. 11, pp. 2566–2575, Nov. 2014, doi: 10.1016/J.JMATPROTEC.2014.05.017.

[100] Y. Feng, J. Liu, K. Li, H. Li, J. Deng, and Y. Liu, “Waveform Optimization of Piezoelectric Micro-Jet for the Control of Metal Micro-Droplet Ejection,” *IEEE Trans. Ind. Electron.*, vol. 69, no. 4, p. 3967, 2022, doi: 10.1109/TIE.2021.3071680.

[101] M. Ma, X. Wei, X. Shu, and H. Zhang, “Producing solder droplets using piezoelectric membrane-piston-based jetting technology,” *J. Mater. Process. Technol.*, vol. 263, pp. 233–240, Jan. 2019, doi: 10.1016/J.JMATPROTEC.2018.08.029.

[102] E. W. Collings, A. J. Markworth, J. K. Mccoy, and J. H. Saunders, “Splat-quench solidification of freely falling liquid-metal drops by impact on a planar substrate,” 1990.

[103] A. M. Worthington, “On the forms assumed by drops of liquids falling vertically on a horizontal plate,” *Proceeding R. Soc. London*, 1876, doi: http://doi.org/10.1098/rspl.1876.0048.

[104] A. Bondi, “THE SPREADING OF LIQUID METALS ON SOLID SURFACES Surface Chemistry of High-Energy Substances,” *Chem. Rev.*, 1952.

[105] C. Dey Modak, A. Kumar, A. Tripathy, and P. Sen, “Drop impact printing,” *Nat. Commun.*, 2020, doi: 10.1038/s41467-020-18103-6.

[106] P. Kant, R. B. J. Koldeweij, K. Harth, M. A. J. Van Limbeek, D. Lohse, and D. L. Designed, “Fast-freezing kinetics inside a droplet impacting on a cold surface,” *PNAS*, vol. 117, no. 6, pp. 2788–2794, 2020, doi: 10.1073/pnas.1912406117/-/DCSupplemental.y.

[107] X. Han *et al.*, “Droplet Bouncing: Fundamentals, Regulations, and Applications,” *Small*, 2022, doi: 10.1002/smll.202200277.

[108] T. Bennett and D. Poulikakos, “Splat-quench solidification: estimating the maximum spreading of a droplet impacting a solid surface,” 1993.

[109] D. A. Bolleddula, “Droplet impact and spreading of viscous dispersions and volatile solutions,” 2011.

[110] C. Josserand and S. T. Thoroddsen, “Drop Impact on a Solid Surface,” *Rev. Fluid Mech*, vol. 48, pp. 365–91, 2016, doi: 10.1146/annurev-fluid-122414-034401.

[111] X. Yang, V. H. Chhasatia, and Y. Sun, “Oscillation and Recoil of Single and Consecutively Printed Droplets,” *Langmuir*, vol. 29, 2013, doi: 10.1021/la303980j.

[112] R. Rioboo, M. Marengo, and C. Tropea, “Time evolution of liquid drop impact onto solid, dry surfaces,” *Exp. Fluids*, vol. 33, pp. 112–124, 2002, doi: 10.1007/s00348-002-0431-x.

[113] R. Rioboo, C. Tropea, and M. Marengo, “Outcomes from a drop impact on solid surfaces,” *At. Sprays*, 2001, doi: 10.1615/AtomizSpr.v11.i2.40.

[114] A. L. Yarin, “Drop Impact Dynamics: Splashing, Spreading, Receding, Bouncing,” *Annu. Rev. Fluid Mech*, 2006, doi: 10.1146/annurev.fluid.

[115] Y. D. Shikhmurzaev, “Solidification and dynamic wetting: A unified modeling framework,” *Phys. Fluids*, vol. 33, p. 72101, 2021, doi: 10.1063/5.0054431.

[116] J. E. Sprittles and Y. D. Shikhmurzaev, “The Dynamics of Liquid Drops and their Interaction with Solids of Varying Wettabilities,” *Phys. Fluids*, vol. 24, 2012.

[117] Š. Šikalo, H.-D. Wilhelm, and I. V Roisman, “Dynamic contact angle of spreading droplets: Experiments and simulations,” *Phys. Fluids*, vol. 17, p. 62103, 2005, doi: 10.1063/1.1928828.

[118] H.-Y. Kim and J.-H. Chun, “The recoiling of liquid droplets upon collision with solid surfaces,” *Phys. Fluids*, vol. 13, 2001, doi: 10.1063/1.1344183.

[119] S. Schiaffino, “The fundamentals of molten microdrop deposition and solidification,” Massachusetts Institute of Technology, 1996.

[120] S. Schiaffino and A. A. Sonin, “Molten droplet deposition and solidification at low Weber numbers,” *Phys. Fluids*, vol. 9, p. 3172, 1997, doi: 10.1063/1.869434.

[121] M. R. Predtechensky, Y. D. Varlamov, S. N. Ul’iankin, A. N. Cherepanov, and V. N. Popov, “Spreading and Solidification of Liquid Metal Droplets on a Substrate:Experiment, Analytical Model, and Numerical Simulation,” 2000.

[122] W. Z. Fang, F. Zhu, W. Q. Tao, and C. Yang, “How different freezing morphologies of impacting droplets form,” *J. Colloid Interface Sci.*, vol. 584, pp. 403–410, Feb. 2021, doi: 10.1016/J.JCIS.2020.09.119.

[123] D. B. Van Dam and C. Le Clerc, “Experimental study of the impact of an ink-jet printed droplet on a solid substrate,” *Phys. Fluids*, vol. 16, p. 3403, 2004, doi: 10.1063/1.1773551.

[124] I. S. BAYER and C. M. MEGARIDIS, “Contact angle dynamics in droplets impacting on flat surfaces with different wetting characteristics,” *J. Fluid Mech*, vol. 558, pp. 415–449, 2005, doi: 10.1017/S0022112006000231.

[125] H. Dong, W. W. Carr, and J. F. Morris, “Visualization of drop-on-demand inkjet: Drop formation and deposition,” *Rev. Sci. Instrum*, vol. 77, p. 85101, 2006, doi: 10.1063/1.2234853.

[126] M. Pasandideh-Fard, Y. M. Qiao, S. Chandra, and J. Mostaghimi, “Capillary effects during droplet impact on a solid surface,” *Phys. Fluids*, vol. 8, p. 650, 1996, doi: 10.1063/1.868850.

[127] R. B. J. Koldeweij *et al.*, “Initial solidification dynamics of spreading droplets,” *Phys. Rev. Fluids*, vol. 6, p. 121601, 2021, doi: 10.1103/PhysRevFluids.6.L121601.

[128] S. Schiaffino and A. A. Sonin, “On the theory for the arrest of an advancing molten contact line on a cold solid of the same material,” *Phys. Fluids*, vol. 9, p. 2227, 1997, doi: 10.1063/1.869345.

[129] S. Schiaffino and A. A. Sonin, “Motion and arrest of a molten contact line on a cold surface: An experimental study,” *Phys. Fluids*, vol. 9, p. 2217, 1997, doi: 10.1063/1.869344.

[130] M. Pasandideh-Fard, R. Bhola, S. Chandra, and J. Mostaghimi, “Deposition of tin

droplets on a steel plate : Simulations and experiments," *Int. J. Heat Mass Transf.*, 1998, doi: 10.1016/S0017-9310(98)00023-4.

[131] A. I. Fedorchenko and A.-B. Wang, "Non-equilibrium solidification of the molten metal droplets impacting on a solid surface," 2007, doi: 10.1016/j.ijheatmasstransfer.2006.12.025.

[132] T. Bennett and D. Poulikakos, "Heat transfer aspects of splat-quench solidification: modelling and experiment," 1994.

[133] H. P. Li, H. J. Li, L. H. Qi, J. Luo, and H. S. Zuo, "Simulation on deposition and solidification processes of 7075 Al alloy droplets in 3D printing technology," *Trans. Nonferrous Met. Soc. China (English Ed.*, vol. 24, no. 6, pp. 1836–1843, 2014, doi: 10.1016/S1003-6326(14)63261-1.

[134] R. Ghafouri-Azar, S. Shakeri, S. Chandra, and J. Mostaghimi, "Interactions between molten metal droplets impinging on a solid surface," *Int. J. heat*, 2003.

[135] W. Li *et al.*, "Computational study on structures of vertical columns formed by successive droplets," *J. Mater. Process. Technol.*, vol. 288, p. 116903, Feb. 2021, doi: 10.1016/J.JMATPROTEC.2020.116903.

[136] S. Haferl and D. Poulikakos, "Transport and solidification phenomena in molten microdroplet pileup," *J. Appl. Phys.*, vol. 92, 2002, doi: 10.1063/1.1492019.

[137] C.-H. Wang, H.-L. Tsai, Y.-C. Wu, and W.-S. Hwang, "Investigation of molten metal droplet deposition and solidification for 3D printing techniques," *J. Micromechanics Microengineering*, vol. 26, no. 9, p. 095012, Sep. 2016, doi: 10.1088/0960-1317/26/9/095012.

[138] Y. Dou, J. Luo, L. Qi, H. Lian, and X. Hou, "Generation mechanism and suppression method of landing error of two successively deposited metal droplets caused by coalescence and solidification," *Int. J. Heat Mass Transf.*, vol. 172, p. 121100, Jun. 2021, doi: 10.1016/j.ijheatmasstransfer.2021.121100.

[139] L. H. Qi, Y. P. Chao, J. Luo, J. M. Zhou, X. H. Hou, and H. J. Li, "A novel selection method of scanning step for fabricating metal components based on micro-droplet deposition manufacture," *Int. J. Mach. Tools Manuf.*, vol. 56, pp. 50–58, 2012, doi: 10.1016/j.ijmachtools.2011.12.002.

[140] S. Haferl and D. Poulikakos, “Experimental investigation of the transient impact fluid dynamics and solidification of a molten microdroplet pile-up,” *Int. J. Heat Mass Transf.*, vol. 46, no. 3, pp. 535–550, Jan. 2003, doi: 10.1016/S0017-9310(02)00289-2.

[141] M. Liu, H. Yi, H. Cao, R. Huang, and L. Jia, “Heat accumulation effect in metal droplet-based 3D printing: Evolution mechanism and elimination Strategy,” *Addit. Manuf.*, vol. 48, p. 102413, Dec. 2021, doi: 10.1016/J.ADDMA.2021.102413.

[142] T. Hussain, D. G. Mccartney, and P. H. Shipway, “Bonding between aluminium and copper in cold spraying: story of asymmetry,” *Mater. Sci. Technol.*, vol. 28, 2012, doi: 10.1179/1743284712Y.0000000051.

[143] Y. Chao, L. Qi, H. Zuo, J. Luo, X. Hou, and H. Li, “Remelting and bonding of deposited aluminum alloy droplets under different droplet and substrate temperatures in metal droplet deposition manufacture,” *Int. J. Mach. Tools Manuf.*, vol. 69, pp. 38–47, Jun. 2013, doi: 10.1016/J.IJMACHTOOLS.2013.03.004.

[144] X. K. Suo, M. Yu, W. Y. Li, M. P. Planche, and H. L. Liao, “Effect of Substrate Preheating on Bonding Strength of Cold-Sprayed Mg Coatings,” *J. Therm. Spray Technol.*, vol. 21, no. 5, 2012, doi: 10.1007/s11666-012-9803-9.

[145] M. Fang, S. Chandra, and C. B. Park, “Experiments on Remelting and Solidification of Molten Metal Droplets Deposited in Vertical Columns,” *J. Manuf. Sci. Eng.*, 2007, doi: 10.1115/1.2540630.

[146] T. Hussain, D. G. Mccartney, P. H. Shipway, and D. Zhang, “Bonding Mechanisms in Cold Spraying: The Contributions of Metallurgical and Mechanical Components,” *J. Therm. Spray Technol.*, vol. 18, 2009, doi: 10.1007/s11666-009-9298-1.

[147] K. Wang, L. Kong, Y. Tao, T. Li, and T. Xiong, “Numerical Simulation of Minimal Average Bonding Strength to Suppress Rebounding in Cold Spraying Cu/Cu: A Preliminary Study,” *J. Therm. Spray Technol.*, vol. 24, 2015, doi: 10.1007/s11666-014-0150-x.

[148] H. Assadi, F. Gärtner, T. Stoltenhoff, and H. Kreye, “Bonding mechanism in cold gas spraying,” *Acta Mater.*, vol. 51, no. 15, pp. 4379–4394, Sep. 2003, doi: 10.1016/S1359-6454(03)00274-X.

[149] E. E. Balić, M. Hadad, P. P. Bandyopadhyay, and J. Michler, “Fundamentals of adhesion of thermal spray coatings: Adhesion of single splats,” *Acta Mater.*, vol. 57, no. 19, pp. 5921–5926, Nov. 2009, doi: 10.1016/j.actamat.2009.08.042.

[150] J. A. Dantzig and M. Rappaz, *Solidification*. CRC Press Taylor & Francis Group, 2016.

[151] K. Nagashio, H. Murata, and K. Kuribayashi, “Spreading and solidification behavior of molten Si droplets impinging on substrates,” *Acta Mater.*, vol. 52, no. 18, pp. 5295–5301, Oct. 2004, doi: 10.1016/j.actamat.2004.07.039.

[152] P. DAVID A., K. E. EASTERLING, and Y. S. MOHAMED, *Phase Transformations in Metals and Alloys*, THIRD EDIT. CRC Press Taylor & Francis Group, 2009.

[153] C. Bishop, S. A. Spencer, K. S. Schmaltz, and C. Amon, “Microstructural investigation of SDM microcasting droplets,” 1997.

[154] J. Berry *et al.*, “Toward multiscale simulations of tailored microstructure formation in metal additive manufacturing,” *Mater. Today*, vol. 51, pp. 65–86, Dec. 2021, doi: 10.1016/J.MATTOD.2021.09.024.

[155] C. H. Amon, K. Schmaltz, R. Merz, and F. B. Prinz, “Numerical and Experimental Investigation of Interface Bonding Via Substrate Remelting of an Impinging Molten Metal Droplet,” *J. Heat Transfer*, 1996.

[156] K. Nagashio, H. Murata, and K. Kuribayashi, “In situ observation of solidification behavior of Si melt dropped on Si wafer by IR thermography,” *J. Cryst. Growth*, vol. 275, 2004.

[157] H.-S. Zuo, H.-J. Li, L.-H. Qi, J. Luo, S.-Y. Zhong, and Y.-F. Wu, “Effect of non-isothermal deposition on surface morphology and microstructure of uniform molten aluminum alloy droplets applied to three-dimensional printing,” *Appl. Phys. A*, 2015, doi: 10.1007/s00339-014-8735-2.

[158] Y. Idell, N. Watkins, A. Pascall, J. Jeffries, and K. Blobaum, “Microstructural Characterization of Pure Tin Produced by the Drop-on-Demand Technique of Liquid Metal Jetting The thermal diffusion from the droplet to,” *Metall. Mater. Trans. A*, vol. 50, 2019, doi: 10.1007/s11661-019-05357-z.

[159] J. de Ruiter, D. Soto, and K. K. Varanasi, “Self-peeling of impacting droplets,” *Nat. Phys.*, vol. 14, no. 1, pp. 35–39, Jan. 2018, doi: 10.1038/nphys4252.

[160] P. Kant, R. B. J. Koldeweij, K. Harth, M. A. J. Van Limbeek, D. Lohse, and D. L. Designed, “Fast-freezing kinetics inside a droplet impacting on a cold surface,” *Proc. Natl. Acad. Sci. U. S. A.*, vol. 117, no. 6, pp. 2788–2794, 2020, doi: 10.1073/pnas.1912406117/-/DCSupplemental.y.

[161] C. Hun and L. E. Scriven, “Hydrodynamic Model of Steady Movement of a Solid / Liquid / Fluid Contact Line,” *J. Colloid Interface Sci.*, vol. 35, no. 1, pp. 85–101, Jan. 1970, doi: 10.1016/0021-9797(71)90188-3.

[162] Y. D. Shikhmurzaev, “Singularities at the moving contact line. Mathematical, physical and computational aspects,” *Phys. D Nonlinear Phenom.*, vol. 217, no. 2, pp. 121–133, May 2006, doi: 10.1016/J.PHYSD.2006.03.003.

[163] N. Sedighi, S. Murad, and S. K. Aggarwal, “Molecular dynamics simulations of nanodropletspreading on solid surfaces, effect of droplet size,” *Fluid Dyn. Res*, vol. 42, p. 35501, 2010, doi: 10.1088/0169-5983/42/3/035501.

[164] Y. Yang and B. B. Laird, “Droplet spreading on a surface exhibiting solid-liquid interfacial premelting,” *Acta Mater.*, vol. 143, pp. 319–328, Jan. 2018, doi: 10.1016/J.ACTAMAT.2017.10.018.

[165] T. Lee and L. Liu, “Lattice Boltzmann simulations of micron-scale drop impact on dry surfaces,” *J. Comput. Phys.*, vol. 229, no. 20, pp. 8045–8063, Oct. 2010, doi: 10.1016/J.JCP.2010.07.007.

[166] D. D. Holm, L. Ó. Náraigh, and C. Tronci, “A geometric diffuse-interface method for droplet spreading,” *Proceeding R. Soc. A*, 2019, doi: 10.1098/rspa.2019.0222.

[167] Y. D. Shikhmurzaev, *Capillary Flows with Forming Interfaces*. Chapman and Hall/CRC, 2007.

[168] Y. Sui, H. Ding, and P. D. M. Spelt, “Numerical Simulations of Flows with Moving Contact Lines,” *Annu. Rev. Fluid Mech*, vol. 46, pp. 97–119, 2014, doi: 10.1146/annurev-fluid-010313-141338.

[169] J. U. Brackbill, D. B. Kothe, and D. B. Kothe, “A Continuum Method for Modeling

Surface Tension," *Artic. J. Comput. Phys.*, vol. 100, pp. 335–354, 1992, doi: 10.1016/0021-9991(92)90240-Y.

[170] S. F. Kistler, *Hydrodynamics of wetting*. 1993.

[171] R. G. Cox, "The dynamics of the spreading of liquids on a solid surface," *J. Fluid Mech*, vol. 168, pp. 169–194, 1986, doi: 10.1017/S0022112086000332.

[172] J. Göhl, A. Mark, S. Sasic, and F. Edelvik, "An immersed boundary based dynamic contact angle framework for handling complex surfaces of mixed wettabilities," *Int. J. Multiph. Flow*, vol. 109, pp. 164–177, Dec. 2018, doi: 10.1016/J.IJMULTIPHASEFLOW.2018.08.001.

[173] M. Pasandideh-Fard, S. D. Aziz, S. Chandra, and J. Mostaghimi, "Cooling effectiveness of a water drop impinging on a hot surface," *Int. J. Heat Fluid Flow*, vol. 22, no. 2, pp. 201–210, Apr. 2001, doi: 10.1016/S0142-727X(00)00086-2.

[174] I. Malgarinos, N. Nikolopoulos, M. Marengo, C. Antonini, and M. Gavaises, "VOF simulations of the contact angle dynamics during the drop spreading: Standard models and a new wetting force model," *Adv. Colloid Interface Sci.*, vol. 212, pp. 1–20, Oct. 2014, doi: 10.1016/J.CIS.2014.07.004.

[175] I. V Roisman, R. Rioboo, and C. Tropea, "Normal impact of a liquid drop on a dry surface: model for spreading and receding," *Proc. R. socity A*, vol. 458, pp. 1411–1430, 2002, doi: 10.1098/rspa.2001.0923.

[176] S. Das *et al.*, "Oscillation characteristics of low Weber number impinging micro-droplets," *Theor. Comput. Fluid Dyn.*, vol. 33, pp. 197–213, 2019, doi: 10.1007/s00162-019-00489-9.

[177] A. Kumar Jaiswal and S. Khandekar, "Drop-on-Drop Impact Dynamics on a Superhydrophobic Surface," *Langmuir*, vol. 37, 2021, doi: 10.1021/acs.langmuir.1c01779.

[178] P. Attané, F. Girard, and V. Morin, "An energy balance approach of the dynamics of drop impact on a solid surface," *Phys. Fluids*, vol. 19, p. 12101, 2007, doi: 10.1063/1.2408495.

[179] S. Chandra and C. T. Avedisian, "On the collision of a droplet with a solid surface,"

Proceeding R. Soc. London, vol. 432, pp. 13–41, 1991.

[180] T. Mao, D. C. S. Kuhn, and H. Tran, "Spread and Rebound of Liquid Droplets upon Impact on Flat Surfaces," *AIChE J.*, vol. 43, 1997, doi: https://doi.org/10.1002/aic.690430903.

[181] G. Trapaga, E. F. Matthys, J. J. Valencia, and J. Szekely, "Fluid Flow, Heat Transfer, and Solidification of Molten Metal Droplets Impinging on Substrates: Comparison of Numerical and Experimental Results," *Metall. Trans. B*, vol. 23B, 1992.

[182] D. Jia, Y. Liu, P. Yi, X. Zhan, J. Ma, and J. Mostaghimi, "Splat formation mechanism of droplet-filled cold-textured groove during plasma spraying," *Appl. Therm. Eng.*, vol. 173, p. 115239, Jun. 2020, doi: 10.1016/J.APPLTHERMALENG.2020.115239.

[183] B. Kang, J. Waldvogel, and D. Poulikakos, "Remelting phenomena in the process of splat solidification," *J. Mater. Sci.*, vol. 30, no. 19, pp. 4912–4925, Oct. 1995, doi: 10.1007/BF01154504.

[184] L. J. Zarzalejo, K. S. Schmaltz, and C. H. Amon, "Molten droplet solidification and substrate remelting in microcasting Part I: numerical modeling and experimental verification," *Heat Mass Transf.*, vol. 34, pp. 477–485, 1998.

[185] Q. Xu, V. . Gupta, and E. . Lavernia, "Thermal behavior during droplet-based deposition," *Acta Mater.*, vol. 48, no. 4, pp. 835–849, Feb. 2000, doi: 10.1016/S1359-6454(99)00389-4.

[186] P. Vishnoi, "COMPUTATIONAL MODELING OF DROPLET DEPOSITION AND COALESCENCE FOR DROP-WISE ADDITIVE MANUFACTURING," 2018.

[187] J. Du and Z. Wei, "Numerical analysis of pileup process in metal microdroplet deposition manufacture," *Int. J. Therm. Sci.*, vol. 96, pp. 35–44, Oct. 2015, doi: 10.1016/J.IJTHERMALSCI.2015.04.016.

[188] M. M. Yovanovich, "Thermal Interface Joint Conductance and Resistance," pp. 1–4.

[189] W. E. J. Stewart, "Determination of thermal contact resistance between metals using a pulse technique," *Dr. Diss.*, no. 195, 1972.

[190] M. Mantelli and M. M. Yovanovich, “16 Thermal Contact Resistance,” *Spacecr. Therm. Control Handb. Vol. I Fundam. Technol.*, pp. 599–638, 2002.

[191] R. K. Chin, J. L. Beuth, and C. H. Amon, “Thermomechanical Modeling of Successive Material Deposition in Layered Manufacturing,” in *International Solid Freeform Fabrication Symposium*, 1996.

[192] S. D. Aziz and S. Chandra, “Impact, recoil and splashing of molten metal droplets,” *Int. J. Heat Mass Transf.*, vol. 43, no. 16, pp. 2841–2857, Aug. 2000, doi: 10.1016/S0017-9310(99)00350-6.

[193] A. Jafari, S. . Seyedein, and M. Haghpanahi, “MODELING OF HEAT TRANSFER AND SOLIDIFICATION OF DROPLET/SUBSTRATE IN MICROCASTING SDM PROCESS,” *IUST Int. J. Eng. Sci.*, 2008.

[194] A. Hussein, L. Hao, C. Yan, and R. Everson, “Finite element simulation of the temperature and stress fields in single layers built without-support in selective laser melting,” *Mater. Des.*, vol. 52, pp. 638–647, Dec. 2013, doi: 10.1016/j.matdes.2013.05.070.

[195] H. Fukanuma, R. Huang, Y. Tanaka, and Y. Uesugi, “Mathematical Modeling and Numerical Simulation of Splat Cooling in Plasma Spray Coatings,” *J. Therm. Spray Technol.*, vol. 18, 2009, doi: 10.1007/s11666-009-9366-6.

[196] W. Wang, R. A. Lambert, and R. H. Rangel, “Parametric study of multi-splat solidification/remelting including contact resistance effects,” *Int. J. Heat Mass Transf.*, vol. 51, no. 19–20, pp. 4811–4819, Sep. 2008, doi: 10.1016/J.IJHEATMASSTRANSFER.2008.02.015.

[197] T. Bennett and D. Poulikakos, “Heat transfer aspects of splat-quench solidification: modelling and experiment,” 1994.

[198] S. C. Gupta, *The classical Stefan problem: basic concepts, modelling and analysis with quasi-analytical solutions and methods*. Elsevier, 2017.

[199] H. S. Carslaw and J. C. Jaeger, *Conduction of Heat in Solids*. Oxford University Press, 1959.

[200] H. Yi, L. Qi, J. Luo, and N. Li, “Hole-defects in soluble core assisted aluminum

droplet printing: Metallurgical mechanisms and elimination methods," *Appl. Therm. Eng.*, vol. 148, pp. 1183–1193, Feb. 2019, doi: 10.1016/J.APPLTHERMALENG.2018.12.013.

[201] J. Madejski, "Solidification of droplets on a cold surface," *Int. J. Heat Mass Transf.*, vol. 19, no. 9, pp. 1009–1013, Sep. 1976, doi: 10.1016/0017-9310(76)90183-6.

[202] K. Ma, C.-J. Li, and C.-X. Li, "Narrow and Thin Copper Linear Pattern Deposited by Vacuum Cold Spraying and Deposition Behavior Simulation," *J. Therm. Spray Technol.*, doi: 10.1007/s11666-020-01102-w.

[203] A. Valarezo, K. Shinoda, and S. Sampath, "Effect of Deposition Rate and Deposition Temperature on Residual Stress of HVOF-Sprayed Coatings," *J Therm Spray Tech*, 2020, doi: 10.1007/s11666-020-01073-y.

[204] A. A. Abubakar, A. F. M. Arif, S. K. Al-Athel, and S. S. Akhtar, "Modeling Residual Stress Development in Thermal Spray Coatings: Current Status and Way Forward," *J. Therm. Spray Technol.*, vol. 26, 2017, doi: 10.1007/s11666-017-0590-1.

[205] X. Tian, S. Xiong, Y. Zhang, and K. Zhang, "Simulation of thermal stress in ion beam sputtered Ta 2 O 5 /SiO 2 multilayer coatings on different substrates by finite element analysis," *Surf. Coatings Technol.*, vol. 362, pp. 225–233, Mar. 2019, doi: 10.1016/j.surfcoat.2019.02.004.

[206] J. Haider, M. Rahman, B. Corcoran, and M. S. J. Hashmi, "Simulation of thermal stress in magnetron sputtered thin coating by finite element analysis," *J. Mater. Process. Technol.*, vol. 168, no. 1, pp. 36–41, Sep. 2005, doi: 10.1016/j.jmatprotec.2004.09.093.

[207] M. Wenzelburger, M. Escribano, and R. Gadow, "Modeling of thermally sprayed coatings on light metal substrates: - layer growth and residual stress formation," *Surf. Coatings Technol.*, vol. 180–181, pp. 429–435, Mar. 2004, doi: 10.1016/j.surfcoat.2003.10.125.

[208] H. L. Wei *et al.*, "Mechanistic models for additive manufacturing of metallic components," *Prog. Mater. Sci.*, vol. 116, p. 100703, Feb. 2021, doi: 10.1016/J.PMATSCI.2020.100703.

[209] M. Alimardani, E. Toyserkani, and J. P. Huissoon, "A 3D dynamic numerical

approach for temperature and thermal stress distributions in multilayer laser solid freeform fabrication process," *Opt. Lasers Eng.*, vol. 45, no. 12, pp. 1115–1130, Dec. 2007, doi: 10.1016/J.OPTLASENG.2007.06.010.

[210] J. C. Heigel, P. Michaleris, and E. W. Reutzel, "Thermo-mechanical model development and validation of directed energy deposition additive manufacturing of Ti-6Al-4V," *Addit. Manuf.*, vol. 5, pp. 9–19, Jan. 2015, doi: 10.1016/j.addma.2014.10.003.

[211] E. R. Denlinger, M. Gouge, J. Irwin, and P. Michaleris, "Thermomechanical model development and in situ experimental validation of the Laser Powder-Bed Fusion process," *Addit. Manuf.*, vol. 16, pp. 73–80, Aug. 2017, doi: 10.1016/J.ADDMA.2017.05.001.

[212] C. Li, J. F. Liu, X. Y. Fang, and Y. B. Guo, "Efficient predictive model of part distortion and residual stress in selective laser melting," *Addit. Manuf.*, vol. 17, pp. 157–168, Oct. 2017, doi: 10.1016/J.ADDMA.2017.08.014.

[213] N. . Klingbeil, J. . Beuth, R. . Chin, and C. . Amon, "Residual stress-induced warping in direct metal solid freeform fabrication," *Int. J. Mech. Sci.*, vol. 44, no. 1, pp. 57–77, Jan. 2002, doi: 10.1016/S0020-7403(01)00084-4.

[214] H. Yi, L. Qi, J. Luo, D. Zhang, and N. Li, "Direct fabrication of metal tubes with high-quality inner surfaces via droplet deposition over soluble cores," *J. Mater. Process. Technol.*, vol. 264, pp. 145–154, Feb. 2019, doi: 10.1016/J.JMATPROTEC.2018.09.004.

[215] L. H. Qi, S. Y. Zhong, J. Luo, D. C. Zhang, and H. S. Zuo, "Quantitative characterization and influence of parameters on surface topography in metal micro-droplet deposition manufacture," *Int. J. Mach. Tools Manuf.*, vol. 88, pp. 206–213, Jan. 2015, doi: 10.1016/J.IJMACHTOOLS.2014.09.009.

[216] W. Xiong, L. Qi, J. Luo, D. Zhang, J. Liang, and H. Yi, "Experimental investigation on the height deviation of bumps printed by solder jet technology," *J. Mater. Process. Technol.*, vol. 243, pp. 291–298, May 2017, doi: 10.1016/j.jmatprotec.2016.12.031.

[217] M. Jehle *et al.*, "Direct printing of electrical connections from metal melts using

StarJet technology," *2017 IEEE 19th Electron. Packag. Technol. Conf. EPTC 2017*, vol. 2018-February, pp. 1–4, Jan. 2018, doi: 10.1109/EPTC.2017.8277490.

[218] S. Gorsse, C. Hutchinson, M. Gouné, and R. Banerjee, "Additive manufacturing of metals: a brief review of the characteristic microstructures and properties of steels, Ti-6Al-4V and high-entropy alloys," *Sci. Technol. Adv. Mater.*, vol. 18, 2017, doi: 10.1080/14686996.2017.1361305.

[219] B. Himmel, D. Rumschoettel, and W. Volk, "Tensile properties of aluminium 4047A built in droplet-based metal printing," *Rapid Prototyp. J.*, vol. 25, no. 2, pp. 427–432, 2019, doi: 10.1108/RPJ-02-2018-0039.

[220] H. Zuo, H. Li, L. Qi, and S. Zhong, "Influence of Interfacial Bonding between Metal Droplets on Tensile Properties of 7075 Aluminum Billets by Additive Manufacturing Technique," *J. Mater. Sci. Technol.*, vol. 32, no. 5, pp. 485–488, May 2016, doi: 10.1016/J.JMST.2016.03.004.

[221] X. S. Jiang, L. H. Qi, J. Luo, H. Huang, and J. M. Zhou, "Research on accurate droplet generation for micro-droplet deposition manufacture," *Int. J. Adv. Manuf. Technol.*, vol. 49, no. 5–8, pp. 535–541, 2010, doi: 10.1007/s00170-009-2403-2.

[222] S. X. Cheng, T. Li, and S. Chandra, "Producing molten metal droplets with a pneumatic droplet-on-demand generator," *J. Mater. Process. Technol.*, vol. 159, no. 3, pp. 295–302, Feb. 2005, doi: 10.1016/J.JMATPROTEC.2004.05.016.

[223] R. Zamora, J. J. Hernández Ortega, J. López, F. Faura, and J. Hernández, "Development of a facility for molten metal micro-droplets generation. Application to microfabrication by deposition," *Procedia Eng.*, vol. 132, pp. 110–117, 2015, doi: 10.1016/j.proeng.2015.12.486.

[224] R. M. Young and E. Pfender, "Nusselt number correlations for heat transfer to small spheres in thermal plasma flows," *Plasma Chem. Plasma Process.*, vol. 7, no. 2, pp. 211–229, 1987, doi: 10.1007/BF01019179.

[225] E. Toyserkani, A. Khajepour, and S. Corbin, "3-D finite element modeling of laser cladding by powder injection: effects of laser pulse shaping on the process," *Opt. Lasers Eng.*, vol. 41, no. 6, pp. 849–867, Jun. 2004, doi: 10.1016/S0143-8166(03)00063-0.

[226] M. Xue, Y. Heichal, C. Sanjeev, and J. Mostaghimi, “Modeling the impact of a molten metal droplet on a solid surface using variable interfacial thermal contact resistance,” *J Mater Sci*, vol. 42, pp. 9–18, 2007, doi: 10.1007/s10853-006-1129-x.

[227] T. J. Miller, S. J. Zinkle, and B. A. Chin, “Strength and fatigue of dispersion-strengthened copper,” *J. Nucl. Mater.*, vol. 179–181, no. PART 1, pp. 263–266, Mar. 1991, doi: 10.1016/0022-3115(91)90076-J.

[228] W. D. Jenkins, T. G. Digges, and C. R. Johnson, “Tensile Properties of Copper, Nickel, and 70-Percent-Cop-per-30-Percent-Nickel and 30-Percent-Copper-70-Percent-Nickel Alloys at High Temperatures,” *J. Res. Natl. Bur. Stand. (1934).*, vol. 58, 1957.

[229] M. P. Mughal, H. Fawad, and R. Mufti, “Finite element prediction of thermal stresses and deformations in layered manufacturing of metallic parts,” *Acta Mech.*, vol. 183, pp. 61–79, 2006, doi: 10.1007/s00707-006-0329-4.

[230] Y. Zhong, H. Fang, Q. Ma, and X. Dong, “Analysis of droplet stability after ejection from an inkjet nozzle,” *J. Fluid Mech*, vol. 845, pp. 378–391, 2018, doi: 10.1017/jfm.2018.251.

[231] T. Wang, T.-H. Kwok, and C. Zhou, “In-situ Droplet Inspection and Control System for Liquid Metal Jet 3D Printing Process,” *Procedia Manuf.*, vol. 10, pp. 968–981, 2017, doi: 10.1016/j.promfg.2017.07.088.

[232] D. Zhao, H. Zhou, Y. Wang, J. Yin, and Y. Huang, “Drop-on-demand (DOD) inkjet dynamics of printing viscoelastic conductive ink,” *Addit. Manuf.*, vol. 48, p. 102451, Dec. 2021, doi: 10.1016/J.ADDMA.2021.102451.

[233] L. Herran, “Jet instability and dropelt formation for bio-printing applications,” Clemson University, 2013.

[234] R. M. Verkouteren and J. R. Verkouteren, “Inkjet Metrology II: Resolved Effects of Ejection Frequency, Fluidic Pressure, and Droplet Number on Reproducible Drop-on-Demand Dispensing,” vol. 27, p. 24, 2011, doi: 10.1021/la201728f.

[235] T. Wang, T.-H. Kwok, and C. Zhou, “In-situ Droplet Inspection and Control System for Liquid Metal Jet 3D Printing Process,” *Procedia Manuf.*, vol. 10, pp. 968–981, 2017, doi: 10.1016/j.promfg.2017.07.088.

[236] M. Tsai, W. Hwang, H. H. Chou, and P. H. Hsieh, “Effects of pulse voltage on inkjet printing of a silver nanopowder suspension,” *Nanotechnolog*, 2008, doi: 10.1088/0957-4484/19/33/335304.

[237] S. Y. Zhong, L. H. Qi, J. Luo, H. S. Zuo, X. H. Hou, and H. J. Li, “Effect of process parameters on copper droplet ejecting by pneumatic drop-on-demand technology,” *J. Mater. Process. Technol.*, vol. 214, no. 12, pp. 3089–3097, 2014, doi: 10.1016/J.JMATPROTEC.2014.07.012.

[238] D. Sivakumar, K. Katagiri, T. Sato, and H. Nishiyama, “Spreading behavior of an impacting drop on a structured rough surface,” *Phys. Fluids*, vol. 17, p. 100608, 2005, doi: 10.1063/1.2033627.

[239] W. Zhang, T. Yu, J. Fan, W. Sun, and Z. Cao, “Droplet impact behavior on heated micro-patterned surfaces,” *J. Appl. Phys*, vol. 119, p. 114901, 2016, doi: 10.1063/1.4943938.

[240] A. T. Paxson and K. K. Varanasi, “Self-similarity of contact line depinning from textured surfaces,” *Nat. Commun.*, vol. 4, no. 1, p. 1492, Jun. 2013, doi: 10.1038/ncomms2482.

[241] N. Wang, F. Wang, F. Pan, S. Yu, and D. Pan, “Highly Efficient Silver Catalyst Supported by a Spherical Covalent Organic Framework for the Continuous Reduction of 4-Nitrophenol,” *ACS Appl. Mater. Interfaces*, vol. 13, p. 3220, 2021, doi: 10.1021/acsami.0c20444.

[242] B. Akhavan *et al.*, “Direct covalent attachment of silver nanoparticles on radical-rich plasma polymer films for antibacterial applications,” *J. Mater. Chem. B*, vol. 6, p. 5845, doi: 10.1039/c8tb01363b.

[243] H. Najafi-Ashtiani, F. Jing, D. G. McCulloch, and B. Akhavan, “ITO-free silver-doped DMD structures: HiPIMS transparent-conductive nano-composite coatings for electrochromic applications,” *Sol. Energy Mater. Sol. Cells*, vol. 231, p. 111268, Oct. 2021, doi: 10.1016/J.SOLMAT.2021.111268.

[244] W. Sim, R. T. Barnard, M. A. T. Blaskovich, and Z. M. Ziora, “antibiotics Antimicrobial Silver in Medicinal and Consumer Applications: A Patent Review of the Past Decade (2007-2017),” *Antibiotics*, 2018, doi: 10.3390/antibiotics7040093.

[245] J. Fernandes *et al.*, “Silver nanoparticle conductive inks: synthesis, characterization, and fabrication of inkjet-printed flexible electrodes,” *Sci. Rep.*, 2020, doi: 10.1038/s41598-020-65698-3.

[246] S. N. Baig, I. Kammakakam, and W. Falath, “Nanomaterials: a review of synthesis methods, properties, recent progress, and challenges,” *Mater. Adv*, vol. 2, pp. 1821–1871, 2021, doi: 10.1039/d0ma00807a.

[247] J. Vaithilingam *et al.*, “Combined Inkjet Printing and Infrared Sintering of Silver Nanoparticles using a Swathe-by-Swathe and Layer-by-Layer Approach for 3-Dimensional Structures,” *Appl. Mater. interfaces*, 2017, doi: 10.1021/acsami.6b14787.

[248] B. Akhavan *et al.*, “Plasma activated coatings with dual action against fungi and bacteria,” *Appl. Mater. Today*, vol. 12, pp. 72–84, Sep. 2018, doi: 10.1016/J.APMT.2018.04.003.

[249] S. Lin, B. Zhao, S. Zou, J. Guo, Z. Wei, and L. Chen, “Impact of viscous droplets on different wettable surfaces: Impact phenomena, the maximum spreading factor, spreading time and post-impact oscillation,” *J. Colloid Interface Sci.*, vol. 516, pp. 86–97, Apr. 2018, doi: 10.1016/J.JCIS.2017.12.086.

[250] S. Yin *et al.*, “Cold spray additive manufacturing and repair: Fundamentals and applications,” *Additive Manufacturing*, vol. 21. Elsevier B.V., pp. 628–650, 01-May-2018, doi: 10.1016/j.addma.2018.04.017.

[251] J. W. Elmer, J. Klingmann, and K. Van Bibber, “Diffusion bonding and brazing of high purity copper for linear collider accelerator structures,” *Phys. Rev. Spec. Top. - Accel. Beams*, vol. 4, no. 5, p. 053502, May 2001, doi: 10.1103/PhysRevSTAB.4.053502.

[252] K. Yang, M. Fukumoto, T. Yasui, and M. Yamada, “Study of Substrate Preheating on Flattening Behavior of Thermal-Sprayed Copper Particles,” *J. Therm. Spray Technol.*, 2007, doi: 10.1007/s11666-010-9515-y.

[253] J. W. Krumpfer and T. J. McCarthy, “Smooth surfaces without contact angle hysteresis,” *Faraday Discuss.*, 2010, doi: 10.1039/c005270c.

[254] S. Annuar, R. Mahmoodian, M. Hamdi, and K.-N. Tu, “Intermetallic compounds in

3D integrated circuits technology: a brief review," *Sci. Technol. Adv. Mater.*, vol. 18, no. 1, pp. 693–703, 2017, doi: 10.1080/14686996.2017.1364975.

[255] M. O, G. Vakanas, N. Moelans, M. Kajihara, and W. Zhang, "Formation of compounds and Kirkendall vacancy in the Cu-Sn system," *Microelectron. Eng.*, vol. 120, pp. 133–137, May 2014, doi: 10.1016/j.mee.2013.09.009.

[256] Y. Yang, H. Lu, C. Yu, and Y. Li, "Void formation at the interface in Sn/Cu solder joints," *Microelectron. Reliab.*, vol. 51, no. 12, pp. 2314–2318, Dec. 2011, doi: 10.1016/j.microrel.2011.06.026.

[257] J. Feng, C. Hang, Y. Tian, B. Liu, and C. Wang, "Growth kinetics of Cu 6 Sn 5 intermetallic compound in Cu-liquid Sn interfacial reaction enhanced by electric current," *Sci. Rep.*, vol. 8, p. 1775, 2018, doi: 10.1038/s41598-018-20100-1.

[258] F. Fanicchia *et al.*, "Residual stress and adhesion of thermal spray coatings: Microscopic view by solidification and crystallisation analysis in the epitaxial CoNiCrAlY single splat," *Mater. Des.*, vol. 153, pp. 36–46, 2018, doi: 10.1016/j.matdes.2018.04.040.

[259] J. A. S. B. Cardoso, A. Almeida, and R. Vilar, "Microstructure of a coated single crystalline René N5 part repaired by epitaxial laser deposition," *Addit. Manuf.*, vol. 49, p. 102515, Jan. 2022, doi: 10.1016/J.ADDMA.2021.102515.

[260] S. W. Yao, T. Liu, C. J. Li, G. J. Yang, and C. X. Li, "Epitaxial growth during the rapid solidification of plasma-sprayed molten TiO2 splat," *Acta Mater.*, vol. 134, pp. 66–80, Aug. 2017, doi: 10.1016/j.actamat.2017.05.052.

[261] A. Hadadzadeh, B. S. Amirkhiz, S. Shakerin, J. Kelly, J. Li, and M. Mohammadi, "Microstructural investigation and mechanical behavior of a two-material component fabricated through selective laser melting of AlSi10Mg on an Al-Cu-Ni-Fe-Mg cast alloy substrate," *Addit. Manuf.*, vol. 31, p. 100937, Jan. 2020, doi: 10.1016/j.addma.2019.100937.

[262] A. Chaudhuri, Y. Raghupathy, D. Srinivasan, S. Suwas, and C. Srivastava, "Microstructural evolution of cold-sprayed Inconel 625 superalloy coatings on low alloy steel substrate," *Acta Mater.*, vol. 129, pp. 11–25, May 2017, doi: 10.1016/j.actamat.2017.02.070.

[263] C. Borchers, F. Gä Rtner, T. Stoltenhoff, H. Assadi, and H. Kreye, “Microstructural and macroscopic properties of cold sprayed copper coatings,” *J. Appl. Phys.*, vol. 93, p. 20010, 2003, doi: 10.1063/1.1573740.

[264] Z. Zou, M. Simonelli, J. Katrib, G. Dimitrakis, and R. Hague, “Refinement of the grain structure of additive manufactured titanium alloys via epitaxial recrystallization enabled by rapid heat treatment,” *Scr. Mater.*, vol. 180, pp. 66–70, Apr. 2020, doi: 10.1016/J.SCRIPTAMAT.2020.01.027.

[265] P. Karimi *et al.*, “Columnar-to-equiaxed grain transition in powder bed fusion via mimicking casting solidification and promoting in situ recrystallization,” *Addit. Manuf.*, vol. 46, p. 102086, Oct. 2021, doi: 10.1016/J.ADDMA.2021.102086.

[266] X. Zou *et al.*, “Grain refinement by dynamic recrystallization during laser direct energy deposition of 316L stainless steel under thermal cycles,” *J. Manuf. Process.*, vol. 76, pp. 646–655, Apr. 2022, doi: 10.1016/J.JMAPRO.2022.01.057.

[267] H. E. Sabzi *et al.*, “Grain refinement in laser powder bed fusion: The influence of dynamic recrystallization and recovery,” *Mater. Des.*, vol. 196, p. 109181, Nov. 2020, doi: 10.1016/J.MATDES.2020.109181.

[268] S. Mirzababaei, B. K. Paul, and S. Pasebani, “Microstructure-property relationship in binder jet produced and vacuum sintered 316 L,” *Addit. Manuf.*, vol. 53, p. 102720, May 2022, doi: 10.1016/J.ADDMA.2022.102720.

[269] X. Luo *et al.*, “Circumventing the strength–ductility trade-off of β-type titanium alloys by defect engineering during laser powder bed fusion,” *Addit. Manuf.*, vol. 51, p. 102640, Mar. 2022, doi: 10.1016/J.ADDMA.2022.102640.

[270] S. Gao *et al.*, “Recrystallization-based grain boundary engineering of 316L stainless steel produced via selective laser melting,” *Acta Mater.*, vol. 200, pp. 366–377, Nov. 2020, doi: 10.1016/J.ACTAMAT.2020.09.015.

[271] M. Gäumann, S. Henry, F. Cléton, J. D. Wagnière, and W. Kurz, “Epitaxial laser metal forming: analysis of microstructure formation,” *Mater. Sci. Eng. A*, vol. 271, no. 1–2, pp. 232–241, Nov. 1999, doi: 10.1016/S0921-5093(99)00202-6.

[272] F. Fanicchia *et al.*, “Residual stress and adhesion of thermal spray coatings: Microscopic view by solidification and crystallisation analysis in the epitaxial

CoNiCrAlY single splat," *Mater. Des.*, vol. 153, pp. 36–46, Sep. 2018, doi: 10.1016/J.MATDES.2018.04.040.

[273] Y. Li *et al.*, "Multi-scale microstructural investigation of a laser 3D printed Ni-based superalloy," *Addit. Manuf.*, vol. 34, p. 101220, Aug. 2020, doi: 10.1016/J.ADDMA.2020.101220.

[274] J.-Y. Juang *et al.*, "Copper-to-copper direct bonding on highly (111)-oriented nanotwinned copper in no-vacuum ambient OPEN," doi: 10.1038/s41598-018-32280-x.

[275] C.-M. Liu *et al.*, "Low-temperature direct copper-to-copper bonding enabled by creep on (111) surfaces of nanotwinned Cu," *Sci Rep*, vol. 5, 2015, doi: 10.1038/srep09734.

[276] Q. Wu, T. Mukherjee, A. De, and T. DebRoy, "Residual stresses in wire-arc additive manufacturing – Hierarchy of influential variables," *Addit. Manuf.*, vol. 35, p. 101355, Oct. 2020, doi: 10.1016/j.addma.2020.101355.

[277] T. Mukherjee, W. Zhang, and T. DebRoy, "An improved prediction of residual stresses and distortion in additive manufacturing," *Comput. Mater. Sci.*, vol. 126, pp. 360–372, Jan. 2017, doi: 10.1016/j.commatsci.2016.10.003.

[278] T. DebRoy *et al.*, "Additive manufacturing of metallic components – Process, structure and properties," *Progress in Materials Science*, vol. 92. Elsevier Ltd, pp. 112–224, 01-Mar-2018, doi: 10.1016/j.pmatsci.2017.10.001.

[279] H. H. Yu, M. Y. He, and J. W. Hutchinson, "Edge effects in thin film delamination," 2001.

[280] A. M. Kamara and K. Davey, "A numerical and experimental investigation into residual stress in thermally sprayed coatings," *Int. J. Solids Struct. 44*, 2007, doi: 10.1016/j.ijsolstr.2007.06.031.

[281] A. A. Abubakar *et al.*, "Modeling Residual Stress Development in Thermal Spray Coatings: Current Status and Way Forward," *J Therm Spray Tech*, 2017, doi: 10.1007/s11666-017-0590-1.

[282] D. Tang, "Effect of substrate preheating temperature and coating thickness on

residual stress in plasmasprayed hydroxyapatite coating," in *OP Conf. Series: Materials Science and Engineering*, 2015, doi: 10.1088/1757-899X/87/1/012097.

[283] G. Vastola, G. Zhang, Q. X. Pei, and Y. W. Zhang, "Controlling of residual stress in additive manufacturing of Ti6Al4V by finite element modeling," *Addit. Manuf.*, vol. 12, pp. 231–239, Oct. 2016, doi: 10.1016/j.addma.2016.05.010.

[284] W. Liu, G. X. Wang, and E. F. Matthys, "Thermal analysis and measurements for a molten metal drop impacting on a substrate: cooling, solidification and heat transfer coefficient," *Int. J. Heat Mass Transf.*, vol. 38, no. 8, pp. 1387–1395, May 1994, doi: 10.1016/0017-9310(94)00262-T.

[285] X. Zhao, Z. Jia, W. Li, and Y. Li, "Numerical simulation of micro droplet formation combined with pneumatic and piezoelectric drive," *Microsyst. Technol.*, vol. 25, 2019, doi: 10.1007/s00542-018-4237-z.

[286] T. Chang *et al.*, "In-situ monitoring for liquid metal jetting using a millimeter-wave impedance diagnostic," *Sci. Rep.*, 2020, doi: 10.1038/s41598-020-79266-2.

[287] Y. Watanabe, C. Yoshida, K. Atsumi, M. Yamada, and M. Fukumoto, "Influence of Substrate Temperature on Adhesion Strength of Cold-Sprayed Coatings," *J. Therm. Spray Technol.*, 2014, doi: 10.1007/s11666-014-0165-3.

[288] R. S. C. Paredes, S. C. Amico, and A. S. C. M. D'Oliveira, "The effect of roughness and pre-heating of the substrate on the morphology of aluminium coatings deposited by thermal spraying," *Surf. Coatings Technol.*, vol. 200, no. 9, pp. 3049–3055, Feb. 2006, doi: 10.1016/J.SURFCOAT.2005.02.200.

[289] M. Froend, V. Ventzke, F. Dorn, N. Kashaev, B. Klusemann, and J. Enz, "Microstructure by design: An approach of grain refinement and isotropy improvement in multi-layer wire-based laser metal deposition," *Mater. Sci. Eng. A*, vol. 772, p. 138635, Jan. 2020, doi: 10.1016/J.MSEA.2019.138635.

[290] A. Durga *et al.*, "Grain refinement in additively manufactured ferritic stainless steel by in situ inoculation using pre-alloyed powder," *Scr. Mater.*, vol. 194, p. 113690, Mar. 2021, doi: 10.1016/J.SCRIPTAMAT.2020.113690.

[291] S. Gao, R. Liu, R. Huang, X. Song, and M. Seita, "A hybrid directed energy deposition process to manipulate microstructure and properties of austenitic stainless

steel," *Mater. Des.*, vol. 213, p. 110360, Jan. 2022, doi: 10.1016/J.MATDES.2021.110360.

[292] F. Fanicchia *et al.*, "Residual stress and adhesion of thermal spray coatings: Microscopic view by solidification and crystallisation analysis in the epitaxial CoNiCrAlY single splat," *Mater. Des.*, vol. 153, pp. 36–46, Sep. 2018, doi: 10.1016/j.matdes.2018.04.040.